Towards a Ge-Sb-Se/S hyperspectral imaging probe for early cancer diagnosis

The University of Nottingham
UNITED KINGDOM · CHINA · MALAYSIA

Harriet Parnell, BSc (Hons)

Supervisors: Prof. Angela B Seddon and Dr. Colin Scotchford

Research Division: Materials, Mechanics and Structures

Thesis submitted to the University of Nottingham for the degree of Doctor of Philosophy

February 2018

Abstract

Owing to their vitreous nature and mid-infrared (MIR) transparency, chalcogenide glasses are a promising material for remote hyperspectral imaging. For medical applications, such as *in-vivo* cancer diagnosis, Ge-Sb-Se glasses are a particularly interesting material since, it is believed that Sb-containing chalcogenides are less toxic than their As-containing equivalents. For passive optical fibres which aim to deliver and collect MIR light to and from tissue samples, the main challenge which faces their performance is the removal of extrinsic optical losses. Hence, this Project explores and develops high purity Ge-Sb-Se/S bulk glasses and optical fibres.

Focussing on the $Ge_xSb_{10}Se_{90-x}$ atomic % (at. %) glass series, bulk samples are initially characterised before the fibre-drawing capability of each composition is assessed. Although stoichiometric $Ge_{25}Sb_{10}Se_{65}$ at. % and non-stoichiometric $Ge_{20}Sb_{10}Se_{70}$ at. % glasses both exist within the same two-dimensional, overconstrained network, results from their fibre-drawing investigations reveal a significant difference in their resistance against crystallisation. Whereas, non-stoichiometric $Ge_{20}Sb_{10}Se_{70}$ at. % is shown to produce stable optical fibres with promising low losses, it is found that stoichiometric $Ge_{25}Sb_{10}Se_{65}$ at. % repeatedly crystallises into a single phase of monoclinic $GeSe_2$.

To produce a low numerical aperture (NA) step-index fibre (SIF), it is suggested that a $Ge_{20}Sb_{10}Se_{70}$ at. % core glass is paired with a $Ge_{20}Sb_{10}Se_{67}S_3$ at. % cladding glass. Substituting 3 at. % Se for 3 at. % S in the $Ge_{20}Sb_{10}Se_{70-x}S_x$ at. % series, is found to increase the glass transition temperature (T_g) by 10 °C and decrease the refractive index by 0.01. It is calculated, that for a SIF consisting of a $Ge_{20}Sb_{10}Se_{70}$ at. % core and a $Ge_{20}Sb_{10}Se_{67}S_3$ at. % cladding, the NA would be 0.25 at 3.1 µm wavelength. Co-extruded at 267±0.1 °C, and then subsequently drawn into 200 ±5 µm diameter SIF, optical loss measurements demonstrate that MIR light can be successfully guided through a large, circular $Ge_{20}Sb_{10}Se_{70}$ at. % core. The core-cladding ratio is found to be 95 %.

Calculations using the Antoine equation are used to investigate the optimal conditions required for the bake-out of Se, S and Sb impurities prior to batching. For a high-purity $Ge_{20}Sb_{10}Se_{70}$ at. % core glass, a distillation technique is developed using 1000 ppm wt. $TeCl_4$ as a hydrogen getter [H] and 700 ppm wt. Al as an oxygen getter [O]. It is shown, that to successfully distil Ge-Sb-Se glass, with [H] and [O] getters, two primary challenges must be overcome. The first suggests that there must be sufficient removal of $HCl_{(g)}$, prior to the start of distillation, in order to avoid a vapour barrier once the silica glass distillation rig is sealed. The second advises precise temperature control, with necessary monitoring, so that there is no separation of Ge-Sb-Se material, either before or after it has distilled.

Successful distillation, is eventually achieved in an open system *i.e.* under flowing vacuum, at a temperature close to 693 °C. Optical fibre loss measurements, conducted on 18 m length of 200 ±10 μm diameter fibre, reveal that the distillation of $Ge_{20}Sb_{10}Se_{70}$ at. % core glass with 1000 ppm wt. $TeCl_4$ and 700 ppm wt. Al, removes the Ge-O absorption peak at 7.9 μm and significantly reduces, if not removes, all of the Se-H peaks as well. The lowest background loss is also found as 0.44 dB/m at 6.4 μm wavelength.

As a preliminary investigation into the biocompatibility of Ge-Sb-Se glasses for medical applications, two *in-vitro* cytotoxicity test are explored *viz.*: a direct contact protocol with an alamarBlue® assay and an elution protocol with a neutral red assay. Due to contradictory results between Trial 1 and Trial 2, it is suggested that further work is required to confirm the cytotoxicity of etched *vs.* non-etched Ge-Sb-Se fibres.

Overall, there has been significant progress made during this Project, towards the fabrication of high purity Ge-Sb-Se/S SIFs for use in a MIR imaging probe for early cancer diagnosis.

Publications

Parnell H, Furniss D, Tang Z, Neate N, Benson TM, Seddon AB, ‘Compositional dependence of crystallization in Ge-Sb-Se glasses relevant to optical fibre making’, Journal of the American Ceramic Society, 2017, **101**, p 208-219.

Parnell H, Butterworth J, Sakr H, Tang Z, Furniss D, Benson TM, Scotchford C and Seddon AB, ‘Ge-Sb-Se glass fibre-optics for *in-vivo* mid-infrared optical biopsy’, SPIE Proceedings, 2016, **9703**.

Publications in preparation

Parnell H, Furniss D, Tang Z, Benson TM and Seddon AB, ‘Low loss Ge-Sb-Se optical glass fibres for mid-infrared photonics’, *to be submitted, 2018*.

Parnell H, Furniss D, Tang Z, Benson TM and Seddon AB, ‘Low numerical aperture Ge-Sb-Se/S chalcogenide step-index fibres for mid-infrared photonics’, *to be submitted, 2018*.

Parnell H, Scotchford C, Kubiena T, Gan W and Seddon AB, ‘*In-vitro* cytotoxicity assessment of Ge-Sb-Se fibres for medical applications’, *to be submitted, 2018*.

Acknowledgements

I would like to thank the following people for their encouragement and support during my PhD:

First and foremost, I would like to thank Professor Angela Seddon for inspiring me to pursue a PhD and for being an incredible ambassador for women in engineering. Your guidance, support and supervision has been second-to-none and I thank you for helping me realise my potential. I would also like to thank all the other members of the Mid-infrared Photonics Group, including Professor Trevor Benson, for your support during Monday morning RGMs. I would like to specifically acknowledge Dr David Furniss and Dr Zhuoqi Tang, who are incredibly talented researchers. You helped build my confidence in the labs and were always so generous with your time.

I would also like to thank Dr Colin Scotchford for his supervision and guidance through the thesis write up.

To all my friends and resident tutors at Derby Hall, I thank you for sharing in my trials and tribulations and for always being on hand after a long day in the labs. Thank you for making me laugh and for keeping me smiling- particularly following a difficult night on duty!

Of course, thank you to my family and to Will, for your ongoing support through every chapter in my life. Although it’s taken my entire PhD to teach you what three elements are in my glass, your love and understanding have always laid the perfect foundations for my future.

Thank you all.

“Glass is much more gentile, graceful, and noble than any metal. It is more delightful, polite, and slightly than any other material at this day known to the world”

Antonio Neri, 1612.

(1998, Perspectives on History of Glass Composition)

Glossary of symbols and abbreviations

Chemicals			
Al	Aluminium	**O**	Oxygen
Ge	Germanium	**S**	Sulfur
H	Hydrogen	**Sb**	Antimony
HCl	Hydrochloric acid	**Se**	Selenium
HF	Hydrofluoric acid	**$TeCl_4$**	Tellurium chloride

Techniques	
DSC	Differential scanning calorimetry
DTA	Differential thermal analysis
EDX	Energy dispersive X-ray analysis
FTIR	Fourier transform infrared spectroscopy
SEM	Scanning electron microscopy
TEM	Transmission electron microscopy
TMA	Thermal mechanical analysis
XRD	X-ray diffractometry

Abbreviations/ miscellaneous	
ANOVA	Analysis of variance
ASTM	American Society for Testing
at. %	Atomic %
BB	Broadband
BSE	Backscattered electrons
CONM	Chemically ordered network model
dB/m	Decibels per meter
DMEM	Dulbecco’s Modified Eagle’s Medium
DTGS	Deuterated triglycine sulfate
E_c	Activation energy of crystallisation

Abbreviations/ miscellaneous (cont.)	
Et al.	Et alia (and others)
FBS	Foetal bovine serum
FEWS	Fibre evanescent wave spectroscopy
FIR	Far-infrared
Glo	Globar
HMDS	Hexamethyldisilazane
ICDD-PDF	International Centre for Diffraction Data Powder Diffraction File
ID/OD	Inner diameter / outer diameter
InSb	Indium antimonide
In-vitro	Performed or taking place outside a living organism
In-vivo	Performed or taking place in a living organism
IR	Infrared
ISO	International Organisation for Standards
k	Boltzmann constant
KBr	Potassium bromine
MCN	Mean coordination number
MCT	Mercury cadmium telluride
MIR	Mid-infrared
M_g	Dilatometric softening point
MM	Multimode
m.p.	Melting point
n	Refractive index
N_{bb}	Number of bond bending constraints
N_{bs}	Number of bond stretching constraints
N_t	Total number of contraints
NA	Numerical aperture
NIR	Near-infrared
NRU	Neutral red uptake

Abbreviations/ miscellaneous (cont.)	
p	Vapour pressure
PBS	Phosphate Buffer Solution
r.f.	Radio frequency
RFU	Relative fluorescence
SAED	Selected area electron diffraction
SE	Secondary electrons
SI	Single index
SIF	Step index fibre
SM	Single mode
T_c	Crystallisation temperature
T_f	Fictive temperature
T_g	Glass transition temperature
T_m	Melting temperature
TIR	Total internal reflection
vol. %	Volume %
WAT	Weak absorption tail
wt. %	Weight %
5N/6N	99.999 %/ 99.9999 % purity
ΔG	Gibbs free energy change
ΔT	Temperature change
λ	Wavelength
µm	Micrometre
θ	Angle

Table of contents

Chapter 1: Introduction

Recent statistics released by Cancer Research UK now reveal that 1 in 2 people, born after 1960, will be diagnosed with cancer at some point during their lifetime[1, 2]. Diagnosing patients whilst they are in the early stages of the disease is of paramount importance for their survival yet, the Gold Standard[3] for cancer diagnosis still relies on a lengthy biopsy procedure, using dyes and optical microscopy, conducted by a histopathologist[4]. However, new research[5, 6] which focuses on a group of mid-infrared (MIR) transmitting glasses, known as the chalcogenides, could offer a unique potential to study early stage cancer *in-vivo* thus, providing an immediate diagnosis for the patient.

Unlike conventional silica optical fibres used in telecommunications, chalcogenide glasses have larger atoms and weaker bonds, which pushes their fundamental absorption to longer infrared (IR) wavelengths[7]. Depending on the composition, chalcogenide glasses can provide transparency between 0.6 to 20 µm wavelength[8] which importantly, covers the atmospheric windows of 3-5 µm and 8-12 µm[9] and thus, the molecular fingerprints[10-12] of all biological species. As one of only a few materials able to transmit MIR light (other examples include: monocrystalline Ge, polycrystalline ZnSe[9]), the additional vitreous nature of chalcogenide glasses, makes them particularly unique candidate remote hyperspectral imaging .

However, before chalcogenide glasses can fulfil this potential, further research is required to find non-toxic compositions which have a wide MIR spectral transmission range, high optical homogeneity, stability against crystallisation and, most importantly, high chemical purity. Extrinsic losses, caused by impurity absorptions such as oxygen, hydrogen and carbon[8], or scattering centres, such as crystals and inclusions[13], significantly limit the photonic application of chalcogenide glasses. Consequently, studying the sources of these extrinsic losses, as well as developing methods through which to eliminate them, remains one of the most active research areas in chalcogenide glasses.

Further challenges associated with the development of a MIR hyperspectral imaging probe, also include the pairing of two chalcogenide compositions during the fabrication of step-index fibres (SIF). For successful delivery and collection of MIR light to and from a tissue sample, chalcogenide SIFs should be prepared with a higher refractive index core, surrounded by a lower refractive index cladding. Therefore, careful compositional selection is required, so that the chosen chalcogenide glasses are similar enough in thermal properties to extrude/ fibre-draw together, creating a high quality SIF interface yet, disparate enough in optical properties so that the desired numerical aperture (NA) is achieved as well as permitting total internal reflection (TIR).

1.1 Aims and objectives of the Project

The overall aim of this Project, is to explore and investigate the properties of chalcogenide glasses and optical fibres, which will eventually assist in the passive transmission of MIR light within a hyperspectral imaging probe, for early cancer diagnosis. Since, the focus of this research is based on a medical application, non-arsenic containing Ge-Sb-Se chalcogenide glasses, will be primarily considered. It is hoped that the results of this work will not only improve the understanding of Ge-Sb-Se glasses, specifically relevant to optical fibres, but will also allow a high-quality MIR transmitting material to be made, through the development of a sophisticated purification technique. To achieve the overall aim, this Project has several objectives:

1. To investigate the Ge-Sb-Se chalcogenide glass system and determine which composition is most suitable for optical fibre applications.

2. To study the crystallisation behaviour of Ge-Sb-Se glasses relevant to fibre-drawing.

3. To develop a low numerical aperture, step-index fibre based on the Ge-Sb-Se/S chalcogenide glass systems.

4. To develop a purification technique which is capable of producing low loss, Ge-Sb-Se optical fibres.

5. To investigate the *in-vitro* cytotoxicity of Ge-Sb-Se optical fibres and gain a greater understanding of their potential in medical applications.

1.2 Structure of the Thesis

The structure of the thesis is presented in Figure 1.1 and shows that a literature review, focussing on Ge-Sb-Se/S glasses, their properties, fabrication methods and applications, is first presented in Chapter 2 followed by the experimental techniques, outlined in Chapter 3. This Project is split into four experimental results and discussion chapters as shown in Figure 1.1, which comply with the objectives listed in section 1.1. Where necessary, the Reader is directed to relevant results and discussions in other chapters.

Chapter 4, based on the Author's publication Parnell *et al.*[14], initially presents the fibre-drawing capabilities of two compositions from the $Ge_xSb_{10}Se_{90-x}$ at. % (atomic %) glass system before exploring their crystallisation behaviours using bulk glass characterisation techniques. Based on these results, Chapter 5 then focusses on the non-stoichiometric $Ge_{20}Sb_{10}Se_{70}$ at. % composition which is combined with a second $Ge_{20}Sb_{10}Se_{67}S_3$ at. % composition, to form the core and cladding glasses, respectively, of a step-index-fibre. The preparation and distillation techniques of high-purity $Ge_{20}Sb_{10}Se_{70}$ at. % glass is then discussed in Chapter 6, as well as presenting the low loss results from an 18 m length of $Ge_{20}Sb_{10}Se_{70}$ at. % optical fibre. Chapter 7 then focusses more towards the application of Ge-Sb-Se glasses, through an initial investigation into their cytotoxicity with 3T3 fibroblast cells.

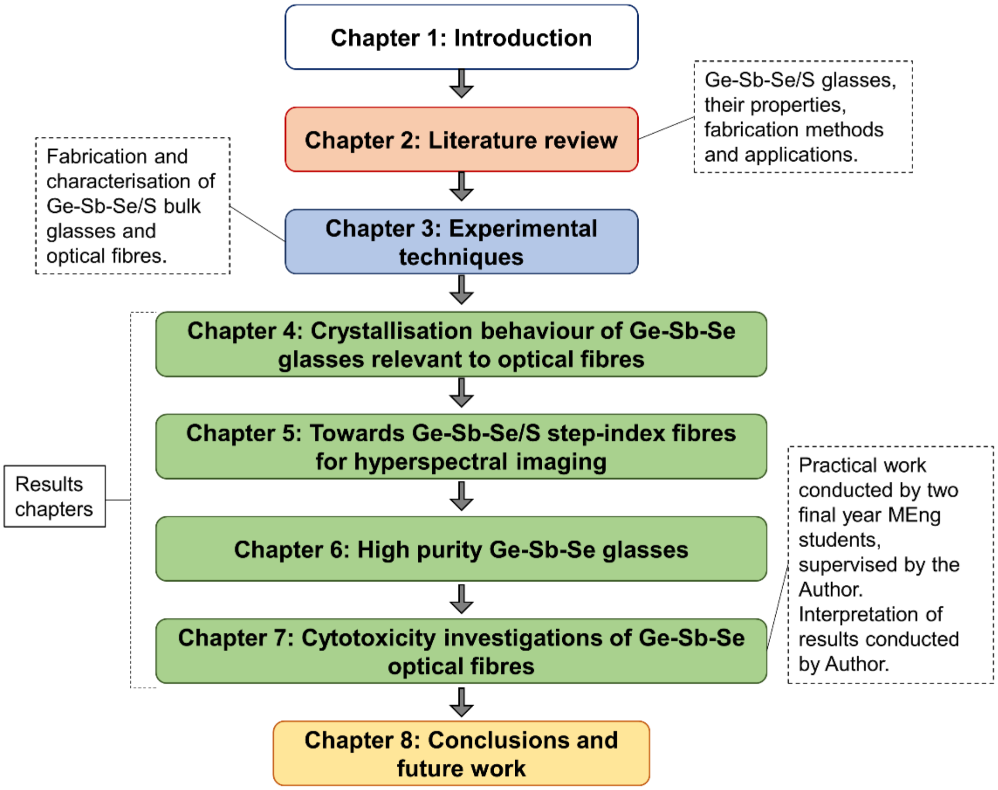

Figure 1.1: Structure of thesis.

Chapter 2: Literature review

This chapter is an introduction to the theory and recent progress in chalcogenide glasses, specifically within the Ge-Sb-Se/S systems. Section 2.1 will provide a brief overview of glass science, covering their fundamental characteristics and properties. Section 2.2 will then focus on the chalcogenide glasses, specifically discussing the Ge-Sb-Se and Ge-Sb-Se-S systems, and their current understanding within the literature. As this project aims to produce high purity Ge-Sb-Se/S glasses for mid-infrared (MIR) hyperspectral imaging, section 2.3 will explore optical loss mechanisms associated with chalcogenide glasses, before discussing purification techniques in section 2.4, which have helped to minimise these. Section 2.5 will then provide a brief introduction into fibre optics and the fabrication of step index fibres (SIF) before moving onto section 2.6 which discusses their potential applications. For use in a biomedical device section 2.7, reveals what measures have already been taken to ensure their suitability within the medical industry.

2.1 Glass science fundamentals

Glasses are one of the most ancient materials used in human history with earliest records dating as far back as 7000 BC[15, 16]. First considered to have semi-precious status, it took several millennia before the ornamental material was transformed into one with purpose and function, due to the advent of glass blowing around 50 BC[17]. Glass science only really became significant by the late 19th century when Abbe and Schott published ‘Glastechnisches Laboratorium, Schott and Genossen’ which contained 44 optical glass compositions[15]. Then in 1920 Turner directed a systematic approach for measuring the physical properties of glasses which improved our understanding of the term ‘glass’, allowing it to describe other non-crystalline solids, and not just oxide glass[17].

Overtime, there has been a variety of attempts to define a glass[18] with most old textbooks[19, 20] containing the American Society for Testing Materials (ASTM) version as ‘an inorganic product of fusion which has been cooled to a rigid condition without crystallisation'[21]. However, this restrictive definition does not consider other fabrication routes, such as vapour deposition or a sol gel route. Here it is defined as 'an X-ray amorphous material which exhibits a glass transition; this being defined as a phenomenon in which a solid amorphous phase exhibits with changing temperature a more or less sudden change in the derivative thermodynamic properties, such as heat capacity and expansion coefficient, from crystal-like to liquid-like values'[22].

2.1.1 Formation of a glass: volume- temperature diagram

The easiest way to illustrate glass formation, and the relationship between liquid, crystalline and glassy forms, is through the volume-temperature diagram seen in Figure 2.1. When a liquid (point a) is cooled to its liquidus (point b), there is a gradual decrease in enthalpy as it begins to contract. From here it can take one of two routes. If the rate of cooling is sufficiently slow, there is enough time for nuclei present in the melt to crystallise, as demonstrated by the significant decrease in volume from point b-e in Figure 2.1. On further cooling the stable crystal will continue to contract (point f). If however, the rate of cooling is sufficiently fast (from point b), then molecular motions are constrained and crystallisation is avoided. The supercooled liquid will instead have a small decrease in volume before entering a glass transition temperature, T_g, range. As stated in the most recent definition, this is an integral property of glass and is the one characteristic which separates it from other amorphous materials. T_g signifies the passage of a supercooled liquid to a glass and can be defined by: 1) the temperature at which the shear viscosity equals 10^{13} Poise[23] or 2) where the liquid and vitreous portions of Figure 2.1 intersect, which is usually at $2T_m/3$[23]. Only below T_g is it correct to describe the material as a glass.

Once the supercooled liquid has entered the glass transition region it can take a variety of routes depending on the cooling rate. For faster cooling rates (to point c) the resulting glass will have larger volume whereas a slower cooling rate (to point d) would allow more time for configurational changes to occur, thus producing a higher density glass.

The fictive temperature of a glass(T_f) defines the structure of a glass and can be found upon reheating[24]. By extrapolating along the glass line (*e.g.* along c or d), T_f can be found at the point where this intersects the supercooled liquid, equilibrium line (T_{f1} and T_{f2} in Figure 2.1). Therefore, both T_g and T_f depend on the cooling rate of the glass and it is often assumed that the two are equal[25, 26].

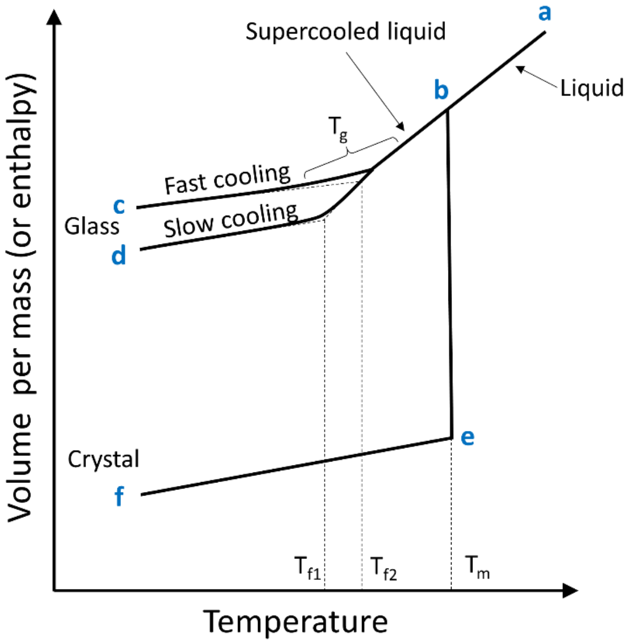

Figure 2.1: Volume per mass (or enthalpy) vs. temperature graph demonstrating the relationship between the glassy, liquid and solid state[16, 20].

Considering Figure 2.1, glass is a state of matter rather than a single composition. Its atomic structure is composed of covalently bonded atoms which lack periodicity and long-range order[20], effectively appearing like a frozen snapshot of a liquid but behaving like a solid. As thermodynamics predicts, systems will naturally move towards the lowest energy state (*i.e.* most stable) which is usually an ordered crystalline solid. However, for glasses, kinetics has overruled this behaviour due to a lack of time during solidification. Instead, a non-ideal state is formed and the glass remains disordered with greater energy content than the parent crystalline phase. This means at any given opportunity, above its T_g, a glass will transform into its preferred crystalline state. Figure 2.2 shows a two-dimensional representation of each structure, highlighting the difference in atomic arrangement.

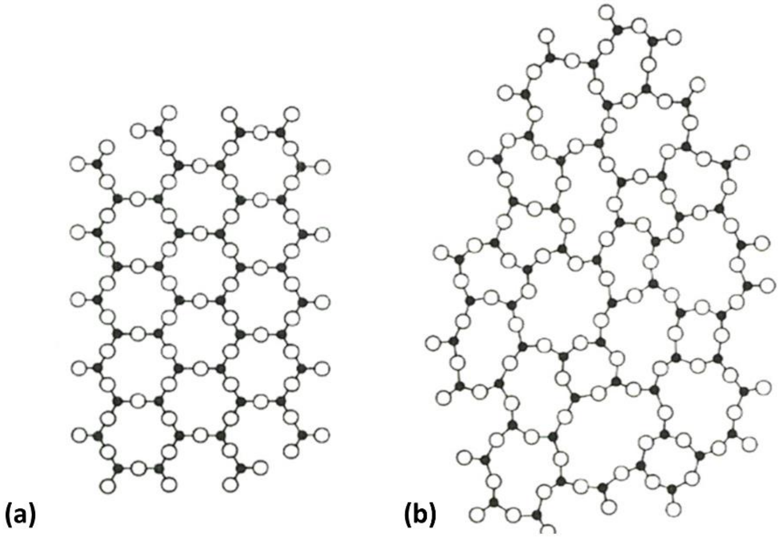

Figure 2.2: Adapted diagram of a two-dimensional representation of the structure of (a) a hypothetical crystalline compound and (b) the corresponding glassy form[27].

Therefore, understanding the fundamental characteristics of crystallisation and associated conditions that may favour this transition, is of great importance in glass science.

2.1.2 Crystallisation

Crystallisation, often referred to as devitrification if formed from an amorphous material[28], is governed by two important factors -nucleation and the crystal growth rate. This being the formation of a submicroscopic nucleus and subsequent growth into a macroscopic crystalline phase. A brief overview of the two stages are given here.

2.1.2.1 Nucleation

Nucleation can occur either homogeneously or heterogeneously. In homogenous nucleation the glass-crystal transition begins in the absence of any foreign boundaries *i.e.* the nucleation is spontaneous influenced by local fluctuations of density and kinetic energy[29]. This type of nucleation has been traditionally theorised by Volmer[30], Becker and Doring[31], Frenekel[32] and Zeldovich[33]. During homogeneous transformation, two types of energy must be considered for a newly formed spherical nucleus with a radius of $\boldsymbol{r}$: 1) the specific free energy, per unit volume, associated with the liquid-solid phase change, $\boldsymbol{\Delta g_v}$ and 2) the interfacial tension between the embryo and the liquid *i.e.* the energy required to form a new surface, $\boldsymbol{\gamma}$**.** Along with the elastic distortion energy associated with structural change, $\boldsymbol{\Delta G_E}$, the Gibbs free energy change (ΔG) can be examined using **equation 2.1**[34].

$$\Delta G = -\frac{4}{3}\pi r^3 \Delta g_v + 4\pi r^2 \gamma + \Delta G_E \qquad \textbf{Equation 2.1}$$

If ΔG is negative, then surface tension energy and elastic strain are smaller than the volume change *i.e.* embryos are of a critical size ***r****, and therefore the nucleus will grow[29]. If ΔG is positive then the energy associated with crystal-liquid interface is greater than the free energy associated with crystallisation. In this case the embryos are smaller than r* and too unstable to grow[29]. This relationship is demonstrated in Figure 2.3 and it should be noted that both r* and ΔG* decrease with increasing undercooling.

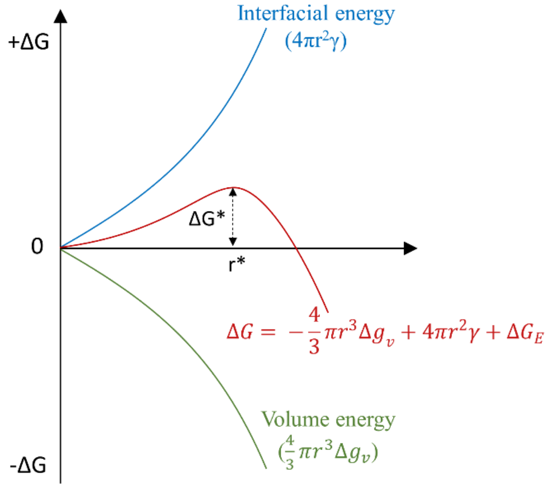

Figure 2.3: Adapted schematic diagram of the change in Gibbs free energy (ΔG) as a function of the radius size (r)[29].

Practically however, it is almost impossible to remove all foreign bodies from the glass *e.g.* impurities, dust on the surface or even the wall of the melting vessel. These heterogeneous sites can influence the ΔG* barrier and reduce it by a factor related to the contact angle of the nucleus on the foreign surface, see **equation 2.2[29].**

$$\textbf{(a)}\ \Delta G^*_{het} = \Delta G^*_{homo} f(\theta)$$

$$(\boldsymbol{b})\ f(\theta) = \frac{(2+cos\theta)(1-cos\theta)^2}{4} \qquad \textbf{Equation 2.2}$$

So long as the contact angle (θ) is small, heterogeneous nucleation rather than homogeneous nucleation will occur[29]. The nucleation rate, $\boldsymbol{I}$, is shown in **equation 2.3**[16] where A is a constant, W^* and ΔG_D are the thermodynamic and kinetic free energy barriers to nucleation, k is the Boltzmann constant and T is the absolute temperature in Kelvin[16]. This equation looks at the number of nuclei per unit volume formed per unit time, and is determined by dividing the concentration of nuclei by the total time spent at the nucleation temperature during the isothermal heat treatment. Simply put, it addresses the thermodynamic barrier associated with the free energy change when a nucleus forms as well as, the kinetic barrier associated with the rearrangement of atoms to allow the crystal to grow.

$$I = A \exp[-(W^* + \Delta G_D)/kT] \qquad \textbf{Equation 2.3}$$

2.1.2.2 Crystal growth

The rate at which nucleation and crystal growth occurs, as a function of temperature, can be seen in Figure 2.4. Above T_1 the material is in a liquid state and there is no driving force towards the formation of a nucleus. As the temperature is lowered the material passes through a metastable zone of cooling. Here, ΔG (equation 2.1) will be positive as r* will be large. Therefore, nuclei with a radius <r* may form but will be too unstable for growth. As the temperature decreases further past T_2, the driving force towards the supercooled liquid-crystal transformation increases, and so the r* will be smaller. Eventually, r* will become so small significant numbers of stable nuclei will form and crystal growth will occur highlighted by the shaded region in Figure 2.4. However, with a continual decrease in temperature towards T_3, the viscosity of the material increases and acts as a kinetic barrier to both nucleation and growth.

Although Figure 2.4 suggests that no crystals will grow within the metastable zone of supercooling, this is only applicable to homogeneous nucleation. If foreign particles are present within the melt, and have radii above the critical size, crystal growth can be detected between T_1 and T_2.

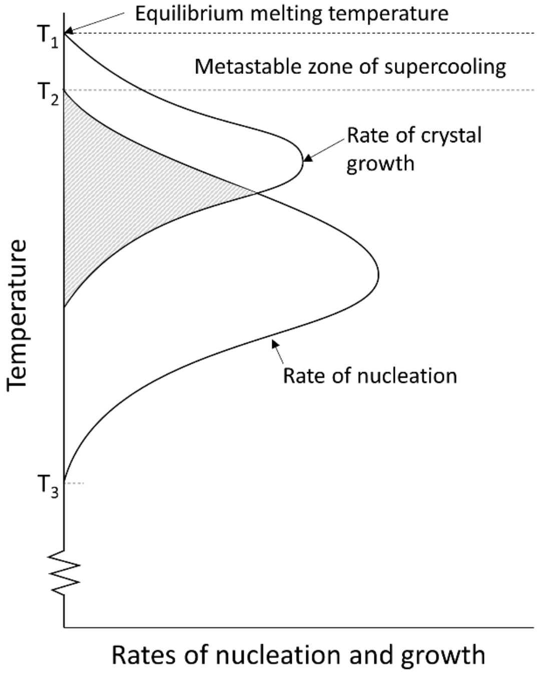

Figure 2.4: Adapted diagram of the effect of temperature on the rates of homogeneous nucleation and crystal growth[20]*.*

Equation 2.4 provides a general model for the crystal growth rate, U, where a_o is the interatomic separation distance, v is the vibrational frequency and ΔE and ΔG are the kinetic and thermodynamic barriers to crystal growth[16].

$$U = a_o v \exp\left(-\frac{\Delta E}{kT}\right)\left[1 - \exp\left(\frac{\Delta G}{kT}\right)\right] \qquad \textbf{Equation 2.4}$$

The basic models used to describe crystal growth rates will not be discussed in detail here but include: normal growth, screw dislocation growth and surface crystallisation[29].

2.2 Chalcogenide glasses

Chalcogenide glasses are based on one or more of the chalcogen elements, sulfur (S), selenium (Se) or tellurium (Te)[35-37]. With a valence shell of ns^2np^3, they are found in Group XVI of the Periodic Table[38] and are predominantly formed through covalent bonds with maximum ionic character reaching 9 %[36]. Their compositions depend on the formation of a covalent polymeric framework with elements of a similar electro-negativity[39], such as Ge, As, Sb, or Ga. Large atomic masses when chemically bonded generate low energy phonons, which give chalcogenide glasses their characteristic optical transparency far into the infrared wavelength region[40, 41] as demonstrated by Figure 2.5.

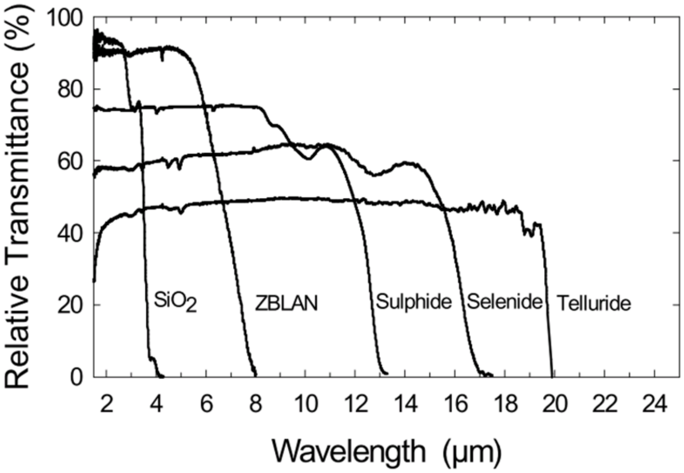

Figure 2.5: Transmission spectra of several glasses with an optical thickness between 2-3 mm[42].

Unlike oxide- or halide-based glasses, the atomic ratio between the positive elements (As, Ge, Sb *etc*) and the negative elements (Se, S, Te *etc*) is not always constant[43] as chalcogenide glasses are able to form homogenous bonds (-Se-Se-) which result in a broad glass-forming region where stoichiometry, and thus physical properties, can be uniquely tailored[13]. For example the As-S system, which was the first chalcogenide compositions investigated over fifty years ago,[44, 45] can have an atomic As/S ratio within the range of 1.5 ~ 9[46]. For this reason chalcogenide glasses are expressed using the atomic percentage or ratio of the constituent elements *e.g.* $Ge_{20}As_{10}Se_{70}$ at. %.

Table 2.1 summarises some of the key physical parameters of two chalcogenide glasses binary As_2S_3 at. % and ternary $Ge_{33}As_{12}Se_{65}$ at. %, as well as silica glass for comparison.

Table 2.1: Adapted comparison of the key physical properties of As_2S_3 and $Ge_{33}As_{12}Se_{65}$ (in atomic %) chalcogenide glass and silica glass[13]*.*

Property	**As_2S_3**	**$Ge_{33}As_{12}Se_{65}$**	**Silica glass**
Glass transition temperature, T_g /°C	180	362	1175
Thermal expansion coefficient /°C	21.4×10^{-6}	12×10^{-6}	0.55×10^{-6}
Density, kg/m^3	3200	4400	2200
Young's Modulus /GPa	15.9	22.1	72.2
Refractive index	2.41 (5 µm)	2.49 (5 µm)	1.458 (0.59 µm)

2.2.1 Ge-Sb-Se chalcogenide glass system

Said to be less toxic than their arsenic-containing counterparts[47], the Ge-Sb-Se glass system has received growing interest for application in a variety of forms *i.e.* bulk, fibre or thin films[48-61]. Defined by 5-35 atomic % (at. %) Ge, 5-40 at. % Sb and the remainder Se[62], Ge-Sb-Se compositions exhibit robustness, relatively good thermal, mechanical and chemical properties and high transparency across the 2-16 µm wavelength range.[62-65] Like other chalcogenide systems, the physical properties of Ge-Sb-Se glasses are dependent on their composition, which can be described by a number of structural models. One is the chemically ordered network model (CONM)[66, 67] which assumes that the formation of heteropolar bonds are preferred over homopolar bonds and gives rise to a Ge-Sb-Se system made up of tetrahedral-like [$GeSe_4$] and pyramidal-like [$SbSe_3$] chemically stable units[68]. At certain combinations, the structure is assumed to be formed entirely from heteropolar bonds as the Ge and Sb are fully coordinated by Se; this is commonly known as a stoichiometric glass or the 'chemical threshold' of a system[68]. It is at this threshold where an extremum occurs for a number of properties such as the glass transition temperature (T_g), density and refractive index[47] as seen in Figure 2.6.

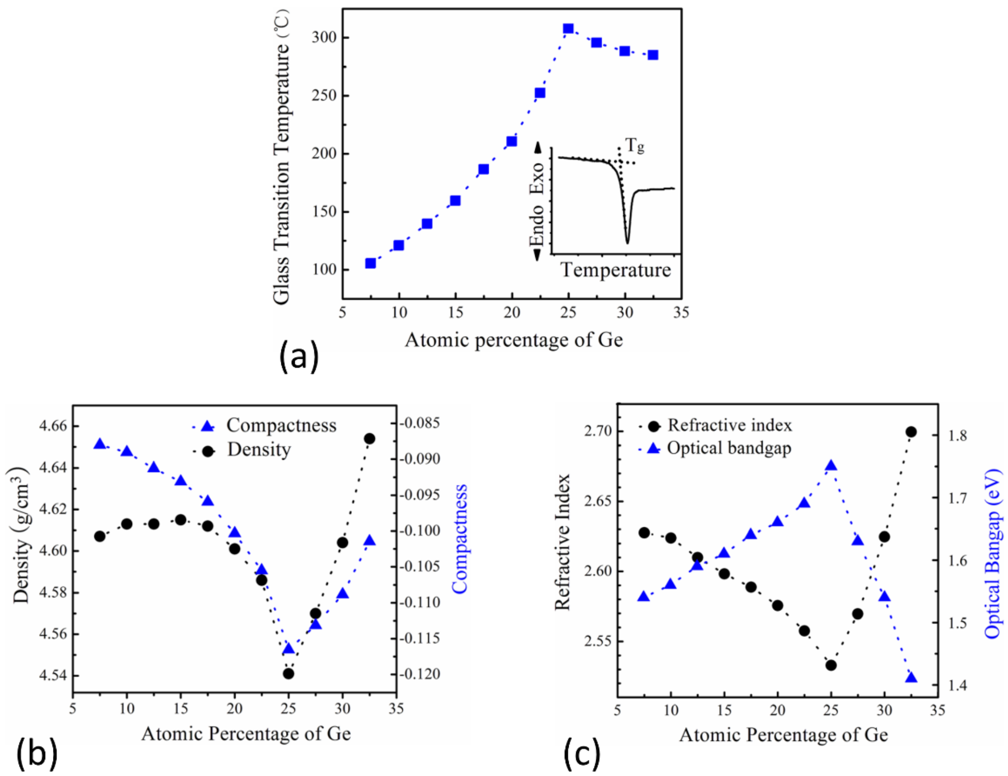

Figure 2.6: Adapted graphs showing the threshold behaviour of the Ge$_x$Sb$_{10}$Se$_{90-x}$ *at. % system for several physical properties: (a) glass transition temperature,* T_g*; (b) density and Compactness; and (c) refractive index and optical bandgap*[47].

Another approach is given by the topological models, i.e. the ‘Constraint Theory’[69] and structural dimensionality considerations[70], where the properties are proposed to be dependent on the mean coordination number (MCN). This latter approach predicts two topological thresholds where the network changes from a floppy state to a rigid network, with a subsequent change from a two- to three-dimensional structure, at MCN= 2.4, and MCN= 2.67, respectively[69, 70]. For binary systems, such as As-Se, and ternary systems, such as Ge-As-Se, where all of the elements concerned have similar atomic masses and radii, the relationship between physical properties and the MCN is relatively well understood[49]. However, for the Ge-Sb-Se glasses, the elemental Sb has a larger atomic radius than its neighbouring Ge or Se (133 pm, 125 pm and 103 pm, respetively[71]), topological models are not as accurate in predicting their physical properties[49, 72] and these are dictated more by their chemical composition- a relationship that is less well understood at present.

2.2.2 Ge-Sb-Se-S chalcogenide system

The best chalcogenide compositions for fibre-drawing procedures are usually those with binary or ternary systems[13]. However, it is also true that an increase in the number of constituent elements forming the basis of the chalcogenide network can also improve their glass-forming ability, particularly complex glasses with four or more elements[73]. Like selenide glasses, sulfide glasses are easy to form and often exhibit superior glass stability *e.g.* in atomic ration As_2Se_3 *vs.* As_2S_3[13]. As with the Ge-Sb-Se glass system, Ge-Sb-S chalcogenides have also been investigated for use in several different forms *i.e.* bulk, thin films and optical fibres[74-79]. However, there is little documented work on the combined Ge-Sb-Se/S system, including their ability to be drawn into optical fibres.

Nevertheless, those that do exists include two systematic approaches taken by Wang *et al*.[80] and Guery *et al.*[81]. Each investigation explored the substitution of one chalcogen element for another (*i.e.* either S for Se[81] or Se for S[80]) and assessed the impact of this on several physical properties in Ge-Sb-Se/S glasses. It was seen that with increasing S content, both the linear and nonlinear refractive indices decreased whilst the T_g, optical band gap and laser damage threshold increased[80]. Using a parallel plate viscometer, it was also shown that log-viscosity curves shift to a lower temperature when sulfur is substituted by selenium[81].

However, the elemental substitution of one chalcogen for another had little effect on the structure of the glass and any observed change in physical property, was primarily caused by the difference in strength between the S-Ge(Sb) and Se-Ge(Sb) chemical bonds[80]. Through Raman spectroscopy and X-ray photoelectron spectroscopy Guery *et al.*[81] found that there was a change in dominant bonds as one chalcogen was substituted for another. In sulfur-rich Ge-Sb-Se/S glasses, the dominant GeS_4 molecular units were gradually replaced by Sb-based bonds (*e.g.* Sb-Sb or $SbSe_{3/2}$ pyramidal units) with an increase in the selenium content. It was also shown that because the ratio of $GeS_{4/2}$ to $SbSe_{3/2}$ is not linear with the S/Se substitution, neither was the trend in physical properties *e.g.* micro-hardness, T_g, viscosity *etc*. The constant T_g value present between x=30-45 in the $Ge_{28}Sb_{12}S_{60-}$

$_xSe_x$ glass range (Figure 2.7) reflects this switch in dominant bonds. Thus, the change of the dominant bond type in Ge-Sb-Se/S networks is at the centre of the glass property modifications exhibited by the glass family[81].

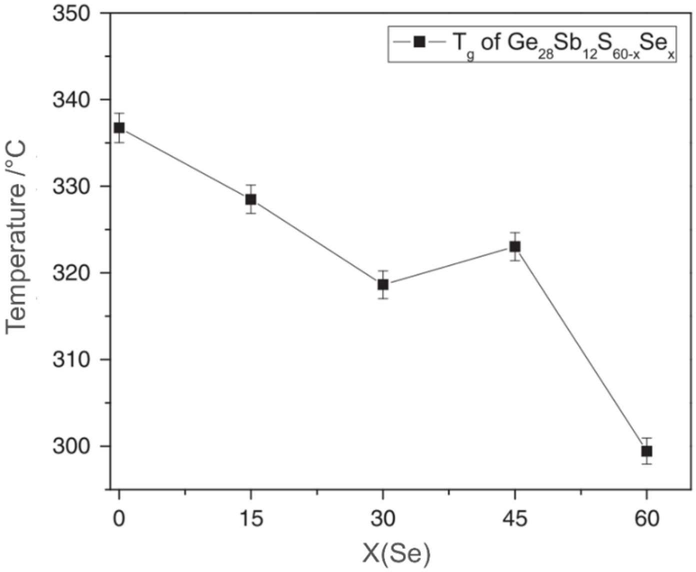

Figure 2.7: Change in the glass transition temperature, T_g, as a function of the substitution of S by Se in Ge-Sb-Se/S glasses[81].

2.3 Optical loss mechanisms in chalcogenide glasses

Mid-infrared optical fibres, which encompasses the chalcogenide glasses, can be defined as fibre optics that can transmit wavelengths greater than approximately 3 μm[5]. Unlike conventional silica fibre-optics, chalcogenides are limited to non-telecommunication short haul applications as even the best reported losses exhibit a few decibels per meter (dB/m) rather than silica's <1 dB/km[13].

2.3.1 Intrinsic loss mechanisms

Intrinsic losses are those which are inherent to a specific glass composition and are an unavoidable characteristic. They are defined by three physical phenomena: electronic absorption at short wavelengths (Urbach edge), multiphonon absorptions at long wavelengths and Rayleigh scattering[7], as depicted in Figure 2.8. Unique to chalcogenide glasses, Figure 2.8 also shows a fourth loss mechanism, weak absorption tail (WAT), which typically conceals the Rayleigh scattering loss for high-quality chalcogenide glasses. Altogether, these intrinsic losses contribute to the total and theoretical minimal loss for a given glass composition.

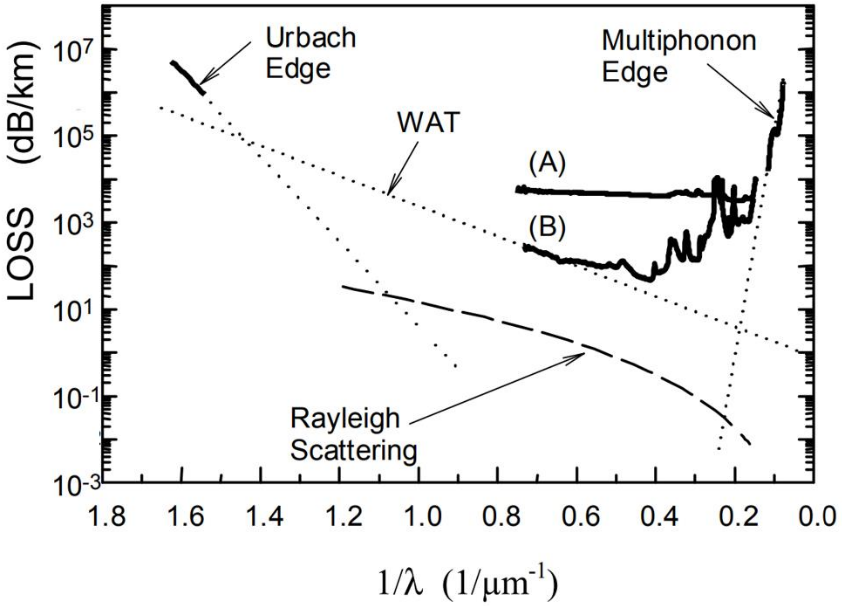

Figure 2.8: Estimation of theoretical minimum loss in a sulfide fibre made by Sanghera and Aggarwal [82, 83]. (A) Represents a poor quality glass whilst (B) represents a high quality glass.

The electronic absorption edge, which defines the short wavelength limit[84], is determined by the optical bandgap, and this in turn, depends on the electronic configuration and position of atoms in the material[7]. For theoretical crystalline materials that have perfect long range order, there will be a well-defined bandgap and a steep rise in shorter wavelength absorption. However, crystal defects and temperature introduce a little disorder to the system resulting in the Urbach tail[85] (Figure 2.8) where the electronic edge shifts slightly towards the longer wavelengths. For amorphous materials, the short-range atomic order remains however the long range atomic arrangement does not reflect the parent crystalline material. Therefore, the electronic edge will most likely exist in the same wavelength range but will be less defined[86].

Intrinsic scattering losses can be categorised by the size of their scattering centres. 1) Rayleigh scattering occurs when centres are much smaller than the incident wavelength; 2) Rayleigh-Gans scattering occurs when the centre and wavelength are approximately the same size; and 3) wavelength-independent scattering occurs when the centres are much larger than the wavelength[7]. All three scattering mechanisms can arise through extrinsic loss introduced by impurities or lattice defects (see section 2.3.2) however, Rayleigh scattering can also be intrinsic to a material and arise through density fluctuations[83].

The weak absorption tail is influenced by the medium range order and localised energy states in the bandgap, and is sensitive to the glass purity and thermal history[7]. The WAT will typically range from the optical bandgap, across the transmission window, to the multiphonon edge.

How far into the mid-infrared region a chalcogenide composition can transmit, is determined by the multiphonon absorption edge (see Figure 2.8) which is related to the vibrational phonons within the atomic network of a glass *i.e.* depending on the atomic masses and bond strength. Compared to oxide-containing glasses, chalcogenide glasses have larger atoms with weaker bonds and so their inherent vibrational resonance occurs at longer wavelengths. Furthermore, unlike fluoride glasses, the infrared multiphonon edge is not featureless but instead reveals an absorption structure. For chalcogenide glasses, the multiphonon structure arises from linear combinations and overtones of the fundamental modes[13]. Whereas other infrared-transmitting materials may exhibit a smooth exponential multiphonon edge due to the overlap of high-order phonon processes[13], chalcogenide networks are formed through strong covalent bonds. Therefore, their multiphonon edges has less of an overlap which results in a well-defined structure as demonstrated in Figure 2.9 for two chalcogenide compositions (A) As_2S_3 and (B) $As_{38}Ge_5Se_{57}$. Figure 2.9 also shows the multiphonon edge shift to longer wavelengths for heavier Se-containing glasses[87].

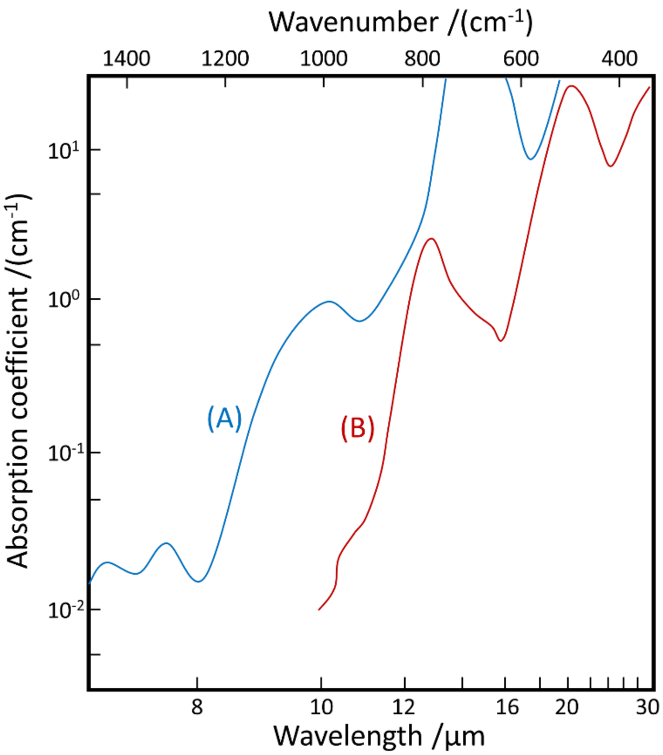

Figure 2.9: Adapted schematic diagram of the multiphonon edge of bulk (A) As_2S_3 and (B) $As_{38}Ge_5Se_{57}$ glasses[87].

2.3.2 Extrinsic loss mechanisms

The extrinsic loss is the dominant type of optical loss in chalcogenide glasses and can be categorised into: 1) those coming from impurity absorptions (*e.g.* oxides and hydrides) or 2) those arising from scattering centres (*e.g.* gas bubbles, inclusions or crystals)[88]. Unlike intrinsic loss mechanisms, extrinsic losses can theoretically be eliminated so long as nucleation is fully suppressed. In practice however, it is extremely difficult to remove all hydrogen impurities from a chalcogenide melt and so even the most purified glass will likely present some hydrogen absorption *e.g.* Se-H at 4.6 µm[13]. Table 2.2 lists relevant impurity absorptions across the mid-infrared spectral region.

*Table 2.2: Impurity absorptions in chalcogenide glasses. An * denotes where the information was not given. In the 'impurity assigned' column, (w)(m)(s)(vs) subscripts refer to weak, medium, strong and very strong, respectively.*

Band wavelength		Impurity assigned	Glass composition	Reference
/µm	/cm^{-1}			
1.44	6950	SO-H $_{\text{(overtone)}}$	$As_{40}S_{60}$	Kanamori *et al.*[87]
1.45	*	O-H $_{\text{(w)}}$	*	Lezal *et al.*[35]
1.92	5210	SO-H$_{\text{(combination)}}$	$As_{40}S_{60}$	Kanamori *et al.*[87]
2.05	4880	S-H	As-S	Borisevich *et al.*[89]
		S-H $_{\text{(w)}}$	*	Lezal *et al.*[35]
		S-H$_{\text{(overtone)}}$	$As_{40}S_{60}$	Kanamori *et al.*[87]
2.24	*	O-H $_{\text{(m)}}$	*	Lezal *et al.*[35]
2.29	4370	SO-H$_{\text{(combination)}}$	$As_{40}S_{60}$	Kanamori *et al.*[87]
2.32	*	Se-H	As-Se	Borisevich *et al.*[89]
		Se-H $_{\text{(w)}}$	*	Lezal *et al.*[35]
2.54	3940	S-H$_{\text{(combination)}}$	$As_{40}S_{60}$	Kanamori *et al.*[87]
2.54	*	S-H $_{\text{(w)}}$	*	Lezal *et al.*[35]
2.77	3610	$H_2O$$_{\text{(molecular)}}$	$As_{40}S_{60}$	Kanamori *et al.*[87]
2.78	*	O-H $_{\text{(m)}}$	*	Lezal *et al.*[35]
	3600	OH	As_2Se_3	Moynihan *et al.*[90]
2.79	*	H_2O	As-S/As-Se	Borisevich *et al.*[89]
2.80	3570	SO-H	Ge-S	Shibata *et al.*[91]
2.84	3520	OH	As_2Se_3	Moynihan *et al.*[90]
2.86	*	H_2O	As-S/As-Se	Borisevich *et al.*[89]
2.91	3440	SO-H$_{\text{(fundamental)}}$	$As_{40}S_{60}$	Kanamori *et al.*[87]
2.92	*	OH^-	As-Se	Borisevich *et al*[89]
	3420	SeO-H	As_2Se_3	Moynihan *et al.*[90]
	3420	O-H	$Ge_5As_{38}Se_{57}$	Kanamori *et al.*[92]
2.93	*	O-H $_{\text{(vs)}}$	*	Lezal *et al.*[35]
3.11	*	S-H	As-S	Borisevich *et al.*[89]
		S-H $_{\text{(m)}}$	*	Lezal *et al.*[35]
	3215	S-H$_{\text{(combination)}}$	$As_{40}S_{60}$	Kanamori *et al.*[87]
3.17	*	S-H	As_2Se_3	Snopatin *et al.*[93]
3.41	*	C-H $_{\text{(m)}}$	*	Lezal *et al.*[35]
3.5	2857	Se-H	$As_{39}Se_{42.4}Te_{18.6}$/ $As_{39}Se_{42.7}Te_{18.3}$	Shiryaev *et al.*[94]
3.5	*	C-H $_{\text{(m)}}$	*	Lezal *et al.*[35]
3.53	*	Se-H	As-Se	Borisevich *et al.*[89]
		Se-H $_{\text{(w)}}$	*	Lezal *et al.*[35]
	2830	Se-H	As_2Se_3	Moynihan *et al.*[90]
3.65	*	S-H	As-S	Borisevich *et al.*[89]
3.7	*	S-H $_{\text{(m)}}$	*	Lezal *et al.*[35]
3.69	2710	S-H$_{\text{(combination)}}$	$As_{40}S_{60}$	Kanamori *et al.*[87]
4.0	2500	S-H	As_2S_3	Churbanov *et al.*[95]
		S-H	Ge-S	Shibata *et al.*[91]

Band wavelength		Impurity assigned	Glass composition	Reference
/µm	/cm^{-1}			
4.01	2500	S-H	As_2Se_3	Snopatin *et al.*[93]
		S-H	As-Se	Borisevich *et al.*[89]
		S-H $_{(s)}$	*	Lezal *et al.*[35]
4.03	2480	S-H$_{(fundamental)}$	$As_{40}S_{60}$	Kanamori *et al.*[87]
4.1	2439	Se-H	$As_{39}Se_{42.4}Te_{18.6}$/ $As_{39}Se_{42.7}Te_{18.3}$	Shiryaev *et al.*[94]
4.12	*	Se-H	As-Se	Borisevich *et al.*[89]
4.12	*	Se-H $_{(m)}$	*	Lezal *et al.*[35]
	2430	Se-H	As_2Se_3	Moynihan *et al.*[90]
4.3	2326	CO_2 (artefact from atmosphere)	$As_{39}Se_{42.4}Te_{18.6}$/ $As_{39}Se_{42.7}Te_{18.3}$	Shiryaev *et al.*[94]
4.33	*	CO_2 (artefact from atmosphere)	As_2Se_3	Snopatin *et al.*[93]
		CO_2 (artefact from atmosphere)	As-S/As-Se	Borisevich *et al.*[89]
		CO_2 (artefact from atmosphere)	As_2S_3	Churbanov *et al.*[95]
4.5	2222	Se-H	As_2S_3	Churbanov *et al.*[95]
*	2200	Se-H	$Ge_{28}Sb_{12}Se_{60}$	Klocek *et al.*[96]
4.57	*	Se-H	$As_{39}Se_{42.4}Te_{18.6}$/ $As_{39}Se_{42.7}Te_{18.3}$	Shiryaev *et al.*[94]
		Se-H	As-Se	Borisevich *et al.*[89]
		Se-H $_{(s)}$	*	Lezal *et al.*[35]
	2190	Se-H	As_2Se_3	Moynihan *et al.*[90]
		Se-H	$Ge_5As_{38}Se_{57}$	Kanamori *et al.*[92]
4.65	*	CS_2	As-S	Borisevich *et al.*[89]
4.7	2128	Se-H	As_2Se_3	Devyatyth *et al.*[97]
		Se-H	$Te_{20}Se_{30}As_{40}I_{10}$	Zhang *et al.*[98]
4.92	2030	Ge-H	Ge-S	Shibata *et al.*[91]
4.94	2025	Carbon	$As_{40}S_{60}$	Kanamori *et al.*[87]
4.95	*	Ge-H	As-S/As-Se (?)	Borisevich *et al.*[89]
		COS	As_2S_3	Churbanov *et al.*[95]
5.0	2000	Se-H	$As_{39}Se_{42.4}Te_{18.6}$/ $As_{39}Se_{42.7}Te_{18.3}$	Shiryaev *et al.*[94]
5.48	1825	AsO-H	$As_{40}S_{60}$	Kanamori *et al.*[87]
6.2	*	O-H	$Te_{20}Se_{30}As_{40}I_{10}$	Zhang *et al.*[98]
6.3	1587	H_2O	$As_{39}Se_{42.4}Te_{18.6}$/ $As_{39}Se_{42.7}Te_{18.3}$	Shiryaev *et al.*[94]
		O-H $_{(s)}$	*	Lezal *et al.*[35]
	1585	$H_2O_{(molecular)}$	As_2Se_3	Moynihan *et al.*[90]
6.31	*	H_2O	As-S/As-Se	Borisevich *et al.*[89]

Band wavelength		Impurity assigned	Glass composition	Reference
/µm	/cm^{-1}			
6.32	1580	$H_2O_{(molecular)}$	$As_{40}S_{60}$	Kanamori *et al.*[87]
6.68	*	CS_2	As-S	Borisevich *et al.*[89]
7.8	*	CSe_2	As-Se	Borisevich *et al.*[89]
	*	Se-H	As-Se	Borisevich *et al.*[89]
	1280	Ge-O$_{(combination)}$	$GeSe_2$	Vlček *et al.*[99]
7.9	*	Ge-O	As-S/As-Se (?)	Borisevich *et al.*[89]
	1270	Oxide	$Ge_5As_{38}Se_{57}$	Kanamori *et al.*[92]
8.0	1250	Se-H	$Te_{25}As_{40}Se_{35}$	Shiryaev *et al.*[100]
8.13	1230	Ge-O$_{(combination)}$	$Ge_{25}Sb_{15}Te_{60}$	Nishii *et al.*[101]
8.63	*	S-O	As_2S_3	Churbanov *et al.*[95]
9.27	*	Si-O$_{(vs)}$	*	Lezal *et al.*[35]
9.1-9.6	*	Si-O	As-S/As-Se	Borisevich *et al.*[89]
10.4	*	Ge-O$_{(m)}$	*	Lezal *et al.*[35]
10.6	943	Se-O	As_2S_3	Churbanov *et al.*[95]
10.67	*	Se-O	As-Se	Borisevich *et al.*[89]
		Se-O$_{(w)}$	*	Lezal *et al.*[35]
10.77	*	Ge-O$_{(s)}$	*	Lezal *et al.*[35]
10.8	925	AsO-H	$As_{40}S_{60}$	Kanamori *et al.*[87]
11.06	*	Se-O	As-S/As-Se	Borisevich *et al.*[89]
		Se-O$_{(vs)}$	*	Lezal *et al.*[35]
11.40	*	Ge-O$_{(vs)}$	*	Lezal *et al.*[35]
12.40	*	Ge-O$_{(vs)}$	*	Lezal *et al.*[35]
12.5	*	Si-O$_{(m)}$	*	Lezal *et al.*[35]
	800	Ge-O$_{(stretching)}$	$GeSe_2$	Vlček *et al.*[99]
12.8	*	Ge-O	As-S/As-Se	Borisevich *et al.*[89]
13.07	765	Ge-O$_{(stretching)}$	$Ge_{25}Sb_{15}Te_{60}$	Nishii *et al.*
13.55	*	Sb-O$_{(m)}$	*	Lezal *et al.*[35]
13.96	*	Se-O$_{(s)}$	*	Lezal *et al.*[35]
14.53	*	Sb-O$_{(s)}$	*	Lezal *et al.*[35]
17.60	*	Sb-O$_{(s)}$	*	Lezal *et al.*[35]
18.18	*	Ge-O$_{(m)}$	*	Lezal *et al.*[35]
20.0	500	Ge-O$_{(bending)}$	$GeSe_2$	Vlček *et al.*[99]

2.4 Purification of chalcogenide glasses

Regardless of the final investigation, *e.g.* practical application or scientific interest, chalcogenide glasses should be prepared with as high a purity as possible. Commercially available raw elements are commonly available with 99.999 % purity however, this is commonly in reference to the cationic impurities and does not include oxides/hydrides for example. Typically, commercial batches of chalcogen elements will contain 0.1-0.01 ppm wt. % metal impurities but will contain 1-100 ppm wt. % of hydrogen, oxygen and silicon[102] (~10^{-3} mol. %[35]). To improve the quality of the glass, chalcogenides can be purified through several routes. Relevant approaches are described in sections 2.4.1 to 2.4.5.

2.4.1 Precursor impurity bake-out procedure

For pure chalcogens, that have a vapour pressure lower than their associated impurities, a basic purification procedure can be used whereby as-bought elements are heated under vacuum to appropriate processing temperatures[37]. Carried out prior to batching, this step can help to remove surface oxides and/or moisture. Danto *et al.*[103] have found that the vapour pressures of SeO_2 and As_2O_3 are several orders of magnitude higher than the elemental Se and As, respectively. By heating Se up to 250 °C and As up to 290 °C, for a period of 2 hours, there was successful dissociation and volatilisation of surface contaminants. However, the literature presents some discrepancies for the temperatures used during reactant purification as Hilton *et al.*[104] purified Se and As at 300 °C and 600 °C, respectively, as well as 700 °C for Sb. The time spent at these temperatures, was not given.

The relationship between vapour pressure and temperature can be estimated by the Antoine equation, seen in equation 2.5[105], where p is the vapour pressure, T is temperature and A, B and C are component-specific constants.

$$\log_{10} p = A - \frac{B}{C + T}$$ **Equation 2.5**

Nevertheless, not all constituent elements used in chalcogenide glasses, can be purified through impurity vaporisation as demonstrated by Table 2.3. Even at a temperature of 600 °C, Te still has a vapour pressure higher than that of TeO_2. Therefore, basic purification *via* impurity sublimation is not possible, but may be possible through component sublimation leaving behind the less volatile impurity.

Table 2.3: Vapour pressures of elemental As, Se and Te and their oxides[37]. '-hyphen- indicates where data were not available.

Temperature /°C	**Vapour pressure /mmHg**					
	As	**As_2O_3**	**Se**	**SeO_2**	**Te**	**TeO_2**
300	0.12	49.2	0.24	200	-	-
600	-	-	-	-	10	0.005

Additional physical properties of pure substances relevant to this work are presented in Table 2.4. Here it is shown that elemental Sb, Se and S have higher boiling points (1587 °C, 685 °C and 444.72 °C, respectively) than their oxide counterparts (1425 °C, 315 °C and -10 °C, respectively) whereas, the boiling point of elemental Ge (in °C) is more than double its corresponding oxide, 2830 °C and 1200 °C, respectively. Note that the melting point of SeO_2 (340 °C) refers to the melting of its monoclinic crystals following the sublimation of SeO_2[106].

*Table 2.4: Physical properties of relevant chalcogens and their associated oxides[107-109]. *Denotes the sublimation of SeO_2 at 315 °C, which condenses into white monoclinic crystals which melt at 340 °C[106].*

Inorganic species	**Formula weight /gmol^{-1}**	**Density /kgm^{-3}**	**Melting point /°C**	**Boiling point /°C**
Antimony (Sb)	121.760	6697	630.7	1587
Antimony trioxide (Sb_2O_3)	291.52	5700	655	1425
Germanium (Ge)	72.61	5323	937.3	2830
Germanium dioxide (GeO_2)	104.61	4250	1115	1200
Selenium (Se)	78.96	4810	217	685
Selenium dioxide (SeO_2)	110.96	3950	340*	315*
Sulfur (S)	32.066	1920	106.8	444.72
Sulfur dioxide (SO_2), α	64.058	-	-75.5	-10

2.4.2 Precursor distillation

Chalcogenide glasses can also be purified through the distillation of starting elements, with or without a getter. An example of this method is given once again by Hilton *et al.*[104] who used several interconnected chambers, through which, elemental Se and Sb (or As) could distil. With a boiling point of 2830 °C[110] and low vapour pressures of 1.01 $x10^{-9}$ atm at 927 °C[111], it is hard to distil elemental Ge. Therefore, Hilton *et al.*[104] housed Ge in the central, compounding chamber prior to distillation. Relevant chambers were independently heated to 300 °C (Se), 700 °C (Sb and Ge) and 350 °C (As) so to initiate oxide-surface treatment (similar to section 2.4.1). Here Hilton *et al.*[104] also suggests keeping the elements at this temperature for 16-18 hours. The pressure was then reduced, whilst maintaining ~300 °C across reactant chambers, and the system was closed using a hydrogen torch. Elements were then distilled through a porous quartz frit into the compounding chamber at temperatures of 650 °C to 700 °C for both Se and As, and 1000 °C for Sb[104]. They found that the distillation of Sb through the frit was extremely slow and, for the required 178 g, it took ~8 days at 1000 °C. The compounding chamber, which contained Ge, was not heated during distillation and was eventually sealed for melting. For subsequent precursor distillations, Hilton *et al.*[104] suggest starting the procedure with both Ge and Sb in the compounding chamber, as well as ~5 mg of aluminium.

Alternatively, precursor distillation can be achieved with all elements starting in one chamber. An example of this technique is documented by Zhang *et al.*[112], where Ge, Sb and Se, along with a trace amount of magnesium, were all distilled from chamber A to chamber B. Once again, distillation was carried out in a closed system, under vacuum (~10^{-3} Pa). The temperature of chamber A, which contained the constituent elements, was progressively increased to 950 °C, whilst chamber B (*i.e.* the final melting chamber) was kept below 500 °C[112] to encourage condensation of the distillates.

2.4.3 Chalcogenide glass distillation

Chalcogenides can also be purified from pre-melted, homogenised glass[60, 113] using the conventional melt-quench procedure which will be outlined in section 3.3. In addition to the elements batched during the initial melt Ge, Sb and Se for example, getters can also be introduced to reduce the oxygen [O] and hydrogen [H] content. $TeCl_4$ is often used as the [H] getter producing high-volatile HCl whilst, magnesium (Mg)[112, 114] or aluminium (Al) are frequently used as the [O] getter to form low-volatile MgO or Al_2O_3, respectively[8, 102, 115, 116]. As with section 2.4.2, all chambers are then evacuated before glass distillation begins.

2.4.4 Ge-Sb-Se glass distillation

Specific details of Ge-Sb-Se distillation have been published by several authors[54, 112, 113] however, all report slightly different experimental conditions.

Karaksina *et al.*[113] used 700 ppm wt. Al and 1000 ppm wt. $TeCl_4$ for the [O] and [H] getters, respectively. After an initial melt of the batched elements at 850 °C for 8 hours, a double distillation was then carried out in an open, then closed, vacuum system. During the open-vacuum distillation, the charged end (containing the pre-distilled melt), was kept at 650-700 °C for 12 hours; then during the closed-vacuum system, it was reduced to 600-650 °C for 8 hours[113]. Following distillation, the Ge-Sb-Se glass was homogenised at 750 °C, cooled in water and then annealed at T_g.

As mentioned in section 2.4.2, Zhang *et al.*[112] used a higher temperature of 950 °C during the distillation of elemental Ge, Sb and Se and also used Mg as the [O] getter during the single-stage distillation. There is no mention of a [H] getter.

Furthermore, Zhang *et al.*[54] use 250 ppm wt. % $GaCl_3$ (5N) as the [H] getter whilst introducing a much smaller amount of 50 ppm wt. % Al (5N) as the [O] getter. For a Ge-Sb-Se/Ge-Se core-cladding structure, they were able to produce fibre with a background loss of ~1 dB/m with an 8 dB/m Se-H impurity peak at 4.55 µm.

For comparison, particularly in chapter 6, Table 2.5 shows the optical losses for the best chalcogenide glasses to date.

Table 2.5: Optical losses for a selection of chalcogenide glass fibres.SM is single-mode; MM is multi-mode and SI is single-index[8]

Core/cladding structure	Type of fibre	Minimum loss		Reference
		Loss, dB/km	Wavelength, µm	
As_2S_3/As-S	MM	12	3.0	Snopatin *et al.*[115]
	SM	100	2.2	
$As_{38}S_{25}Se_{37}/As_{38}S_{27}Se_{35}$	MM	60	4.8	Churbanov *et al.*[117]
	SM	190	4.8	
$As_{35}Se_{65}$	SI	70	2.68; 3.8	Shiryaev *et al.*[118]
$As_{40}Se_{60}/As_{38}Se_{62}$	MM	67	6-6.5	
$As_{48}Se_{52}/As_{46}Se_{54}$	MM	260	3.1	Shiryaev *et al.*[119]
		400	6.0	
$GeSe_4$	SI	100	6.6	Troles *et al.*[114]
$Ge_2As_{38}Se_{40}Te_{20}/Ge_2As_{36}Se_{44}Te_{18}$	MM	150	6.6	Shiryaev *et al.*[120]
$As_{40}Se_{30}Te_{50}$	SI	40	6.6	Shiryaev *et al.*[100]
$As_{39}Se_{42.4}Te_{18.6}/As_{39}Se_{42.7}Te_{18.3}$	SM	330	7.5	Shiryaev *et al.*[94]
$Ge_{10}As_{21}Se_{69}$	SI	83	6.6	Tang *et al.*[116]
$Ge_{15}Sb_{20}S_{65}$	SI	50	2.3	Désévédavy *et al.*[121]
$Ge_{15}As_{16}Se_{63}In_3I_3$	SI	400	6.5-7.5	Karaksina *et al.*[122]
1300 ppmwt Pr^{3+}-$Ge_{15}As_{16}Se_{63}In_3I_3$	SI	580	2.72	
2000 ppm Pr^{3+}-$Ge_{15}As_{16}Se_{63}In_3I_3/Ge_2As_{39}S_{59}$	MM	1000	6.5-7	Karaksina *et al.*[123]
1300 ppm Pr^{3+}-$Ga_3Ge_{17}As_{18}\cdot Se_{62}/Ga_{2.5}Ge_{17.5}As_{15}Se_{65}$	MM	1250	2.95	

2.4.5 Other purity considerations

The only source of impurities discussed so far, are those associated with the initial glass components. However, there are two other sources that should be considered. The first addresses the vessel used for chalcogenide synthesis. Even after $HF_{aq.}$

etching and air/vacuum baking, silica glass ampoule can still introduce impurities into the chalcogenide glass *e.g.* [OH], [H_2O] and silicon dioxide[124]. Impurities with a high diffusion coefficient value, such as hydrogen, can enter the glass during melting. It was found that with a 100-ppm hydrogen-containing silica glass, [H] begins to enter the chalcogenide melt at 650 °C[125]. **Equation 2.6[102]** described the relationship between the temperature, T, and the hydrogen entrance rate, v ($kg \cdot m^{-2} s^{-1}$).

$$\ln v = -11.2 - \left(\frac{15300}{T}\right) \quad (873\ K \leq T \leq 1023\ K) \qquad \textbf{Equation 2.6}$$

According to Devyatykh *et al.*[126], when a chalcogenide melt interacts with the impurities from the melting vessel, a layer of reaction products can form near the interface, forming heterophase inclusions of α- and β-cristobalite[126]. These heterophase sites then act as impurity absorption and scattering centres, contributing to the overall optical loss.

The second source of impurities is the chalcogenide environment and residual vacuum gases during the glass synthesis. Chalcogenides are prone to oxidation, particularly at higher temperatures however, it can be minimised if a vacuum of 10^{-3}-10^{-5} Pa or less is used during fabrication[102].

2.5 Step index fibres (SIF)

2.5.1 Introduction to infrared fibre optics

As with all fibre-optics, the basic principle of light guiding within an infrared-transmitting glass is by total internal reflection (TIR). This process encompasses the reflection and refraction of light at a boundary between two materials with different refractive indices[13]. The refractive index of a material, n, is defined by **equation 2.7[127]** as the ratio of the speed of light in a vacuum (c) / the speed of light in the material (c_m).

$$n = {}^{c}/_{c_m} \qquad \textbf{Equation 2.7}$$

As a ratio, it does not have any units but fundamentally shows that the lower the refractive index, the faster the speed of light in that material.

Optical fibres can have a variety of structures to help guide light and the simplest of these is the step-index fibre (SIF), seen in Figure 2.10 (a). SIF consist of a solid-core material, with refractive index n_1, surrounded by a cladding material with a refractive index n_2. To guide light successfully through a SIF, the refractive index of the core must be greater than that of the cladding.

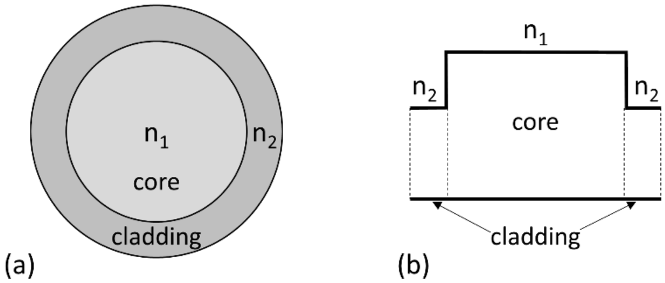

Figure 2.10: (a) schematic diagram of a step-index fibre (SIF) cross-section and (b) a SIF refractive index profile.

When an incoming ray, otherwise known as the incident ray, approaches a material with lower refractive index, it can take one of two routes: 1) it will be totally reflected back into the higher refractive index material (Figure 2.11 (a)) or 2) some light will also be partially refracted into the lower refractive index material (Figure 2.11 (b))[13].

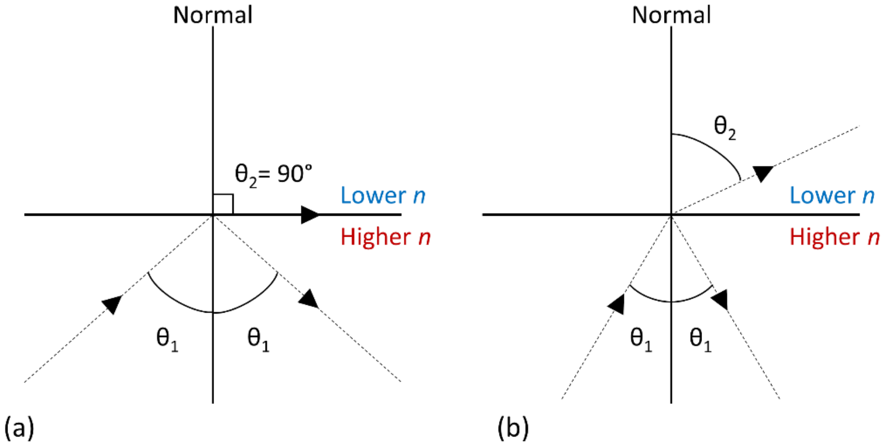

Figure 2.11: Adapted schematic diagram showing (a) incoming rays which are fully reflected and (b) incoming rays which are both reflected into the higher index material and refracted into the lower index material[13].

The angle in which the incidence ray approaches an optical boundary is therefore of significant importance and is measured with respect to the normal; this being a line perpendicular to that of the boundary. The relationship between the refractive indices of core and cladding, as well as the sine of the ray angles can be described by Snell's law, seen in **equation 2.8**. Here, n_1 and n_2 refer to the refractive indices of the two materials and $sin\vartheta_1$ and $sin\vartheta_2$ refer to the angles of incidence and refraction, respectively[127].

$$n_1 \sin\theta_1 = n_2 \sin\theta_2 \qquad \textbf{Equation 2.8}$$

At some point the angle of incidence will result in a 90° refraction, where the outgoing ray will travel along the optical boundary[127], see Figure 2.11 (a). This incoming angle is referred to as the critical angle and will dictate whether or not TIR will occur. For incidence angles greater than the critical angle (Figure 2.12 (a)) the outgoing ray will reflect back into the higher refractive index core and continue to travel down the fibre *i.e.* TIR occurs (Figure 2.12 (c)). However, for incidence angles smaller than the critical angle (Figure 2.12 (b)) some of the ray is refracted into the lower-refractive cladding. This loss of light is often referred to as the evanescent wave, and although it is problematic for most photonic applications, this phenomenon finds use during fibre evanescent wave spectroscopy (FEWS), discussed in section 2.7.

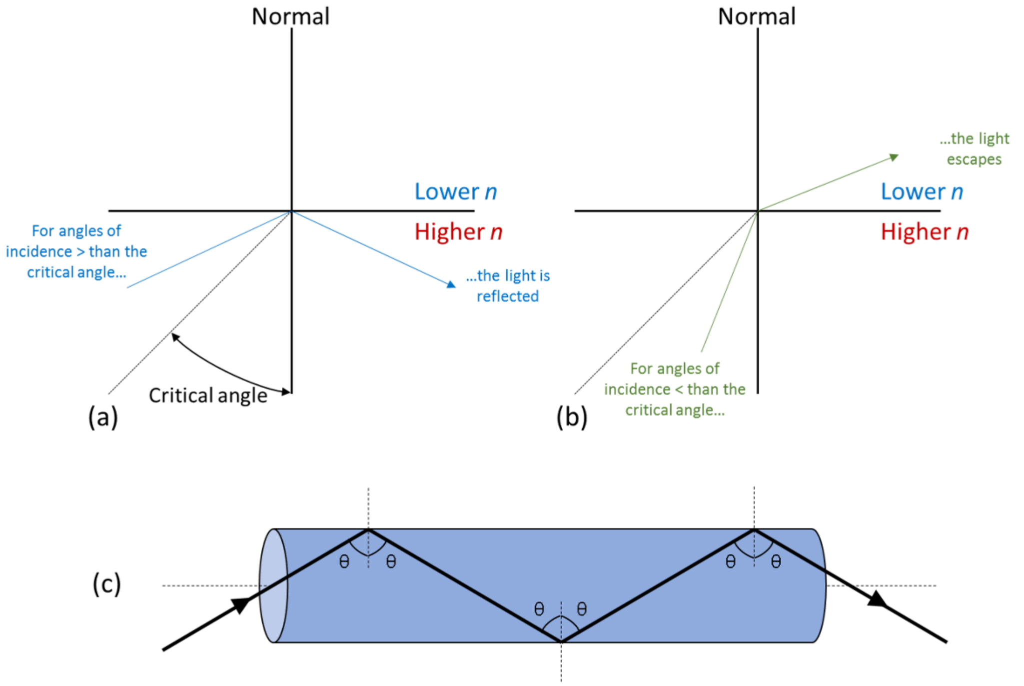

Figure 2.12: Adapted schematic diagram of incidence rays (a) greater than that of the critical angle or (b) smaller than the critical angle. For angles of incidence greater than the critical angle, total internal reflection will occur (c).

The numerical aperture (NA) of an optical fibre, refers to its light gathering capabilities *i.e.* a dimensionless number that characterises a range of angles from which a system can accept or emit light. Closely related to the critical angle, the NA will only include incidence rays that propagate by TIR. More importantly, it will also indicate what type and size of detector should be coupled with the SIF, for efficient light collection[128].

Based on the refractive indices of the core and cladding, the NA can be calculated from **equation 2.9**[**127, 128**].

$$NA = \sqrt{n_{core}^2 - n_{cladding}^2} \quad (no\ units) \qquad \textbf{Equation 2.9}$$

The most common type of MIR fibre is a large-core, multimode (MM) SIF shown in Figure 2.13 (a). Launching light into MM fibres tends to be simpler than single mode (SM) fibres (see Figure 2.13 (b)) as the core radius is much larger than the wavelength of light, λ[13]. For SM fibres the core diameter may only be several times that of the λ, which results in a ray propagating a more direct pathlength in the fibre.

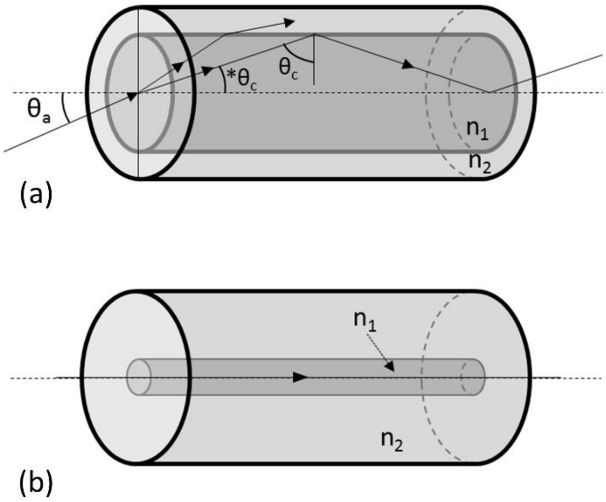

Figure 2.13: Adapted schematic diagram showing (a) multimode (MM) fibre showing guided ($\vartheta < *\vartheta_c$) and unguided ($\vartheta > *\vartheta_c$) rays and (b) single mode (SM) fibre with small core[13].

Since MM fibres interact with the core-cladding boundary numerous times during TIR, their propagation losses tend to be higher than those for SM fibres because their path length tends to be longer through the glass[129]. For SIF with a high NA, there is also an increased tendency for light to scatter at the core-cladding interface.

2.5.2 Losses in optical fibres

The lower refractive index glass acting as the cladding in a SIF, not only assists TIR, it also acts as a protective layer. During fabrication and/or handling, the surface of an optical fibre may become contaminated with dust or grease. As demonstrated in section 2.5.1, the interaction of the incidence ray with the core-cladding optical boundary, largely dictates further propagation. For unstructured fibres, whereby air acts as the lower refractive index material (n = ~1[127]), unavoidable points of contamination will change the optical properties of this interface. Therefore, local changes in the critical angle for an incoming ray, will result in an increased amount of light escaping the core. This phenomena is less likely to happen for SIF with a second cladding material.

Although Figure 2.12 suggested that all rays that meet the critical angle requirement will be reflected back into the core, a small proportion of the initial incidence light is also lost at the boundary by Fresnel reflection[127]. This is particularly a problem at the end of a fibre when the light is emitted into the air. Typically <4 % of the incoming ray is lost during Fresnel reflection from window glass however, the exact proportion can be determined by **equation 2.10**, where n_1 is the refractive index of the core and n_2 is the refractive index of the second material *i.e.* cladding or air.

$$Reflected\ power = \left({n_1 - n_2}/{n_1 + n_2}\right)^2 \qquad \textbf{Equation 2.10}$$

Thus, for the selenide chalcogenide glasses, reflected loss is approx. 20 % of the reflection.

The final type of losses are those associated with bending. It has already been discussed that the critical angle of an incidence ray for TIR is measured against the normal- that being a line perpendicular to the refractive index boundary. For optical fibres that have little or no bend at all, the light will propagate as predicted, see Figure 2.14 (a). However, if a significant bend is introduced to the system the perpendicular normal line will change position as demonstrated by Figure 2.14 (b). In this instance, when the original incidence ray approaches the core-cladding boundary, it no longer exceeds the critical angle and so will instead refract out of the core. Therefore, the tighter the bend, the more significant the loss. Typically, the losses are greater for fibres with lower NA and longer wavelengths[129] however, they are adequately minimised if the radius of the bend is as least 50 mm[127].

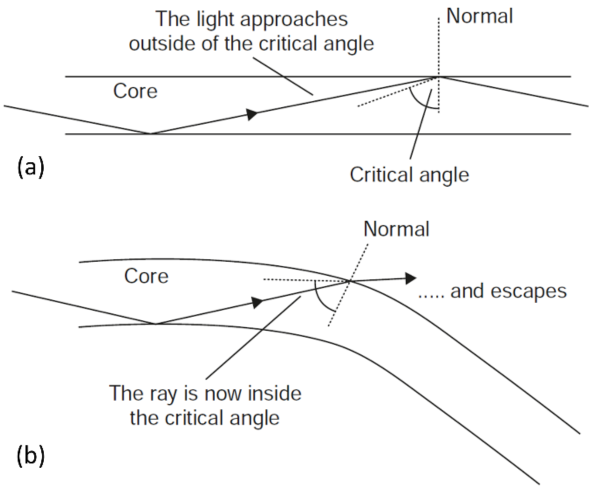

Figure 2.14: (a) Original critical angle for a straight optical fibre, (b) altered critical angle for the same optical fibre but with a bend[127].

2.5.3 Step index fibre (SIF) fabrication

Depending on the desired fibre geometry, SIFs can be made *via* a number of routes. For small-core fibres, used in supercontinuum generation (SCG)[130] *e.g.*, a rod-in-tube method is most suitable and consists of a relatively thin cane, for instance ~2 mm in diameter[54], being inserted into a larger tube. This tube can either be formed from an as-annealed glass boule, drilled to form the hole[131] or from an as-annealed glass boule which has been extruded through a spider die[96]. The intermediate cane in our laboratory cleverly consists of the core-cladding structure which makes for a particularly pristine inner core/cladding boundary; this cane is then inserted into a second cladding tube so that a final fibre with a small core can be achieved.

However, for larger core SIFs, a stacked extrusion may be more appropriate. During this procedure, in our laboratories, two carefully prepared glass boules are loaded into the extruder barrel, cladding first followed by the core (see section 3.4.1 for more details). With a constant load, the two boules are pushed through a die to form the step-index structured preform. Specific details of this procedure can be found elsewhere[132-134].

From here, in our laboratories, both types of preforms can then be drawn to fibre by means of the in-house radio frequency fibre-drawing furnace[116]. Most fibre-drawings are carried out under an inert atmosphere, *e.g.* He[135] or dry nitrogen[136], however, this is particularly critical for the rod-in-tube preforms which are more problematic in forming a high quality interface between the core and cladding. In this case, a vacuum is also applied[136].

Alternatively, SIFs can also been drawn directly from chalcogenide glass melts *via* a double crucible method as in the laboratories of the groups of Churbanov *et al*.[117] and Sanghera[136]. In this procedure, the core and cladding glass boules are loaded into the inner and outer crucibles, respectively[136]. Both glasses are heated above T_m for initial fining, before the temperature is lowered to begin fibre drawing. The diameter of the core and cladding is controlled by adjusting the pressure above each crucible[41].

2.6 Applications of chalcogenide glass

The applications of chalcogenide glasses can be categorised into two groups: 1) passive applications, where the light simply transmits from one location to another with no interaction or 2) active applications, where the propagating light is modified, not including scattering, absorption or end face reflection losses[42]. Types of active chalcogenide fibre applications include fibre lasers, amplifiers, bright sources, gratings and non-linear effects[42].

Since chalcogenide glasses are capable of transmitting longer wavelengths of light than conventional silica glasses, they offer unique potential to several sectors such as the civil, medical and military. Table 2.6 lists some early examples of passive chalcogenide applications, including hyperspectral imaging through coherent fibre bundles, to which this project has been working towards.

Table 2.6: Passive applications of IR transmitting chalcogenide glasses, adapted from[137].

Applications		Reference
Laser Power Delivery	5.4 µm (CO laser)	Nishii *et al.*[138] Busse *et al.*[139]
	10.6 µm (CO_2 laser)	
	Atmospheric Transmission (2-5 µm) windows	Busse *et al.*[140] Aggarwal *et al.*[141]
	Medical Applications (2-10 µm)	Sanghera *et al.*[142]
Chemical Sensing	Aqueous, non-aqueous, toxic chemicals	Shibata *et al.*[143] Heo *et al.*[144] Sanghera *et al.*[145]
	Polymers, paints, pharmaceuticals	Shibata *et al.*[143]
	Condition based maintenance	
	Cone penetrometer system	Nau *et al.*[146]
	Active coatings	Sanghera *et al.*[147]
	Bio-medical	Rigas *et al.*[148]
Temperature Monitoring	Grinding ceramics	Ueda *et al.*[149]
Thermal Imaging and Hyperspectral Imaging	Coherent fibre bundles	Suto *et al.*[150] Saito *et al.*[151] Nishii *et al.*[152]
Near Field Microscopy	Imaging and spectroscopy	Sanghera *et al.*[153]
Fibre Multiplexing	Fibre couplers	Schaafsma *et al.*[154]

2.6.1 Mid-infrared imaging: early cancer diagnosis

Spanning 3-25 µm wavelength[4, 5], the mid-infrared region of light covers an important diagnostic tool known as the molecular fingerprint[4]. Most biological species will exhibit characteristic vibrations, within the MIR region, which can be collected *via* the well-established technique of infrared spectroscopy. By combining this chemical analysis with the spatial resolution of microscopy, a newly emerging technique, known as MIR-chemical imaging[155-158], has received growing interest for a variety of biomedical disciplines. Rather than a simple morphological image, acquired through conventional visible-light microscopy, MIR-imaging instead produces a functional image with chemical identities.

This new technology could prove particularly beneficial in the detection of early-stage cancer where the current Gold Standard diagnosis, still relies on a lengthy biopsy procedure, conducted by a histopathologist[159]. Recent statistics now reveal that over half of the UK population, under 65 years of age, will be diagnosed with cancer at some point within their lifetime[1]. Diagnosing patients whilst they are in the early stages of the disease is of paramount importance to their survival yet, by the time a tumour is visible through white-light endoscopy, it is often in an advanced stage[159].

Although it is relatively difficult to distinguish specific molecules within the MIR fingerprint region, as many biomolecules share bond vibrations, Fourier transform infrared spectroscopy (FTIR) can be used to quantify them into groups *e.g.* glycogens, proteins, fat or nucleic acid (see Figure 2.15).

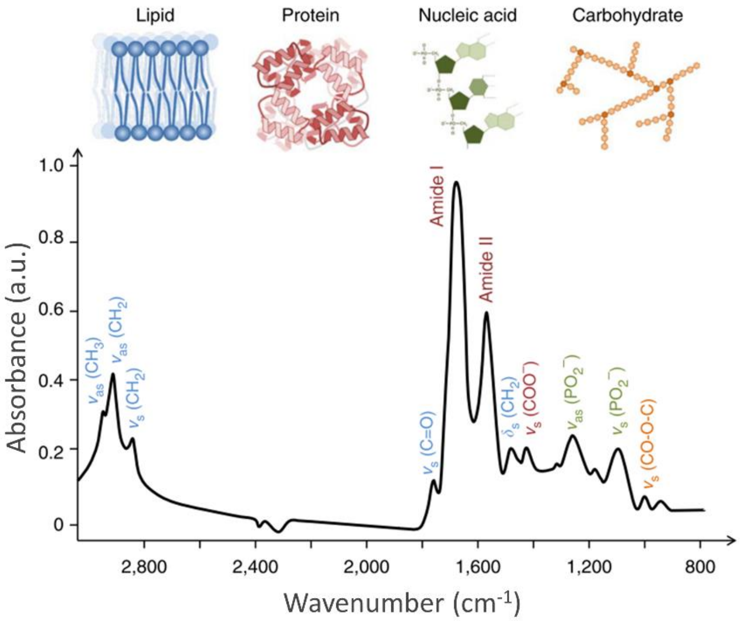

Figure 2.15: Typical biological fingerprint showing biomolecular peaks from 3,000-800 cm^{-1}, where v= stretching vibrations, δ= bending vibrations, s= symmetric vibrations and as= asymmetric vibrations[11].

Primarily due to a weak MIR light source[4, 5], FTIR has largely investigated excised tissues *ex-vivo* nevertheless, research has demonstrated that the biomolecular composition of diseased tissue is predictably altered in respect to the adjacent normal tissue[10]. This principle has allowed concepts such as the spectral barcode to develop, which has been shown to differentiate between non-tumoral and tumoral tissue samples, see Figure 2.16. Here, Nallala *et al.* [12] compared the FTIR, MIR-chemical image with that of an adjacently excised, dye-stained tissue using conventional optical microscopy. Using some of the clustered groups identified in Figure 2.15, an enhanced MIR image was produced.

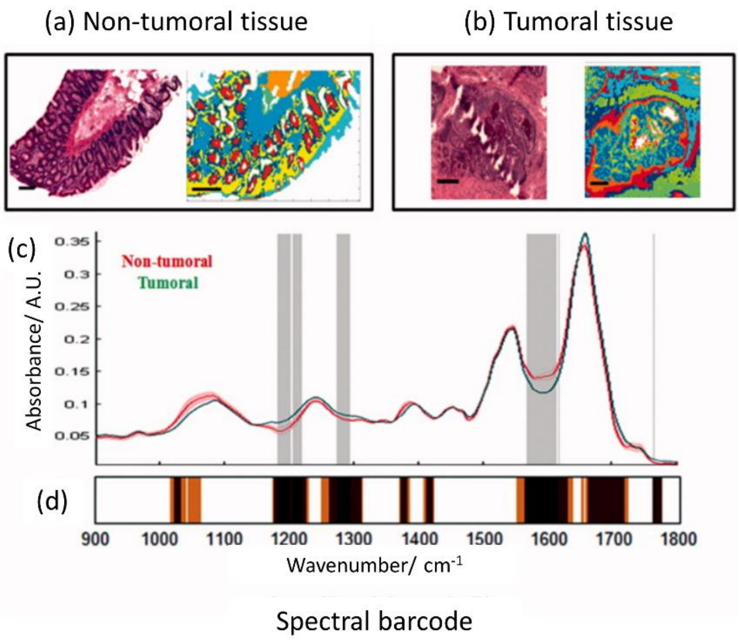

Figure 2.16: (a) Non-tumour, excised colon tissue showing: left, dye-stained optical micrograph using conventional histopathology and right, MIR chemical imaging (false-colour); (b) tumour, excised colon tissue showing: left, dye-stained optical micrograph using conventional histopathology and right, MIR chemical imaging (false-colour); (c) and (d) show the simplified 'spectral barcode' concept. (Adapted from[12]).

However, so far most research into MIR-chemical imaging has been conducted on tissue samples removed from the body. In an ideal diagnosis, the detection of early-stage cancer would be carried out *in-vivo* and provide an immediate response.

2.6.2 Coherent fibre-optic bundles

In order for MIR imaging to be conducted *in-vivo*, a new raft of components must be developed including the passive optical fibre that will transmit the MIR light, and form the basis of the fibre optic probe. Of course, chalcogenide glasses are one of the few materials which can deliver this specification.

A group of fibres that can transmit an image are often referred to as a coherent fibre bundle[13], and consist of a fibre array that is maintained from one end to the other. The fabrication of such bundle is not particularly straight forward especially when considering the work conducted by Zhang *et al.*[160] who managed to bundle 810,000 coherent As_2S_3 fibres into a 110 mm^2 space. Nevertheless, several techniques have shown successful in manufacturing chalcogenide coherent bundles including: 1) a wrapping/ribbon method[152, 161-163] and 2) the stack and draw[160, 164, 165].

One of the few, if not the only, documented work on Ge-Sb-Se fibre bundles was conducted by Klocek *et al.*[96] in 1987. Here, both cylindrical and square SIFs were formed through the rod-in-tube method with core-fibre ratios of 0.6 to 0.9. Table 2.7 highlights some of the physical properties associated with each combined composition.

Table 2.7: Relevant physical properties of individual compositions and resulting step-index fibres (SIFs) Taken from[96].

Core/ cladding fibre composition /at. %	**Tg /°C**	**Thermal expansion coefficient /(10^{-6} /°C)**	**Measured NA (10 % cutoff)**	**Residual compressive stress /kpsi**
$Ge_{28}Sb_{12}Se_{60}$/ $Ge_{32}Sb_8Se_{60}$	300/ 309	14.1/ 13.1	0.57	0.82 to 1.65
$Ge_{25}Sb_{15}Se_{60}$/ $Ge_{28}Sb_{12}Se_{60}$	278/ 300	14.8/ 14.1	0.45	1.42 to 2.63

With careful consideration of potential fibre crosstalk, several coherent bundle prototypes were fabricated *via* the ribbon method and shown in Figure 2.17.

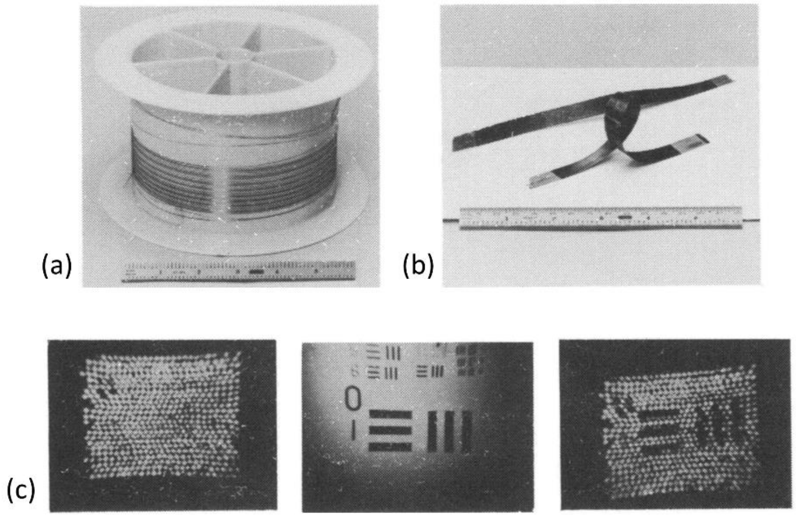

Figure 2.17: Ge-Sb-Se coherent fibre bundle prototypes: (a) drum with 250 µm diameter fibre; (b) flexible ribbon bundle with 75 µm diameter fibres; (c) coherent imaging bundle with 300 µm diameter fibres shown with and without a test pattern image under a transmission IR microscope. Taken from[96].

2.7 Cytotoxicity evaluation of the biocompatibility of chalcogenide glass

Biocompatibility is a term best described by Williams as "the ability of a material to perform with an appropriate host response in a specific application"[166]. This concept encompasses several factors which can be used to define a material's biocompatibility i.e. 1) toxicology, 2) extrinsic organisms, 3) mechanical effects and 4) cell-biomaterial interactions[167]. Similar to metals and ceramics, glasses can release ions during use, which are considered toxic if they have a negative impact on cells outside a living organism (*in-vitro*) or adjacent tissues within a living organism (*in-vivo*). Measuring the cytotoxicity of a material is relatively well understood and is clearly defined through the European International Organisation for Standardisation (ISO) standard ISO 10993[168]. In particular section 5 of this standard (ISO 10993-5:2009) covers Tests for *in-vitro* cytotoxicity. Inevitably simplistic, it is hard for *in-vitro* test to mimic the multi-cell complexity of an *in-vivo* study however, the preliminary investigations do provide an excellent screening method.

Although there has been several reports on the toxicity of various constituent elements *e.g.* Ge[110, 169], Se[170, 171], Sb[172], little work has been documented on chalcogenide glass systems as a whole.

Of those that exist, early work by Keirsse *et al.*[173] focussed on the $Te_2As_3Se_5$ composition and its possible effects in protein aggregation and cell division. By keeping a concentrated serum albumin solution (100 mg/ml) in contact with the $Te_2As_3Se_5$ fibre for 4 hours, fibre evanescent wave spectroscopy (FEWS) was conducted every 15 mins so that the amide I band frequency domain between 1700-1600 cm^{-1} (5.88- 6.25 µm wavelength) could be analysed. If the protein began to unfold the formation of a new band at 10620 cm^{-1} (0.94 µm wavelength) should have been present. However, no significant changes occurred during the 4 hour period and thus implied $Te_2As_3Se_5$ glass fibres do not induce protein denaturation. With similar results[173], $Te_2As_3Se_5$ fibre fragments were also exposed to a developing prokaryotic *P. mirabilis* biofilm for investigations into cell growth and communication impacts. Through two protocols no difference was observed between the $Te_2As_3Se_5$ fibres and the control showing that both biocompatibility tests therefore, supported the $Te_2As_3Se_5$ inertness towards living organisms.

Subsequent work by Wilhelm *et al.*[174] also investigated Te-As-Se fibres for use as functionalised infrared-sensors, where attached living cells selectively recognise hazardous species. Unlike infrared-transmitting silver halide fibres, which tend to deteriorate when in contact with a biological species[175], chalcogenide glasses are considered more chemically stable. Therefore, Wilhelm *et al.*[174] investigated the biocompatibility of $Te_2As_3Se_5$ fibres and their chemical stability in a variety of states and environments. Using a WST-1 assay mammalian cells from the A549 cell line and rat alveolar macrophages (NRL8686, from American Tissue Type Culture Catalogue), the cytotoxicity of $Te_2As_3Se_5$ fibres were evaluated *via* both a direct and indirect protocol. They concluded that fresh $Te_2As_3Se_5$ fibres did not show a toxic response following a couple of days in the biological solution whereas, $Te_2As_3Se_5$ fibres which had been stored in air for a long time did. This was most probably caused by the dissolution of a nanometer-thick oxide layer which had formed over time on the surface of the chalcogenide fibres[174] *i.e.* the Te-As-Se did not induce a cytotoxic response but rather, the oxide layer that had grown on the its surface.

Once again focussing on the Te-As-Se chalcogenide glass system and a FEWS technique, Bureau *et al.*[176], aimed to monitor changes in the chemical fingerprints of healthy lung cells (A549), which were attached to a tapered region of a Te-As-Se chalcogenide fibre, during exposure to toxic agents in the solution. The surfactant Triton was used as an example since this was known to disrupt cell membranes. Through qualitative analysis of micrographs (optical equipment not specified), Bureau *et al.*[176] were able to demonstrate that, prior to the addition of Triton, lung cells (A549) readily attach to the surface of a Te-As-Se fibre, spreading out across its surface and thus provided a large contact area from which the Te-As-Se could collect infrared spectra. Quantitative FEWS results showed that from the initial exposure of lung cell (A549) to Triton, there was a loss in membrane integrity, which caused the cells to round up and lose contact with the fibre as demonstrated by the schematic diagram in Figure 2.18.

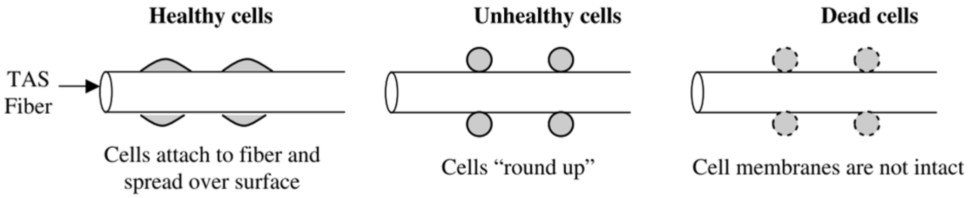

Figure 2.18: Schematic representation of cell behaviour on Te-As-Se fibres exposed to Triton[176].

Although the Te-As-Se chalcogenide glass system has been central to all cytotoxicity investigations thus far, it has often been reported that Sb-containing glasses are less toxic than As-containing glasses[47]. However, to the best of the Author's knowledge, there are no experimental reports to support this claim.

The only tangible piece of evidence could be found from a study into low-loss waveguides conducted by Du *et al.*[75], who expressed their desire to use Ge-Sb-S glasses, over the conventional As-S or As-Se, due to its superior resistance to oxidation[177]. Since, Te-As-Se chalcogenide glasses have been able to demonstrate adequate biocompatibility in their fresh state[174], non-arsenic containing Ge-Sb-S glasses may well indeed have better biocompatibility.

Chapter 3: Experimental techniques

This chapter provides a detailed overview of all the experimental procedures used to fabricate, process and characterise the investigated chalcogenide glasses. A list of all the chemicals, used during this Project are initially listed in section 3.1 before listing of all of the personal melt, extrusion, fibre-drawing and distillation codes in section 3.2. Glass melting, including ampoule purification, chalcogenide purification and batching, is discussed in section 3.3 before, section 3.4 details preform extrusion and fibre drawing methods. Bulk characterisation techniques are outlined in section 3.5 *viz.*: X-ray diffractometry (XRD), differential scanning calorimetry (DSC), differential thermal analysis (DTA), thermal mechanical analysis (TMA) (*i.e.* viscosity-temperature and thermal expansion coefficient (TEC)), scanning electron microscopy (SEM), transmission electron microscopy (TEM), energy dispersive X-ray analysis (EDX) and Fourier transform infrared spectroscopy (FTIR). Section 3.6 will then detail the optical fibre characterisation and then finally, section 3.7 will provide an experimental overview of the two *in-vitro* cytotoxicity procedures, as well as their corresponding assays, that were used to evaluate the biocompatibility of several chalcogenide glasses.

3.1 List of chemicals used

Table 3.1 lists all the chemicals used for glass batching whilst Table 3.2 lists all other chemicals used elsewhere in this research.

Table 3.1: Source and cationic purity of glass precursors and distillation getter chemicals.

Chemical	**Source**	**Purity /%**	**Comments**
Melting chemicals			
Germanium	Materion	99.999	Packaged by vendor under argon atmosphere
Antimony	Cerac	99.9999	
Selenium	Materion	99.999	
Sulfur	Materion	99.999	
Distillation chemicals			
$TeCl_4$	Alfa Aesar	99.9	
Aluminium	Alfa Aesar	99.9999	

Table 3.2: Source and purity of all other chemicals used during this project.

Chemical	Source	Purity	Comments
Acetone	Fisher chemicals	99.8+ %	All glass samples and relevant equipment were washed x3 with acetone and then x3 with isopropanol
Isopropanol	Fisher chemicals	HPLC (99.9+ %)	
Deionised water	Chemistry stores		Used to rinse glassware
Hydrofluoric acid	Rockwood Electronic Materials	Isoclean grade	Etching glassware
Polishing oil	Buelher		Polishing and cutting glass samples
1000 ppm SiC grinding powder	Buelher		Grinding glass samples
0.25 – 6 µm diamond paste	Buelher		Polishing glass samples
Argon	BOC	99.999 %	Purge gas
Nitrogen	BOC	99.998 %	Purge gas
5 %Hydrogen/ Nitrogen	BOC	Standard	Regeneration of glovebox dehydrant and copper coil (for removal of oxygen)
Oxygen	BOC	Standard	Oxy-propane torch
Propane	Calor gas	Standard	Oxy-propane torch
Liquid nitrogen	BOC		Cold traps

3.2 Glass melting, extrusion, fibre-drawing and distillation codes

For full details on each melt, extrusion, fibre-draw or distillation, please refer to **appendix 1** which chronologically outlines both the personal and research group glass code for each type of process, as well as other relevant information. For simplicity, Table 3.3 lists only the personal codes as well as the corresponding as-batched compositions for all glasses that will later be referred to in Chapters 4-7.

Table 3.3: List of codes for each process of glass melts, extrusions, fibre-drawing and distillation for all glasses investigated in this project. For further details on each, please refer to appendix 1.

Glass melting			
Glass melt code	**Composition /at. %**	**Glass melt code**	**Composition /at. %**
M_HAP001	$Ge_{25}Sb_{10}Se_{65}$	M_HAP009	$Ge_{25}Sb_{10}Se_{65}$
M_HAP002	$Ge_{25}Sb_{10}Se_{65}$	M_HAP010	$Ge_{20}Sb_{10}Se_{70}$
M_HAP003	$Ge_{25}Sb_{10}Se_{65}$	M_HAP011	$Ge_{20}Sb_{10}Se_{70}$
M_HAP004	$Ge_{25}Sb_{10}Se_{65}$	M_HAP012	$Ge_{25}Sb_{10}Se_{65}$
M_HAP005	$Ge_{20}Sb_{10}Se_{70}$	M_HAP013	$Ge_{20}Sb_{10}Se_{67}S_3$
M_HAP006	$Ge_{20}Sb_{10}Se_{70}$	M_HAP014	$Ge_{20}Sb_{10}Se_{70}$ + 1000 ppm wt. $TeCl_4$
M_HAP007	$Ge_{20}Sb_{10}Se_{67}S_3$	M_HAP015	$Ge_{20}Sb_{10}Se_{70}$ + 1000 ppm wt. $TeCl_4$
M_HAP008	$Ge_{20}Sb_{10}Se_{67}S_3$	M_HAP016	$Ge_{20}Sb_{10}Se_{70}$ + 1000 ppm wt. $TeCl_4$
Extrusion			
Extrusion code	**Composition /at. %**	**Extrusion code**	**Composition /at. %**
E_HAP001	$Ge_{20}Sb_{10}Se_{70}$	E_HAP004	$Ge_{20}Sb_{10}Se_{67}S_3$
E_HAP002	$Ge_{20}Sb_{10}Se_{70}$	E_HAP005	$Ge_{25}Sb_{10}Se_{65}$
E_HAP003	$Ge_{20}Sb_{10}Se_{67}S_3$	E_HAP006	$Ge_{20}Sb_{10}Se_{70}$/ $Ge_{20}Sb_{10}Se_{67}S_3$
Fibre-drawing			
Fibre-drawing code	**Composition /at. %**	**Fibre-drawing code**	**Composition /at. %**
F_HAP001	$Ge_{25}Sb_{10}Se_{65}$	F_HAP006	$Ge_{20}Sb_{10}Se_{70}$
F_HAP002	$Ge_{25}Sb_{10}Se_{65}$	F_HAP007	$Ge_{20}Sb_{10}Se_{70}$/ $Ge_{20}Sb_{10}Se_{67}S_3$
F_HAP003	$Ge_{20}Sb_{10}Se_{70}$	F_HAP008	$Ge_{20}Sb_{10}Se_{70}$
F_HAP004	$Ge_{20}Sb_{10}Se_{67}S_3$	F_HAP009	$Ge_{22}Sb_{8}Se_{70}$/ $Ge_{24}Sb_{4}Se_{72}$
F_HAP005	$Ge_{25}Sb_{10}Se_{65}$	F_HAP010	$As_{40}Se_{60}$

Key: M= melt; HAP= Authors' initials; E= extrusion; F= fibre-drawing; D= distillation.

Table 3.3: List of codes for each process of glass melts, extrusions, fibre-drawing and distillation for all glasses investigated in this project. For further details on each, please refer to appendix 1. (continued)

Distillation			
Distillation code	**Composition /at. %**	**Distillation code**	**Composition /at. %**
D_HAP001	$Ge_{20}Sb_{10}Se_{70}$	D_HAP003	$Ge_{20}Sb_{10}Se_{70}$ + 1000 ppm wt. % $TeCl_4$ + 700 ppm wt. % Al
D_HAP002	$Ge_{20}Sb_{10}Se_{70}$ + 1000 ppm wt. % $TeCl_4$ + 700 ppm wt. % Al	D_HAP004	$Ge_{20}Sb_{10}Se_{70}$ + 1000 ppm wt. % $TeCl_4$ + 700 ppm wt. % Al

Key: M= melt; HAP= Authors' initials; E= extrusion; F= fibre-drawing; D= distillation.

3.3 Glass melting

This section covers the glass melting of bulk chalcogenide glasses including: batch components, ampoule preparation, batching and purification of starting elements, and melting. The basic details associated with each fabrication stage was recorded on a 'glass melt sheet' of which an exemplar can be seen in **appendix 2**.

3.3.1 Batching components

All chemicals batched during the project are shown in Table 3.1 and have a purity between 99.999 – 99.9999 % as quoted by the corresponding sources. However, these values only take into consideration the cationic impurities present in the raw elements and ignore anionic impurities, such as oxygen and hydrogen, which can vary from one supplier to the next. As Chapters 4 and 5 will show, even with a simple purification procedure, described in section 3.3.4.1, the presence of oxygen or hydrogen within a chalcogenide glass will result in impurity absorptions across the MIR region, ultimately diminishing their MIR transmitting ability. The majority of the anionic impurities present in the as-received batch chemicals were thought to originate from the surfaces of these chemicals. Therefore, batched chemicals purchased during the project were ordered in the smallest bottles provided e.g. 25 g/ bottle for Sb (ABSCO, UK) so that they remained sealed, under the argon conditions prepared by the supplier, until required for glass batching. Furthermore, all chemicals were stored inside an MBraun 150B-G glovebox, with integral H_2O and O_2 sensors, under a N_2 (O_2- free ‘white spot’, BOC) atmosphere which was monitored to keep O_2 below 0.1 ppm and H_2O below 0.1 ppm.

3.3.2 Silica glass ampoule preparation

During this project silica glass ampoules (<1 ppm OH) supplied by both Baumbach UK, and Multilab UK, were used as containment to make the chalcogenide glasses. **Appendix 1** explains that glasses M_HAP001 to M_HAP009 were made using Baumbach ampoules whereas glasses M_HAP010 to M_HAP016 were made in Multilab ampoules. The change in supplier followed a number of ampoules that failed during the chalcogenide glass melting, including M_HAP004, which raised concerns over the quality of Baumbach ampoules. **Appendix 1** also explains, that after the successive ampoule fails, $HF_{aq.}$ etching would also be carried out in house using a 40 vol. (volume) % HF in water concentration for 5 minutes at ambient temperature, which was then rinsed three times with distilled water, all within a fume cupboard.

Depending on the final investigation, glasses were melted in various sized ampoules that were referred to by their inner and outer diameter (ID/OD mm) e.g. 8/12 mm. Table 3.4 shows the dimensions of all of the ampoules used in this Project as well as the typical uses for each of the final chalcogenide glass boules. The size of each boule, and thus the weight of the batched elements, was ultimately decided by the final intended investigation. However, the length of the ampoule, and its batched contents, were limited to the size of the stable, hot zone region within the rocking furnace. This will be discussed in more detail in section 3.3.5.

Table 3.4: Silica glass ampoule dimensions used in this Project. For cells that contain two ampoule dimensions, either vessel will produce the same-sized chalcogenide glass boule following sealing and melting.

Silica glass ampoule dimensions and hence final chalcogenide glass bulk shape.	**Typical use for final chalcogenide glass boule**	**Typical mass/ g**
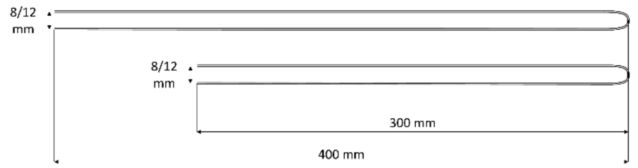	Bulk glass characterisation e.g. XRD, DSC	13-19
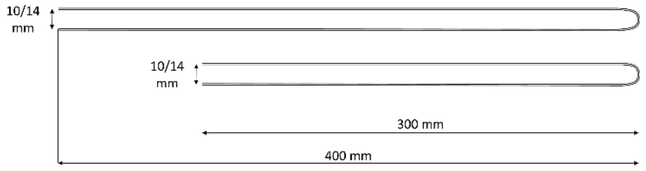	Bulk glass characterisation e.g. FTIR Drawing from an as-annealed 10 mm preform	30
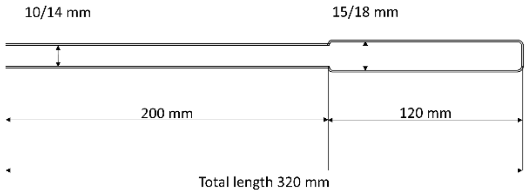	Small scale extrusion (4.7 mm diameter) for TMA samples and unstructured fibre	30
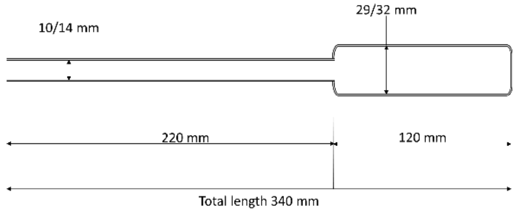	Large scale extrusion (10 mm diameter) for structured extrudate and fibre	85

Key: XRD= X-ray Diffraction; DSC= differential scanning calorimetry; FTIR= Fourier-transform infrared spectroscopy and TMA= thermomechanical analysis.

Following $HF_{aq.}$ etching, the ampoule was immediately transferred to a class 10,000 clean room, where all subsequent ampoule preparation steps were completed. This started with a minimum of 24 hours spent in a 70 °C drying oven (Heraeus) under an air environment. Ampoule baking was split into two steps: air baking and then vacuum baking. The schedules of both procedures are outlined in Table 3.5. During air baking, the ampoule was placed vertically, with the open end upwards, in a tube furnace (TF105/4.5/1ZF, Instron) and heated to 1000 °C so that any carbon deposits on the surface of the ampoule could be removed in the atmosphere. The same schedule was then repeated for the vacuum baking using a turbo pump (Pfeiffer Ltd, Mode:Duo 2) which supplied a drawing vacuum (~10^{-5} Pa) so that any physisorbed and chemisorbed water could be removed from the internal surface of the ampoule. The ampoule was then kept under vacuum using a valve and taken to a nitrogen atmosphere glovebox (MBraun 150B-G, ≤0.1 ppm O_2, ≤0.1 ppm H_2O) before batching the same day.

*Table 3.5: Silica glass ampoule containment preparation including prior $HF_{aq.}$ cleaning, air and vacuum baking schedules. *100 h dwell at the end was to allow the ampoule to remain at 70 °C until working hours. Preparation steps 3 and 4 were carried out in a vertical (TF105/4.5/1ZF, Instron) furnace bore.*

Ampoule preparation step		**Schedule**	**Location**
1	**$HF_{aq.}$ etch and distilled water rinse**	40 % concentration $HF_{aq.}$, 5 mins	Fume cupboard
2	**Drying**	~24 h	70 °C oven, class 10,000 clean room
3	**Air bake**	Step to 70 °C Ramp to 1000 °C @ 200 °C/h Dwell for 6 h at 1000 °C Ramp to 70 °C @ 200 °C/h Dwell for 100 h at 70 °C*	Tube furnace, class 10,000 clean room
4	**Vacuum bake**	Step to 70 °C Ramp to 1000 °C @ 200 °C/h Dwell for 6 h at 1000 °C Ramp to 70 °C @ 200 °C/h Dwell for 100 h at 70 °C*	Tube furnace, class 10,000 clean room

3.3.3 Batching and sealing

The term batching refers to the weighing out of each chemical which has been correctly calculated using a computer program, designed by Dr David Furniss, so that the desired glass composition, and total mass, can be achieved. Using a balance (Sartorious, model BP221S accurate to ±0.1 mg) in a nitrogen atmosphere glovebox (MBraun 150B-G, ≤0.1 ppm O_2, ≤0.1 ppm H_2O), each glass chemical was weighed to 4 decimal places. However, due to the static build up, weights ± 0.2 mg outside of the calculated values were deemed acceptable for batching (thus

±0.001 % on a 20 g total melt). To avoid cross-contamination, chemicals were weighed out individually using separate plastic boats (Fisher) and separate stainless steel tweezers. Again to minimise contamination, chemicals were poured directly from the boat into the prepared ampoule.

Using a Saunder's valve, the ampoule, and its batched chemicals, was temporarily sealed, so that it could be moved from the glovebox to a fume cupboard where it was attached to a vacuum system. First a rotary pump (VRC 200-7.0) was used to lower the vacuum to 1 Pa inside the ampoule before a diffusion pump (Edwards B30207240) was used to draw a high vacuum of 10^{-3} Pa. Two different vacuum systems were used in this project: one for ampoules that contained sulfur i.e. $Ge_{20}Sb_{10}Se_{67}S_3$ at. % and another for ampoules that did not i.e. $Ge_{20}Sb_{10}Se_{70}$ at. % and $Ge_{25}Sb_{10}Se_{65}$ at. %. Sulfur is comparatively a low density element which, when placed under vacuum, could have been drawn up into the pumping system and could later have acted as a source of contamination. Therefore, both the rotary and diffusion pumps were protected by an inline cold trap, which was cooled with liquid nitrogen (BOC) to freeze out volatile species.

Sealing occurred approximately 30 mins after the ampoule had been put under vacuum and was completed using an oxy-propane (CALOR Gas) torch (Jensons, Junior Jet 7). To reduce the amount of silica fume and possibly silicon monoxide produced from the silica glass ampoule during sealing, which could be observed as a deposited white fume, the procedure usually took <5 mins. However, the quality of the seal, and thus its durability during melting, prevailed over the time taken and so although <5 mins was preferable, earlier attempts did take as long as 20 min.

The seal was made far enough away from the batched chemicals so that there was minimal heat exposure prior to the final melting. However, as mentioned in section 3.3.1, it was also important that the length of the batched chemicals occupying the ampoule did not significantly exceed the length of the stable hot zone within the rocking furnace. Figure 3.1 shows a typical sealing distance (~ 50 mm) for an 8/12 mm ampoule containing 19 g of batched chemicals (M_HAP012).

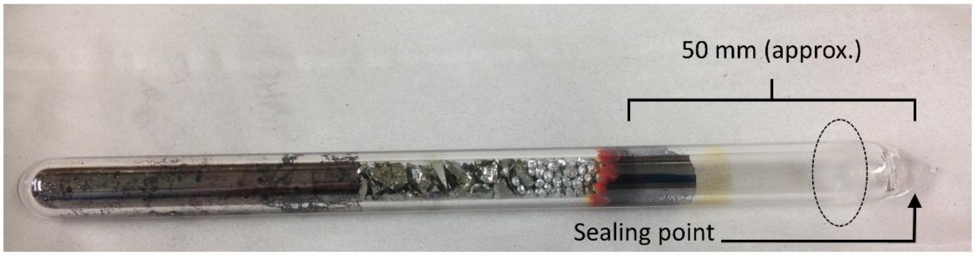

Figure 3.1: Photograph of a typical sealed ampoule. Here it shows that the sealing point was approximately 50 mm from the batched chemicals. Dashed circle highlights a deposited white fume.

3.3.4 Purification methods

Following section 2.3.2, in which the impacts chemical impurities can have on the MIR transmission of chalcogenide glasses was discussed, this section details two methods used in this Project, that helped to minimise these unwanted optical absorptions.

3.3.4.1 Precursor purification

With exception of Ge, the surface oxide impurities from each S, Se and Sb starting component, were minimised prior to glass melting, using a bake out procedure in a small tube furnace (in-house made) with either a 28 mm or 38 mm inner-diameter bore. The purification schedules for each element can be seen in Table 3.6. Depending on the final glass composition (*i.e.* Ge-Sb-Se or Ge-Sb-Se-S) and the size of the silica glass melting ampoule (*i.e.* 8/12 mm, 10/14 mm, 15/18 mm or 29/32 mm diameter) Se was purified by one of two programmes outlined in Table 3.6 (b) and (c). The reasons for the slight change in programme will be explained throughout this section.

Table 3.6: Bake-out purification schedules for Sb, Se and S used in this Project.

(a) Sb	
Step	**Schedule**
1	25 °C → 500 °C @ 250 °C/h, Dwell 0.1 h
2	500 °C → 570 °C @ 100 °C/h, Dwell 3.0 h
3	570 °C → 30 °C @ 300 °C/h. End.
(b) Se (for Ge-Sb-Se glasses in 8/12 mm or 10/14 mm silica glass ampoule)	
Step	**Schedule**
1	25 °C → 200 °C @ 200 °C/h, Dwell 0.1 h
2	200 °C → 260 °C @ 100 °C/h, Dwell 0.5 h
3	260 °C → 30 °C @ 300 °C/h. End.
(c) Se (for Ge-Sb-Se or Ge-Sb-Se-S glasses in 15/18 mm or 29/32 silica glass ampoule)	
Step	**Schedule**
1	25 °C → 200 °C @ 200 °C/h, Dwell 0.1 h
2	200 °C → 260 °C @ 100 °C/h, Dwell 0.5 h
3	260 °C → 320 °C @ 200 °C/h. End.
(d) S	
Step	**Schedule**
1	25 °C →140 °C @ 200 °C/ h
2	Dwell 25 mins
3	Lower furnace then, using gentle flame, encourage any purified S on the inner tube back into the ampoule
4	Raise furnace ~2 mins, lower furnace. End.

Following a similar batching procedure to that discussed in section 3.3.3, Sb was the first component to be purified for any glass melt as it occurred *via* a sublimation technique. This meant that after the schedule outlined in Table 3.6(a), Sb could be easily removed from the purification silica ampoule and then stored in the MBraun glovebox overnight prior to glass melting. Where possible the purified Sb was batched within the next few days. However, if a number of glass melts had been planned within a short timescale, a larger mass of Sb was purified in one go and kept in the MBraun glovebox for up to a month. Sb was purified with an excess of at least 5 g for each glass planned.

Figure 3.2 (a) shows the experimental setup for Sb purification where the batched component length was less than the 60 mm hot zone region on the small tube furnace. This meant that the small tube furnace did not have to be moved throughout the procedure, as all the batched Sb would have been contained within the stable hot zone region of the furnace and thus, would have been at the appropriate purification temperature programmed (*e.g.* 570 °C for Sb). Figure 3.2 (a) also shows that a silica tube was inserted into the silica glass ampoule, prior to purification, so that the volatile impurities would condense on its surface rather than on the silica glass ampoule wall. The same experimental setup shown in Figure 3.2 (a) was also used for Se and S purification where batched components had lengths less than 60 mm.

However, since all the glasses in this Project had a minimum of 65 at. % Se, the as-batched length of Se often exceeded the 60 mm hot zone region of the small tube furnace, particularly for chalcogenide glasses melted in an 8/12 mm or 10/14 mm silica ampoule. In these situations Figure 3.2 (b) shows that the position of the small tube furnace (in-house made, ID=28 or 38 mm), was moved twice within the high-temperature dwell (*i.e.* step 2 in Table 3.6 (b) and (c)) to compensate for the temperature profile of the small tube furnace *i.e.* either side of the 60 mm stable hot zone it would likely have been less than the temperature that was programmed. This movement ensured that all of the batched Se was exposed to the correct 260 °C purification temperature and thus, there was sufficient heating for the sublimation of its impurities.

Positions 1, 2 and 3 marked on the silica glass ampoule in Figure 3.2 (b) indicate where the top of the small tube furnace was moved to. This position was based on the distance between the middle of the small tube furnace hot zone and the top of its alumina tube, approx. 145 mm in length. Figure 3.2 (b) shows the small tube furnace at Position 1. As an example, during a 30 min dwell at 260 °C, the small tube furnace was lowered to Position 2 after 10 mins (as indicated by the dashed outline in Figure 3.2 (b)) and then raised to Position 3 for the final 10 mins.

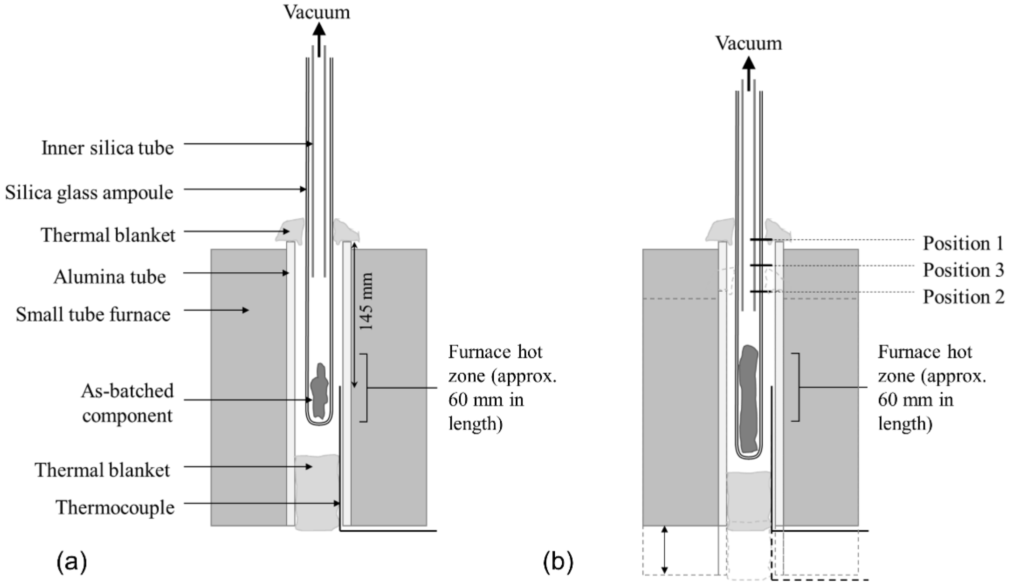

Figure 3.2: (a) Schematic diagram of the Se, Sb and S bake-out purification procedure using a small tube furnace (in-house made, ID=28 or 38 mm). For batched chemicals longer than the ~60 mm hot zone of the small tube furnace (b) shows three positions throughout the procedure.

For Ge-Sb-Se glasses, Se purification was carried out in the final melting ampoule (prior cleaned by the method described in section 3.3.2) and was batched with approximately 0.3 g more than the calculated weight, so to compensate for any volatile loss. For Ge-Sb-Se glasses melted in an 8/12 mm or 10/14 mm silica glass ampoule, Se purification followed schedule (b) in Table 3.6.

However, for Ge-Sb-Se glasses melted in a 15/18 mm or 29/32 mm ampoule, the schedule was modified slightly and instead followed the programme outlined in Table 3.6 (c). Instead of allowing the silica ampoule and its Se contents to drop back to 30 °C at a programmed rate of 300 °C/ h (step 3 in Table 3.6 (b)), the temperature was raised from 260 °C to 320 °C, before removing the ampoule-assembly from the small tube furnace and tilting so that the purified Se was air-quenched at an angle (see Figure 3.3 (a)). The brief increase in temperature up to 320 °C, ensured that the purified Se had a low enough viscosity to flow within the silica glass ampoule and eventually form the solidified Se-angled boule (see Figure 3.3 (b)). By introducing an angle at this stage, there was less chance of the silica glass ampoule mechanically failing during melting (see section 3.3.5) as a consequence of the Se expanding. This technique was not possible for an 8/12 mm or 10/14 mm ampoule, as the angle introduced during tilting would have resulted in a purified Se boule, that was too long for the final melting (Instron, TF105/4.5/1ZF) furnace.

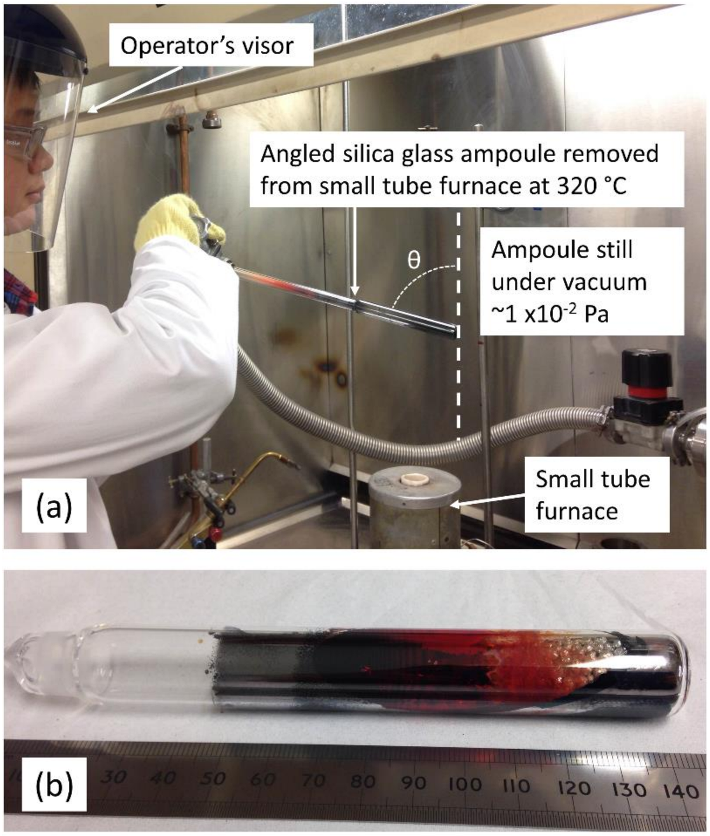

Figure 3.3: (a) Image showing the tilting of purified Se, removed from the small tube furnace (in-house made, ID=28 or 38 mm) at 320 °C, for Ge-Sb-Se glasses in an 15/18 mm or 29/32 mm diameter silica glass ampoule. (b) Image showing a sealed 15/18 mm silica glass ampoule containing the solidified Se-angled boule and batched as-received Ge and purified Sb.

For Ge-Sb-Se-S glasses, Se was purified beforehand in a separate ampoule, prepared by the method described in section 3.3.2. Similar to the aforementioned Se-purification schedule, Se that was purified for Ge-Sb-Se-S glasses was also air quenched from 320 °C (Table 3.6 (c)). However, the purified Se did not need to be angled as it was not purified in the final silica glass melting ampoule. Instead, the purified Se was vertically quenched using a solution of ice, water and NaCl. To reduce the risk of the silica ampoule mechanically failing during quenching, the ice, water and NaCl solution was allowed to gradually quench the purified Se from the bottom of the Se upwards, moving 20 mm up every 10 seconds, see Figure 3.4 (a). Once the purified Se was fully submerged in the ice, water and NsCl solution (*i.e.* past Position 3 in Figure 3.4(a)), it was left for another 30 mins to ensure all the material had cooled and equilibrated (see Figure 3.4 (b)).

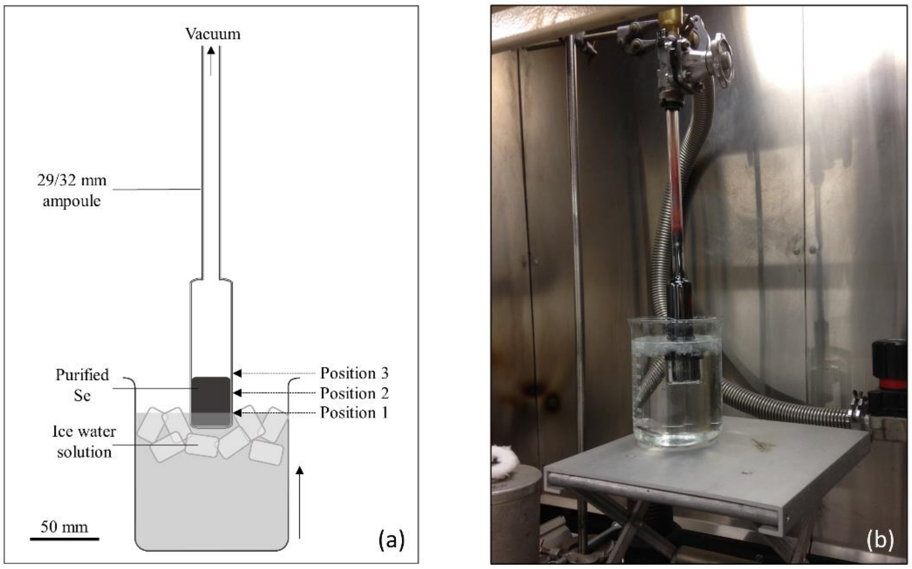

Figure 3.4: Schematic diagram (a) and photograph (b) of Se purification for Ge-Sb-Se-S glasses.

Using the method outlined in section 3.3.3, the purified Se ampoule was sealed. Once cooled, after sealing the ampoule was then cut using a 1.25 mm deep, diamond coated blade (see method described later in section 3.4.1) and transferred to the MBraun glovebox where it could be opened and the purified Se retrieved. Using a pestle and mortar, the purified Se was broken into approximately 5 mm wide pieces which could then be batched into the final ampoule for melting, all carried out in the MBraun glovebox.

However, before the purified Se was batched into the final melting silica glass ampoule, for Ge-Sb-Se-S glasses, the S first had to be purified. This was carried out using the schedule outlined in Table 3.6 (d) and the sulfur was batched with approximately 0.02 g more than the calculated amount to accommodate potential volatile losses.

3.3.4.2 Distillation

To minimise the optical absorption bands associated with oxygen, hydrogen or carbon impurities, in the MIR spectrum of any chalcogenide glass prepared here, it was necessary to distil the as-prepared glass re-melt with getters. Following on from the work carried out by previous Mid-infrared Photonics Group researchers, as well as guidance from the literature [104, 112, 113, 116], three single-stage distillation designs were used during this Project and can be seen in Figure 3.5.

Figure 3.5 (a) shows a 400 mm long, 10/14 mm diameter silica ampoule (Multilab) which was bent in-house using an oxy-propane torch. This was used for a preliminary trial which was a simple distillation of ~5 g of homogenised Ge-Sb-Se glass without any getters. Figure 3.5 (b) and (c) show a more complex silica glass rig (Multilab) design which featured a larger ‘charge’ chamber, into which the starting material was batched; this type of rig had either a 10/14 mm diameter distillate end (b) or a 29/32 mm diameter distillate end (c).

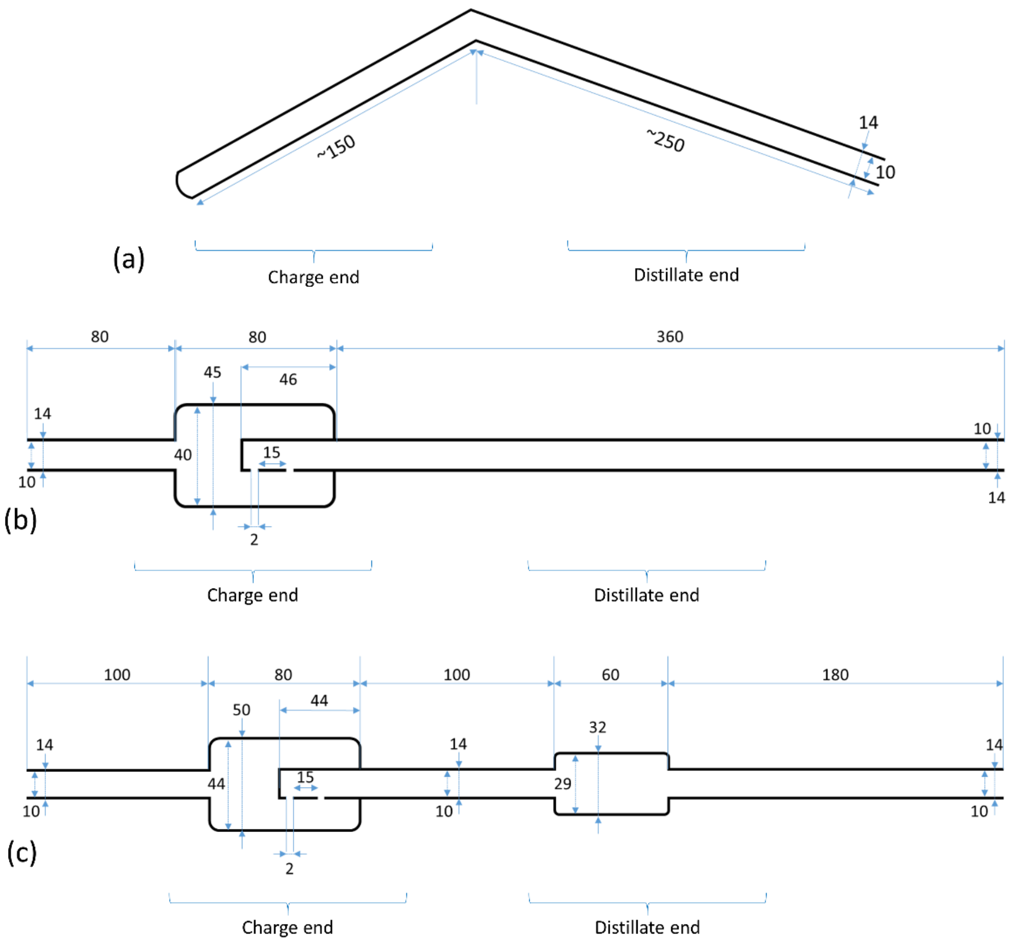

Figure 3.5: Schematic diagrams of three distillation ampoules (Multilab) used during this Project: (a) in-house bent 10/14 mm diameter, 400 mm long silica ampoule; (b) custom-made single distillation ampoule with a 10/14 mm tube at the distillate end; (c) custom-made distillation ampoule with a second 29/32 mm chamber at the distillate end. All dimensions are given in mm. Charge end refers to the heated end containing the starting as-prepared Ge-Sb-Se glass and getters. Distillate end refers to the relatively cooler section of the silica rig where the distilled Ge-Sb-Se condensed.

As with other melt-containment silica glass ampoules (see section 3.3.2), the distillation rigs depicted in Figure 3.5 were cleaned using an $HF_{aq.}$ (40 vol. %) wash and air/vacuum bake procedure as outlined in Table 3.5. Whereas, melting ampoules and the bent tube (Figure 3.5 (a)) underwent one air baking step, the more complex rigs, seen in Figure 3.5 (b) and (c), had to be air baked twice as these distillation rigs were longer than the available furnace. Figure 3.6 (a) shows the orientation of the first air baking run and Figure 3.6 (b) shows the orientation of the second air baking run. Both air bakes were carried out in a vertical (Instron TF105/4.5/1ZF) tube furnace in a class 10,000 cleanroom. This two-stage procedure ensured all of the silica glassware had been heated sufficiently (up to ~1000 °C) so as to drive off any carbonaceous deposits. It was desirable to have the distillate end (Figure 3.6 (b)) within the hot zone for the second run, as the quality of this section of the rig, was the most important for the final Ge-Sb-Se glass.

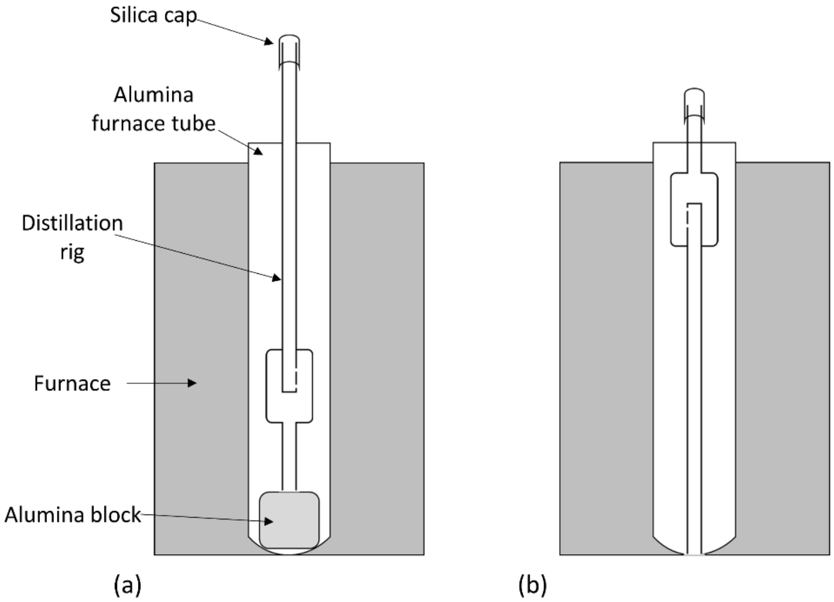

Figure 3.6: Schematic diagram of the two-step air baking procedure for distillation rigs. The first orientation is seen in (a) whilst the second orientation is seen in (b).

The only other difference between the cleaning of the silica glass distillation rig preparation and that of the silica glass ampoule, outlined in Table 3.5, was that the vacuum baking was carried out using a two-zone furnace (Instron, TF1798, tube ID 86mm). In order to create a vacuum, a stainless steel cap was attached to the distillate end of the silica distillation rig, whilst an Edwards valve was attached to the charged end (see Figure 3.7). To improve the vacuum, rubber O-rings were used where any metal-on-metal or silica glass-on-metal interfaces were present. To protect these O-rings during vacuum baking, the procedure was amended to heat up to 800 °C at a rate of 200 °C/ h rather than the 1000 °C used for all other silica glassware (step 4 Table 3.5).

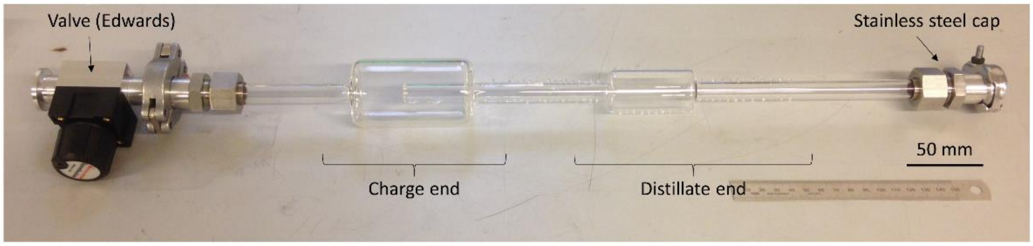

Figure 3.7: Silica distillation rig with vacuum baking fittings. A 29/32 mm diameter distillate end is given here as an example.

All distillations investigated in this Project, started with a premelted homogenised Ge-Sb-Se glass boule. For distillations that included getters, 1000 ppm wt. $TeCl_4$ was used as the hydrogen getter whilst 700 ppm wt. Al was used as the oxygen getter (see Table 3.1). Each getter was introduced to the Ge-Sb-Se glass at different stages.

As with the normal procedure (outlined in sections 3.3.3, 3.3.4.1 and 3.3.5) 1000 ppm wt. $TeCl_4$ was initially batched into a 29/32 mm diameter ampoule (Multilab) which already contained the batched Ge as well as the purified Se and Sb. This gave time, during the chalcogenide glass melting, for the $TeCl_4$ to react with hydrogen within the melt and form HCl gas. Once the as-prepared glass (Ge-Sb-Se +1000 ppm wt. $TeCl_4$) had been quenched and annealed, the ampoule was scored with a diamond blade, and opened in the MBraun glovebox. Using a pestle and mortar, the as-prepared Ge-Sb-Se + 1000 ppm wt. $TeCl_4$ glass was broken and batched into the charged end of the distillation rig along with 700 ppm wt. Al.

As will be discussed throughout section 6, the variables of temperature, time and rig position, determined the overall success of the distillations and these all relied significantly on the operators' observation. Therefore, the final distillation schedules will be discussed in detail in section 6.2. However, as a brief overview, Table 3.7 highlights some of the key stages during distillation, which typically occurred over four consecutive days.

This began with a distillation-preparation Day 1, where the sealed silica distillation rig, containing the premelted homogenised Ge-Sb-Se + 1000 ppm wt. $TeCl_4$ glass and 700 ppm wt. Al, was assembled in the two-zone furnace (Instron, TF1798, tube ID 86mm) and left under vacuum (~1.2×10^{-5} mBar) and at ~300 °C overnight. On Day 2, the temperature of the charged end of the silica distillation rig was progressively increased (to approx. 450 °C) so that the HCl gas could escape with the flowing vacuum. Once enough HCl gas had been removed, the silica distillation rig was sealed, creating a closed system. At the end of Day 2, the two-zone furnace (Instron, TF1798, tube ID 86mm) was left at an angle so to encourage the distilled Ge-Sb-Se glass to run down to the end of the distillate chamber, as temperatures increased to approx. 750 °C. Day 3 consisted primarily on the operator's observation. Once enough Ge-Sb-Se material had distilled from the charged chamber into the distillate chamber, the entire distillation system was allowed to cool to room temperature. On Day 4 the distillate end, containing the distilled Ge-Sb-Se material, was sealed and prepared for melting.

Table 3.7: Distillation procedure overview for Ge-Sb-Se glass with 1000 ppm wt. $TeCl_4$ and 700 ppm wt. Al hydrogen and oxygen getters, respectively.

Day	Description
1	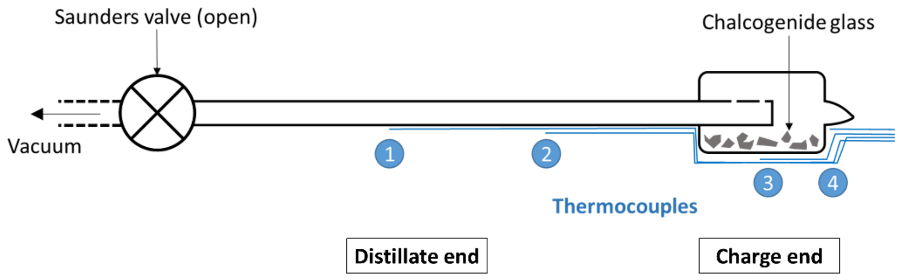 Homogenised Ge-Sb-Se + 1000 ppm wt. $TeCl_4$ glass, was batched into the charge end of the distillation rig, along with 700 ppm wt. Al, in an MBraun glovebox. (Note that Ge-Sb-Se + 1000 ppm wt. $TeCl_4$ glass batching occurred on the same day that it was opened from its premelted silica glass ampoule.) Distillation rig was then sealed. With contents under glovebox atmosphere, relevant thermocouples were attached and the whole assembly was placed in the furnace. Once satisfactory vacuum was reached (~1.2 x10^{-5} mBar), the temperature was left at approx. 300 °C (for the whole of the rig) overnight.

Table 3.7 (Continued)

2	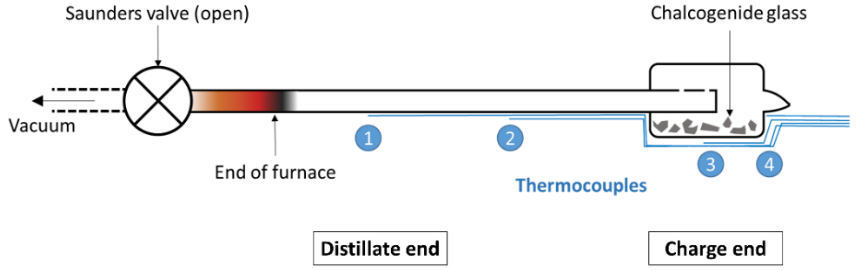
	The temperature of the charge chamber was raised to ~450 °C, and the $HCl_{(g)}$ bake off commenced.
	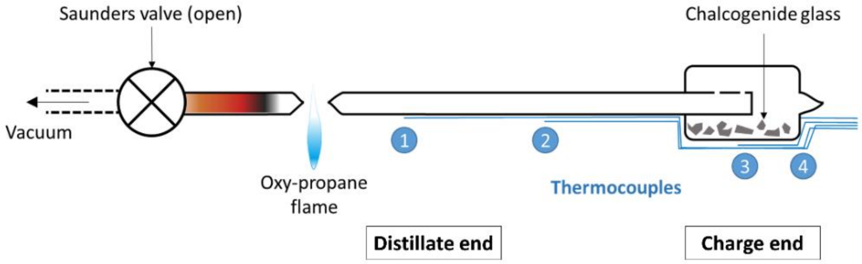
	Once enough $HCl_{(g)}$ had been driven off, as indicated by the red/black colour on the silica glassware, the distillate end was sealed using an oxy-propane torch.
	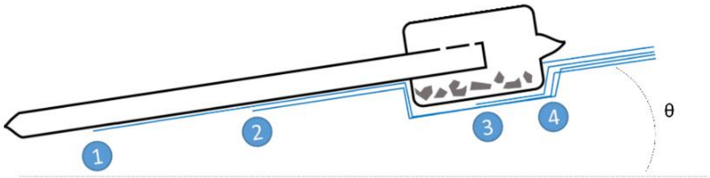
	The furnace was angled, and the temperature of the charged chamber is increased to approx. 750 °C and left overnight. Distillate end had to be kept isothermally at approx. 200 °C.
3	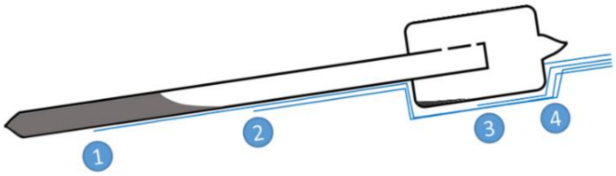
	Once the material had distilled over, leaving ~10 % of the original batch in the charged chamber, the distillation rig (and its contents) was cooled to room temperature.
4	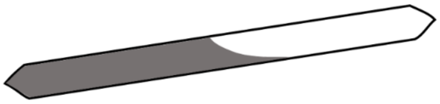
	Final sealing of the distilled material, ready for re-melt.

3.3.5 Chalcogenide glass melting, quenching and annealing

All chalcogenide glasses, melted during this Project, were carried out in a sealed silica glass ampoule within a resistance tube furnace (Instron TF105/4.5/1ZF, tube ID 86 mm with Eurotherm 2408 controller) schematically shown in Figure 3.8. A silica glass ampoule was chosen as it had a T_g of ~1100 °C, well above the melting temperatures of chalcogenide glasses. As indicated in Figure 3.8, an alumina tube was lined with thermal blanket, which helped to insulate and protect the silica glass ampoule and its chalcogenide contents. To help transfer the silica glass ampoule and its chalcogenide glass contents in and out of the furnace, metal wire (0.6 mm diameter, NiCr alloy, Kanthal) was twisted around the top half of the silica glass ampoule, to create a handle-like extension.

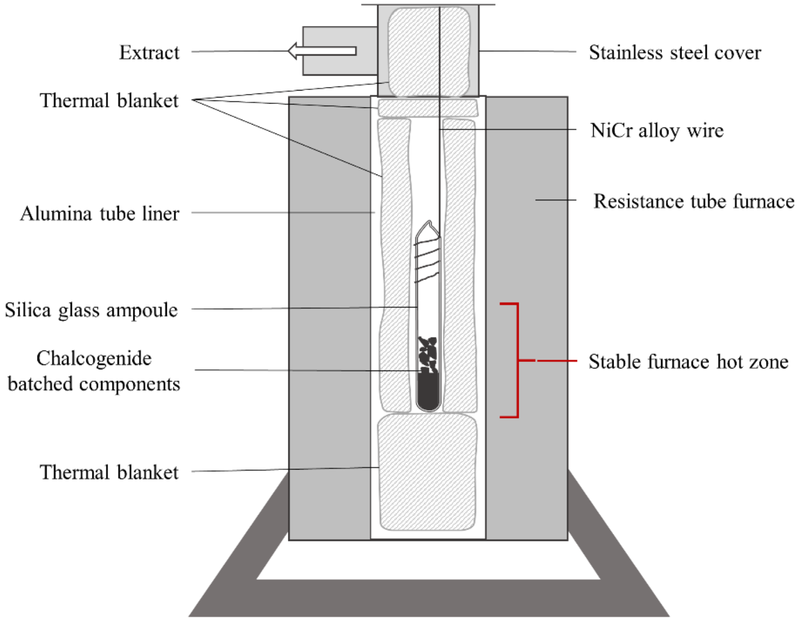

Figure 3.8: Schematic drawing of the resistance tube furnace used for chalcogenide glass melting.

Figure 3.9 (a) shows the experimental setup used to measure the temperature profile of the resistance melting furnace which had been heated to 900 °C. To create an environment, that was representative of the temperatures inside the final silica glass ampoule, the temperature profile was measured by a thermocouple which drawn through a 10/14 mm silica tube (Multilab) (Figure 3.9 (b)).

The thermocouple was gradually pulled out of the resistance furnace 10 mm at a time and at each new point, the thermocouple temperature was recorded following a 10 mins interval, so to allow the reading to equilibrate. Figure 3.9 (b) shows that there was a stable region, approx. 100 mm in length, and was found 150-250 mm from the bottom of the resistance tube furnace. Therefore, sealed silica glass ampoules, containing the chalcogenide glass, were positioned within this stable 'hot zone region' prior to the programme starting (refer to Figure 3.8).

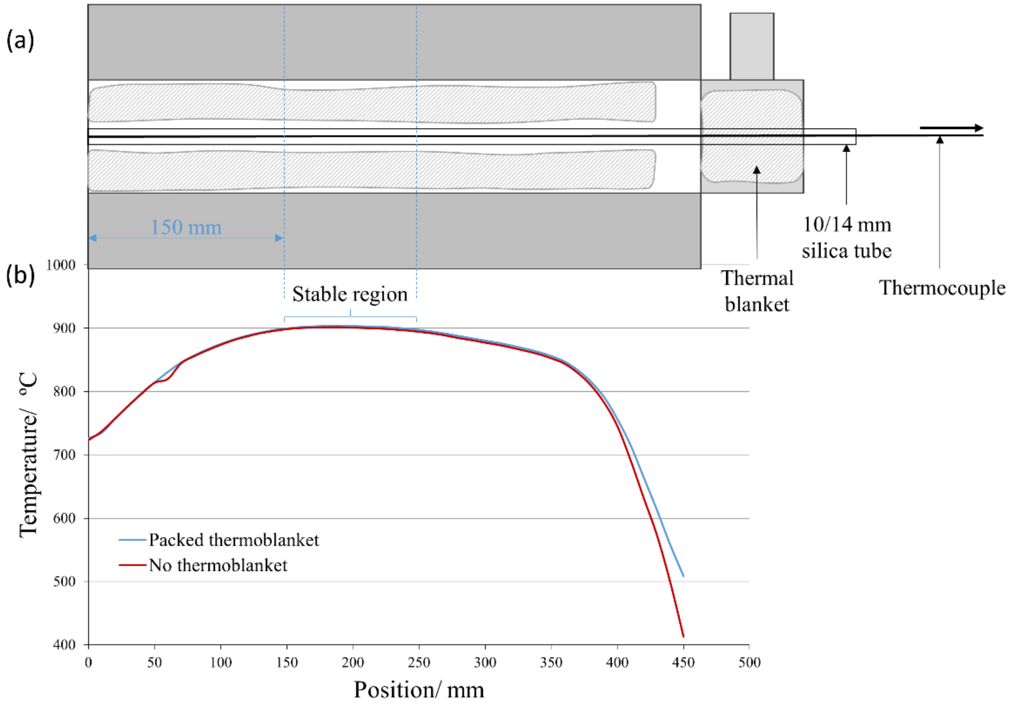

Figure 3.9: (a) Schematic diagram of the experimental setup used to measure the temperature profile of the chalcogenide glass melting, resistance tube furnace (Instron TF105/4.5/1ZF, tube ID 86 mm, Eurotherm 2408 controller). (b) Temperature profile of the resistance tube furnace, with 10/14 mm silica tube and thermocouple, whilst it was held isothermally at 900 °C. In total two runs were carried out to investigate the effect of thermal blanket insulation when it was either 1) packed or 2) not there at all. The scale of both (a) and (b) are the same, as indicated by the position of the thermocouple along the x-axis of (b).

To ensure each Ge-Sb-Se/S chalcogenide glass melt was properly homogenised, the resistance tube furnace (Instron, TF105/4.5/1ZF) was modified so that it could be rocked ±30° about the horizontal axis at certain stages during the melting schedule, detailed in Table 3.8. The speed at which it could be rocked was controlled and, for all chalcogenide glasses melted during this Project, 0.5 mins was spent at the end of each rocking cycle.

Table 3.8 provides an overview of the entire Ge-Sb-Se/S chalcogenide glass melting schedule from the start of melting in the resistance tube furnace (Instron, TF105/4.5/1ZF) (steps 1-7), to the chalcogenide glass quenching in a small tube furnace (in-house made, ID 28 mm or 38 mm bore) (step 8), and then finally chalcogenide glass annealing in a larger tube furnace (Instron, TF105/4.5/1ZF) (steps 9-10).

From Table 3.8, it can be seen that rocking was started once the resistance tube furnace (Instron, TF105/4.5/1ZF) was at 450 °C (step 4), and was continued as the chalcogenide glass melt was ramped up to, and then held isothermally, at 900 °C for 12 h (step 5). The temperature at which the rocking begun was changed once in this Project following the failure of M_HAP004 (see Table 3.3). Originally, glasses M_HAP001 to M_HAP004 began rocking during step 4 when the temperature was ramped from 300 °C to 900 °C at 40 °C/h. However, the failure of M_HAP004, raised concerns over the safety of this lower temperature and the programme was altered to start rocking after a dwell at 450 °C, as outlined in Table 3.8.

Table 3.8: Chalcogenide melting and annealing temperature/time schedules for all glasses investigated during this Project (excluding re-melts). For each step a schematic diagram illustrates the orientation of the melting furnace and whether it was being rocked or was stationary.

Step	Melting Schedule	Furnace details
1	Load sealed silica ampoule, containing chalcogenide material, into furnace (Instron, TF105/4.5/1ZF).	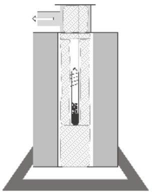 Vertical furnace No Rocking
2	Ramp from 25 °C to 450 °C @ 40 °C/h.	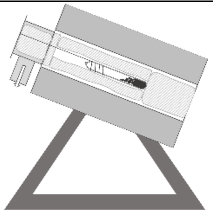 Furnace at 30° angle No Rocking
3	Dwell 2 h @ 450 °C.	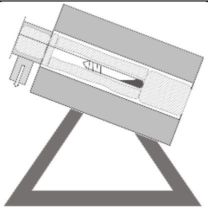 Furnace at 30° angle No Rocking
4	Ramp from 450 °C to 900 °C @ 40 °C/h.	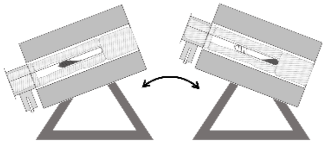 Furnace at 30° angle Rocking
5	Dwell 12 h @ 900 °C.	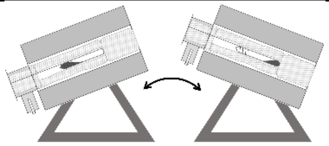 Furnace at 30° angle Rocking
6	Ramp from 900 °C to 700 °C @ 50 °C/h.	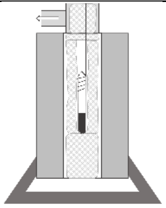 Vertical furnace No Rocking

Table 3.8 (cont.)

Step	Melting Schedule	Furnace details
7	Dwell 1 h @ 700 °C.	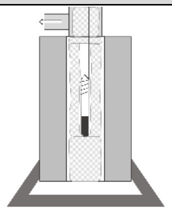 Vertical furnace No Rocking
8	(a) Quench in air to ambient (0.5 - 2.0 mins). (b) Quench in small tube furnace set at T_g (0.5 - 2.0 mins). (c) Progressively quench chalcogenide glass, from top to bottom of the boule, with nitrogen gas.	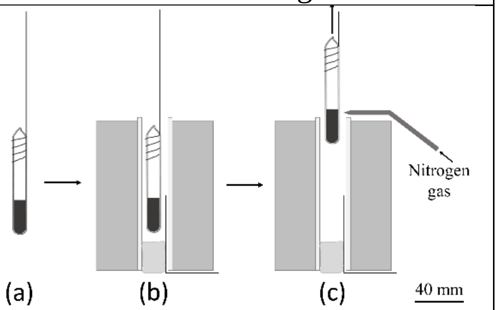 Small quenching furnace
Step	**Annealing Schedule**	**Furnace details**
9	Dwell for 0.5 h, 10 °C below T_g	Vertical in annealing furnace
10	Turn furnace off and allow to cool to RT (~24 h).	

Key: T_g= glass transition temperature; RT= room temperature.

Following a 1 h vertical dwell at 700 °C, the melt was quenched using the procedure summarised in Step 8 of Table 3.8. Depending on the batched weight, the silica ampoule containing the chalcogenide glass melt, was taken out of the 700 °C furnace and held vertically in the air for 0.5 – 2.0 mins. 0.5 mins was used for chalcogenide glass melts of ~20 g whereas, 2.0 mins was used for chalcogenide glass melts of ~80 g. Then, again weight dependant, the silica ampoule and its contents, was placed in a small tube furnace (in-house made, ID 28 mm or 38 mm bore) for 0.5 – 2.0 mins, which had been set to the glass' T_g at least 10 h before quenching.

To minimise the risk of the chalcogenide boule cracking, as it cooled and contracted inwards away from the silica glass ampoule walls during annealing, N_2-jet-quenching technology was used. This involved N_2 (99.998 %, BOC), being directed towards the surface of the silica ampoule, at a point where the top of the chalcogenide melt was found (see (c) in step 8 of Table 3.8). The N_2-jet was held at this point until the top of chalcogenide melt had separated from the silica ampoule. This was seen by a sudden change in colour (dark grey to shiny light grey) and took approx. 15 secs. Following this initial separation, the N_2 gas jet was gradually moved round the silica glass ampoule from the top of the chalcogenide boule to the end.

The N_2-jet-quenched silica ampoule, containing the quenched chalcogenide boule, was then immediately placed in an annealing furnace (Instron,TF105/4.5/1ZF), preheated to T_g – 10 °C, where it was held for approximately 0.5 h, before the furnace was turned off and the chalcogenide glass melt inside the silica ampoule was allowed to cool, with the furnace, to ambient temperature (took approx. 24 h).

To remove the chalcogenide glass boule from the silica glass ampoule, a diamond-coated, circular cutting saw (Buehler) was used to make several approximately 1.25 mm deep cuts along the length of the ampoule which did not penetrate the ampoule inner wall. Using a flat screw driver, the ampoule was cracked open and the boule removed. If the chalcogenide boule was to be used during a subsequent distillation, this opening of the silica glass ampoule would have been carried out in the MBraun glovebox. If the chalcogenide glass boule was for bulk characterisation, extrusion (see section 3.4.1) or fibre-drawing (see section 3.4.2), the silica glass ampoule was opened in the ambient atmosphere.

3.4 Chalcogenide glass shaping

The ultimate goal of this Project was to produce low optical loss chalcogenide glasses based on Ge-Sb-Se, which could be drawn into SIF for use in a MIR fibre optic imaging probe. As will be discussed throughout section 4, optical fibres were drawn from two types of preforms as follows: 1) a 10 mm diameter, as-annealed preform taken straight from its silica glass ampoule melt-containment or 2) 4.7mm or 10 mm diameter preforms which had been extruded from as-annealed 15 mm or 29 mm boules, respectively. It will also be discussed in section 3.5.4, how the 4.7 mm extruded preform was useful for thermomechanical analysis (TMA).

3.4.1 Extrusion

As-annealed chalcogenide glass boules were primarily extruded, during this Project, to form structured and unstructured, fibre-drawing preforms.

All extrusions were made using an in-house extruder, shown in Figure 3.10 (a), which was designed and built by Dr David Furniss, of the MIR Photonics Group, Faculty of Engineering, University of Nottingham. Although the extruder could be tilted through 90°, all chalcogenide glasses extruded in this Project, were extruded vertically.

Depending on which sized barrel, punch and die were inserted into the main frame of the extruder furnace (Figure 3.10(a)) preforms were extruded with either a ~4.7 mm or ~10 mm diameter. All 4.7 mm diameter preforms extruded in this Project were unstructured, single Ge-Sb-Se/S compositions and were approximately 110 mm long. The 10 mm diameter preform co-extruded in this Project was structured with a Ge-Sb-Se core and a Ge-Sb-Se-S cladding, for further detail see section 5.3.1. Figure 3.10(b) and (c) is shown a schematic overview of the stages involved for the extrusion of both the unstructured and structured preforms, respectively.

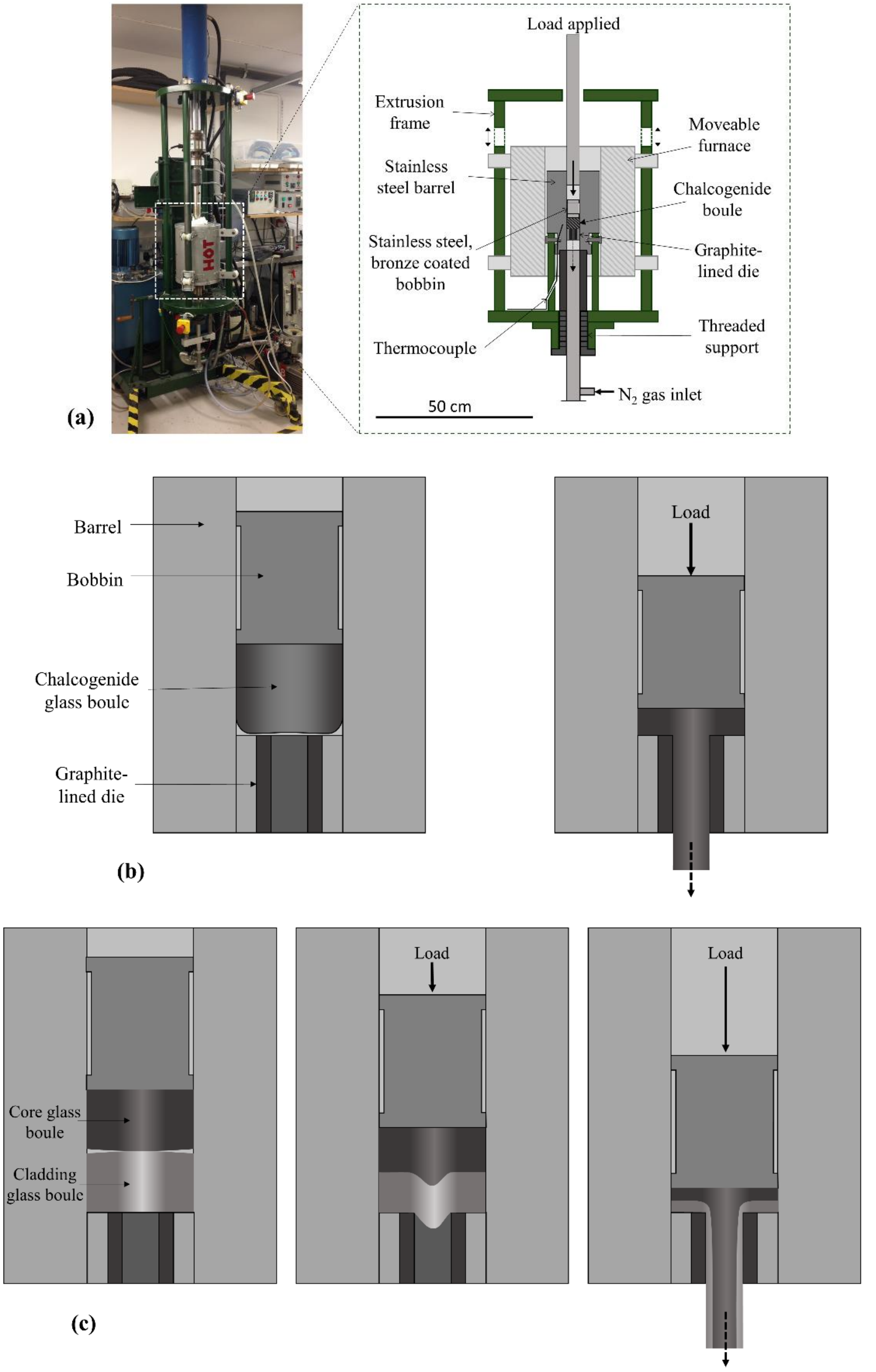

Figure 3.10: Extrusion process: (a) photograph and enlarged schematic diagram of the in-house designed and built extruder. Glass boules were heated in-situ to just above T_g before a load was applied. Schematic diagrams show: (b) extrusion of a single, unstructured glass and (c) co-extrusion of both a core and cladding composition.

To prepare all chalcogenide glass boules for extrusion, they first had to be cut using a diamond coated, circular cutting saw (Buehler). To prepare the 15 mm diameter boules, used to make unstructured ~4.7 mm diameter extruded preforms, the preparation was relatively simple because there was no critical chalcogenide-chalcogenide interface. Therefore, a single saw cut, parallel to the bottom of the as-annealed 15 mm diameter chalcogenide glass, produced a boule that was usually also approx. 15 mm in height.

However, the chalcogenide glass boules which had been melted, quenched and annealed in 29 mm ID silica glass ampoule, required a few more steps in order to extrude a core/cladding structured ~10 mm OD preform, with a pristine core-cladding interface. This is because the core and gladding chalcogenide glass boules were co-extruded together.

Firstly, it was important that the core and cladding boules had identical cylindrical geometry, with faces that were perpendicular to the applied load (see Figure 3.10 (c)). This was achieved using a cantilever assembly, pictured in Figure 3.11(a) and (b), which allowed two cuts made at once across one the as-annealed 29 mm diameter boule, producing a cylindrical sample approximately 15 mm in height, with top and bottom faces parallel. To avoid the formation of voids appearing along the extruded core-cladding boundary, the mating surfaces were ground and polished flat and to a 1 µm finish. The chalcogenide glass boules were first ground using 1000 grit SiC powder (Buehler) in oil (polishing oil, Buehler) and then polished in progressive stages using 6 µm, 3 µm, and then 1 µm diamond paste (Buehler) with careful washing using acetone followed by isopropanol as each medium was changed for the next finer. The final polished boules were scrupulously washed in acetone and then isopropanol and then air dried. In Figure 3.11(a) and (b) the difference is highlighted between in appearance of the saw cut and 1 µm polished surface, respectively, for the same side of a 29 mm diameter boule.

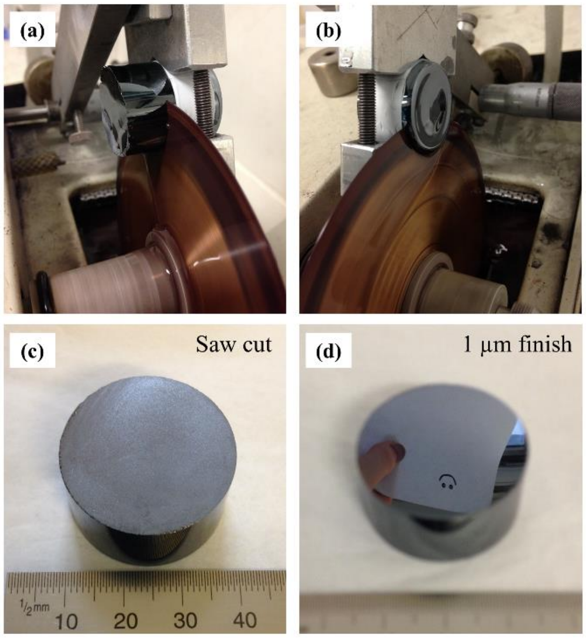

Figure 3.11: Preparation of glass boules for co-extrusion: (a) and (b) show the cantilever assembly used to make two parallel cuts across one chalcogenide glass boule without demounting the sample; (c) the surface of the glass boule after being cut with a diamond saw and (d) the same boule as in (c) but polished to a 1 µm finish.

Once the chalcogenide glass boules had been prepared and correctly loaded into the extruder barrel, the assembly was then place in the extruder furnace, where the extruder piston was lowered and the system was purged with nitrogen gas ('white spot', BOC). From the moment the furnace was started, until the end of the extrusion programme, the die temperature, bobbin position, and load, were monitored using Pico Technology logging software. An exemplar record can be seen in **appendix 3**. For each of the three glass compositions ($Ge_{25}Sb_{10}Se_{65}$ at. %, $Ge_{20}Sb_{10}Se_{70}$ at. % and $Ge_{20}Sb_{10}Se_{67}S_3$ at. %, see Table 3.3) extruded in this Project, the temperature was initially raised 50 °C above the respective T_g before the load was applied. On average, extrusions lasted approximately 6 hrs.

3.4.2 Fibre drawing

Unstructured chalcogenide glass fibres were either drawn from an as-annealed glass rod (~ 70 mm long and 10 mm diameter) or from an extruded rod (~ 90 mm long and 4.7 mm diameter). SIF were drawn from co-extruded rods (~100 mm long and 10 mm in diameter). In Figure 3.12 (a) is shown the customised Heathway draw-tower (housed in a class 10,000 cleanroom) that was used for fibre-drawing. The fibre-drawing furnace was purged using nitrogen gas (‘white-spot’, BOC) which had been freeze-dried as it travelled through a copper coil immersed in liquid nitrogen. The chalcogenide glass preform was hung vertically on the tower and was heated to a viscosity of above $10^{4.5}$ Pas by means of a graphite ring receptor, heated by radio frequency from a copper coil, and drawn to fibre (Figure 3.12 (b)).

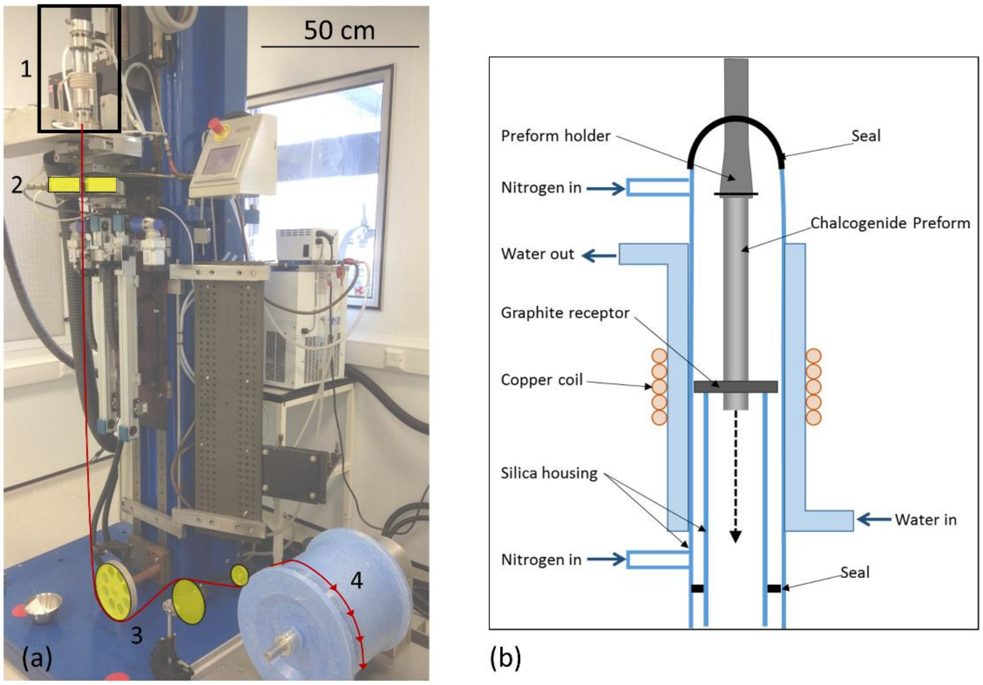

Figure 3.12: (a) Customised Heathway drawing tower housed in a class 10,000 cleanroom; (b) enlarged schematic diagram of the in-house customised radio frequency fibre drawing furnace.

It was not possible to measure, and thus control, the exact temperature of the chalcogenide glass preforms during fibre drawing as any thermocouple in the furnace would have been heated independently by the radio frequency. Instead, the temperature at which the chalcogenide glass preform begun to draw fibre, was controlled by the percentage of power given by the copper coil. **Appendix 4** shows a typical fibre drawing report, listing the parameters: power percentage, glass composition and preform preparation.

To achieve an optical fibre with a specific diameter, equation 3.1 was used to calculate the preform feed-in/ fibre feed-out rate. For example, if a 200 µm diameter fibre was desired from a 10 mm diameter preform, a feed-in rate of 2 mm/min would give a feed-out rate of 5,000 mm/min.

$$\begin{gathered} Preform\ diameter/Desired\ fibre\ diameter = (Ans.1)^2 = Ans.2 \\ Feed\ in\ (mm) \times Ans.2 = Feed\ out\ (mm) \end{gathered} \qquad \textbf{Equation 3.1}$$

Chalcogenide glass fibre was wound on-line onto a 1 m diameter drum (see Figure 3.12 (a)) and the tension on the fibre was controlled by the speed by which the drum rotated. Thus, the speed of drum rotation helped to control the fibre diameter. Once fibre-drawing had been completed, the 1 m diameter drum with wound chalcogenide fibre, was stored in the class 10,000 cleanroom until further use. Fibre loss measurements, described in section 3.6, were carried out within two days of fibre drawing.

3.5 Bulk glass characterisation

To assess the properties and overall success of the chosen chalcogenide glass composition, bulk glass characterisations was employed. Techniques included: X-ray diffractometry (XRD) to investigate the amorphous nature of the glass; differential scanning calorimetry (DSC) to find the glass transition temperature (T_g); differential thermal analysis (DTA) to find higher temperature characteristics such as the crystallisation and melting temperatures (T_c and T_m respectively); thermal mechanical analysis (TMA) to measure the viscosity and thermal expansion coefficient; scanning electron microscopy (SEM) to image either bulk glass or fibre samples; transmission electron microscopy (TEM) to investigate potential crystallisation; energy dispersive X-ray analysis (EDX) to measure the composition of bulk and fibre samples and Fourier transform infrared spectroscopy (FTIR) to evaluate the MIR optical transmission of bulk glass samples.

3.5.1 X-ray diffractometry (XRD)

(a) Background

XRD is a technique based on the constructive interference between monochromatic X-rays and a sample. Incoming X-rays are diffracted by the lattice planes of crystalline phases present in a sample, which are orientated at the correct angle to fulfil Bragg’s Law, seen in equation 3.2; where n is an integer, λ is wavelength, d is the spacing between the layers of atoms and θ is the angle between the incoming rays and the surface of the crystal. Once the diffracted X-rays are detected and processed, the diffraction peaks are converted into unique d-spacings for identification.

$$n\lambda = 2dsin\theta$$ **Equation 3.2**

(b) Method

The amorphicity of the chalcogenide glasses was analysed using XRD in a Siemens D500 diffractometer, with CuKα radiation, in the 2θ range 10° to 70°. The programmed run had a step size of 0.05°, 40 seconds was spent at each step so the total run time was 13.2 h. If the sample was not fully amorphous, identification of the XRD peaks was achieved by comparing the measured diffraction pattern with International Centre for Diffraction Data Powder Diffraction File (ICDD PDF) standards.

(c) Sample preparation and safety

XRD samples were either small pieces of bulk glass, or approximately 2 m of 200 µm diameter fibre, which were both washed with acetone to remove any contamination. Since powdered XRD samples were investigated in this Project, a face mask was worn throughout preparation as a safety precaution. Furthermore, all samples were ground using an agate pestle and mortar inside a drawing fume cupboard, during which they were submerged in a pool of acetone so to minimise the chances of fine particles becoming airborne. Although the powdered particle size was unknown, it was found that if the sample was not ground finely enough, the final XRD pattern would be noisier and potentially misinterpreted. Figure 3.13 shows two XRD curves from the same XRD Ge-Sb-Se bulk sample: (a) a relatively coarse Ge-Sb-Se powder was run first then, (b) it was ground a little finer for the second run. The arrows in Figure 3.11 show two regions, within the XRD pattern, where the noise has been reduced.

Once the sample had been correctly prepared, it was then transferred into the indent in a standard aluminium XRD holder. A silicate glass microscope slide was used to flatten off the sample so that the sample holder indent was fully filled flush with the powdered sample yet the powder did not protrude out.

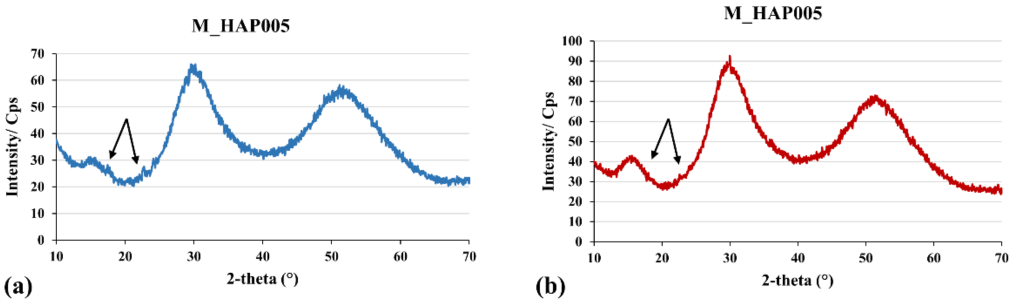

Figure 3.13: XRD patterns highlighting that a coarse-powdered sample of $Ge_{20}Sb_{10}Se_{70}$ *at. % (M_HAP005) (a) gave rise to a nosier XRD pattern compared to the fine-powdered sample (b) of the same glass.*

3.5.2 Differential scanning calorimetry (DSC)

(a) Background

Differential scanning calorimetry (DSC) is a technique used to study how a material's heat capacity changes with temperature. It works by measuring the difference in heat flow between a sample of known mass and an empty reference pan. The energy required to maintain the two pans at the same temperature, during constant heating/cooling rates, can be used to produce a typical heat flow graph seen in Figure 3.14. The endothermic curve can be extrapolated, as shown, to calculate the onset-T_g value [178].

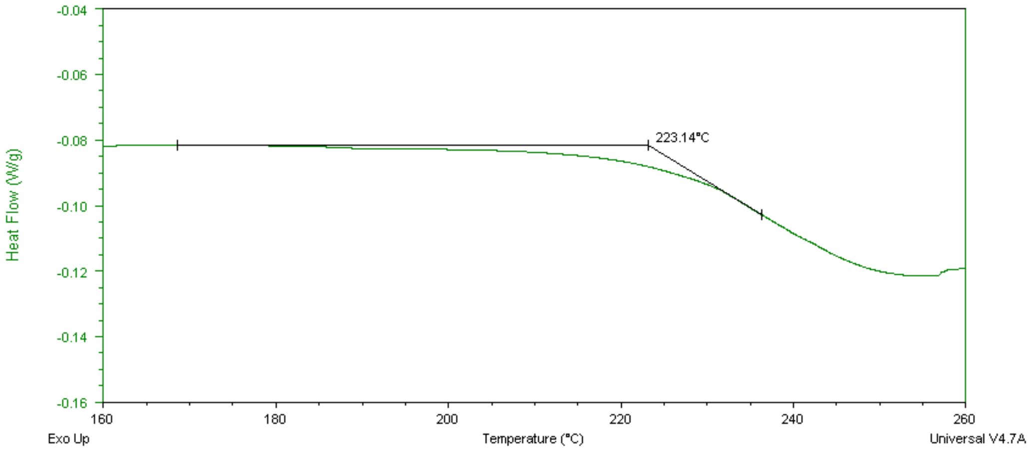

Figure 3.14: Enlarged section of a differential scanning calorimetry (DSC) curve with tangents measuring the onset-T_g value from the first endothermic transition.

(b) Method

Measured in a Perkin Elmer Pyris 1 DSC analyser, under flowing Ar gas (BOC), each sample was run three times and each run consisted of a heating and cooling cycle at 10 °C/min, see Table 3.9. The final temperature reached was dependent on the glass composition and was approximately T_g +50 °C. The endothermic onset-T_g was taken as the average from runs 2 and 3. To remove any artefacts unrelated to the glass sample, a baseline was subtracted from the DSC traces. Baselines were run just before the final measurements using two sealed, empty aluminium pans (Perkin Elmer) over a temperature range that would cover the sample runs seen in Table 3.9 *e.g.* from 35 °C to 500 °C @ 10 °C/min. To calibrate the equipment, Indium (m.p. 156.6 °C) was used for the low temperatures and Zinc (m.p. 419.5 °C) for the high temperatures.

Table 3.9: Typical differential scanning calorimetry (DSC) schedule.

Step	Description
1	Hold for 1 min @ 40 °C
2	Heat from 35 °C to 400 °C @ 10 °C/min
3	Hold for 1 min @ 400 °C
4	Cool from 400 °C to 40 °C @ 10 °C/min
5	Hold for 1 min @ 40 °C
6	Heat from 35 °C to 400 °C @ 10 °C/min
7	Hold for 1 min @ 400 °C
8	Cool from 400 °C to 40 °C @ 10 °C/min
9	Hold for 1 min @ 40 °C
10	Heat from 35 °C to 400 °C @ 10 °C/min
11	Hold for 1 min @ 400 °C
12	Cool from 400 °C to 40 °C @ 10 °C/min

(c) Sample preparation

DSC samples were taken from a cylindrical section of the as-annealed Ge-Sb-Se/S rod, approximately 10 mm below the contraction cone. Washed in acetone and isopropanol, a ~3 mm thick Ge-Sb-Se/S disc was broken in a pestle and mortar before ~20 mg was weighed (Sartorious, model BP221S, ±0.1 mg) in an ambient atmosphere. The broken pieces, ~2-5 mg in weight, were transferred using stainless steel tweezers into an aluminium pan (Perkin Elmer). It was important that all the small pieces contributing to the ~20 mg sample weight, were arranged carefully in the aluminium pan, so that when the aluminium lid (Perkin Elmer) was cold-welded on top, no glassy pieces dented or pierced it. Sample and reference lids and pans were cold-welded using a Perkin Elmer pressure clamp.

3.5.3 Differential thermal analysis (DTA)

(a) Background

Differential thermal analysis (DTA) is another technique used to characterise the thermal properties of a glass. Although DSC provides a more sensitive T_g measurement, the experimental set up of DTA allows the sample to be taken to higher temperatures so that features such as the crystallisation temperature (T_c) and the melting temperature (T_m) can be identified. DTA uses thermocouples to measure the temperature difference (ΔT) between the sample ampoule and reference ampoule when an equal amount of energy is applied to both during isothermal heating. Characteristic temperatures, such as the T_c and T_m, are defined by the exothermic and endothermic peaks, respectively, when the endotherm is plotted downwards, against temperature.

(b) Method

Measurements were carried out in a Perkin Elmer DTA 7 analyser with a single run to 700 °C at a rate of 10 °C/min, under flowing Ar gas, 200 ml/min. A baseline run, made using two empty silica ampoules, was again subtracted from the DTA traces to remove external artefacts. DTA was calibrated using pure Al for the low temperature range (m.p. 660.32 °C) and gold for the high temperature range (m.p. 1064.18 °C).

(c) Sample preparation

Washed in acetone and isopropanol, as-annealed chalcogenide glass samples were broken using an agate pestle and mortar, into small chunks each weighing ~20 mg. A 100 mg sample was weighed (Sartorious, model BP221S accurate to ±0.1 mg) in ambient atmosphere and transferred to a ~3/4.7 mm (ID/OD) silica ampoule using stainless steel tweezers. Under vacuum (10^{-3} Pa) the silica ampoule was sealed using an oxy-propane (BOC) torch. The procedure was then repeated for an empty silica ampoule which acted as the reference. The point at which the silica ampoules were sealed was important, as both the sample and reference silica ampoule had to be of similar height so that the reference was as representative as possible; an example of both is shown in Figure 3.15 (a). In Figure 3.15 (b), the sample-containing silica ampoule is seen on the left and the empty silica reference ampoule, is seen on the right.

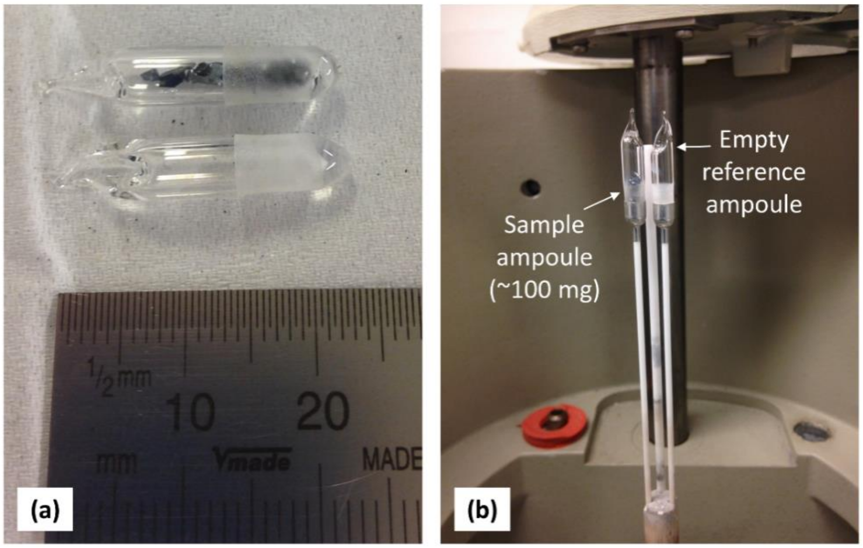

Figure 3.15: Differential thermal analysis (DTA) preparation: (a) comparison between the size of the sample and reference ampoules and (b) both ampoules placed inside the DTA holder.

3.5.4 Thermal mechanical analysis (TMA)

Thermal mechanical analysis (TMA) is a technique used to study the properties of a material with changing temperature. Carried out in a Perkin Elmer TMA-7, both the viscosity and thermal expansion coefficient (TEC) were investigated in this Project.

All samples used for TMA, were cut from extruded rods with a diameter of ~4.7 mm (procedure described in section 3.4.1). Extra care was taken to ensure the cuts were made perpendicular to the length of the extrudate so that final samples had a ~90 ° angle. Three different sized samples were cut, depending on the investigation (*i.e.* viscosity-temperature or TEC), and alternated along the rod (see Figure 3.16). This was to ensure not all TEC samples, for example, came from the same section of extrudate in case the rod was inhomogeneous.

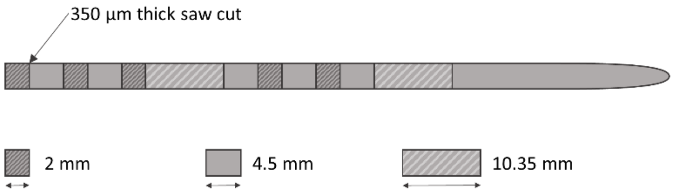

Figure 3.16: Schematic diagram showing thermal mechanical analysis (TMA) samples cut from a ~4.7 mm diameter, extruded rod. Samples cut with a height of ~2 mm and ~4.5 mm were used for viscosity-temperature analysis and samples cut with ~10.35 mm were used for thermal expansion coefficient (TEC) analysis.

3.5.4.1 Viscosity-temperature bulk characterisation

(a) Method

Viscosity-temperature measurements were carried out using the parallel plate technique, in a Perkin Elmer TMA7 thermomechanical equipment with flowing He (BOC) at 20 ml/min. A constant load of 50 mN was applied to sample with a 1.6 mm height whilst, a constant 400 mN was applied to samples with a 4.1 mm height. Samples were heated at 40 °C/min to a temperature approximately 150 °C above T_g or until the programme had been stopped by the user. This was to ensure the samples had not expanded too far that they touch the sides of the machine. Equation 3.3 was used to calculate the minimum sample height. The accuracy of the viscosity-temperature values are ±2 °C and $10^{\pm 0.05}$ Pa.s.

$$Sample\ height\ \times \left(\frac{Sample\ diameter}{Bottom\ plate\ diameter}\right)^2 \qquad \textbf{Equation 3.3}$$

(b) Sample preparation

Samples cut for viscosity-temperature investigations had a height of either 2.0 mm or 4.5 mm (Figure 3.16) so that a viscosity range between ~$10^{4.5}$ – 10^8 Pa.s could be recorded thus, providing suitable temperatures for which to extrude (~$10^{4.5}$ Pa.s) or fibre-draw (~$10^{7.5}$ Pa.s) a composition. As the circular diamond cutting blade was 350 µm in diameter, final sample heights were ~1.6 mm and ~4.1 mm

Before testing, samples were carefully washed three times in acetone and isopropanol, so to remove any residual wax, and then measured for both their heights and diameters.

3.5.4.2 Thermal expansion coefficient, TEC

(a) Method

TEC was also measured on the TMA-7 thermomechanical equipment. Samples were placed in the TMA holder, under a 30 ml/min He (BOC) flow, with a constant force of 100 mN. Samples were heated at a rate of 5 °C/min to a temperature ~40 °C above T_g before being cooled at a rate of 10 °C/min. Thermal expansion, was calculated according to equation 3.4, where *dL* is the change in sample height, *L* is the original height of sample and *T* is the temperature of the specimen.

$$TEC = \left(\frac{dL}{L}\right)\left(\frac{1}{\Delta T}\right) \qquad \textbf{Equation 3.4}$$

(b) Sample preparation

As depicted in Figure 3.16, TEC samples were cut from a ~4.7 mm diameter extruded rod with a height of ~10 mm, taking into consideration the width of the diamond cutting blade. Just like the viscosity-temperature samples, TEC samples were carefully washed three times in acetone and isopropanol, so to remove any residual wax, and then measured for both their heights and diameters.

3.5.5 Scanning electron microscopy (SEM)

(a) Method

SEM with EDX was a useful technique for imaging chalcogenide samples and obtaining elemental compositions. In this Project, a Phillips FEI XL30 SEM system was used in high vacuum mode for SEM measurements in combination with Oxford Instruments INCA software for compositional analysis. The accuracy of the SEM/EDX results was estimated to be ±0.5 at. % for elements heavier than oxygen[179]. To avoid the semi-conducting chalcogenide glass from becoming charged, all samples were coated using an AGAR TURBO carbon coating system and mounted on adhesive carbon tabs.

(b) Sample preparation

Depending on the sample form, preparation varied for each SEM/EDX sample. For simple compositional analysis of as-annealed bulk chalcogenide glass, samples would be prepared following the same sequential polishing technique as described in section 3.4.1. For SEM/EDX analysis of Ge-Sb-Se or Ge-Sb-Se/S fibre-drawn samples, fibres were cleaved and assembled in the setup shown in Figure 3.17. Where surface topography or composition was of interest, samples would remain in the original state (*i.e.* not polished); this was particularly relevant for the SEM samples that will be discussed throughout section 6. All samples were washed prior to analysis with acetone and isopropanol with special care taken keep samples contamination-free.

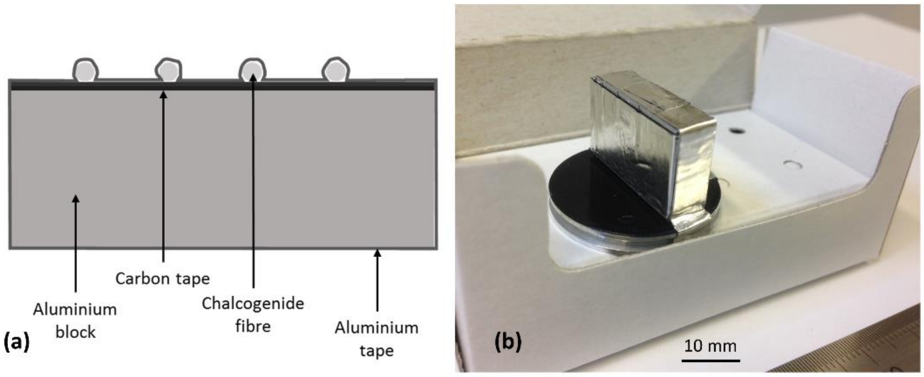

Figure 3.17: Preparation of Ge-Sb-Se/S fibres for scanning electron microscopy (SEM) analysis.

3.5.6 Transmission electron microscopy (TEM)

(a) Method

As there was limited sensitivity to small crystals using the XRD Siemens D500 diffractometer, TEM was used to investigate potential nucleation in Ge-Sb-Se glasses. Using a JEOL 2000FX TEM, samples were first analysed with selected area electron diffraction (SAED) and then, if crystals were discovered, EDX

(Oxford Instruments INCA) for phase identification which had an accuracy of ±1 at. % for elements with atomic masses greater than oxygen[179]. Analysis and data manipulation was supported by Dr. Nigel Neate (senior research technician, University of Nottingham).

(b) Sample preparation

Similar to the XRD procedure outlined in section 3.5.1, samples were prepared in a fine powder form using the agate pestle and mortar (Fisher). Only two compositions were studied by TEM and came from either: 1) an as-annealed bulk $Ge_{25}Sb_{10}Se_{65}$ at. % rod (M_HAP003) or 2) a fibre-drawn $Ge_{25}Sb_{10}Se_{65}$ at. % preform which had also been initially extruded (E_HAP005). The powdered sample, in an isopropanol solution, was transferred into a silicate bottle which was then placed in an ultrasonic bath (Kerry. W. Jennings Company Limited) for 10 mins. Part of this solution was aspirated from the silicate bottle and placed on a copper TEM grid with carbon support film (Cerac).

3.5.7 Fourier transform infrared spectroscopy (FTIR)

(a) Method

FTIR spectroscopy is a technique that can be used to assess the optical transparency of a glass in both bulk and fibre form. Performed on a Bruker IFS 66/S spectrometer, as-annealed bulk glasses were analysed via two optical set-ups. The MIR spectral region was collected using a Globar (Glo) source, KBr (potassium bromine) beamsplitter and a DTGS detector. The NIR region was collected using a tungsten source (W), a broadband beamsplitter (BB) and a DTGS detector. Before measurements, the FTIR spectrometer was purged with dry air (Parker Filtration, FT-It purge gas generator, 75-52-12VDC) for 15 mins to remove the CO_2 peak at approximately 4 µm. Figure 3.18 shows a gradual decrease in the CO_2 absorption for a range of purge times; 15 mins was shown to be the best.

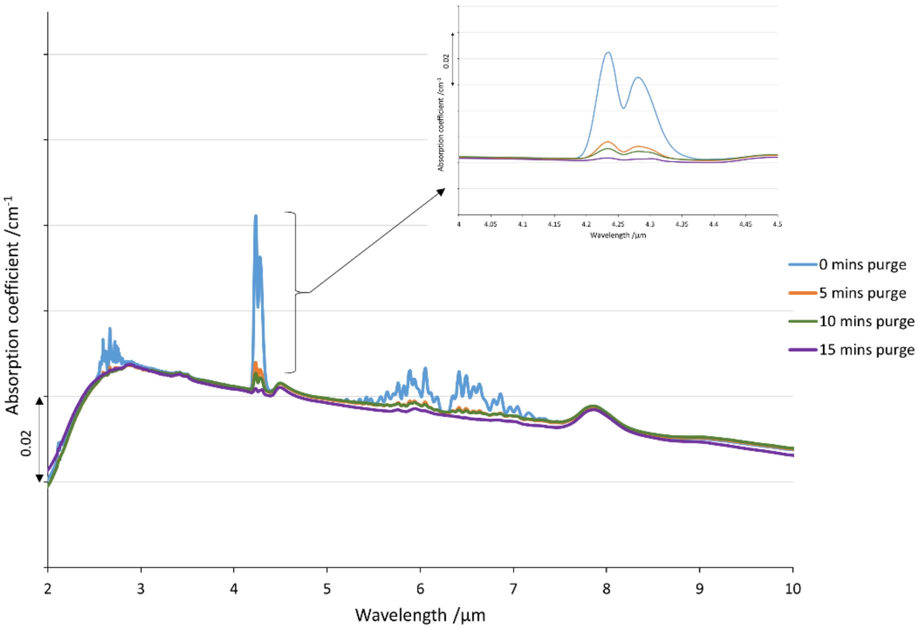

Figure 3.18: Fourier transform infrared spectroscopy (FTIR) curves for runs with various purging times. A 15 min purge was shown to reduce the CO_2 artefact at ~4.2 µm. Inset shows an enlarged view of this region.

Prior to the sample measurements, a background spectrum would have been completed using the empty sample holder and a purge time of 15 mins. This would have been automatically removed by Bruker software during the sample run. The resulting MIR absorption spectrum was divided by their optical pathlength (i.e. the height, 2-3 mm) previously measured by a micrometre (Mitutoyo).

(b) Sample preparation

Bulk FTIR samples were cut and prepared via a similar procedure outlined in section 3.4.1. Samples were cut 2-3 mm in height and polished, both sides, down to a 1 µm finish. Once the sample had been cleaned with acetone and then isopropanol, making sure no residual marks remained on the surface, the polished discs were placed on the sample holder with an aperture diameter of 5 mm.

3.6 Fibre characterisation

Optical fibre loss measurements were carried out within two days of drawing using the cut-back method outlined in Figure 3.19. The FTIR-combined experimental setup for the 2.5 – 10 μm wavelength range included: Globar light source; KBr beam splitter and InSb/MCT detectors (both liquid-nitrogen cooled).

Before conducting the final measurements, a ~1 m length of fibre, taken from the same fibre drawing drum, was used to align the MIR beam. Not only did this step ensure the maximum amount of MIR light reached the detectors, it also gave an indication into the quality of the glass and thus, what length of fibre could be used for the final loss measurements. It was preferable to use the longest possible length of chalcogenide fibre for optical loss measurements, as this allowed final measurements to be dominated by the actual fibre losses, rather than the fibre-end cleave quality. The longest length used in this project was ~18 m (see section 6.3). Fibre alignment was carried out the day before final loss measurements.

Producing good quality cleaves from non-silica fibres was challenging however, an evolved ‘pull’ method proved successful. Using a diamond-tipped scribe (S90R Thorlabs; or 58805-600 Diamond Fibroscribe, Lunzer), a small mark was made on the surface of the fibre (~15 mm from the end). Grasping the fibre either side of the cut, tension was applied ensuring the fibre was not being pulled at an angle. Each cleave was checked by an optical microscope (Nikon Optiphot/Vickers RT2112 with GXoptical detection camera GXCAM-5) and successful Group 1/2 cleaves were saved for further imaging (Nikon Eclipse LV100ND) or SEM-EDX analysis (Phillips FEI XL30 SEM).

For each fibre loss measurement, two groups of cleaves were made along the chalcogenide glass fibre as demonstrated in Figure 3.19. ‘Group 1’ were 3-4 cleaves made near the KBr/MCT detectors and ‘Group 2’ were 3-4 cleaves made after a long piece of chalcogenide fibre was cut back. The initial ‘launch’ cleave, *i.e.* the fibre end closes to the launched MIR light, was the first cleave to be made and remained untouched in the launch position, throughout the remainder of the fibre loss experiment.

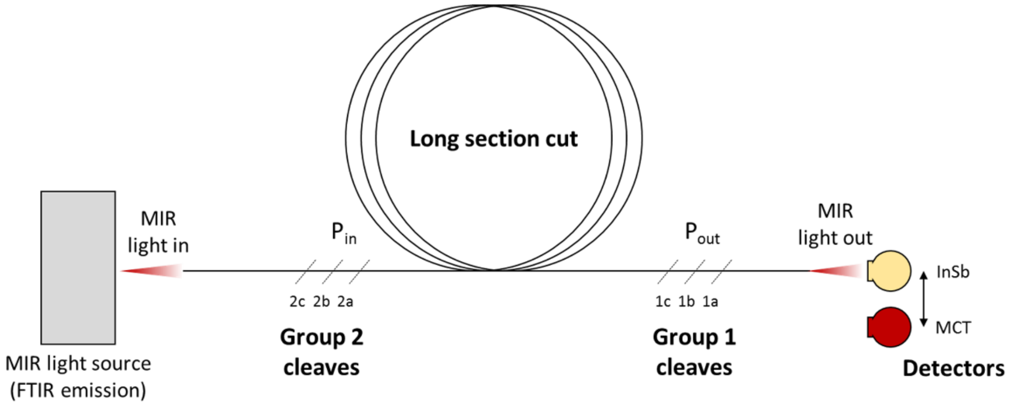

Figure 3.19: Schematic diagram of the optical loss cut-back method used in this work. For shorter MIR wavelengths an InSb detector was used whereas for longer MIR wavelengths an MCT detector was used. The two spectra were then combined together for the final loss measurements.

To calculate the optical fibre loss, equation 3.5 was used where: L (m) is the length of fibre between the final Group 1 and Group 2 cleaves; I_1 is the light intensity collected from a cleaved fibre-end in Group 1 and I_2 is the light intensity collected from a cleaved fibre-end in Group 2. For a full explanation of the fibre loss cut-back method and subsequent calculations, please refer to Tang *et al.* work [116].

$$Loss\ /(dBm^{-1}) = \frac{-10\log_{10}\frac{I_1}{I_2}}{L}$$ **Equation 3.5**

3.7 Cytotoxicity assessment of Ge-Sb-Se glasses

This section details the experimental procedure for results presented in Chapter 7. The main bulk of practical work was conducted by two MEng students: Mr Teo Kubiena and Mr Wey Chan Gan, supervised by the Author.

3.7.1 Materials, cells and chemicals

The chalcogenide bulk glass and fibres investigated for cytotoxicity are listed in Table 3.10. There were two fibre-drawn Ge-Sb-Se compositions (sample A and B), both of which were used in direct contact (alamarBlue®) and elution test

(Neutral Red) assays, and one as-annealed bulk Ge-Sb-Se glass (sample D) used for contact angle measurements. As a comparison, an As-Se fibre sample C, was also introduced into one of the elution tests, Neutral Red Assays as an initial investigation into the *in-vitro* cytotoxicity of arsenic-containing chalcogenide glass fibres *vs*. arsenic-free.

*Table 3.10: Investigated glass compositions and corresponding forms used for either alamarBlue ®, Neutral Red or contact angle measurements. The melt/ fibre codes shown in **bold** refer to glass samples kindly prepared by other members the Mid-infrared Photonics Group (appendix 1).*

Sample	**Composition /at. %**	**Sample form**	**Diameter /µm**	**Melt/ fibre code**
A	$Ge_{22.5}Sb_{7.5}Se_{70}$/ $Ge_{24}Sb_{4.36}Se_{71.6}$	Core/cladding structured fibre	200-220	**F_HAP009**
B	$Ge_{20}Sb_{10}Se_{70}$	Unstructured fibre	200-220	F_HAP003
C	$As_{40}Se_{60}$	Unstructured fibre	190-200	**F_HAP010**
D	$Ge_{20}Sb_{10}Se_{70}$	As-annealed bulk glass	10,000	M_HAP006

For cell viability investigations, Ge-Sb-Se fibres were cleaved, using a ruby-tipped scribe, into lengths of 6.4 ± 0.1 mm. Similar to the fibre loss procedure outlined in section 3.6, the quality of the cleave was observed both by eye and optical microscopy (Nikon Optiphot/Vickers RT2112 with GXoptical detection camera GXCAM-5). The cytotoxicity of samples A, B and C was investigated through a variety of surface treatments: (i) etched and (ii) non-etched and (iii) oxidised. Etching was achieved through the submersion of cleaved fibres into individual sterilised silica glass vials, filled with propylamine (ACROS OrganicsTM, 99+ %), and placed onto an orbital shaker at 100 rpm for 20 minutes at ambient temperature. This procedure removed the oxide layer, from the surface of the chalcogenide glass, which would otherwise be present in ambient atmosphere[180], i.e. on the non-etched samples, and thus allowed fibres to be immediately investigated in a fresh form state. Some samples from A and C (Table 3.10) were also treated with hydrogen peroxide (Fisher Chemicals, 30 % SLR) so to purposely oxidise the chalcogenide glass surface. This was again carried out in individual sterilised silica glass vials on an orbital shaker but this time left shaking for a duration of 24 hrs at ambient temperature.

Sample D bulk glasses were cut using a rotational diamond blade, from a 10 mm diameter rod-shaped as-annealed preform, and successively polished to a 0.25 µm finish (refer to section 3.4.1). One disc remained in this 0.25 µm polished state for contact angle investigations whilst another was once again treated with hydrogen peroxide, using the aforementioned procedure.

All surface treatments were carried out immediately before the cytotoxicity testing on samples which had initially been washed with acetone (VWR Chemicals, 99.8+ %) and isopropanol (Fisher Scientific, 99.5+ %) and then air dried. Furthermore, all materials were sterilised using an ultra violet (UV) lamp (Triple Red Laboratory Technology, Nuaire Biological Safety Cabinate, Class II) prior to cellular exposure.

3T3 Swiss Albino fibroblasts (ECACC 85022108), were grown in a humidified 5% CO_2 atmosphere at 37 °C, and used in alamarBlue ® and neutral red assays. Cells were cultured at 37 °C with Dulbecco’s Modified Eagle’s Medium (DMEM) supplemented with 8.6 vol. % foetal bovine serum (FBS), 0.5 vol. % L-Glutamine, 1.2 vol. % antibiotics-antimycotics, 1.2 vol. % HEPES Buffer and 0.5 vol. % non-essential amino acids. From here on, the term ‘media’ will refer to this growth solution. Media was changed every 2 days or until cells reached 80 % confluency.

3.7.2 Direct contact test with alamarBlue® assay

The alamarBlue® assay was used in a direct contact assay format, to measure cellular viability and proliferation of 3T3 fibroblast cells when directly exposed to fibres from samples A, B and C (Table 3.10). As a non-toxic, water-soluble, colorimetric redox indicator, alamarBlue® changes from blue (non-fluorescent) to pink (fluorescent) when cells reduce resazurin to resorufin through cell growth. Before cell seeding, 0.6 ml of media was introduced to the basolateral section of a 24- well polystyrene microplate with permeable Corning Transwell Insert’s

(Figure 3.20) whilst 0.1 ml of the medium added to the apical section. The 24-well assembly was then incubated and left to equilibrate at 37 °C for 2 hr.

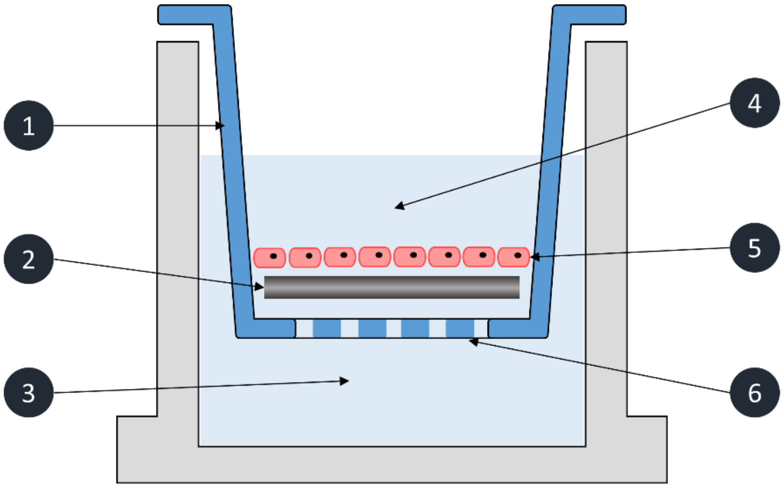

1	Corning© Transwell Insert	**4**	Apical side
2	Chalcogenide glass fibre	**5**	Cell monolayer
3	Basolateral side	**6**	Polycarbonate membrane

Figure 3.20: Schematic diagram of direct contact apparatus used for chalcogenide glass fibre cytotoxicity testing.

3T3 fibroblast cells, with a previously determined number of cells, were next seeded at a rate of 30,000 ±1000 into the individual wells, which by now, also contained the sterilised Ge-Sb-Se fibre samples or were left empty as the negative control (Figure 3.21). Samples were subsequently incubated at 37 °C in 5 % CO_2 and remained untouched until each time point (either day 1, 3, 7 or 14).

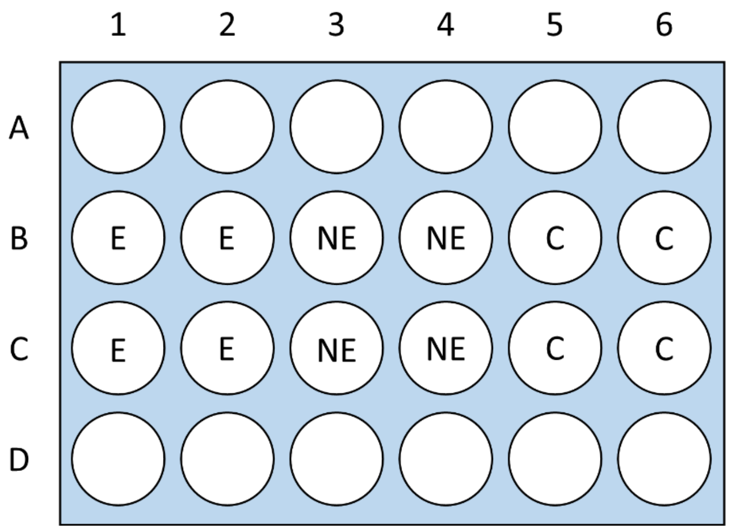

Figure 3.21: Organisation of chalcogenide glass fibre samples in a 24-well plate. E refers to wells with etched fibres; NE refers to wells with non-etched fibres and C refers to empty cells acting as the control. Those wells left blank (i.e. all of row A and D) were not used during the direct-contact, alamarBlue® cytotoxicity assessment.

AlamarBlue® (BIORAD), was diluted to a 1:10 ratio using Hanks Balance Salt Solution (ThermoFisher) in a 50 ml universal, on the day of testing, and kept in a water bath at 37 °C. To prevent the alamarBlue®-solution being exposed to UV light, it was wrapped in aluminium foil until use. At each time point, all of the media was aspirated from either the etched, non-etched or controlled well and the well was washed three times with a Phosphate Buffer Solution (PBS) to remove any residual media. 0.6 ml of alamarBlue® was pipetted back into the basolateral section of each well and 0.39 ml to the apical section (again refer to Figure 3.20). An equal volume was added to four blanks, which had no inserts, so that a fluorescence baseline could be identified. The 24-well plate was then incubated at 37 °C in 5 % CO_2 for 80 mins which was followed by 10 mins on a plate shaker (Heidolph Titramax 100) at 150 rpm; again, the wells were covered in aluminium foil as soon as they had been removed from the incubator.

Three 100 µl aliquots of the tested alamarBlue® indicator were then taken from each sample well and transferred to a new 96-well plate. As fluorescence intensity is sensitive to temperature, the 96-well plate was allowed to equilibrate at room temperature for ~30 mins prior to reading in a microplate fluorescence reader

(Biotek FLx800, 560 nmEX excitation and 590 nmEX emission wavelengths) and processed using KC junior software. Fluorescence values were calculated by subtracting the mean average background, provided by the four blank wells, from each of the averaged sample conditions i.e. etched, non-etched and control.

At the same time as the fluorescence reading, the original 24-well sample plate was returned to the incubator for parallel SEM preparation. This qualitative investigation complemented the results obtained using alamarBlue®, and provide a visual insight to the cell behaviour at each time point. Since alamarBlue® is a non-toxic indicator for cytotoxic evaluation[181], the morphology of the cells was not affected. Following the alamarBlue® assessment, the residual solution was aspirated from the sample wells and the well washed three times with PBS before being submerged in a fixative solution (3 % glutaraldehyde in 0.1 M cacodylate buffer solution) for 30 mins i.e. freezing samples in their final state. Excess fixative was removed and the sample surface was washed three times in ambient temperature with 0.1 M cacodylate buffer solution, allowing 5 mins of exposure for each wash. Cells were post-fixed using, 1 % osmium tetroxide (OsO_4), in aqueous solution, at room temperature for 45 mins. After exposure, the OsO_4 was aspirated off and samples were submerged in 20 vol. % ethanol (Fisher Chemicals, 99.8+ %, 80 vol. % distilled water) for two mins to begin the dehydration process. Further concentrations of ethanol: 40 %, 60 %, 70 %, 80 %, 90 % and 100 % were then used each with an exposure time of 5 mins. The 100 vol. % ethanol solution was applied twice. For the final step, the samples were submerged in hexamethyldisilazane (HMDS) for 5 mins at ambient temperature and then left to evaporate overnight in a fumehood at room temperature.

Fully dehydrated samples on the polycarbonate membrane were then separated, using a scalpel, from the rest of the inserts, mounted on a SEM stub and platinum (Trial 1, section 7.2.1.2)/gold (Trial 2, section 7.2.2.2) coated. Images were captured using a Philips XL30 SEM (Trial 1, section 7.2.1.2) or a JEOL6490LV Variable Pressure SEM (Trial 2, section 7.2.2.2). Magnification calculations were accurate with a 5% error.

3.7.3 Elution test with neutral red assay

Material cytotoxicity was also investigated through an elution procedure where 3T3 fibroblast cells were exposed to chemicals extracts from the chalcogenide glass and fibre samples A, B and C (see Table 3.10) which had received different surface treatments *i.e.* etched, non-etched or oxidised. Quantitative assessment was measured by the uptake and accumulation of neutral red (NR) by viable cells. NR is a dye that is actively endocytosed with the lysosomes of healthy cells and can give an index into the overall viability.

Material was extracted from chalcogenide glass fibre samples A, B and C (Table Table 3.10) using DMEM-FBS media as the carrier due to its known cellular interactions and in accordance with the International Organisation for Standardisation (ISO 10993-5)[182]. Each sample was eluted in a silica glass universal tube at a ratio of 6 cm^2/1 ml (fibre surface area/ carrier ml) whilst being rotated on a roller mixture (Denley Spiramix 5) at 50 rpm for 24 hrs at ambient temperature. At the same time, 3T3 cells were seeded into 48-well plates at a rate of 30,000 ±1000 and incubated at 37 °C in 5 % CO_2. Elution tests and cell seeding preparations was begun simultaneously so that NR assessment could be performed on a cell layer at 70-80 % confluency.

After 24 hrs, the DMEM-FBS media was aspirated from the well plates and replaced with the fibre-exposed solutions at volume concentrations of: 100 %, 75 %, 50 %, 25 % for which DMEM-FBS media was used as the diluent. A 100 % DMEM-FBS solution was also included as the control. Four replicates, of each chalcogenide glass sample, for each volume concentration (*e.g.* four repeats of sample A for 75 %) were then incubated at 37 °C in 5 % CO_2 for 24 hrs.

Before the cell viability could be analysed, a NR solution was prepared by diluting a stock solution with DMEM-FBS media at a ratio of 1:100. The resulting mixture had 50 µg of NR dye (Sigma Aldrich) per 1 ml DMEM-FBS and was maintained at 37 °C to prevent crystalline precipitates affecting the optical density readings.

Following 24 hrs of exposure to the eluted material, the varying concentration solutions were aspirated from the wells and replaced with 300 µl aliquots of the working NR solution for 45 mins at 37 °C and 5 % CO_2. Unincorporated dye was then removed and cells were washed with PBS solution. The final step required 300 µl of destain solution (50 vol. % distilled water, 49 vol. % ethanol and 1 vol. % glacial acetic acid) to cover the cells and the entire universal tube and its contents were shaken at 150 rpm (Heidolph Titramax 100) for 10 mins, resulting in the uptake and reduction of NR dye from cells. Optical density was then measured and quantified at 490 nm/630 nm wavelengths on a Biotek Elx800 with KC junior software.

Chapter 4: Crystallisation behaviour of Ge-Sb-Se glasses relevant to optical fibres

One of the primary driving forces behind this research, was to investigate non-arsenic containing chalcogenide glasses that could act as MIR passive optical fibres in a hyperspectral imaging probe, for early cancer diagnosis. As discussed in in section 2.2.1, the Ge-Sb-Se glass system has received growing interest due to their lower toxicity than similar Ge-As-Se glasses[47]. Although there are a substantial number of reports on their bulk glass properties[48, 49, 51-53, 56-58] (non-exhaustive), less known about their fibre drawing capabilities[54, 59, 60, 96].

Therefore, this section focusses on two compositions from the Ge-Sb-Se glass system and assesses their ability to be drawn into MIR optical fibres. Section 4.1 will first address the bulk and structural properties of each investigated glass before the fibre-drawing results are presented in section 4.2 and 4.3 for the non-stoichiometric $Ge_{20}Sb_{10}Se_{70}$ at. % glass and the stoichiometric $Ge_{25}Sb_{10}Se_{65}$ at. % glass, respectively. Section 4.4 will then explore relevant crystallisation in Ge-Sb-Se glasses before summarising the main results in section 4.5.

4.1 Bulk characterisation of Ge-Sb-Se glasses

The two investigated glasses, from the $Ge_xSb_{10}Se_{90-x}$ at. % system, are presented in Table 4.1 along with their measured scanning electron microscopy- energy dispersive X-ray spectroscopy (SEM-EDX) chemical compositions and corresponding differential scanning calorimetry DSC onset-glass transition temperatures (T_g).

Table 4.1: Nominal as-batched and measured chemical compositions (found by SEM-EDX) of $Ge_{20}Sb_{10}Se_{70}$ at. % (M_HAP008) and $Ge_{25}Sb_{10}Se_{65}$ at. % (M_HAP002) bulk glasses, along with their respective glass transition temperatures (T_g), mean coordination number (MCN) and total number of constraints (N_t).

Specimen	**Nominal composition /at. %**			**SEM-EDX composition /at. %**			**Onset T_g /°C**	**MCN**	N_t
	Ge	**Sb**	**Se**	**Ge**	**Sb**	**Se**			
Non-stoichiometric $Ge_{20}Sb_{10}Se_{70}$	20	10	70	20.5	10.0	69.5	214 ±2	2.5	3.25
Stoichiometric $Ge_{25}Sb_{10}Se_{65}$	25	10	65	25.4	9.6	65.0	314 ±2	2.6	3.5

Furthermore, in Table 4.1, equation 4.1 has been used to calculate the glass MNC (m)[183] and equation 2 has been used to find the total number of constraints (N_t)[69], where the number of bond stretching constraints (N_{bs})= m/2 and the number of bond bending constraints (N_{bb})= 2m-3.

$$m = \frac{\alpha N_{Ge} + \beta N_{Sb} + \gamma N_{Se}}{100} \qquad \textbf{Equation 4.1}$$

$$N_t = N_{bs} + N_{bb} \qquad \textbf{Equation 4.2}$$

According to the topological models of Phillips and Thorpe[69] and Tanaka[70] both compositions exist as a two-dimensional overconstrained network, where layered structures are connected by weaker, intermolecular van der Waals bonds. For $Ge_xSb_{10}Se_{90-x}$ at. % glasses that fall in between the topological transitions, Ge atoms can be incorporated into the corrugated-like layers and increase the rigidity of the network[70]. Therefore, the non-stoichiometric $Ge_{20}Sb_{10}Se_{70}$ at. % glass (MCN= 2.5) would have a slightly less rigid structure than the stoichiometric $Ge_{25}Sb_{10}Se_{65}$ at. % glass (MCN= 2.6).

Since the physical properties of a glass are closely related to its atomic structure, the DSC results presented in Table 4.1 revealed that the non-stoichiometric $Ge_{20}Sb_{10}Se_{70}$ at. % glass (M_HAP008) had a lower T_g (214 ±2 °C) than the stoichiometric $Ge_{25}Sb_{10}Se_{65}$ at. % glass (M_HAP002) (314 ±2 °C). This suggested that with a 5 at. % increase in Ge content in the $Ge_xSb_{10}Se_{90-x}$ at. % system, there was a 100 °C increase in T_g. This observation was supported by Wei *et al*. [47] and Wang *et al.*[48] who also reported T_g values of 221.4 °C and 316. 6 °C for the non-stoichiometric $Ge_{20}Sb_{10}Se_{70}$ at. % and stoichiometric $Ge_{25}Sb_{10}Se_{65}$ at. % compositions, respectively.

As discussed in section 3.5.2, each as-annealed Ge-Sb-Se glass sample was run three times during DSC analysis but, only runs 2 and 3 were used for T_g measurements. The reason for this is demonstrated by the DSC curves in Figure 4.1, where the first run of both the non-stoichiometric $Ge_{20}Sb_{10}Se_{70}$ at. % (Figure 4.1 (a)) and stoichiometric $Ge_{25}Sb_{10}Se_{65}$ at. % (Figure 4.1 (b)) glasses had an onset-T_g value 2 °C and 1 °C lower, respectively, than runs 2 and 3. This highlighted the importance of having a controlled 10 °C/min heating and cooling rate during DSC analysis, since the glass for run 1 still had the thermal history of the quenching and annealing steps (see section 3.3.5). This dependency, of the T_g on the heating and cooling rates, is a well-documented phenomenon[184-186].

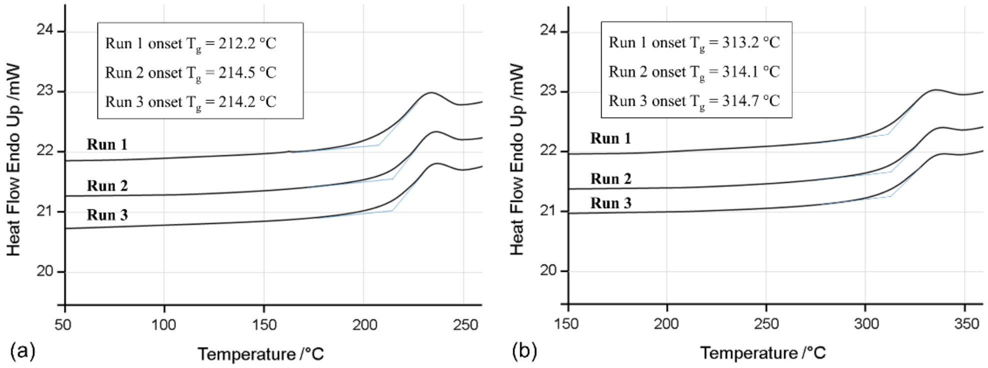

Figure 4.1: Differential scanning calorimetry results for (a) non-stoichiometric $Ge_{20}Sb_{10}Se_{70}$ at. % and (b) stoichiometric $Ge_{25}Sb_{10}Se_{65}$ at. %. Final onset T_g measurements calculated from second and third run.

4.2 Non-stoichiometric $Ge_{20}Sb_{10}Se_{70}$ at. % optical fibres

4.2.1 Fibre-drawing from an as-annealed non-stoichiometric $Ge_{20}Sb_{10}Se_{70}$ at. % preform

Fibre drawing investigations began with the non-stoichiometric $Ge_{20}Sb_{10}Se_{70}$ at. % composition (M_HAP010), where an as-annealed 10 mm diameter preform was drawn to a 200 ±8 µm diameter unstructured fibre (F_HAP006). In Figure 4.2, the optical loss measurements for a ~7 m length, of 205 ±10 µm diameter non-stoichiometric $Ge_{20}Sb_{10}Se_{70}$ at. % fibre, drawn straight from the as-annealed preform, is presented. Since all of the Ge-Sb-Se glasses presented in this chapter were only purified *via* a simple bake-out of the Sb and Se precursors (see section 3.3.4.1), relatively large impurity absorption bands were expected. In Figure 4.2 it was revealed that several absorption bands were present across the 2-10 µm wavelength region. Se-H exhibited its strongest absorption, of 16.2 dB/m at 4.5 µm, with weaker absorptions at 4.1 µm, 3.5 µm and 2.3 µm[35]. Although Ge-O only displayed one absorption band at 7.9 µm[89], it was in fact the strongest impurity absorption for the considered wavelength region, at 18 dB/m. Other impurity absorptions included the O-H band at 2.9 µm,[35] molecular H_2O bending absorption at 6.3 µm[94] and CO_2 absorption centred at 4.3 µm, likely to be an artefact from the measured atmosphere[89, 93-95]. Nevertheless, the unstructured $Ge_{20}Sb_{10}Se_{70}$ at. % fibre (F_HAP006) delivered a relatively low baseline loss, meaning low extrinsic scattering loss between the 5.5 and 7.2 µm wavelength region (aside from the molecular H_2O absorption at 6.3 µm), with the lowest background loss of 0.60 ± 0.1 dB/m found at 6.0 µm. In total, over 100 m of non-stoichiometric $Ge_{20}Sb_{10}Se_{70}$ at. % fibre (F_HAP006) was successfully drawn from the 10 mm diameter, as-annealed, preform and showed good low-loss potential for distillation investigations (see Chapter 6).

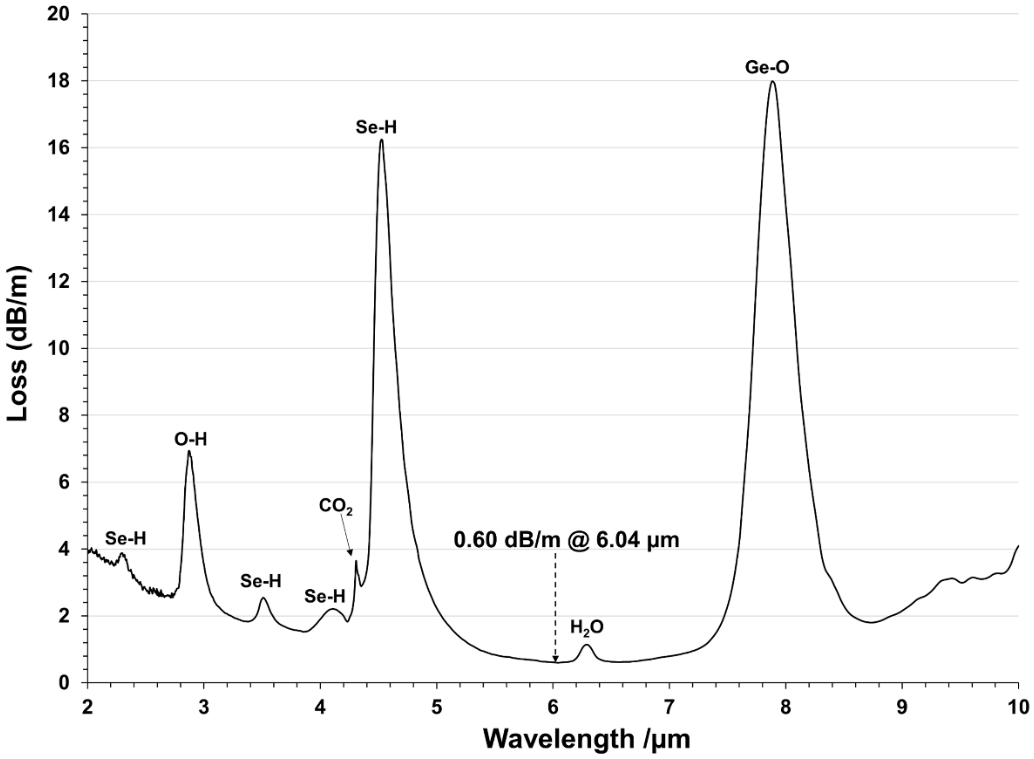

Figure 4.2: Optical loss spectrum of the unstructured, non-stoichiometric $Ge_{20}Sb_{10}Se_{70}$ at. % optical fibre (F_HAP006) drawn from an as-annealed preform (M_HAP010).

Furthermore, in Figure 4.3 the Fourier-transform infrared spectroscopy (FTIR) spectrum of a 2.1 mm thick, as-annealed $Ge_{20}Sb_{10}Se_{70}$ at. % bulk sample is presented. The electronic absorption (see section 2.3.1) is indicated by a horizontal reference line, drawn 3 units (absorption coefficient /cm^{-1}) higher than the baseline, which intercepted the spectrum at 0.8 µm. Aside from the structured multiphonon edge, beginning at 15.7 µm, the only other feature visible at the scale of Figure 4.3 (a), was the Ge-O impurity absorption at 12.8 µm (0.13 cm^{-1} absorption). Nevertheless, in Figure 4.3 (b), an enlarged image revealed more impurity absorptions across the 2-12 µm wavelength region. Amongst several impurities highlighted in Figure 4.3 (b), similar to the optical losses seen in Figure 4.2, a large Ge-O absorption was seen at 7.9 µm (absorption 0.003 cm^{-1}) and a large Se-H absorption was seen at 4.5 µm (absorption 0.002 cm^{-1}).

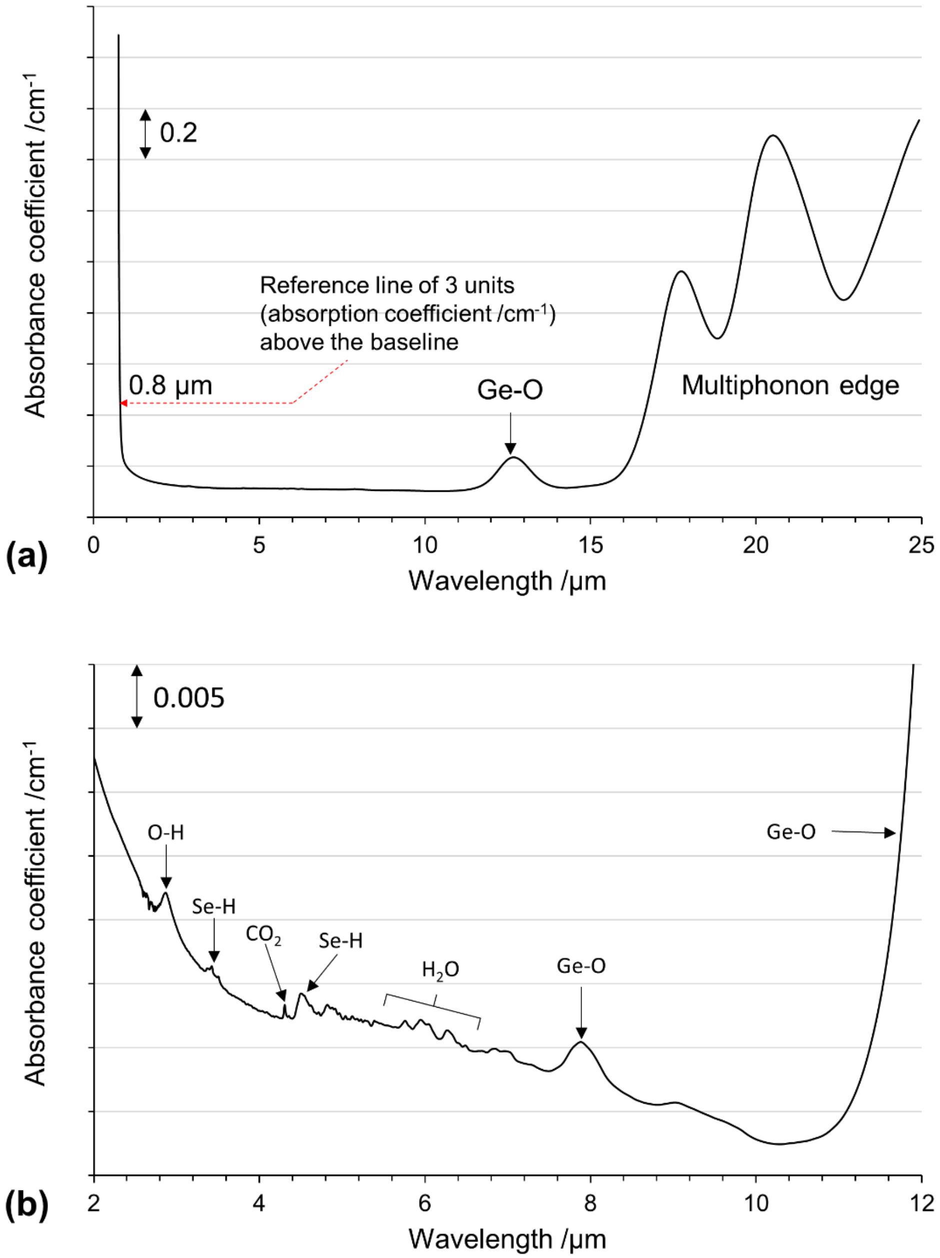

Figure 4.3: (a) Fourier-transform infrared spectroscopy (FTIR) spectrum of the as-annealed, non-stoichiometric $Ge_{20}Sb_{10}Se_{70}$ at. % bulk glass (M_HAP010) with an enlarged region from 2-12 µm wavelength shown in (b).

4.2.2 Fibre-drawing from an extruded non-stoichiometric $Ge_{20}Sb_{10}Se_{70}$ at. % preform

For remote sensing applications, where hyperspectral imaging is of interest, successful compositions will need to be combined into a step-index fibre (SIF), which has been often achieved through co-extrusion[132]. This will be discussed in more detail during Chapter 5. Therefore, the non-stoichiometric $Ge_{20}Sb_{10}Se_{70}$ at. % glass was also extruded (M_HAP005, E_HAP002), from the as-annealed bulk glass into a 4.7 ±0.03 mm diameter preform, and then fibre drawn to assess its thermal stability through the two heated processing steps. In Figure 4.4, the fibre-drawing results from the extruded non-stoichiometric $Ge_{20}Sb_{10}Se_{70}$ at. % preform (E_HAP002, F_HAP003), are presented.

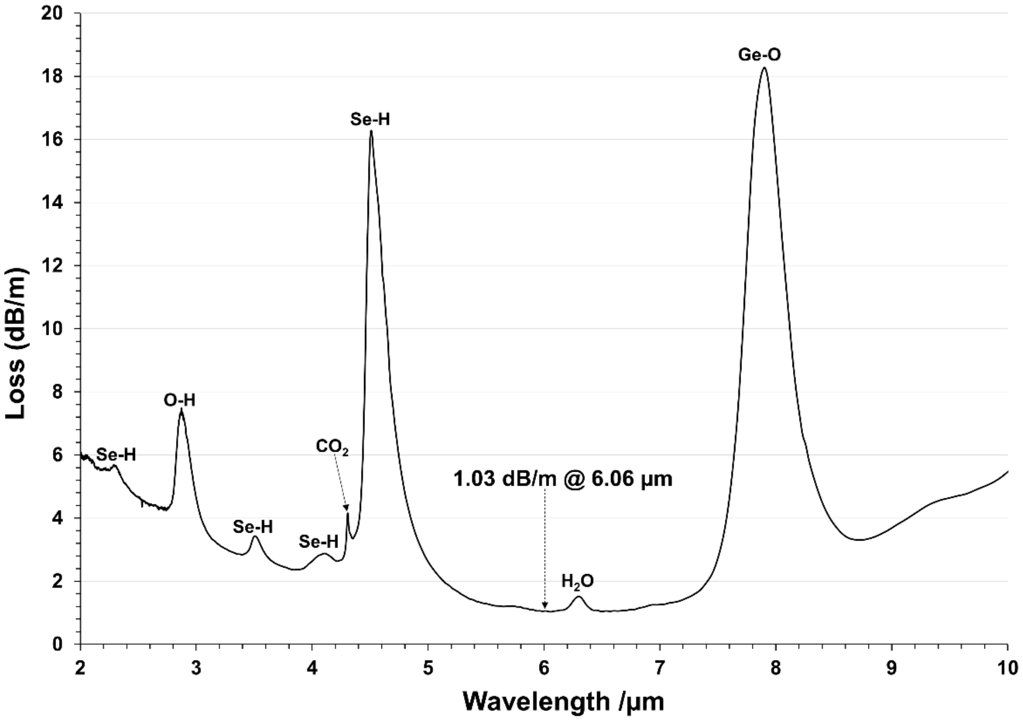

Figure 4.4: Optical loss spectrum of the unstructured, non-stoichiometric $Ge_{20}Sb_{10}Se_{70}$ at. % optical fibre drawn from an extruded preform (E_HAP002, F_HAP003).

As expected, the optical loss measurements on the ~ 6 m length of 218 ±7 μm diameter fibre (F_HAP003) showed a similar result to Figure 4.2, with weak impurity absorptions (e.g. Se-H at 3.5 μm) across the 2-10 μm wavelength region, as well as the two dominant bands at 4.5 µm (16.1 dB/m) for Se-H and at 7.9 µm (18.3 dB/m) for Ge-O. The lowest loss for the extruded non-stoichiometric $Ge_{20}Sb_{10}Se_{70}$ at. % optical fibre (F_HAP003) was found at a similar wavelength position to the equivalent as-annealed $Ge_{20}Sb_{10}Se_{70}$ at. % glass (F_HAP006) at 6.1 µm wavelength, with a loss of 1.03 ±0.2 dB/m. Although the extruded $Ge_{20}Sb_{10}Se_{70}$ at. % preform (E_HAP002) produced fibres with losses 0.4 dB/m higher than the as-annealed $Ge_{20}Sb_{10}Se_{70}$ at. % preform (M_HAP010), previous work conducted by Tang *et al.*[116] has shown it is possible to make low loss chalcogenide fibres with an extrusion step. Therefore, the 0.4 dB/m difference presented here, was likely due to an uncontrolled variation in the quality of measured cleaves or a slight increased fluctuation in fibre diameter along the investigated section.

Overall, the losses experienced by the non-stoichiometric $Ge_{20}Sb_{10}Se_{70}$ at. % optical fibres, drawn from either an as-annealed or an extruded preform, are comparable thus showing that the composition has the potential to produce low loss Ge-Sb-Se fibres, irrespective of the method of preform fabrication.

4.3 Stoichiometric $Ge_{25}Sb_{10}Se_{65}$ at. % optical fibres

Using the same approach, as that outlined in section 4.2, an as-annealed stoichiometric $Ge_{25}Sb_{10}Se_{65}$ at. % preform (M_HAP002), of 10 mm diameter, was prepared for fibre-drawing.

4.3.1 Fibre-drawing from an as-annealed stoichiometric $Ge_{25}Sb_{10}Se_{65}$ at. % preform

Reported to have the lowest crystallisation ability in the $Ge_xSb_{10}Se_{90-x}$ at. % glass series[185] and stability against decomposition at higher temperatures[187], Figure 4.5(a) reveals how an unexpected ‘skin-like’ layer appeared around the neck of the preform which proved detrimental to the fibre-drawing of stoichiometric $Ge_{25}Sb_{10}Se_{65}$ at. % glass (M_HAP002). As a comparison, the neck-down region of the as-annealed non-stoichiometric $Ge_{20}Sb_{10}Se_{70}$ at. % preform (M_HAP010) is shown in Figure 4.5(b) and reveals a smooth transition from bulk glass to optical fibre, following a successful fibre draw. In total, less than 5 m of the stoichiometric $Ge_{25}Sb_{10}Se_{65}$ at. % fibre was collected, from the as-annealed 10 mm diameter preform, which not only fluctuated in diameter (approximately 50 – 500 µm) but also had numerous surface defects arising from the detachment of the 'skin-like' layer, examples of which are shown in Figure 4.5(c) and (d).

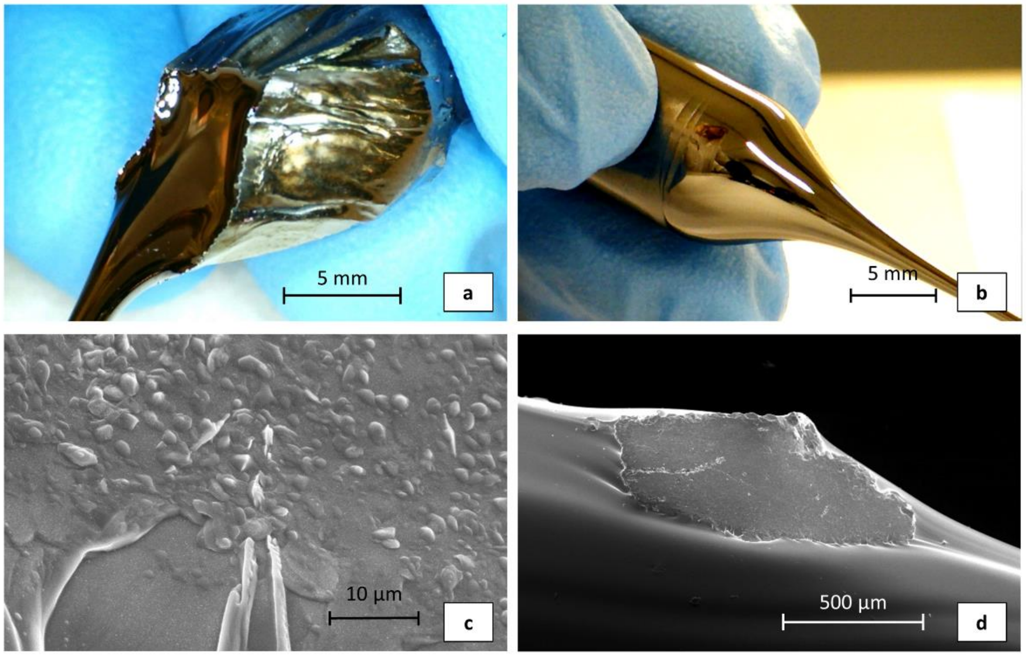

Figure 4.5: a) stoichiometric $Ge_{25}Sb_{10}Se_{65}$ at. % preform (M_HAP002) imaged after fibre-drawing; b) non-stoichiometric $Ge_{20}Sb_{10}Se_{70}$ at. % preform (M_HAP010) imaged after fibre-drawing; c) and d) SEM micrographs of sections of the 'skin-like' layer which had detached from the bulk of the stoichiometric $Ge_{25}Sb_{10}Se_{65}$ at. % preform (M_HAP002) onto the fibre (F_HAP001).

In Figure 4.6 (a), the optical loss spectrum of the stoichiometric $Ge_{25}Sb_{10}Se_{65}$ at. % fibre (F_HAP001), with a 200 ± 20 µm diameter (excluding surface defect diameters), can be seen. When compared to the non-stoichiometric $Ge_{20}Sb_{10}Se_{70}$ at. % optical fibre loss measurements (see Figure 4.2), the stoichiometric $Ge_{25}Sb_{10}Se_{65}$ at. % fibre had significantly higher optical attenuation with a minimum background loss of 21.4 ± 2.1 dB/m at 6.60 µm wavelength. As discussed in section 2.3.2, optical loss in chalcogenide glasses can arise from scattering centres such as bubbles, inclusions and crystals. However, as demonstrated by the optical microscope images in Figure 4.6 (b), (c) and (d), the cleaves taken during fibre loss measurements showed no evidence of such defects.

Furthermore, SEM-EDX analysis on a bulk sample of the as-annealed, stoichiometric preform (M_HAP002), revealed a homogenous $Ge_{25.4}Sb_{9.6}Se_{65.0}$ ±0.5 at. % composition.

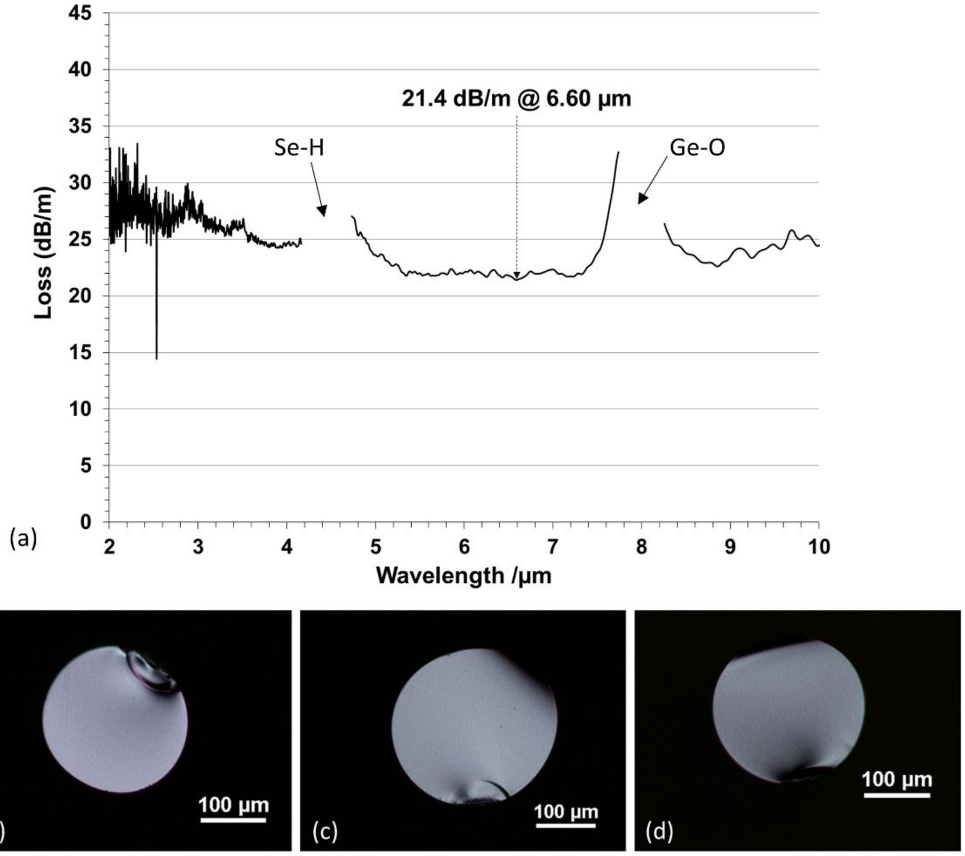

Figure 4.6: (a) Optical loss spectrum of the unstructured, stoichiometric $Ge_{25}Sb_{10}Se_{65}$ at. % optical fibre (F_HAP001) drawn from an as-annealed preform (M_HAP002).Optical micrographs show the (b) launch, (c) Group 1 and (d) Group 2 cleaves taken from the optical loss measurements of (a).

Since the impurity bands could not be collected from the stoichiometric $Ge_{25}Sb_{10}Se_{65}$ at. % optical fibre loss measurements (F_HAP001), FTIR was conducted on a 1.9 mm thick bulk sample taken from the as-annealed stoichiometric $Ge_{25}Sb_{10}Se_{65}$ at. % preform prior to fibre-drawing (see section 3.5.7). In Figure 4.7 (a) the multiphonon edge (see section 2.3.1) of the $Ge_{25}Sb_{10}Se_{65}$ at. % glass can be seen as well as a large Ge-O impurity absorption at 12.5 µm wavelength[35, 89, 99]. In Figure 4.7 (b), an enlarged region of the FTIR spectrum shows two significant absorptions at 4.5 µm (0.001 cm^{-1} absorption) and at 7.9 µm (0.003 cm^{-1} absorption) denoting to the impurity absorptions of Se-H and Ge-O, respectively. These were similar to the impurity absorptions seen by the FTIR spectrum of non-stoichiometric $Ge_{20}Sb_{10}Se_{70}$ at. % (M_HAP010) glass (Figure 4.3). Unfortunately, there was no near-infrared (NIR) data collected for the stoichiometric $Ge_{25}Sb_{10}Se_{65}$ at. % bulk sample (M_HAP002) therefore, the MIR detector limit is highlighted in Figure 4.7 (a) and (b).

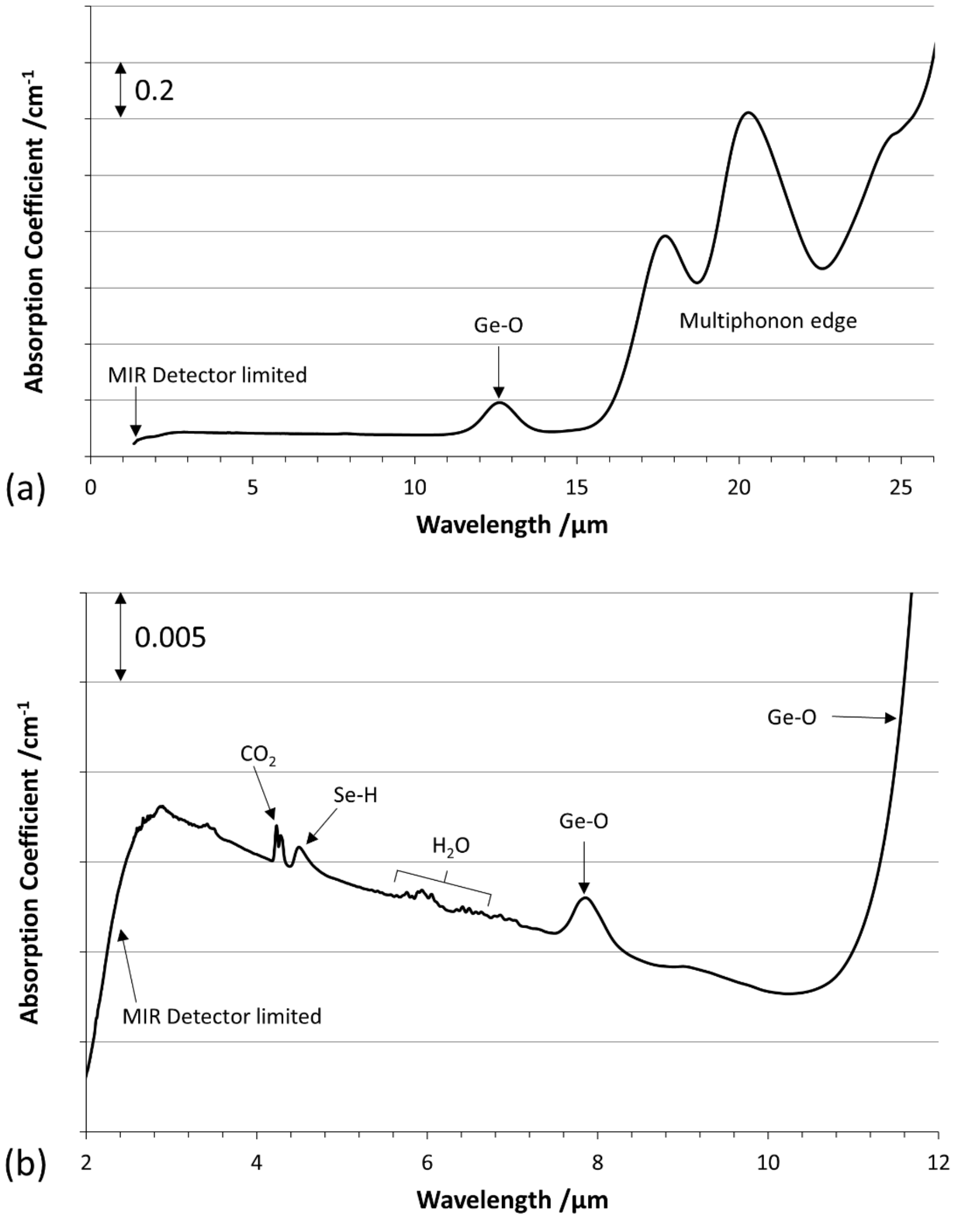

Figure 4.7: FTIR spectra of the as-annealed stoichiometric $Ge_{25}Sb_{10}Se_{65}$ at. % bulk glass with a sample thickness of 1.9 mm.

4.3.2 Fibre-drawing from an extruded stoichiometric $Ge_{25}Sb_{10}Se_{65}$ at. % preform

The identity of the 'skin-like' layer seen around the as-annealed, stoichiometric $Ge_{25}Sb_{10}Se_{65}$ at. % preform (M_HAP002) (Figure 4.5 (a)) was matched using XRD to crystalline monoclinic $GeSe_2$ (ICDD-PDF-01-071-0117), manifesting as the sharp peak at 15.1 °2θ in Figure 4.8 (a). Although, initial XRD results suggested that the stoichiometric $Ge_{25}Sb_{10}Se_{65}$ at. % preform (M_HAP002) was amorphous prior to fibre drawing (Figure 4.8 (b)), the Scherrer equation (see Equation 4.3) explains how small crystals could have been hard to detect: whereby, peak broadening (B) is inversely proportional to the crystallite size (L), with K acting as the constant of proportionality and θ is the Bragg angle:

$$\boldsymbol{B(2\theta) = \frac{K\lambda}{L cos\theta}} \qquad \textbf{Equation 4.3}$$

Furthermore, due to the external appearance of the crystalline $GeSe_2$ layer, it was hard to confirm whether it had derived from the composition's poor resistance to crystallisation (i.e. mediated by homogeneous nucleation), or whether it had grown from contaminant nuclei on the surface of the stoichiometric $Ge_{25}Sb_{10}Se_{65}$ at. % preform. It is recognised that the use of high temperatures during melting can introduce impurities from the silica ampoule containment, such as silicon dioxide and hydrogen, which react with the chalcogenide glass to produce a thin layer of reaction products on its surface[102] thus, potentially providing heterogeneous points from which crystalline $GeSe_2$ could have grown.

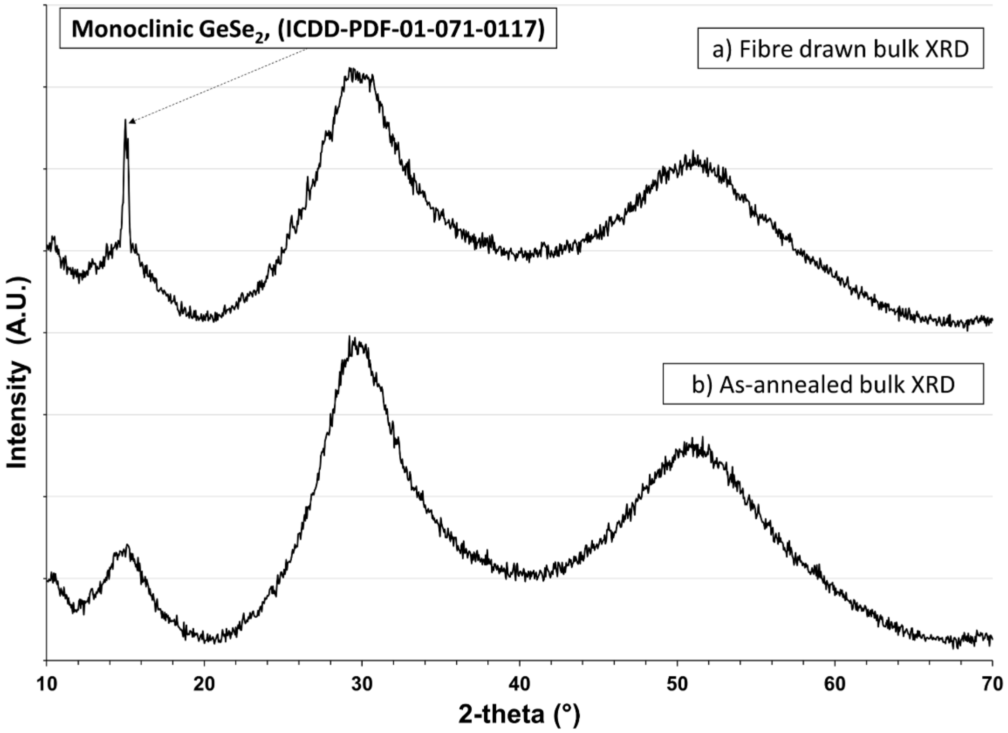

Figure 4.8: Comparison of the X-ray diffraction (XRD) patterns for the as-annealed stoichiometric $Ge_{25}Sb_{10}Se_{65}$ at. % preform (M_HAP002) taken: a) after fibre drawing and b) before.

Similar to the non-stoichiometric $Ge_{20}Sb_{10}Se_{70}$ at. % composition (section 4.2.2), a 15 mm diameter as-annealed stoichiometric $Ge_{25}Sb_{10}Se_{65}$ at. % boule (M_HAP009, E_HAP005) was extruded into a 4.7 ±0.03 mm diameter rod ready for fibre-drawing. If the crystalline $GeSe_2$ layer had grown from contaminant nuclei on the surface of the $Ge_{25}Sb_{10}Se_{65}$ at. % preform (M_HAP002), the process of extrusion should have removed the outermost layer of the as-annealed boule (M_HAP009) thus producing a good quality extrudate, with potential contaminants left on the inside of the extrusion barrel. However, like the result seen in Figure 4.5(a), the same ‘skin-like’ layer once again appeared around the neck of the extruded $Ge_{25}Sb_{10}Se_{65}$ at. % preform during the fibre-drawing (F_HAP005). This was again identified *via* XRD as crystalline monoclinic $GeSe_2$ (see Figure 4.9).

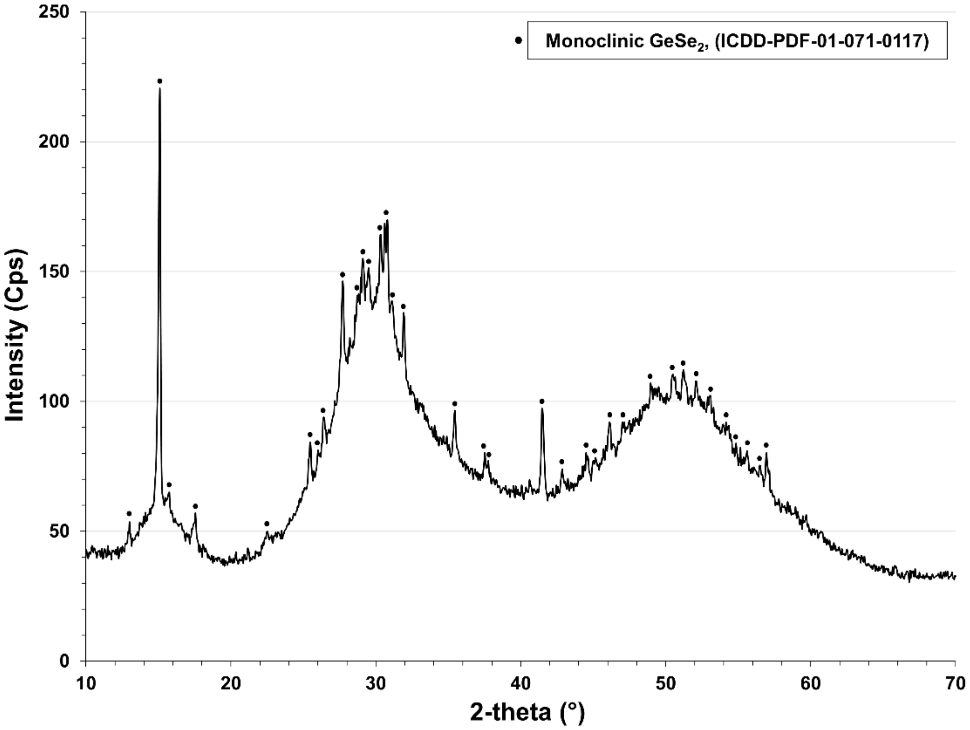

Figure 4.9: Powder X-ray diffraction (XRD) pattern of extruded $Ge_{25}Sb_{10}Se_{65}$ at. % preform (E_HAP005), post fibre-drawing.

When comparing the XRD patterns from the fibre-drawn as-annealed (Figure 4.8 (a)) and the extruded (Figure 4.9) stoichiometric $Ge_{25}Sb_{10}Se_{65}$ at. % preforms, there was a noticeable difference in the number of diffraction peaks present. Although the XRD pattern of each preform, after fibre-drawing, presented a dominant peak at 15.1 °2θ, the extruded preform (E_HAP005), after fibre drawing, showed an increase in peak intensity as well as further diffraction peaks at greater 2-theta (°) angles. This signified a higher proportion of crystalline $GeSe_2$ within the stoichiometric $Ge_{25}Sb_{10}Se_{65}$ at. % XRD sample (E_HAP005, F_HAP005).

However, this dissimilarity between the number of XRD peaks, does not necessarily mean that an extrusion step in the stoichiometric $Ge_{25}Sb_{10}Se_{65}$ at. % glass prior to fibre-drawing, had caused an increased amount of crystallisation. When both $Ge_{25}Sb_{10}Se_{65}$ at. % samples were prepared for XRD, a small section of the preform containing the crystalline $GeSe_2$ 'skin-like' layer was selected and ground into a powder. As the crystalline $GeSe_2$ phase was predominantly a surface feature, depicted by the preform (E_HAP005) cross-section in Figure 4.10, a larger diameter preform would have given a larger volume to surface ratio. Therefore, it was likely that the powdered XRD sample from the 4.7 ± 0.03 mm diameter extruded stoichiometric $Ge_{25}Sb_{10}Se_{65}$ at. % preform (E_HAP005), post fibre-drawing, proportionally contained more of the outer $GeSe_2$ crystalline layer, making it easier to detect the crystal peaks with lower intensities.

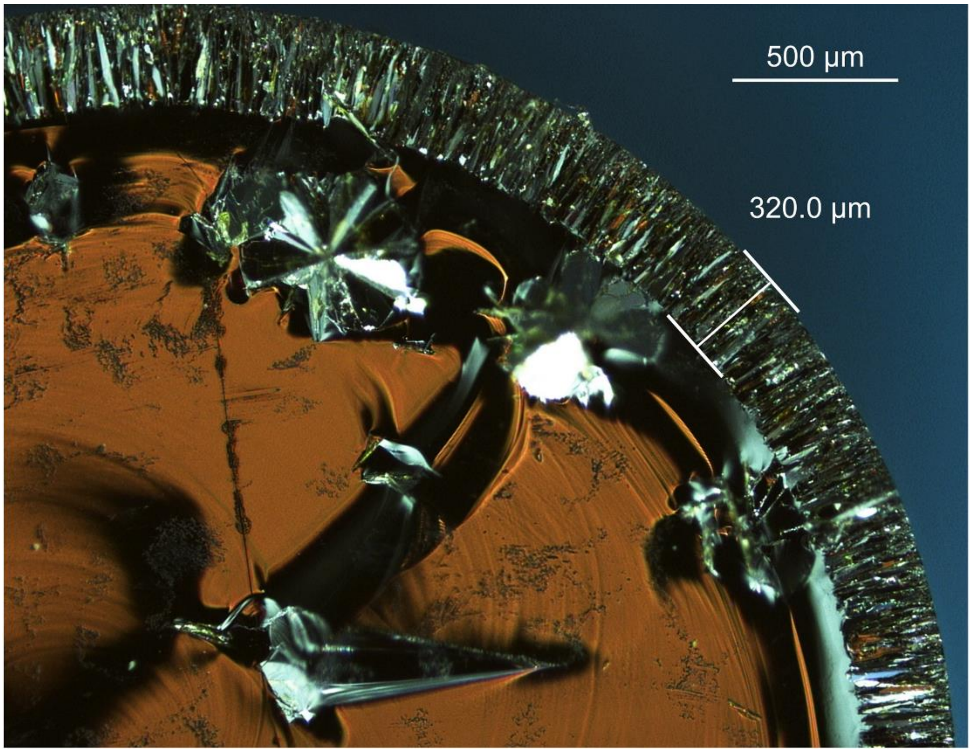

Figure 4.10: Optical reflection micrograph of a cross-section from the 4.7 ±0.03 mm diameter extruded, stoichiometric $Ge_{25}Sb_{10}Se_{65}$ at. % preform following fibre drawing (E_HAP005, F_HAP005).

Overall, the discrepancy in fibre-drawing results between the non-stoichiometric $Ge_{20}Sb_{10}Se_{70}$ at. % (section 4.2) and the stoichiometric $Ge_{25}Sb_{10}Se_{65}$ at. % (section 4.3) compositions, suggests that although both glasses fell within the same topological, overconstrained region, there was a significant difference in their thermal stability at each respective fibre-drawing temperature. Therefore, the results would be best described by their chemical composition (*i.e.* using the CONM) rather than by their MCN.

4.4 Crystallisation in Ge-Sb-Se glasses relevant to fibre drawing

The growth of crystalline $GeSe_2$ in Ge-Sb-Se glasses has often been demonstrated in controlled heat-treated environments[188, 189]. Yet, in all these cases, the bulk Ge-Sb-Se glasses crystallised into at least two phases: Sb_2Se_3, with an activation energy of crystallisation (E_c) of 282.01 kJ/mol[189], and $GeSe_2$, with an E_c of 762.02 kJ/mol[189]. As a commonly crystallising phase in Ge-Sb-Se glasses, with the lowest E_c, the lack of Sb_2Se_3 observed by XRD within the crystalline surface of the stoichiometric $Ge_{25}Sb_{10}Se_{65}$ at. % preform tip after fibre-drawing (Figure 4.8 and Figure 4.9) was unexpected. Therefore, the following section focussed on the type of crystallisation present in, the seemingly more susceptible, stoichiometric $Ge_{25}Sb_{10}Se_{65}$ at. % glass.

4.4.1 Single phase crystallisation in stoichiometric $Ge_{25}Sb_{10}Se_{65}$ at. % glass, investigated *via* XRD

To support the single phase crystallisation seen in Figure 4.8 and Figure 4.9, an in-depth study was carried out using the XRD diffraction peaks of the stoichiometric $Ge_{25}Sb_{10}Se_{65}$ at. % (from Figure 4.9)(E_HAP005, F_HAP005) in comparison to two ICDD-PDF standards, which are presented in Table 4.2. Although only the top 20 diffraction intensities have been presented in Table 4.2, the XRD pattern of the stoichiometric $Ge_{25}Sb_{10}Se_{65}$ at. % preform-tip sample post fibre-drawing (E_HAP005, F_HAP005), was in fact compared to the full XRD data point set for each standard (200 values). Overall, the crystalline peaks presented by the stoichiometric $Ge_{25}Sb_{10}Se_{65}$ at. % sample were in excellent agreement with the $GeSe_2$ standard (ICDD-PDF-01-071-0117) but were a poor match with any Sb_2Se_3 standard; orthorhombic Sb_2Se_3 (ICDD-PDF-01-072-1184) is given as an example.

Table 4.2: X-ray diffraction (XRD) data for the extruded, stoichiometric $Ge_{25}Sb_{10}Se_{65}$ at. % sample, post fibre-drawing, which is compared to monoclinic $GeSe_2$ (ICDD-PDF-01-071-0117) and orthorhombic Sb_2Se_3 (ICDD-PDF-01-072-1184) standards. Although the full 200 data points sets for each standard have been compared with those of the stoichiometric $Ge_{25}Sb_{10}Se_{65}$ at. % sample, only the top 20 intensities are tabulated here. The quoted intensities here for the stoichiometric $Ge_{25}Sb_{10}Se_{65}$ at. % have been calculated from a subtracted background and thus are approximates. Bold values indicate a match between the sample and a standard peak.

$Ge_{25}Sb_{10}Se_{65}$ at.% Sample		ICDD-PDF-01-071-0117 $GeSe_2$		ICDD-PDF-01-072-1184 Sb_2Se_3	
2-Theta /°	**Intensity /%**	**2-Theta /°**	**Intensity /%**	**2-Theta /°**	**Intensity /%**
-	-	12.9	16.92	-	-
-	-	13.7	16.22	-	-
15.1	**100.00**	**15.0**	**100.00**	**15.0**	**17.72**
-	-	15.5	14.61	-	-
-	-	15.7	33.03	-	-
-	-	-	-	16.9	55.46
17.5	**7.40**	**17.5**	**18.82**	-	-
-	-	-	-	23.9	20.82
25.4	**10.60**	**25.4**	**46.75**	-	-
26.4	**8.90**	**26.3**	**24.52**	-	-
-	-	-	-	27.4	48.45
27.7	**25.60**	**27.6**	**28.23**	-	-
-	-	-	-	28.3	77.58
28.7	**11.70**	**28.6**	**16.22**	-	-
29.1	**17.70**	**29.1**	**36.24**	-	-
29.4	**12.70**	**29.4**	**25.93**	-	-
30.3	**24.50**	**30.2**	**22.62**	-	-
-	-	30.6	27.73	-	-
30.7	**28.90**	**30.7**	**22.32**	-	-
31.1	**8.00**	**31.1**	**16.82**	**31.2**	**100.00**
-	-	-	-	31.3	64.66
31.9	**17.50**	**31.9**	**18.42**	-	-
-	-	-	-	32.3	63.36
-	-	-	-	33.2	20.32
-	-	-	-	34.1	45.65
35.4	**12.50**	**35.4**	**14.21**	-	-
-	-	-	-	35.7	28.93
37.5	7.50	-	-	-	-
-	-	37.7	14.11	-	-
-	-	-	-	38.1	18.32
-	-	-	-	38.9	28.83
41.5	**27.50**	**41.4**	**12.31**	**41.5**	**22.92**
-	-	-	-	45.0	27.63
-	-	-	-	45.2	28.03
-	-	-	-	45.3	24.12
-	-	-	-	45.8	35.94
-	-	-	-	45.9	20.12
46.1	9.30	-	-	-	-
49.0	**7.40**	**48.9**	**14.01**	-	-
50.5	7.10	-	-	-	-
51.2	9.00	-	-	-	-
-	-	-	-	52.0	33.83
56.9	11.00	-	-	-	-

Although, the atomic % of Sb is less than half of the Ge atomic % in the stoichiometric $Ge_{25}Sb_{10}Se_{65}$ at. % composition, Wakkad *et al*. [189] have shown that both Sb_2Se_3 and $GeSe_2$ phases can be detected in a heat treated $Ge_{32.5}Sb_{7.5}Se_{60}$ at. % sample using XRD *i.e.* within a Ge-Sb-Se glass that has an even greater atomic % difference between 32 at. % Ge and 7.5 at. % Sb. Therefore, the fact that there was less Sb than Ge within the stoichiometric $Ge_{25}Sb_{10}Se_{65}$ at. % sample (E_HAP005, F_HAP005), had no influence on the single crystalline phase presented in the XRD results of Table 4.2.

4.4.2 Single phase crystallisation in stoichiometric $Ge_{25}Sb_{10}Se_{65}$ at. % glass, investigated *via* TEM

The same stoichiometric $Ge_{25}Sb_{10}Se_{65}$ at. % preform-tip (made *via* extrusion) post fibre-drawing (E_HAP005, F_HAP005) was then analysed by transmission electron microscopy (TEM) (see section 3.5.6). As expected, the sample taken from the neck-down region of the fibre-drawn $Ge_{25}Sb_{10}Se_{65}$ at. % preform (E_HAP005, F_HAP005), contained a high volume of crystals which were initially detected by TEM selected area electron diffraction (TEM-SAED) (Figure 4.11 (a)) and later confirmed as crystalline $GeSe_2$ *via* two TEM techniques, as follows.

The first method used TEM-EDX, which enabled the identification of the crystalline section seen in Figure 4.11 (b) (2) as $Ge_{34.3}Se_{65.7} \pm 0.5$ at. %. The second was measurement of the diffraction angles, and thus the d-spacings, using points from the TEM-SAED pattern in Figure 4.11 (a). These d-spacings, along with the equivalent Miller indices, matched the monoclinic $GeSe_2$ (ICDD-PDF-01-071-0117) standard already identified by XRD in Table 4.2. All results were reproducible and, once again, there was no evidence of a second Sb_2Se_3 phase. Therefore, the TEM investigation also supported the rationale of single phase $GeSe_2$ crystallisation in the stoichiometric $Ge_{25}Sb_{10}Se_{65}$ at. % glass, during fibre-drawing.

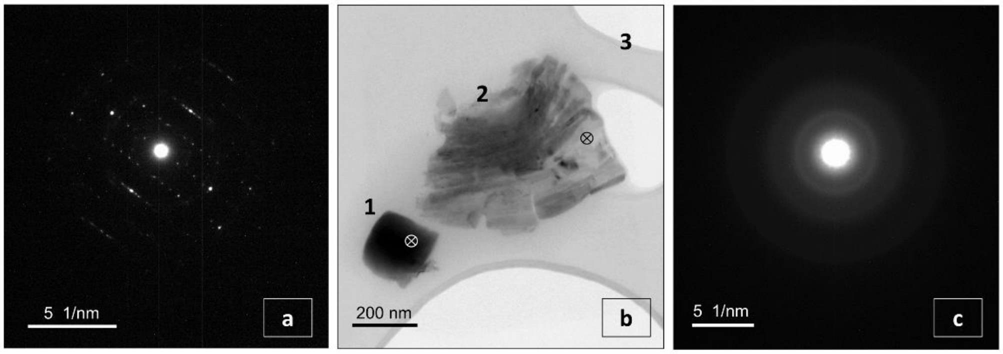

Figure 4.11: (a) Transmission electron microscopy-selected area electron diffraction (TEM-SAED) and a (b) TEM micrograph of the extruded, stoichiometric $Ge_{25}Sb_{10}Se_{65}$ *at. % following fibre-drawing (E_HAP005, F_HAP005) showing an amorphous region (1), crystalline region (2) and the background carbon film (3). The points at which EDX was conducted are shown by a crossed circle. c) TEM-SAED of the as-annealed, stoichiometric* $Ge_{25}Sb_{10}Se_{65}$ *at. % preform (M_HAP002) prior to fibre-drawing.*

Furthermore, TEM analysis also offered an insight into the location-point from which the stoichiometric $Ge_{25}Sb_{10}Se_{65}$ at. % glass may have crystallised. Figure 4.11 (c) shows the TEM-SAED pattern, taken from the as-annealed stoichiometric $Ge_{25}Sb_{10}Se_{65}$ at. % preform (M_HAP002) prior to fibre drawing. All of the analysed material was shown to be amorphous, as demonstrated by the broad halos shown in Figure 4.11 (c), thereby supporting the XRD results presented in Figure 4.8 (b). These observations taken together suggest that the stoichiometric $Ge_{25}Sb_{10}Se_{65}$ at. % composition readily formed a glass through the conventional melt/quench technique but, due to a poor resistance to crystallisation, later devitrified during fibre-drawing; contrary to its apparent thermal stability[187, 190].

Bletskan *et al.*[191] have shown that layers of crystalline $GeSe_2$ readily form from tetrahedral $GeSe_4$ units, which are an integral structure within Ge-Sb-Se glasses. The atomic ordering associated with a random network of $GeSe_4$ tetrahedra bares particular resemblance to the atomic order in high temperature, crystalline $GeSe_2$[192] and more specifically, high temperature monoclinic $GeSe_2$ (PDF 01-071-0117)[193]. Not only does this match the $GeSe_2$ crystalline phase identified by Table 4.2 (ICDD-PDF-01-071-0117) but it also supports the idea that the amorphous $Ge_{25}Sb_{10}Se_{65}$ at. % preform (M_HAP005 and E_HAP005) devitrified during the high temperature heat-treatment of the glass during its fibre-drawing.

4.4.3 Two phase crystallisation in stoichiometric $Ge_{25}Sb_{10}Se_{65}$ at. % glass, investigated *via* DTA

As a final investigation, shown in Figure 4.12, differential thermal analysis (DTA) (see section 3.5.3) was used to explore the thermal properties of both the non-stoichiometric $Ge_{20}Sb_{10}Se_{70}$ at. % (M_HAP010) and the stoichiometric $Ge_{25}Sb_{10}Se_{65}$ at. % (M_HAP012) glasses within a controlled environment. Both Ge-Sb-Se glasses initially exhibited an endothermic peak at their respective T_gs which were in agreement with temperatures found by DSC shown in Table 4.1. However, beyond this their thermograms significantly differed from each other *viz.*: the non-stoichiometric $Ge_{20}Sb_{10}Se_{70}$ at. % glass (M_HAP010) (Figure 4.12 (a) 1) smoothly progressed from its T_g into a supercooled and, at higher temperatures, a true melt-liquid, showing no other phase transitions. In contrast, the stoichiometric $Ge_{25}Sb_{10}Se_{65}$ at. % glass (M_HAP012) (Figure 4.12 (a) 2) presented a number of features beyond its onset-T_g at 314 °C.

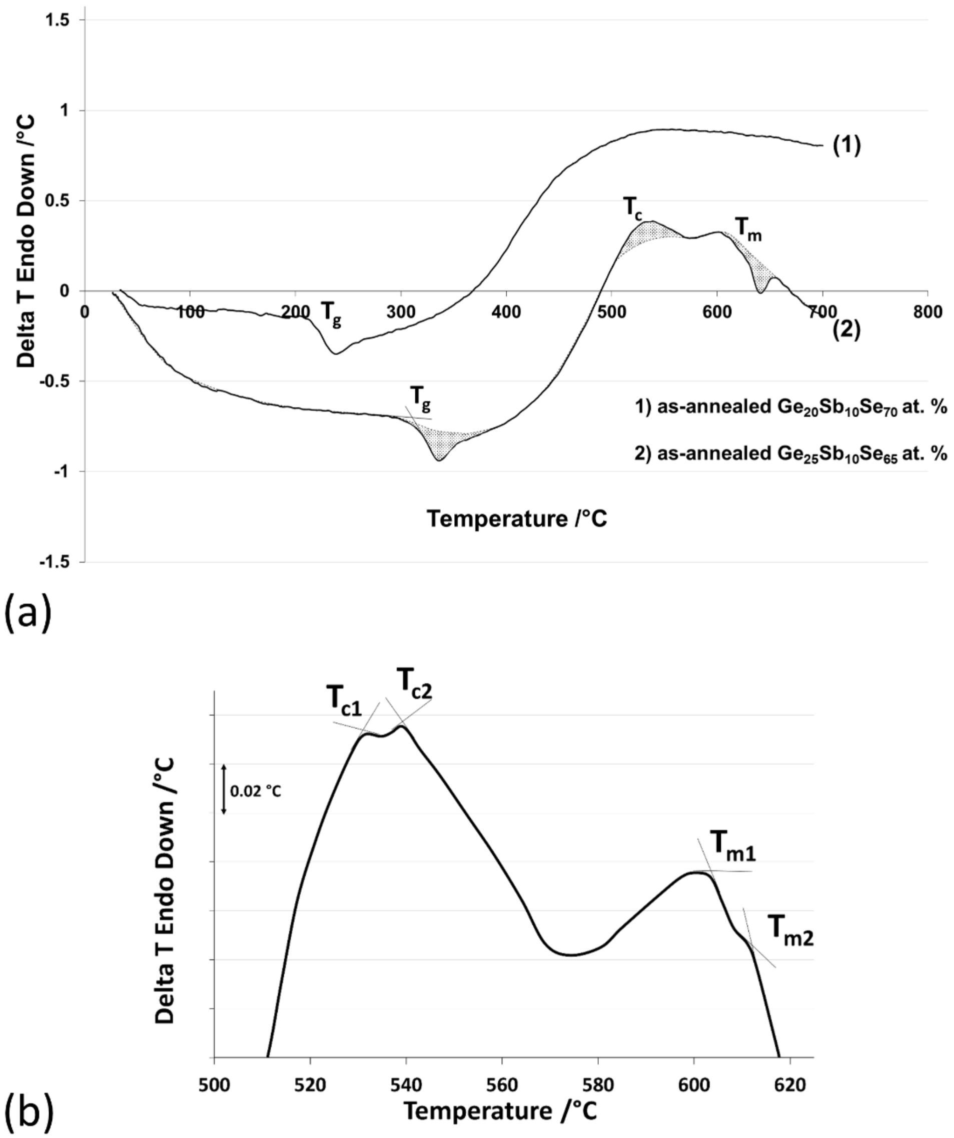

Figure 4.12: (a) Differential thermal analysis (DTA) thermographs of 100 mg of: 1) the as-annealed, non-stoichiometric $Ge_{20}Sb_{10}Se_{70}$ at. % (M_HAP010) and 2) the as-annealed, stoichiometric $Ge_{25}Sb_{10}Se_{65}$ at. % (M_HAP012) samples with a 10 °C/min heating rate. (b) Shows an enlarged section of 2) the as-annealed stoichiometric $Ge_{25}Sb_{10}Se_{65}$ at. % (M_HAP012) run between 500 °C and 620 °C. To aid interpretation of the stoichiometric $Ge_{25}Sb_{10}Se_{65}$ at. % thermogram (2), a dashed black line has been included to show the approximate baseline, as well as shading under the transitional peaks.

Due to the nature of the encapsulated samples (please refer to section 3.5.3), Figure 4.12 displays a baseline gradient within the thermograms even though a background scan was subtracted. To deduce which peaks were associated with a particular phase transition in the as-annealed stoichiometric $Ge_{25}Sb_{10}Se_{65}$ at. % glass sample (M_HAP012), the endothermic event due to the onset-T_g at 314 °C was substituted into the well documented two-thirds rule[178] (Equation 4.4), in Kelvin, where T_m is the liquidus:

$$T_g/T_m \approx 2/3 \qquad \textbf{Equation 4.4}$$

From Equation 4.4, the liquidus was estimated as 608 °C which correlated more with the onset of an endothermic phase transition, *i.e.* the solidus, found in the stoichiometric $Ge_{25}Sb_{10}Se_{65}$ at. % thermogram rather than the liquidus shown as T_m in Figure 4.12 (a) 2. Accordingly, the exothermic peak appearing approximately 80 °C below the solidus, was identified as the crystallisation transition (T_c) in the stoichiometric $Ge_{25}Sb_{10}Se_{65}$ at. % glass. Although initial interpretation of the DTA curve (Figure 4.12 (a) 2) seemed to reveal a single phase transition event at each of the peaks at T_c and T_m, an enlarged region shown by Figure 4.12 (b), showed the presence of two smaller peaks, which overlapped to form the transitions at T_c and T_m. The difference in temperature (ΔT) between the exothermic peaks of T_{c1} and T_{c2} and the endothermic peaks of T_{m1} and T_{m2} (Figure 4.12 (b)) were both ~8 °C. A similar ΔT had already been observed by Wakkad *et al.*[189], who also reported an overlap within the DTA crystallisation peak of Ge-Sb-Se glasses, heated at 10 °C/min. They[189], identified T_{c1} and T_{c2} as crystalline Sb_2Se_3 and $GeSe_2$, respectively, and used Gaussian functions to deconvolute the overlapping peaks and a numerical method described by Ligero *et al.*[194]. Therefore it can be concluded, from the agreement between the results reported here and those of Wakkad *et al*. that, under a controlled 10 °C/min heating rate, the DTA thermogram of the stoichiometric $Ge_{25}Sb_{10}Se_{65}$ at. % glass (M_HAP012) exhibited two overlapping exothermic events, above T_g and below the liquidus, which corresponded firstly to the growth of Sb_2Se_3 and, then at higher temperature, the growth of $GeSe_2$.

During the fabrication of optical fibres (see section 3.4.2), the heating rate used to raise the Ge-Sb-Se preform up to fibre-drawing temperature would have been far greater than the 10 °C/min used in DTA or in isothermal heat-treatments. Due to the set-up of the customised Heathway drawing tower (see section 3.4.2), an accurate heating rate was hard to measure. This is because the final drawing temperature was controlled by the r.f. power used to heat the short graphite receptor. At the start of the fibre-drawing, when the set-up was all at room temperature, the power was increased by 2 % every 2 minutes until the preform began to soften. It took approximately 13 minutes at the start before the stoichiometric $Ge_{25}Sb_{10}Se_{65}$ at. % glass (E_HAP005, F_HAP005) initially softened, and therefore the initial heating rate would have been ~ 40 °C/min to get to the fibre-drawing temperature at a glass-melt viscosity of $\sim 10^{4.5}$ Pa s. After that it was estimated that the heating rate was more like in excess of 100 °C/min for the newly presenting preform-tip moving into the short graphite receptor, as follows. (The actual temperature, and heating rate, of the preform-tip undergoing fibre-drawing was difficult to measure because it is infrared-transparent with low radiance making pyrometry inaccurate, while a thermocouple would r.f. couple.)

From viscosity-temperature measurement by means of the parallel-plate technique (discussed in greater detail in section 5.2.1.2) it was found that, for the non-stoichiometric composition $Ge_{20}Sb_{10}Se_{70}$ at. % (M_HAP005, E_HAP001), the fibre-drawing temperature (assumed at viscosity $\sim 10^{4.5}$ Pa s) was about 360 °C , i.e. ~ 150 °C above T_g (DTA $T_g = 214 \pm 2$ °C). Assuming a similar liquid fragility (*i.e.* ratioing temperatures in Kelvin) for the stoichiometric composition $Ge_{25}Sb_{10}Se_{65}$ at. %, whose DTA $T_g = 314 \pm 2$ °C, the fibre-drawing temperature was estimated to be ~ 490 °C for this stoichiometric glass composition. The preform-tip was projected to have had a volume of the order 0.03 mm^3 which within a minute or two was transformed to the fibre-drawing viscosity of $\sim 10^{4.5}$ Pa s at ~ 490 °C at a heating rate of > 100 °C/min.

Therefore, can heating rate influence the type of crystals to grow?

As previously mentioned, the bond energy of $GeSe_2$ is greater than that of Sb_2Se_3: 273.05 kJ/mol and 215.16 kJ/mol, respectively, (converted from[189]). Furthermore, the activation energy (E_c) for crystal growth is substantially greater for the $GeSe_2$ phase than for the Sb_2Se_3 phase in Ge-Sb-Se glass supercooled melts; typical published values[189] are Sb_2Se_3: E_c of 282.01 kJ/mol, and $GeSe_2$: E_c= 762.02

kJ/mol. At greater heating rates there is not as much time at each successive temperature for crystal growth to occur. It is propose that, during fibre-drawing, the newly presenting glass preform-tip at the short hot-zone of the fibre-drawing furnace, was suddenly exposed to a high temperature of around 490 °C. We further propose that with this high heating rate up to high temperature, the higher temperature phase $GeSe_2$ was more likely to grow. This is because its activation energy is steeper, than that of the lower temperature phase: Sb_2Se_3, and hence the $GeSe_2$ growth rate was greater at the high temperature[189] than that of the Sb_2Se_3.

In addition, at this higher temperature the glass supercooled melt was able to crystallise to the thermodynamically preferred high-temperature phase because diffusion rates were faster, viscosity lower, and kinetic barriers lowered. Wakkad *et al.*[189] identified the higher temperature DSC exotherm as crystallisation of $GeSe_2$.

Therefore, it is concluded that $GeSe_2$ is the primary phase of this system. Crystallisation of $GeSe_2$ is the higher temperature event of the two crystallisation events on DTA (Figure 4.11 (b)) and DSC curves[189]. The lower temperature phase: Sb_2Se_3, is chemically different from the higher temperature phase: $GeSe_2$, and so the high temperature $GeSe_2$ phase is not necessarily reliant on prior growth, nor reliant on decomposition or phase change, of the lower temperature phase: Sb_2Se_3.

4.5 Chapter 4 summary

The main focus of this chapter, was to investigate Ge-Sb-Se glasses that could be drawn into MIR optical fibres for remote sensing applications. The most important points from chapter 5 are summarised below:

- It was found that, regardless of whether the non-stoichiometric $Ge_{20}Sb_{10}Se_{70}$ at. % composition was drawn from an as-annealed or extruded preform, both fabrication routes had the potential to produce low optical loss fibres.
- In contrast, the stoichiometric $Ge_{25}Sb_{10}Se_{65}$ at. % glass, which underwent the same fabrication techniques, showed a poor resistance to crystallisation

and was unable to produce good quality fibres due to the concentric formation of monoclinic $GeSe_2$ (ICDD-PDF-01-071-0117) around the outer surface of the preform.

- Unlike isochronal investigations explored by DTA at a heating rate of 10 °C/min, the rapid heating used during fibre-drawing meant that only the high-temperature phase i.e. monoclinic $GeSe_2$, the primary phase, crystallised from the glass-forming preforms (in the supercooled temperature regime), instead of the anticipated overlap of crystallising Sb_2Se_3 and $GeSe_2$.
- Overall, the discrepancy in fibre-drawing results between the non-stoichiometric $Ge_{20}Sb_{10}Se_{70}$ at. % and the stoichiometric $Ge_{25}Sb_{10}Se_{65}$ at. % compositions, suggested that although both glasses fell within the same topological, overconstrained region, there was a significant difference in their thermal stability at each respective fibre-drawing temperature. Therefore, the results showed that Ge-Sb-Se glasses are best described by their chemical composition (CONM) rather than by their MCN and as such, Ge-Sb-Se glasses chosen for MIR optical fibre applications, should be composed of non-stoichiometric compositions.

Chapter 5: Towards Ge-Sb-Se/S step-index fibres for hyperspectral imaging

Following the successful fibre-drawing of non-stoichiometric $Ge_{20}Sb_{10}Se_{70}$ at. %, (see section 4.2) this chapter will explore a second composition from the Ge-Sb-Se/S glass system, which together, will be co-extruded into a step index fibre (SIF).

Section 5.1 will initially discuss why there was a small additional of S to the original Ge-Sb-Se system before exploring relevant physical properties in section 5.2: section 5.2.1 will first address those associated with the core $Ge_{20}Sb_{10}Se_{70}$ at. % composition whilst section 5.2.2 will address those associated with the cladding $Ge_{20}Sb_{10}Se_{67}S_3$ at. % composition. Section 5.3 will then discuss the co-extrusion of $Ge_{20}Sb_{10}Se_{70}$ at. % core and $Ge_{20}Sb_{10}Se_{67}S_3$ at. % cladding glasses, followed by the fibre-drawing and characterisation of SIFs. Section 5.4 will then provide a chapter summary.

5.1 Ge-Sb-Se/S compositions for SIF with small NA

As shown in section 1.1, one of the objectives of this Project was to develop low numerical aperture (NA) SIF from the Ge-Sb-Se/S glass systems for potential use in a MIR hyperspectral imaging probe. Although the investigated non-stoichiometric $Ge_{20}Sb_{10}Se_{70}$ at. % composition, from section 4.2, had been shown to be a suitable candidate for the prospective SIF, pairing this composition with another suitable Ge-Sb-Sb glass, proved to be a challenge.

As initially demonstrated in section 2.2.1 (Figure 2.6), a small change in composition within the $Ge_xSb_{10}Se_{90-x}$ at. % chalcogenide glass system, resulted in a significant change in material properties *e.g.* the glass transition temperatures for $Ge_{25}Sb_{10}Se_{65}$ at. %, $Ge_{20}Sb_{10}Se_{70}$ at. %, and $Ge_{15}Sb_{10}Se_{75}$ at. % are 316 °C, 211.4 °C and 160.1 °C, respectively[48]. This was also true for Ge-Sb-Se glasses outside of the $Ge_xSb_{10}Se_{90-x}$ at. % system. Whereas $Ge_{17.5}Sb_{15}Se_{67.5}$ at. % has been reported to have a similar T_g (213.3 °C[48]) to that of the non-stoichiometric $Ge_{20}Sb_{10}Se_{70}$ at.

% (214 ±2 °C, see Table 4.1), their refractive indices differed by approx. 0.1[49]. So often is the case with compositional development in chalcogenide glasses, that one physical property cannot be changed without causing an effect to another. Although $Ge_{17.5}Sb_{15}Se_{67.5}$ at. % and $Ge_{20}Sb_{10}Se_{70}$ at. % may possibly extrude and fibre-draw well with one another, due to similar thermal properties, the resulting NA of the SIF, due to large 0.1 different in refractive index, would be too high for the sensitive MIR hyperspectral imaging goal of this Project.

Consequently, a small amount (3 at. %) of Se was substituted for S which, according to the values published by Wang *et al.*[80], would result in a 3 ±1 °C increase in T_g and 0.02± 0.01 decrease in refractive index. Furthermore, very little is known about the Ge-Sb-Se-S chalcogenide glass system, so an investigation into the thermal and optical properties of $Ge_{20}Sb_{10}Se_{67}S_3$ at %, bulk glass and optical fibres, would be novel.

5.2 Characterisation of core $Ge_{20}Sb_{10}Se_{70}$ at. % and cladding $Ge_{20}Sb_{10}Se_{67}S_3$ at. % glasses

In this section, the physical and optical properties of prospective $Ge_{20}Sb_{10}Se_{70}$ at. % core and $Ge_{20}Sb_{10}Se_{67}S_3$ at. % cladding glasses are assessed, as potential candidates for use in a SIF.

5.2.1 Core glass $Ge_{20}Sb_{10}Se_{70}$ at. %

5.2.1.1 Small scale extrusion of $Ge_{20}Sb_{10}Se_{70}$ at. %

To investigate the glass' thermal properties, such as viscosity-temperature and TEC (see section 3.5.4), $Ge_{20}Sb_{10}Se_{70}$ at. % samples (E_HAP001) had to be prepared such that their dimensions fitted within the Perkin Elmer TMA-7. By using the small scale extruder parts, a ~100 mm long rod, with a diameter of ~4.7 mm (a typical extruder diameter variation is ±4 µm over 250 mm length of ~9 mm diameter rod[132]), was produced and can be seen in Figure 5.1. The small length of extrudate, broken from the rest of the rod, was the last section of glass melt to be extruded from the 15 mm diameter boule feed. Often, this section remained stuck in the die and would therefore, be broken away from the rest of the extruded rod for XRD analysis. The inset in Figure 5.1 shows that the extruded rod was X-ray amorphous prior to subsequent TMA analysis.

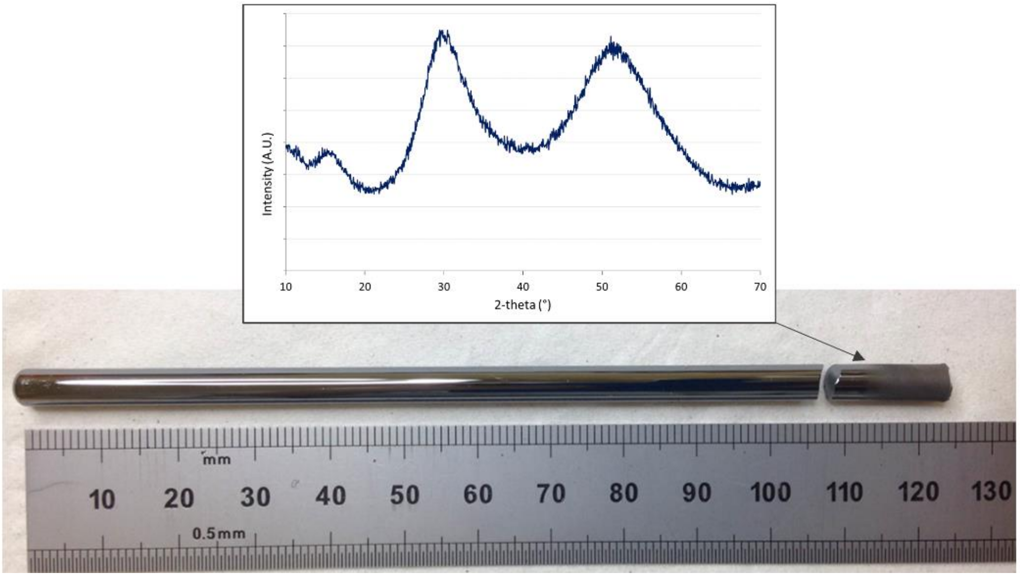

Figure 5.1: Image of the small-scale $Ge_{20}Sb_{10}Se_{70}$ at. % extruded rod with a diameter of ~4.7 mm. Inset shows the XRD curve for a small section of the preform, which was left in the 4.7 mm diameter graphite die at the end of extrusion.

As the quality of the extrudate can impact TMA measurements, the extrusion data was logged (using Pico Technology logging software) and monitored throughout the extrusion procedure to inform whether or not one of the two process variables –temperature or load- should be adjusted. Figure 5.2 (a) shows data-logging for the overall procedure whilst Figure 5.2 (b) shows an enlarged region, at the point where the extrusion rate (~2.9 mm/hour) and temperature (277 ±0.5 °C) both became stable. Once the temperature of the die had reached approximately 50 °C above T_g, a 100 kg load was applied to begin extrusion (at ~4500 secs). Whilst the temperature was manually adjusted until it became steady, the load was increased on two separate occasions: first at ~12,000 secs, with an increase to ~120 kg and then again at ~20,000 secs to compensate for its gradual decrease (see Figure 5.2(a)). This careful observation resulted in a straight 100 mm long preform, with uniform diameter (Figure 5.1).

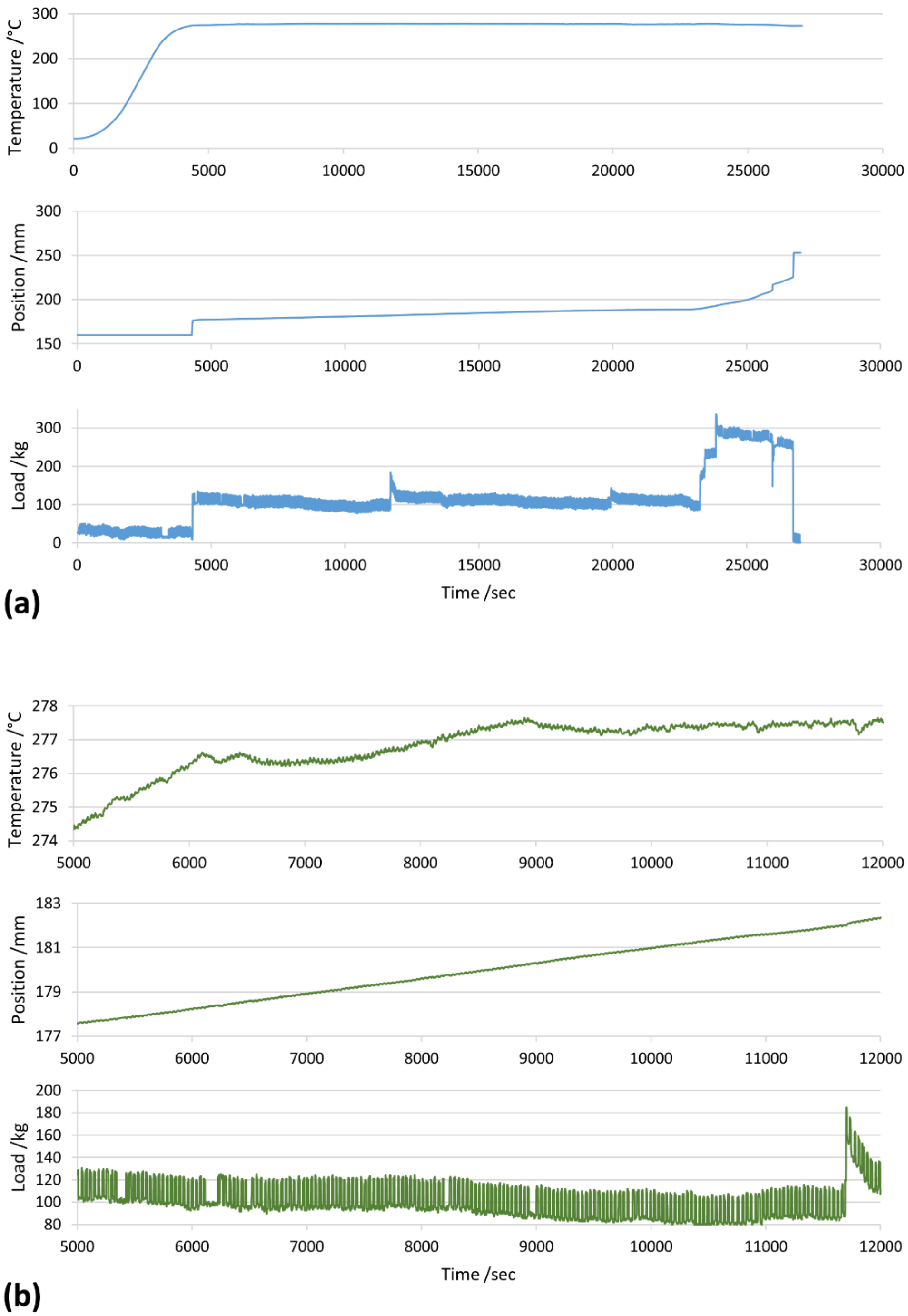

Figure 5.2: Extrusion data logged by means of PLW software for the $Ge_{20}Sb_{10}Se_{70}$ at. % (E_HAP001) core glass: (a) shows the data recorded for the entire extrusion procedure and (b) is an enlarged section of (a) which shows the moment the temperature and extrusion rate became constant. The temperature (°C) was measured by a thermocouple placed near the die; position (mm) is the distance of the bobbin in relation to the top of the extruder; and load (kg) is the applied force on the bobbin.

5.2.1.2 *Viscosity-temperature measurements of $Ge_{20}Sb_{10}Se_{70}$ at. %*

In Figure 5.3, the temperature-viscosity curves for the core $Ge_{20}Sb_{10}Se_{70}$ at. % (E_HAP001) glass, are presented. As described in section 3.3.4, 1.6 mm and 4.1 mm lengths were cut from the ~4.7 mm diameter extruded $Ge_{20}Sb_{10}Se_{70}$ at. % rod (E_HAP001) and investigated to find the viscosity-temperature behaviour, presented in Figure 5.3. As the modified parallel plates used during TMA measurements had a maximum width of ~8 mm, there was a limit to how far the samples could be flattened during the measurement. Therefore, samples with a height of 4.1 mm (400 mN) were used to find higher viscosity-temperatures whilst smaller samples with a height of 1.6 mm (50 mN) could be used to access lower viscosity-temperatures- as they could be pressed with a lower force for longer. The combined log (viscosity) *versus* temperature curves of the $Ge_{20}Sb_{10}Se_{70}$ at. % samples in Figure 5.3, show an almost linear decrease from a viscosity of ~$10^{8.0}$ Pa.s to ~$10^{5.0}$ Pa.s with increasing temperature. Following this, the rate decreases until ~$10^{4.3}$ Pa.s, as shown by the dotted-tangent line, deviating at 339 °C, in Figure 5.3. From the viscosity-temperature results, the temperatures at which the $Ge_{20}Sb_{10}Se_{70}$ at. % glass melt should be held during extrusion (~$10^{7.5}$ Pa.s) and fibre drawing (~$10^{4.5}$ Pa.s) can be found at 274.7 ±0.4 °C and 357.8 ±0.7 °C, respectively.

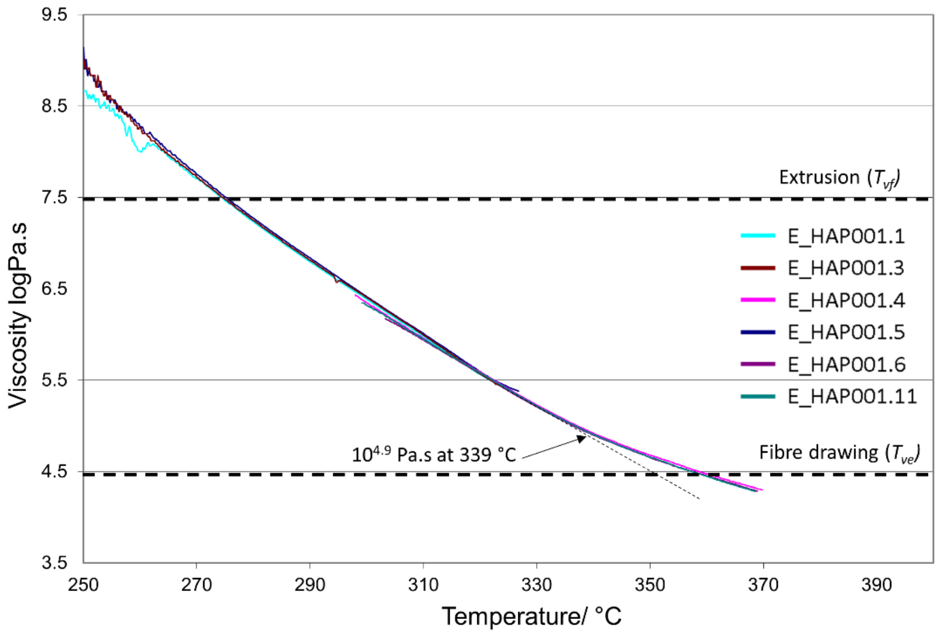

Figure 5.3: Viscosity-temperature measurements for the $Ge_{20}Sb_{10}Se_{70}$ at. % core (E_HAP001) glass composition at a heating rate of 10 °C/min. The horizontal dashed lines indicate the approximate extrusion ($10^{7.5}$ Pa.s) and fibre-drawing ($10^{4.5}$ Pa.s) viscosities. The point at which the measured data points intercept this line indicates the temperature for extrusion (T_{ve}) and fibre-drawing (T_{vf}). The dashed tangent line indicates the start of deviation from the linear fall of the viscosity-temperature curves.

5.2.1.3 Thermal expansion coefficient (TEC) investigation of $Ge_{20}Sb_{10}Se_{70}$ at. %

When a glass is heated or cooled, reversible dimensional changes can be observed on a macroscopic level which are caused by a change in the mean position of the thermal vibrations of the intermolecular bonds. This change is referred to as the thermal expansion coefficient (TEC) of a material and can be defined by the unit change in length with the unit change in temperature (see Equation 3.4)

A mismatch in TEC between two glass compositions relevant for SIFs, can lead to fractures arising from differential stresses, particularly when cooling below the glass transition temperature. To minimise this risk, core and cladding compositions should have either a similar TEC value or indeed the core glass should have a slightly higher TEC, so that a compressive force occurs, on cooling the glass pair to ambient, in the fibre cladding to heal Griffith flaws in the outermost fibre surface. Figure 5.4(a) shows the thermal expansion coefficient *versus* temperature curves, for three consecutive runs from a single extruded $Ge_{20}Sb_{10}Se_{70}$ at. % (E_HAP001) sample, with a height of 10 mm a diameter of ~4.7 mm. All runs had a 5 °C/ min heating rate and 10 °C/min cooling rate. Overall, the change in TEC with temperature is polynomial but considered to be linear over a restricted temperature range. Here TEC was calculated from the gradient of the curves between 40 °C and 100 °C and, similar to DSC measurements (Table 4.1), the average TEC value was taken from runs 002 and 003. Figure 5.4(a) reveals that the first run from the extruded, $Ge_{20}Sb_{10}Se_{70}$ at. % glass (E_HAP001) had a calculated TEC of 20.09 x 10^{-6} /°C whereas, the second and third run had closer TEC values of 19.51 x 10^{-6} /°C and 19.46 x 10^{-6} /°C, respectively. This gave an average TEC (from runs 002 and 003) of 19.49 x10^{-6} °C.

The dilatometric softening point (M_g) can also be found from the TEC curves by using the geometrical technique outlined in Figure 5.4(b); only the second $Ge_{20}Sb_{10}Se_{70}$ at. % run has been given as an example. From the point at which an abrupt change in TEC occurs, to the point at which the sample seems to contract, lies a midpoint on the ordinate where viscosity is approximately $10^{11.5}$ Pa.s *i.e.* M_g. From DSC measurements discussed in section 4.1, the $Ge_{20}Sb_{10}Se_{70}$ at. % glass composition has an onset-T_g value of 214 ±2 °C. Here, the M_g temperature was similarly found at 215 ±2 °C for the first run of the extruded $Ge_{20}Sb_{10}Se_{70}$ at. % (E_HAP001) core glass composition. The M_g points for the second (Figure 5.4 (b)) and third TEC curves were both a little higher at 217 ±2 °C. As was the case for the onset-T_g measurements quoted in Table 4.1, the thermal history of the extruded, $Ge_{20}Sb_{10}Se_{70}$ at. % (E_HAP001) sample has shown to have an effect on the TEC and M_g values. This supports the need to have a standard heating/cooling schedule during measurements and the importance of using the second and third investigative runs for final TMA averages.

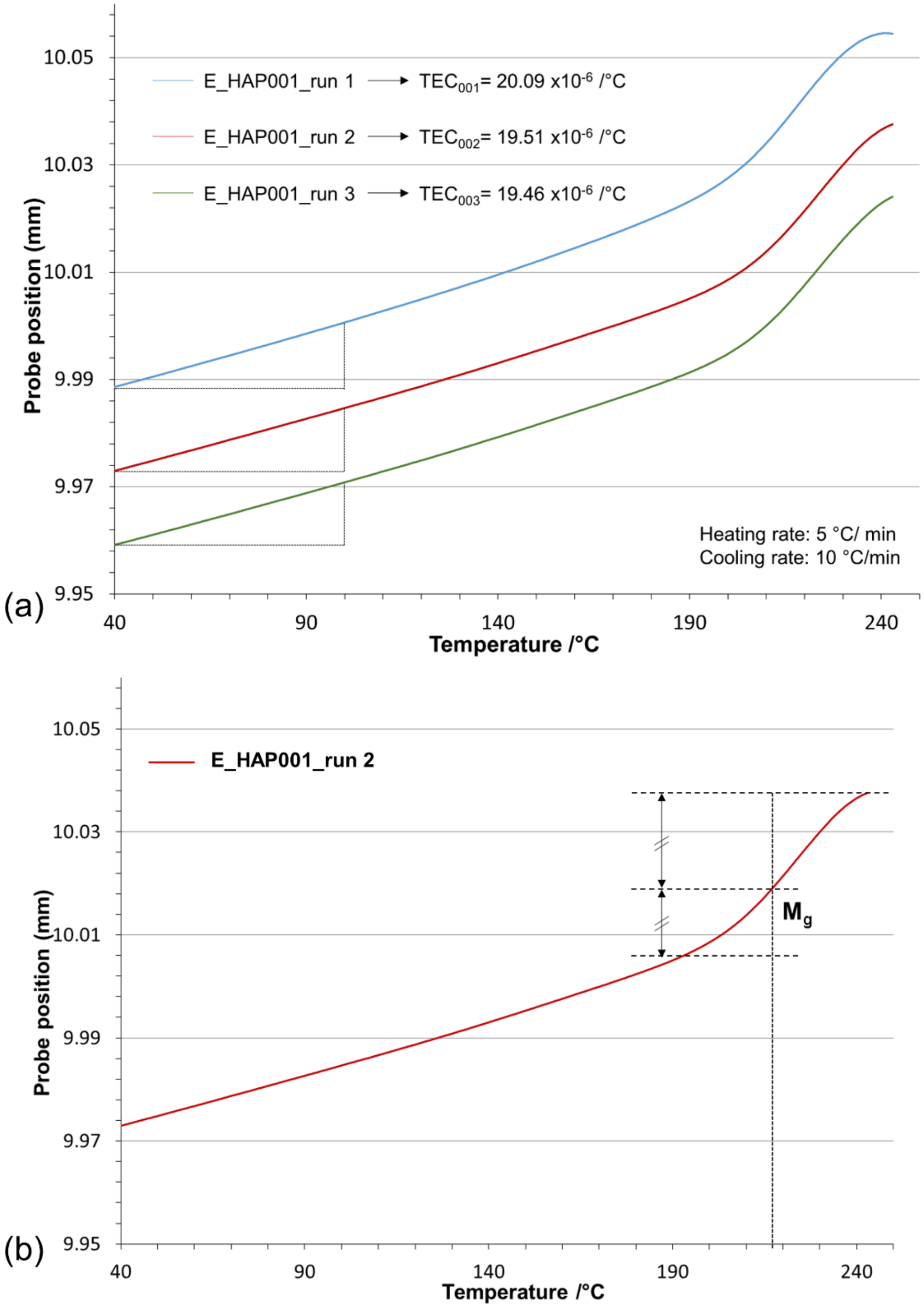

Figure 5.4: (a) Three consecutive thermal expansion curves for the ~4.7 mm diameter, extruded $Ge_{20}Sb_{10}Se_{70}$ at. % core glass sample using a heating rate of 5 °C/min and a cooling rate of 10 °C/min. (b) The thermal expansion coefficient (TEC) was calculated between 40-100 °C and the method used for calculating the dilatometric softening point (M_g) has been shown using the second run in (a) as an example.

5.2.2 Cladding glass $Ge_{20}Sb_{10}Se_{67}S_3$ at. %

5.2.2.1 X-ray diffractometry (XRD) of $Ge_{20}Sb_{10}Se_{67}S_3$ at. %

As this was a new composition, $Ge_{20}Sb_{10}Se_{67}S_3$ at. %, it was important to show that it could form a glass. This was initially confirmed *via* XRD which showed the as-annealed $Ge_{20}Sb_{10}Se_{67}S_3$ at. % (M_HAP008) glass to be X-ray amorphous (Figure 5.5).

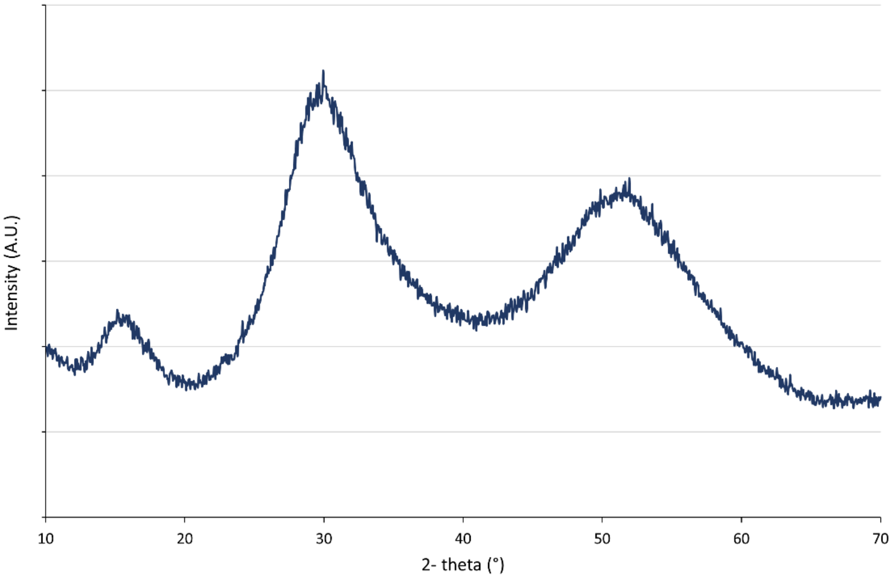

Figure 5.5: Powdered X-ray diffraction (XRD) curve of the as-annealed nominal $Ge_{20}Sb_{10}Se_{67}Se_3$ at. % cladding glass.

5.2.2.2 Differential scanning calorimetry (DSC) of $Ge_{20}Sb_{10}Se_{67}S_3$ at. %

Based on the work of Savage *et al.*[132] and Wang *et al.*[80] the substitution of 3 at. % S for Se should have increased the T_g by approximately 3 °C, due to the formation of stronger –S-bonds[80, 81]. However, as demonstrated by Figure 5.6, DSC analysis showed that the onset-T_g for the as-annealed $Ge_{20}Sb_{10}Se_{67}S_3$ at. % glass (M_HAP008) was in fact 224 ±2 °C, a temperature increase of ~10 °C. SEM-EDX analysis also confirmed that the final glass composition was $Ge_{20.4}Sb_{9.1}Se_{67.3}S_{3.2}$ at. %, and thus, close to the nominally batched.

Furthermore, unlike the previous Ge-Sb-Se samples investigated using DSC (section 4.1), the difference in T_g values between the first and second runs was greater for the $Ge_{20}Sb_{10}Se_{67}S_3$ at. % glass (see Figure 5.6). Whereas, the DSC results obtained for both Ge-Sb-Se glasses investigated in Chapter 4 saw a ~2 °C increase between runs 1 and 2, the $Ge_{20}Sb_{10}Se_{67}S_3$ at. % glass (M_HAP008) had a 10 °C increase. Sometimes if a glass is annealed poorly, a maximum onset-T_g value may be seen for the first DSC run, due to the release of residual strains introduced during quenching. However, this was not the case for the $Ge_{20}Sb_{10}Se_{67}S_3$ at. % glass seen in Figure 5.6.

T_g is a time-dependent phenomenon and so, amongst several other factors, can greatly depend on the materials' heating a cooling rates- as previously mentioned during the $Ge_{20}Sb_{10}Se_{70}$ at. % TEC and M_g discussion. For glasses that have been cooled slowly through T_g (but fast enough to avoid crystallisation) there is more time for configurational changes to occur in the supercooled liquid. This enables the structure to be frozen at a lower temperature and thus the final glass will exhibit a lower T_g; a relationship best described by the fictive temperature (refer to Figure 2.1).

Upon reheating, runs two and three most likely by-passed the cooling curve of run one and therefore, exhibit a T_g 10 °C higher at 224 ±2 °C. This subsequent increase in T_g can be attributed to a change in thermal history and that the $Ge_{20}Sb_{10}Se_{67}S_3$ at. %, more than previously investigated Ge-Sb-Se systems, is dependent on hysteresis.

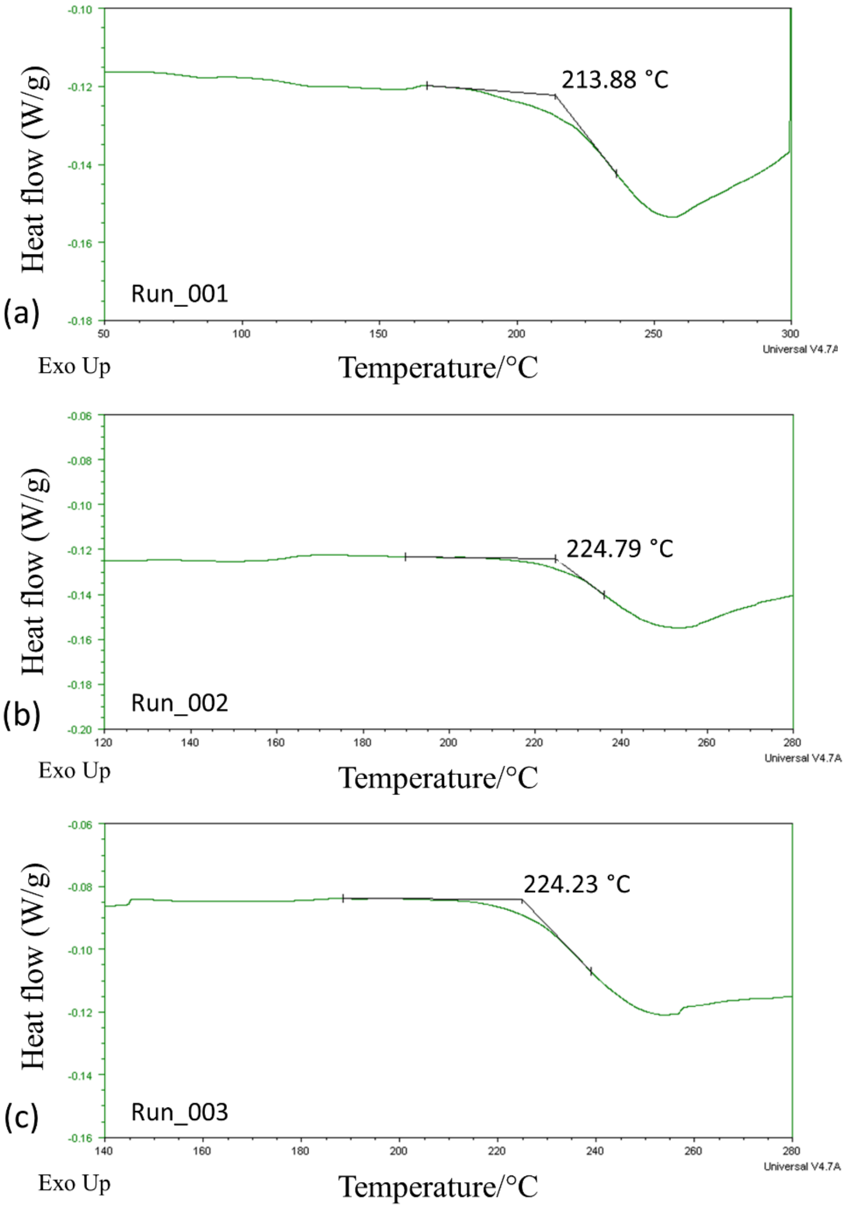

Figure 5.6: Differential scanning calorimetry (DSC) curves of the as-annealed $Ge_{20}Sb_{10}Se_{67}S_3$ at. % cladding glass heated and cooled at a rate of 10 °C/min.

5.2.2.3 Small scale extrusion of $Ge_{20}Sb_{10}Se_{67}S_3$ at. %

Nevertheless, the T_g measured in this Project was based on the onset of the transition, so although the value can give us a good indication about further processing parameters, it does not always tell the full story. Therefore, the prospective cladding glass was also extruded so that, like the core glass in section 5.2.1, TMA could be explored to find the viscosity-temperature behaviour and

TEC. Figure 5.7 shows the ~4.7 mm diameter $Ge_{20}Sb_{10}Se_{67}S_3$ at. % extruded rod (E_HAP003) still attached to the small scale extrusion parts. The first ~100 mm of glass was almost completely linear and used for TMA samples. The remaining ~15 mm was used for XRD analysis and, although not shown here, revealed an X-ray amorphous structure.

Figure 5.7: Photograph of the extruded $Ge_{20}Sb_{10}Se_{67}S_3$ at. % cladding glass (E_HAP003, M_HAP008) with a ~4.7 mm diameter.

Once again the entire extrusion process was monitored and the results were recorded through the Pico Technology logging software, presented in Figure 5.8. After approximately 12000 secs, both the extrusion rate (~2.8 mm/hour) and temperature 282 ±0.5 °C became stable. Unlike, the measured T_g values, there was only ~5 °C difference between the core $Ge_{20}Sb_{10}Se_{70}$ at. % (277 ±0.5 °C) and cladding $Ge_{20}Sb_{10}Se_{67}S_3$ at. % (282 ±0.5 °C) extrusion temperatures, thus showing promise for co-extrusion.

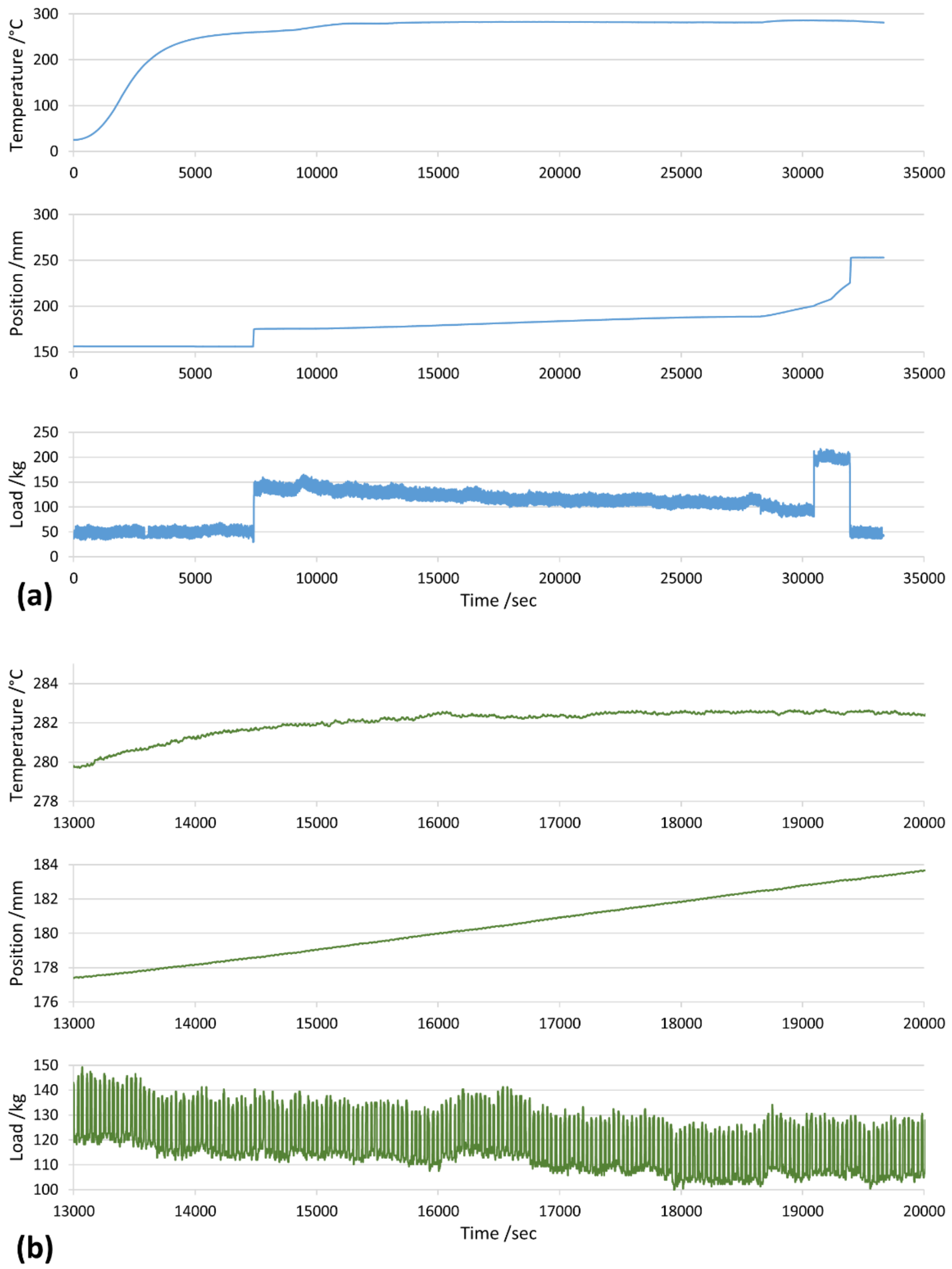

Figure 5.8: Extrusion data logged by PLW software for the $Ge_{20}Sb_{10}Se_{67}S_3$ at. % cladding glass (E_HAP003, M_HAP008): (a) shows the data recorded for the entire extrusion procedure and (b) is an enlarged section of (a) which shows the moment the temperature and extrusion rate became constant. The temperature (°C) is measured by means of a thermocouple placed near the die; position (mm) is the distance of the bobbin in relation to the top of the extruder; and load (kg) is the applied force on the bobbin.

5.2.2.4 Viscosity-temperature measurements of $Ge_{20}Sb_{10}Se_{67}S_3$ at. %

In Figure 5.9 the viscosity-temperature curves for the 4.7 mm diameter, extruded $Ge_{20}Sb_{10}Se_{67}S_3$ at. % (E_HAP003) samples are shown. Although the viscosity-temperature curves of the three samples of equal heights (*i.e.* either 1.6 mm or 4.1 mm) agreed well with one another, the two groups had a slight mismatch in the overlapping region (~310-330 °C) of the viscosity-temperature curves. It was not obvious where this discrepancy had originated from as each of the sample groups had been measured consecutively following calibration. What is more, it was unlikely that this difference was a result of glass inhomogeneity, as the various-sized samples had been alternatively cut from the extruded rod (refer to section 3.5.4).

Overall however, the extruded $Ge_{20}Sb_{10}Se_{67}S_3$ at. % (E_HAP003) sample viscosities showed an almost linear decrease from ~$10^{8.0}$ Pa.s to ~$10^{5.0}$ with increasing temperature, before the rate decreased to ~$10^{4.3}$ Pa.s. According to Figure 5.9, the calculated temperature at which the prospective cladding glass should have been extruded ($10^{7.5}$ Pa.s) was 277.7 ±0.4 °C. This was ~3 °C higher than the temperature used to initially extrude the cladding $Ge_{20}Sb_{10}Se_{67}S_3$ at. % rod (E_HAP003), but the same temperature at which the core $Ge_{20}Sb_{10}Se_{70}$ at. % (E_HAP001) was extruded. Furthermore, Figure 5.9 also shows the temperature at which the $Ge_{20}Sb_{10}Se_{67}S_3$ at. % glass should be fibre-drawn ($10^{4.5}$ Pa.s) is 361.9 ±0.3 °C, ~4 °C higher than that calculated for the core $Ge_{20}Sb_{10}Se_{70}$ at. % glass (E_HAP001, Figure 5.3). Although the TMA results presented in this Project saw a slight shift in the viscosity-temperature curves, similar to the work reported by Guery *et al.*[81], the relatively small 3 °C (at $10^{7.5}$ Pa.s) and 4 °C (at $10^{4.5}$ Pa.s) temperature difference between the core ($Ge_{20}Sb_{10}Se_{70}$ at. %, E_HAP001) and cladding ($Ge_{20}Sb_{10}Se_{67}S_3$ at. %, E_HAP003) glasses, suggested the two compositions would co-extrude and fibre-draw well together.

Unfortunately, there are no TEC data for the extruded $Ge_{20}Sb_{10}Se_{67}S_3$ at. % glass as not long after viscosity measurements, the Perkin Elmer TMA-7 stopped working. However, as the TMA results thus far had shown a good match between the two compositions, it was assumed that the TEC of both $Ge_{20}Sb_{10}Se_{70}$ at. % (core) and $Ge_{20}Sb_{10}Se_{67}S_3$ at. % (cladding) would be similar; thus it is often the case that for a small series of glasses [T_g x TEC] is a constant and so because the T_gs are similar, this suggests that so are their TEC[195]. Therefore, it was decided that work would continue towards the fabrication of the SIF before confirming this.

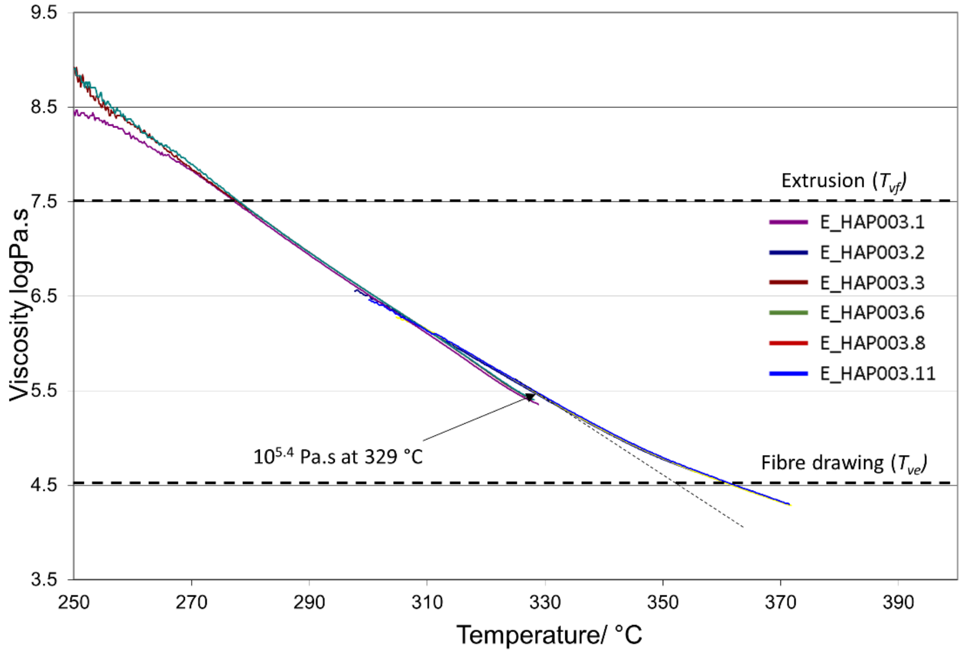

Figure 5.9: Viscosity-temperature measurements for the $Ge_{20}Sb_{10}Se_{67}S_3$ at. % (E_HAP003) cladding glass composition at a heating rate of 10 °C/min. The horizontal dashed lines indicate the approximate extrusion ($10^{7.5}$ Pa.s) and fibre-drawing ($10^{4.5}$ Pa.s) viscosities. The point at which the measured data points intercept this line indicates the temperature for extrusion (T_{ve}) and fibre-drawing (T_{vf}). The dashed tangent line indicates the start of deviation from the linear fall of the viscosity-temperature curves.

5.2.2.5 Fibre-drawing and lost measurements of $Ge_{20}Sb_{10}Se_{67}S_3$ at. % from a ~4.7 mm diameter, extruded rod

Prior to the SIF fabrication, the fibre-drawing capability of $Ge_{20}Sb_{10}Se_{67}S_3$ at. % (E_HAP004) was individually explored, as not only would this provide fibre for refractive index measurements (measurements on pressed fibres by Mr Fang of the MIR Photonics Group, University of Nottingham, UK, see section 5.2.3), but the optical quality could also be assessed *via* the cut back method (section 3.6). Pulled from a second 4.7 mm diameter extruded preform (E_HAP004), Figure 5.10 shows the optical fibre loss for a ~7 m length of 200 ±5 µm diameter, unstructured $Ge_{20}Sb_{10}Se_{67}S_3$ at. % (F_HAP004) fibre; the final section of this fibre-drawn preform is shown in the inset of Figure 5.10 showing a smooth and shiny surface. Since the glass had only been purified *via* the bake-out procedure (see section 3.3.4.1), impurity vibrational absorption bands were expected in the MIR optical window. However, as Figure 5.10 demonstrates, even with the small addition of 3 at. % S to the $Ge_{20}Sb_{10}Se_{70-x}S_x$ system there was a significant increase in impurities *i.e.* the 42.4 dB/m S-H band at 4.03 µm[35]. The additional 14.7 dB/m absorption at ~8.79 µm is also likely to be Si-O[89]. When compared to the original $Ge_{20}Sb_{10}Se_{70}$ at. % core glass fibre loss (Figure 4.4), although still present, the bands at: 2.86 µm (O-H), 4.53 µm (Se-H) and 7.9 µm (Ge-O), had comparatively diminished. Therefore, not only does this suggest that S introduces more –H and –O- to the glass, it will also readily bond with the impurities already present in the Ge-Sb-Se glass. Sanghera *et al.*[83], reported that it was necessary to vacuum distil the as-received S five times at 300 °C, to sufficiently reduced the impurity content. Thus, suggesting that the bake-out purification (see 3.3.4.1) of S would not have made much of an improvement. Nevertheless, even with a fourth element added to the Ge-Sb-Se system, the extruded $Ge_{20}Sb_{10}Se_{67}S_3$ at. % (E_HAP004) preform was still able to produce fibres with a baseline loss of 0.53 dB/m at 5.99 µm wavelength.

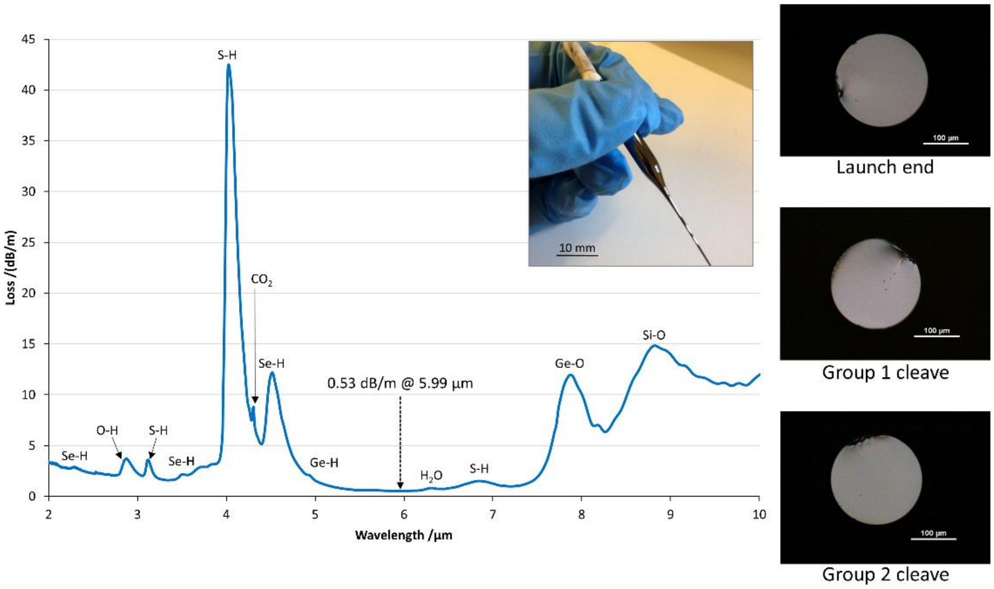

Figure 5.10: Fibre loss spectrum of the extruded, $Ge_{20}Sb_{10}Se_{67}S_3$ at. % cladding glass (F_HAP004) measured over an ~8 m length of ~200 µm diameter fibre. The inset photograph highlights the smooth preform post fibre-drawing whilst the three optical images show the final three cleaves used for the fibre loss measurements.

5.2.3 Refractive index measurements of $Ge_{20}Sb_{10}Se_{70}$ at. % (core) and $Ge_{20}Sb_{10}Se_{67}S_3$ at. % (cladding) glasses

The refractive index measurements presented in this section were kindly conducted by Mr Y. Fang, PhD candidate from the Mid-infrared Photonics Group, University of Nottingham UK.

In Figure 5.11, the refractive index measurements of both the $Ge_{20}Sb_{10}Se_{70}$ at. % core and $Ge_{20}Sb_{10}Se_{67}S_3$ at. % cladding glasses are presented from 2 to 25 µm wavelength and were calculated using an improved Swanepoel method with a two-term Sellmeier mode (full description can be found elsewhere[196]). Chalcogenide FTIR thin films of nominal batch $Ge_{20}Sb_{10}Se_{70}$ at. % (M_HAP005) and $Ge_{20}Sb_{10}Se_{67}S_3$ at. % (M_HAP008) composition were prepared by a hot-pressing technique, which produced films of 25 µm thickness. For comparative accuracy, benchmark refractive indices were also obtained from a $Ge_{20}Sb_{10}Se_{70}$ at. % prism (M_HAP005) and were investigated at 3.1 µm and 3.8 µm wavelengths. Unfortunately, due to the geometry of the ~4.7 mm diameter extruded rod

(E_HAP004) used to draw $Ge_{20}Sb_{10}Se_{67}S_3$ at. % fibres, a suitable bulk glass sample was not available from which to make a $Ge_{20}Sb_{10}Se_{67}S_3$ at. % prism.

Overall, results from Figure 5.11 show that the substitution of 3 at. % Se for 3 at. % S, in the $Ge_{20}Sb_{10}Se_{70-x}S_x$ at. % series, reduced the refractive index of the $Ge_{20}Sb_{10}Se_{67}S_3$ at. % cladding thin film over the 2-25 µm wavelength region. At 3.1 µm wavelength, the core $Ge_{20}Sb_{10}Se_{70}$ at. % thin film had a refractive index of 2.553 whilst the cladding $Ge_{20}Sb_{10}Se_{67}S_3$ at. % thin film had a refractive index of 2.540. With a difference of approx. 0.01, refractive index measurements conducted by Mr Y. Fang, support those reported by Wang *et al*.[80]. As such, a SIF composed of a $Ge_{20}Sb_{10}Se_{70}$ at. % core and $Ge_{20}Sb_{10}Se_{67}S_3$ at. % cladding, would have a numerical aperture (NA) of 0.25 at 3.1 µm wavelength (see inset of Figure 5.11). Ideally, SIFs used in a MIR hyperspectral imaging probe would have a slightly higher NA (approx. 0.4) since this would offer superior light gathering capabilities whilst still only accepting incoming rays for a sensitive area. However, as discussed in section 5.1, tailoring the compositions of the core and gladding Ge-Sb-Se/s glasses so that there was a greater difference in refractive indices, *i.e.* larger NA, would have also incurred a greater difference in T_gs.

Nevertheless, in the inset of Figure 5.11, the NA of a $Ge_{20}Sb_{10}Se_{70}$ at. % core and $Ge_{20}Sb_{10}Se_{67}S_3$ at. % cladding SIF was shown to be lowest at approx. 4.7 µm (0.24) and highest at approx. 23 µm (0.36). For Ge-Sb-Se glasses, Ge and Sb atoms are bonded with Se forming tetrahedral $GeSe_4$ and pyramidal $SbSe_3$ units, whilst Ge-Ge and Sb-Sb bonds are negligible in this system[197]. The basic structural units in the $Ge_{20}Sb_{10}Se_{70}$ at. % core glass consist of $GeSe_4$, $SbSe_3$ and Se-Se. The nearest strong vibrational absorption band in far infrared (FIR) is at 247 cm^{-1} (40.5 µm) which is assigned to Se-8 polymeric rings and $GeSe_4$ structural units[197]. For Ge-Sb-Se-S glasses S will substitute Se and bond initially with Ge, which is supported by their different bond strengths[198]. Therefore, the basic structural units in the $Ge_{20}Sb_{10}Se_{67}S_3$ at. % cladding glass are $GeSe_4$, $SbSe_3$, GeS_4, SbS_3, Se-Se and S-S. Since only 3 at. % S was incorporated into the system, S-S vibrations, assigned to 494 cm^{-1} (20.2 µm), are negligible. The nearest strong vibrational band is at 342 cm^{-1} (29.2 µm) which is caused by the symmetrical stretching vibrations of GeS_4[199].

Since the FIR vibrational absorption band of the $Ge_{20}Sb_{10}Se_{67}S_3$ at. % cladding glass is at a shorter wavelength than that of the $Ge_{20}Sb_{10}Se_{70}$ at. %core glass, the refractive index dispersion of $Ge_{20}Sb_{10}Se_{67}S_3$ at. % decreases faster than that of $Ge_{20}Sb_{10}Se_{70}$ at. %. Therefore, the NA of a $Ge_{20}Sb_{10}Se_{70}$ at. % core and $Ge_{20}Sb_{10}Se_{67}S_3$ at. % cladding SIF increases with the wavelength, as demonstrated in Figure 5.11.

Furthermore, the two prism measurements made on the core $Ge_{20}Sb_{10}Se_{70}$ at. % glass (M_HAP005) at 3.1 µm (using an Intercascade laser (ICL)) and 3.8 µm (using a superK laser), showed refractive index measurements of 2.466 and 2.5438, respectively. These values were slightly lower than those measured on the thin film $Ge_{20}Sb_{10}Se_{70}$ at. % samples (see Figure 5.11). This difference in refractive index measurements was attributed to a difference in thermal history *i.e.* the prism $Ge_{20}Sb_{10}Se_{70}$ at. % sample had been ground and polished from an as-annealed bulk glass (M_HAP005) whilst the thin film sample had been extruded (E_HAP002), fibre-drawn (F_HAP003) and then hot pressed from the initial as-annealed glass (M_HAP005). Nevertheless, using the prism measurements from the $Ge_{20}Sb_{10}Se_{70}$ at. % glass as benchmarks, the accuracy of the thin film measurements was found to be 0.4 %.

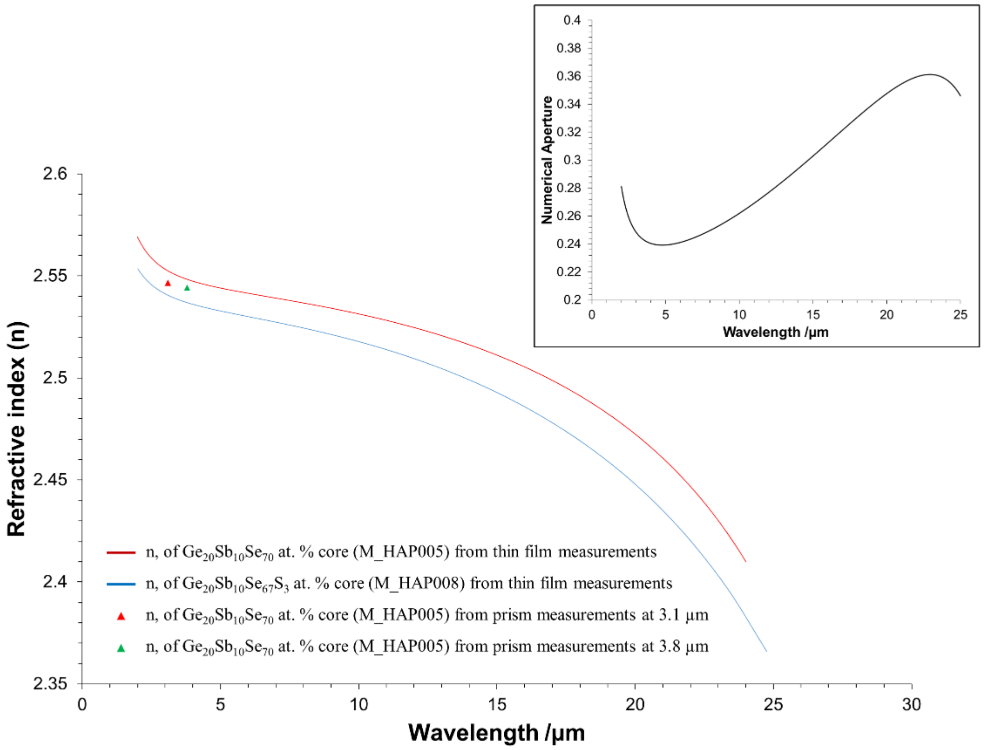

Figure 5.11: Refractive index (n) measurements of core $Ge_{20}Sb_{10}Se_{70}$ at. % (M_HAP005) and cladding $Ge_{20}Sb_{10}Se_{67}S_3$ at. % (M_HAP008) glasses. Inset shows calculated numerical aperture (NA) values for a $Ge_{20}Sb_{10}Se_{70}$ at. % (M_HAP005) and cladding $Ge_{20}Sb_{10}Se_{67}S_3$ at. % (M_HAP008) step index fibre (SIF).

5.3 $Ge_{20}Sb_{10}Se_{70}$ at. % core and $Ge_{20}Sb_{10}Se_{67}S_3$ at. % cladding step index fibres (SIF)

As a quick summary, the most significant results from sections 5.2.1 and 5.2.2, are presented in Table 5.1. It is shown that both the thermal and optical properties of the prospective core $Ge_{20}Sb_{10}Se_{70}$ at. % and cladding $Ge_{20}Sb_{10}Se_{67}S_3$ at. % glasses, are closely matched and thus, should be able to produce stable SIF.

Table 5.1: Overview of the prospective $Ge_{20}Sb_{10}Se_{70}$ at. % (core) and $Ge_{20}Sb_{10}Se_{67}S_3$ at. % (cladding) results thus far, comparing relevant properties for the fabrication of step index fibres (SIFs). T_{ve} and T_{vf} indicates the temperature required to achieve extrusion and fibre-drawing viscosities

Composition /at. %	**Material property**			
	T_g /°C	**T_{ve} /°C**	**T_{vf} /°C**	***RI at 3.1 µm wavelength***
$Ge_{20}Sb_{10}Se_{70}$ (core)	214 ±2	274.7 ±0.4	357.8 ±0.7	2.55
$Ge_{20}Sb_{10}Se_{67}S_3$ (cladding)	224 ±2	277.7 ±0.4	361.9 ±0.3	2.54

5.3.1 Co-extrusion of $Ge_{20}Sb_{10}Se_{70}$ at. % (core) and $Ge_{20}Sb_{10}Se_{67}S_3$ at. % (cladding) glasses

Following the individual investigations into the physical properties of $Ge_{20}Sb_{10}Se_{70}$ at. % (core) and $Ge_{20}Sb_{10}Se_{67}S_3$ at. % (cladding) glasses, the next stage of this Project looked at co-extruding the two compositions into a ~10 mm diameter preform for fibre-drawing.

The preparation of the initial glass boules was of paramount importance, as this ultimately determined the quality of the mating surfaces between the core and the cladding compositions, in the final SIF. Therefore, 29 mm diameter $Ge_{20}Sb_{10}Se_{70}$ at. % core (M_HAP011) and $Ge_{20}Sb_{10}Se_{67}S_3$ at. % cladding (M_HAP013) boules were carefully ground and polished to a 1 µm finish, using the procedure described in section 3.4.1. A large scale vertical extrusion was carried out (see Figure 3.10 (c)).

The overall recorded data for the ~10 mm outer diameter extrudate, obtained from the co-extrusion, is shown in Figure 5.12 (a). In Figure 5.12 (b), the data logged specifically between 8000 and 14000 sec is presented *i.e.* the section where the rate and temperature began to steady. From Table 5.1, it was anticipated that the two glass compositions would co-extrude around 276 ±2 °C hence, this is why the temperature was initially raised to 270 °C, as shown in Figure 5.12(b). However, it was noticed that with the application of the 300 kg load, the rate of extrusion was initially 16.79 mm/h. This extrusion rate was deemed too fast for the production of a highly linear extrudate, with a consistent outer diameter and core-cladding ratio. Therefore, the temperature was decreased to 267±0.1 °C where it was maintained, along with an extrusion rate of 7.77 mm/h and an applied load of 300± 3 kg, until the end of extrusion.

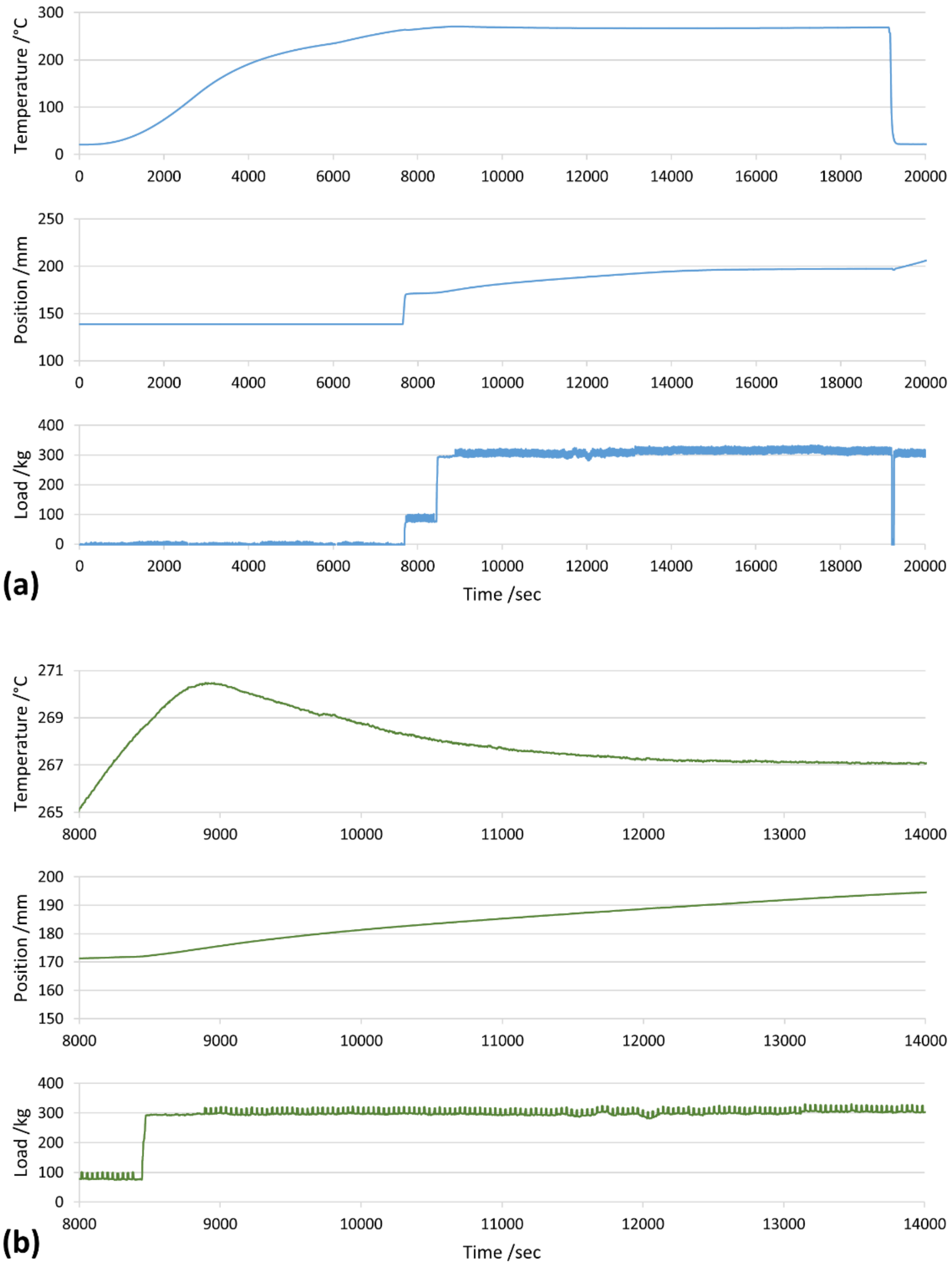

Figure 5.12: Extrusion data logged by PLW software for the co-extrusion (E_HAP006) of $Ge_{20}Sb_{10}Se_{70}$ at. % (core) (M_HAP011) and $Ge_{20}Sb_{10}Se_{67}S_3$ at. % (cladding) (M_HAP013) glasses: (a) shows the data recorded for the entire extrusion procedure and (b) is an enlarged section of (a) which shows the moment that the temperature and extrusion rate became constant. The temperature (°C) was measured by means of a thermocouple placed on the external surface of extrusion die; position (mm) is the distance of the bobbin in relation to the top of the extruder; and load (kg weight) was the applied force on the bobbin.

In Figure 5.13(a) the final extrudate with a diameter of 9.56 ±0.03 mm and a length of 240 ±5 mm is presented. Based on the work by Savage *et al.*[132], and considering the likely flow patterns of the viscous chalcogenide supercooled melt through the 10 ±0.1 mm diameter die, the $Ge_{20}Sb_{10}Se_{70}$ at. % core glass composition was not expected to appear within the first 40 mm of the extruded rod (the start of extrusion is marked as the datum point 0 mm in Figure 5.13(a)). Furthermore, based on the work by Savage *et al.*[132], the desired core/cladding ratio was not expected to reach ~90 % until 120 mm along the extruded rod, as demonstrated by the annotated photograph in Figure 5.13(b). Therefore, it was decided that the co-extruded rod would be broken ~100 mm from the start of extrusion (position 1 in Figure 5.13(b)), with the remaining extrudate used as the fibre drawing preform. Position 2 in Figure 5.13(b) shows the point at which the preform was initially softened by the graphite receptor in the fibre-drawing tower. By heating at this point in the preform, enough material was given so that the diameter of the fibre could stabilise before reaching the anticipated 90 % core-cladding ratio mark at ~120 mm along the fibre; from previous experience this can take 5 ±1 m of drawing before the fibre reaches a steady ±10 μm on a fibre between 150-250 μm outside diameter.

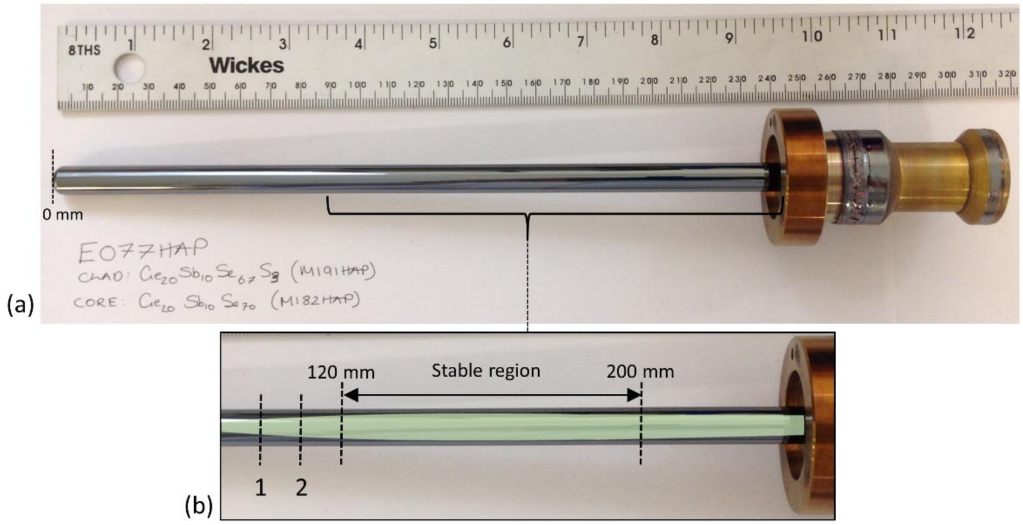

Figure 5.13: (a) Photograph of the co-extruded (E_HAP006) $Ge_{20}Sb_{10}Se_{70}$ at. % (core) (M_HAP011) and $Ge_{20}Sb_{10}Se_{67}S_3$ at. % (cladding) (M_HAP013) rod preform, of length of ~240 mm and a diameter of 9.56 ±0.03 mm. (b) Estimated position of the inner $Ge_{20}Sb_{10}Se_{70}$ at. % core (M_HAP011) glass (shaded green).

5.3.2 Fibre drawing and fibre loss measurements of co-extruded $Ge_{20}Sb_{10}Se_{70}$ at. % (core) and $Ge_{20}Sb_{10}Se_{67}S_3$ at. % (cladding) SIF

Figure 5.14 shows 158 m of SIF (F_HAP007) that was successfully drawn from the Ge-Sb-Se/S co-extruded rod (E_HAP006) onto a 1 m circumference polystyrene drum. Annotations (a)-(f) in Figure 5.14, refer to sections of the preform where the fibre had been drawn from *e.g.* 0-115 mm refers to the initial section of preform that was softened and drawn (spanning positions 1 and 2 in Figure 5.13(b)). As predicted, it took approximately 5 mm of preform before the drawn fibre had a stable 200 ±10 µm diameter, and another ~15 mm of preform before it had a stable 200 ±5 µm diameter. By this point, fibre was being drawn from a section of the preform 130 mm from the start of extrusion and thus, should have been close to the 90 % core/cladding ratio. Therefore, fibre was wound onto the drum with a 2 mm spacing between each turn so that it could easily be removed for the fibre loss measurements. The core $Ge_{20}Sb_{10}Se_{70}$ at. % and cladding $Ge_{20}Sb_{10}Se_{67}S_3$ at. %, co-extruded rod (E_HAP006) was actually able to produce ~69 m of stable 200 ±5 µm diameter from a section of the preform 130-157 mm from the start of extrusion.

Figure 5.14 also shows that fibre with a diameter of 300 ±10 µm (e) and 400 ±10 µm (f) was also drawn from a section of the preform ~157-191 m from the start of extrusion. Note that the change in diameter was not immediate and so the first ~1.5 m of each section would have had a varying diameter. Although not intended for fibre loss measurements, the larger diameter sections were collected for future fibre bundle work (see chapter 8).

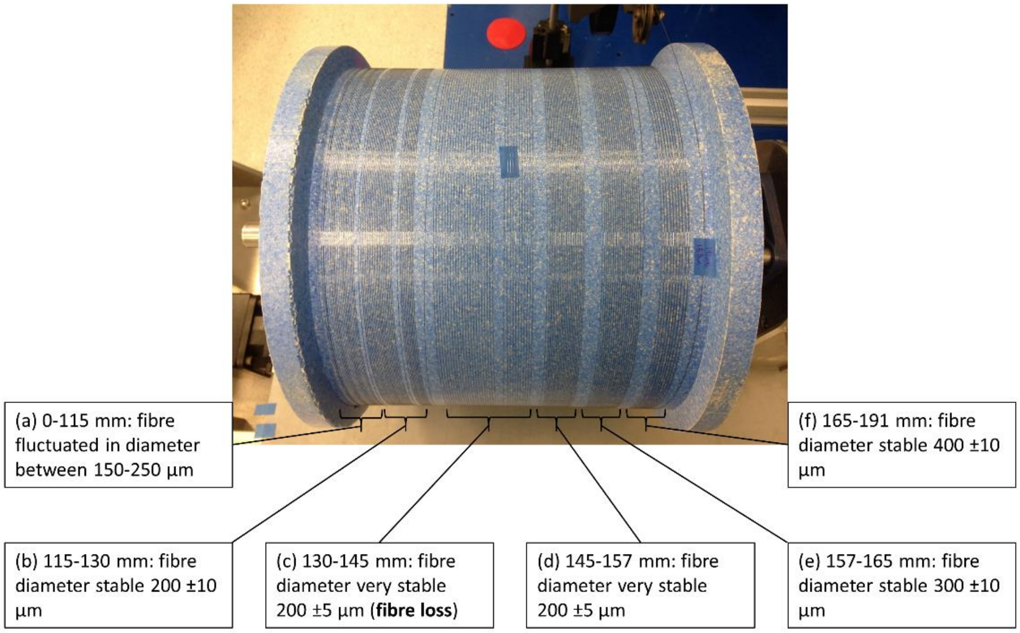

Figure 5.14: Photograph of the co-extruded (E_HAP006), $Ge_{20}Sb_{10}Se_{70}$ at. % (core) and $Ge_{20}Sb_{10}Se_{67}S_3$ at. % (cladding) step index fibre (SIF) (F_HAP007) with varying diameter wound onto the polystyrene drum of 1 m circumference: (a)-(f) detail each section of the SIF collected. Measurements, e.g. (a) 0-115 mm, refer to the section of preform (E_HAP006) from which the SIF was drawn.

Optical fibre loss measurements, presented in Figure 5.15, were conducted on an ~8 m length of 200 ±5 µm diameter SIF which had been collected from the final part section (c) in Figure 5.14. This length had originally been ~2 m longer however, during the transfer from barrel to optical bench, there had been an inadvertent break in the fibre. Initially there were concerns that this was an early indication of stress within the SIF, potentially due to a mismatch in TEC however, the fibre handled well through loss measurements and so there were no further problems. Figure 5.15 shows the final loss measurements for the SIF (green line) along with the respective core ($Ge_{20}Sb_{10}Se_{70}$ at. %, red line) and cladding ($Ge_{20}Sb_{10}Se_{67}S_3$ at. %, blue line) for comparison. Although relatively large vibrational absorption bands were once again present *e.g.* Se-H at 4.5 µm (10.51 dB/m) and Ge-O at 7.9 µm (19.05 dB/m), these impurity absorptions proved effective in demonstrating the successful waveguiding of this SIF.

As discussed in section 2.5.2, some photon energy will always be travelling in the cladding at the core-cladding interface due to the evanescent wave phenomenon and then potentially lost if there is an imperfect optical core-cladding boundary. Therefore, traces of the $Ge_{20}Sb_{10}Se_{67}S_3$ at. % cladding impurity bands *e.g.* S-H at 4.04 µm (42.0 dB/m) or S-O at ~8.85 µm (14.8 dB/m), were expected to show in SIF core glass; however, as Figure 5.15 revealed this was not the case. In fact in Figure 5.15, the only significant difference between the SIF fibre loss and that of the single unstructured core glass, was a slight decrease in the Se-H absorption band at 4.5 µm, as follows: 1) 15.9 dB/m for the $Ge_{20}Sb_{10}Se_{70}$ at. % core (red line) and 2) 10.4 dB/m for the SIF (green line). Since both $Ge_{20}Sb_{10}Se_{70}$ at. % glasses in F_HAP006 and F_HAP007 fibres had been purified *via* the same bake out procedure, the 5.5 dB/m reduction could simply have resulted from an improved user technique.

The absence of impurity vibrational absorption associated with the $Ge_{20}Sb_{10}Se_{67}S_3$ at. % cladding in the SIF loss spectrum (Figure 5.15), suggests that not only was the penetration depth of the evanescent wave small, but there was a successful match between the refractive indices of the core ($Ge_{20}Sb_{10}Se_{70}$ at. %) and cladding ($Ge_{20}Sb_{10}Se_{67}S_3$ at. %) compositions thus promoting efficient propagation of the incident light down the fibre core and small evanescent field penetration into the cladding glass.

The lowest loss for the $Ge_{20}Sb_{10}Se_{70}$ at. % core (M_HAP011) and $Ge_{20}Sb_{10}Se_{67}S_3$ at. % cladding (M_HAP013) SIF was measured as 0.72 dB/m at 6.06 µm wavelength.

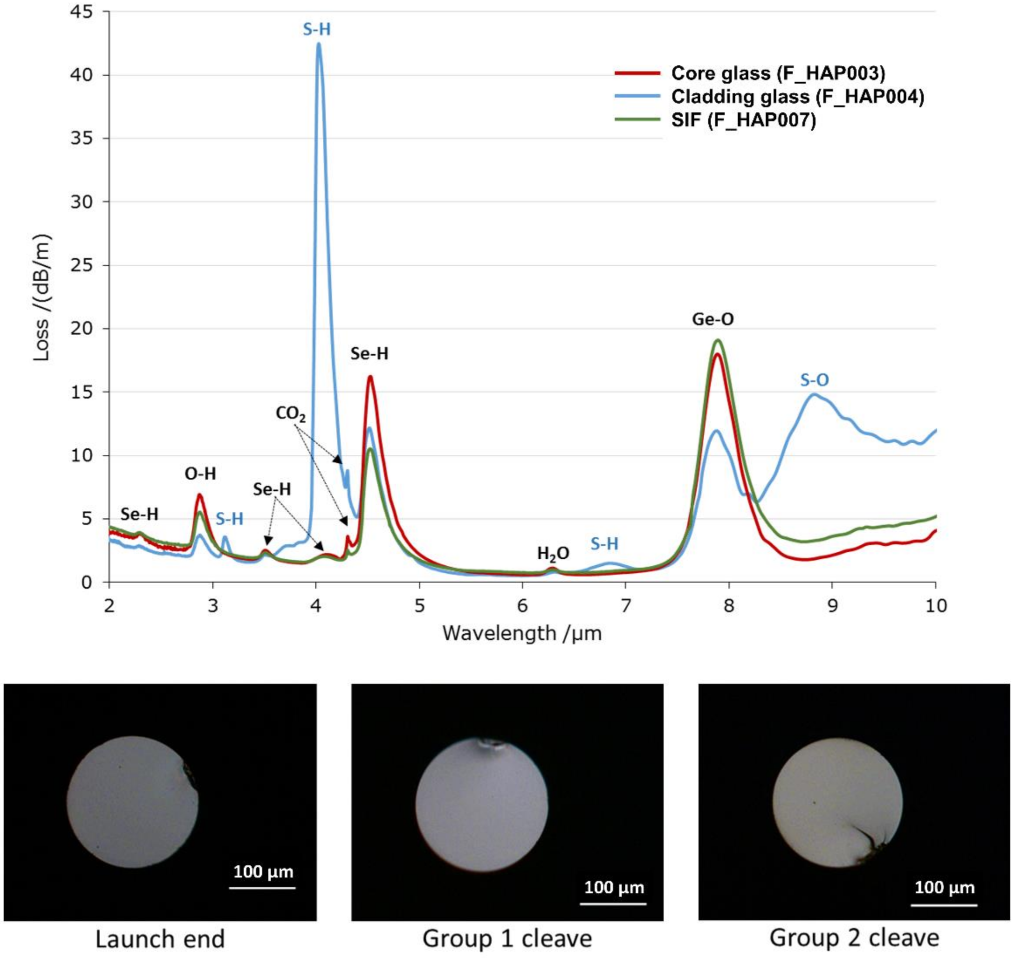

Launch end | Group 1 cleave | Group 2 cleave

Figure 5.15: Combined fibre loss spectra for the: 1) $Ge_{20}Sb_{10}Se_{70}$ at. % core glass (F_HAP003) (red line) the 2) $Ge_{20}Sb_{10}Se_{67}S_{3}$ at. % cladding glass (F_HAP004) (blue line) and the 3) co-extruded, step index fibre (SIF) (F_HAP007) (green line). The three optical images show the final three cleaves used for the SIF loss measurements (F_HAP007).

5.3.3 Scanning electron microscopy (SEM) analysis of $Ge_{20}Sb_{10}Se_{70}$ at. %, $Ge_{20}Sb_{10}Se_{67}S_{3}$ at. % SIF

Following the demonstration of low optical loss of the SIF, as shown in Figure 5.15, the final stage of investigation was to use SEM-EDX imaging and analysis, respectively, to investigate whether: 1) the fibre did indeed have a core/ cladding structure; 2) the final glass compositions were a close match to the nominal $Ge_{20}Sb_{10}Se_{70}$ at. % and $Ge_{20}Sb_{10}Se_{67}S_{3}$ at. % batched, and 3) what core-cladding ratio was eventually achieved.

Since the core and cladding glasses had similar compositions, backscattered electrons (BSE) were used during SEM, to image the SIF structure. As the investigated Ge-Sb-Se/S samples were cleaves taken from during the fibre loss measurements shown in Figure 5.15, fibres had little topological interest. Therefore, the superior sensitivity and surface resolution of secondary electron (SE) detection, was deemed to be of little advantage. BSE images not only detected electrons which had re-emerge from greater depths within the sample, they were also sensitive to the atomic mass of the nuclei from which they scattered. Therefore, heavier elements appeared brighter than the lighter elements as they were more efficient in their backscatter.

As a result, the cladding composition with 3 at. % S ($Ge_{20}Sb_{10}Se_{67}S_3$ at. %) was successfully detected *via* SEM in Figure 5.16, appearing slightly darker than the comparatively heavier $Ge_{20}Sb_{10}Se_{70}$ at. % core. The SIF presented in Figure 5.16 was the launch cleave used during the fibre loss measurements shown in Figure 5.15. From this BSE image, not only was the SIF structure confirmed, but so too was a large circular $Ge_{20}Sb_{10}Se_{70}$ at. % core. From 12 measurements taken round the edge of the BSE image, the cladding thickness was found to be 10.1 ±0.2 µm and only slightly offset to the top-right of Figure 5.16.

All SIF samples investigated using SEM, lacked any voids at the compositional boundary; however, there were several contamination marks as indicated by the dashed white circles in Figure 5.16. Although extra care was taken to protect the cleaved F_HAP007SIF fibre surfaces during SEM preparation (see section 3.5.5), samples were too fragile to be air dusted before viewing. Therefore, the majority of the defects shown in Figure 5.16 were most likely caused by small pieces of debris on the surface of the SIF (F_HAP007). Surfaces defects had an average size of 3± 1.5 µm and were found on the surface of both the core and cladding regions. Unfortunately, no chemical analysis was conducted on the contaminating debris seen in Figure 5.16 nonetheless, their darker appearance, under the backscattered electron mode, suggested that the surface defects had lower relative atomic mass than the glassy core and cladding matrices. Furthermore, when the defects were studied under the secondary electron mode, the foreign debris were clearly visible as light particles on the surface of the SIF cleave.

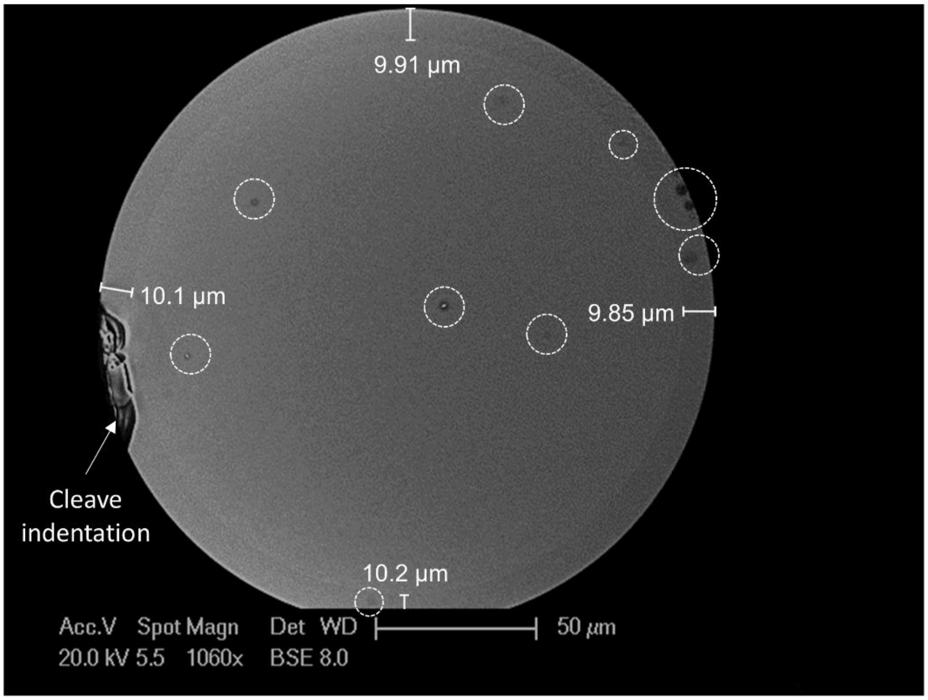

Figure 5.16: Scanning electron microscopy (SEM) image of co-extruded $Ge_{20}Sb_{10}Se_{70}$ at. % (core) and $Ge_{20}Sb_{10}Se_{67}S_3$ at. % (cladding) ~200 µm diameter fibre (F_HAP007). White dotted circles highlight sample contamination.

To investigate the quality of the SIF (F_HAP007) through the full ~8 m length of fibre used during fibre loss measurements (Figure 5.15), three more SEM samples were prepared for analysis using the backscattered electron mode. As well as the original launch fibre seen in Figure 5.17(a), the remaining samples were also taken from cleaves made during fibre loss measurements: (b) the best cleave from Group 1 (c) the first cleave from Group 2 and (d) the final cleave from Group 2. By choosing these cleaves for SEM analysis samples (a)-(d) were well spaced out, as demonstrated by the schematic diagram in Figure 5.17, *i.e.* providing a more reliable view of what the entire SIF would look like. The cleave from Group 1 (Figure 5.17(b)) was furthest from the launch end and had an averaged cladding thickness of 10.1 ±0.4 µm. The first cleave from Group 2 (Figure 5.17(c)) appeared approximately in the middle of the measured SIF, 3.5 m from the launch end, and had an average cladding thickness of 9.96 ±0.5 µm. The final cleave from

Group 2 (Figure 5.17(d)) was approximately 0.7 m from the launch end and had an average cladding thickness of 10.3 ±0.3 µm. Overall, the measurements taken along the ~8 m length of SIF showed that the cladding varied little in thickness as well as the total fibre diameter which had an average of 202.5 ±3.6 µm. Therefore, the core occupied ~95 % of the SIF (F_HAP007) for all samples investigated by SEM. Although this was a little larger than the 90 % intended core-cladding ratio, results had shown that the fabrication method was successful in producing SIFs, and that the section of preform taken from the co-extruded rod (Figure 5.13) did in fact produce fibres with a consistent ~95 % circular core.

Similar to the results seen in Figure 5.16, more surface defects (average diameter of 2 ±0.5 µm) were also observed on the surfaces of both the core and cladding regions of Group 1 and 2 SIF cleaves, even though this is only highlighted for the Group 2 (i) cleave in Figure 5.17 (c). Once again, no chemical analysis was conducted on the surface debris however, under the secondary electron SEM mode, surface defects were seen as separate light particles. However, there was a defect, marked by the asterisk (*) in Figure 5.17 (c), which appeared to be a small crack within the cladding of the SIF (F_HAP007) of length 2.6 µm. Since the thermal expansion coefficient for the $Ge_{20}Sb_{10}Se_{67}S_3$ at. % cladding glass could not be investigated using TMA (see section 5.2.2.4), there was always a concern that the core ($Ge_{20}Sb_{10}Se_{70}$ at. %, M_HAP011) and cladding ($Ge_{20}Sb_{10}Se_{67}S_3$ at. %, M_HAP013) glass compositions would introduce unfavourable residual stresses within the SIF, during the rapid cooling after fibre-drawing. However, no other cracks were observed on any of the other observed SIF (F_HAP007) cleaves and so, the surface defect seen in Figure 5.16 (c) was most likely a scratch introduced during sample handling and SEM preparation.

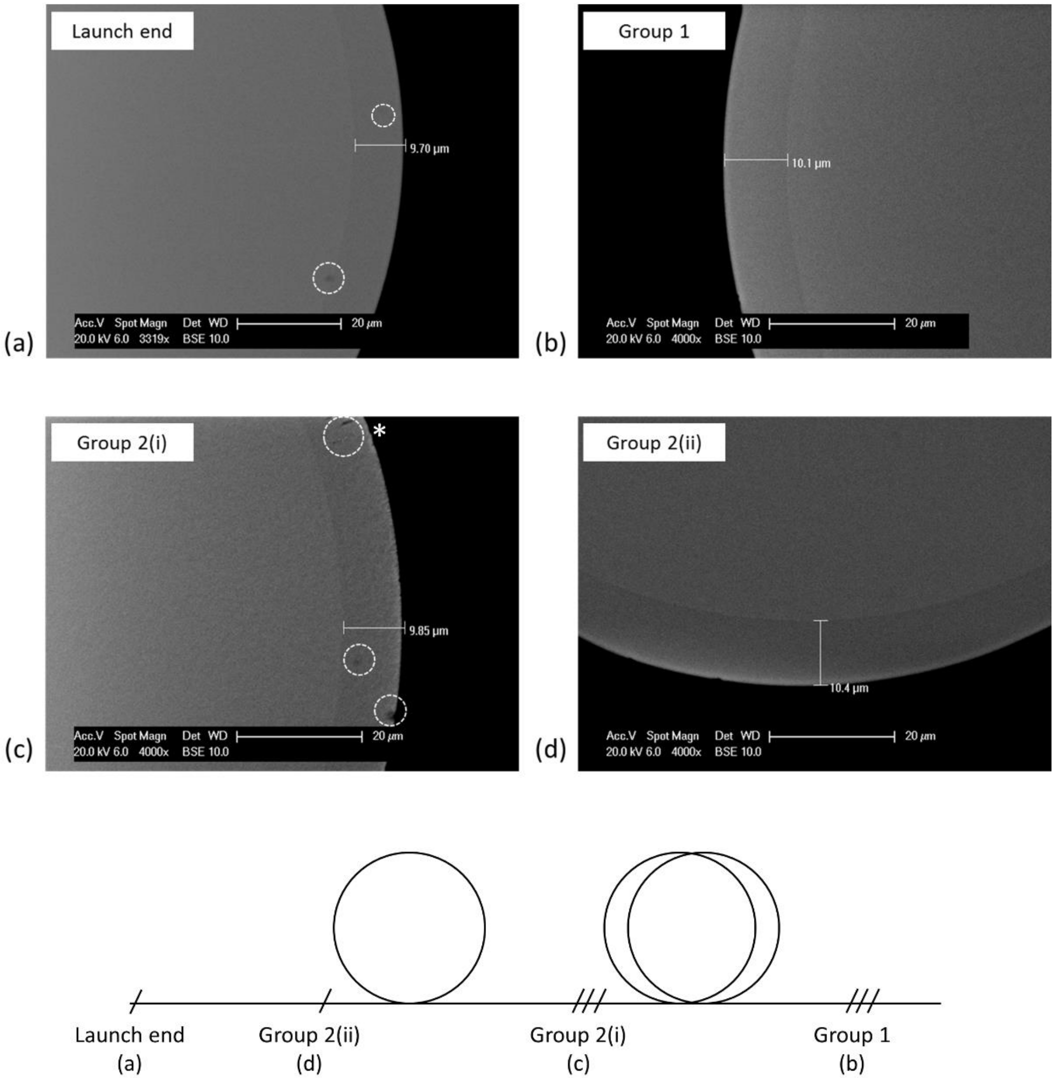

Figure 5.17: Scanning electron microscopy (SEM) images of cleaves made on the co-extruded (E_HAP006) $Ge_{20}Sb_{10}Se_{70}$ *at. % (core)* $Ge_{20}Sb_{10}Se_{67}S_3$ *at. % (cladding) SIF (F_HAP007), during fibre loss measurements (a)-(d). Schematic diagram shows where in the SIF the cleaves came from. Dashed circles highlight surface contaminants.*

The final stage of investigation used SEM-EDX to determine the compositions of both the core and cladding glasses. So far, results have shown that the nominal $Ge_{20}Sb_{10}Se_{70}$ at. % (core) (M_HAP011) and $Ge_{20}Sb_{10}Se_{67}S_3$ at. % (cladding) (M_HAP013) as-annealed glasses have successfully co-extruded together and subsequently produced stable SIF. These results alone show that the two glasses must have had a similar T_g, viscosity and TEC. However, to estimate the final NA of the drawn SIF and to confirm the glass' homogeneity, exact compositions had to be known.

As well as imaging the fibres in Figure 5.17 using backscattered electron SEM mode, each sample was also investigated using EDX. Using the K lines of S, Ge, and Se and the L line of Sb, Table 5.2 shows the measured EDX compositions, taken from point spectra, for each of the SIF samples imaged in Figure 5.17. From the launch end sample to the first cleave of Group 1, approximately 8 m in away, the compositions were relatively stable for both the core and cladding glasses. The Ge at. % was the most constant element for both compositions differing by no more than ±0.2 at. % across all measured samples. There was a slight variation in the Se-content, particularly within the cladding glass, as both the Launch end and Group 1 samples differed by 1.1 at. % Se to that of Group 2(ii). Nevertheless, due to the ±0.5 at. % error incurred for any elements heavier than O during EDX analysis, Table 5.2 showed that overall the achieved compositions of $Ge_{20.4}Sb_{10}Se_{69.6}$ ±0.5 at. % and $Ge_{20.4}Sb_{9.9}Se_{66.5}S_{3.2}$ ±0.5 at. % were close to the nominally batched core ($Ge_{20}Sb_{10}Se_{70}$ at. %) and cladding ($Ge_{20}Sb_{10}Se_{67}S_3$ at. %) glasses, respectively.

As such, the NA values calculated from the refractive index measurements of individual $Ge_{20}Sb_{10}Se_{70}$ at. % core (F_HAP003) and $Ge_{20}Sb_{10}Se_{67}S_3$ at. % cladding (F_HAP004) thin films, were an accurate representation of the final SIF. Therefore, at 3.1 µm wavelength, the $Ge_{20}Sb_{10}Se_{70}$ at. % core (M_HAP011) and $Ge_{20}Sb_{10}Se_{67}S_3$ at. % cladding (M_HAP013) step index fibre (SIF) (F_HAP007) presented in Figure 5.14, most likely had a NA of 0.25.

Table 5.2: Elemental analysis of $Ge_{20}Sb_{10}Se_{70}$ at. % core (M_HAP011) and $Ge_{20}Sb_{10}Se_{67}S_3$ at. % cladding (M_HAP013) step index fibre (SIF) (F_HAP007) using scanning electron microscopy-energy dispersive X-ray spectroscopy (SEM-EDX).

Sample from SIF (F_HAP007)	**Core /at. % (M_HAP011)**	**Cladding /at. % (M_HAP013)**
As-batched composition	$Ge_{20}Sb_{10}Se_{70}$	$Ge_{20}Sb_{10}Se_{67}S_3$
Launch end	$Ge_{20.4}Sb_{10.3}Se_{69.3}$	$Ge_{20.6}Sb_{10.2}Se_{66.0}S_{3.2}$
Group 1	$Ge_{20.5}Sb_{10.2}Se_{69.3}$	$Ge_{20.3}Sb_{10.2}Se_{66.0}S_{3.5}$
Group 2(i)	$Ge_{20.4}Sb_{9.6}Se_{70.0}$	$Ge_{20.4}Sb_{9.5}Se_{66.8}S_{3.3}$
Group 2(ii)	$Ge_{20.2}Sb_{9.7}Se_{70.1}$	$Ge_{20.2}Sb_{9.6}Se_{67.1}S_{3.1}$

Lastly, using elemental mapping in SEM-EDX, the homogeneity of the glasses was also confirmed in Figure 5.18(a)-(e). Using a collection time of ~15 mins, a section of the SIF launch end cleave showed that there was an even distribution of constituent elements across the cross-section of the fibre. Furthermore, through the SEM-EDX mapping technique, specifically for elemental S, the structure of the SIF could be clearly seen in Figure 5.18(b).

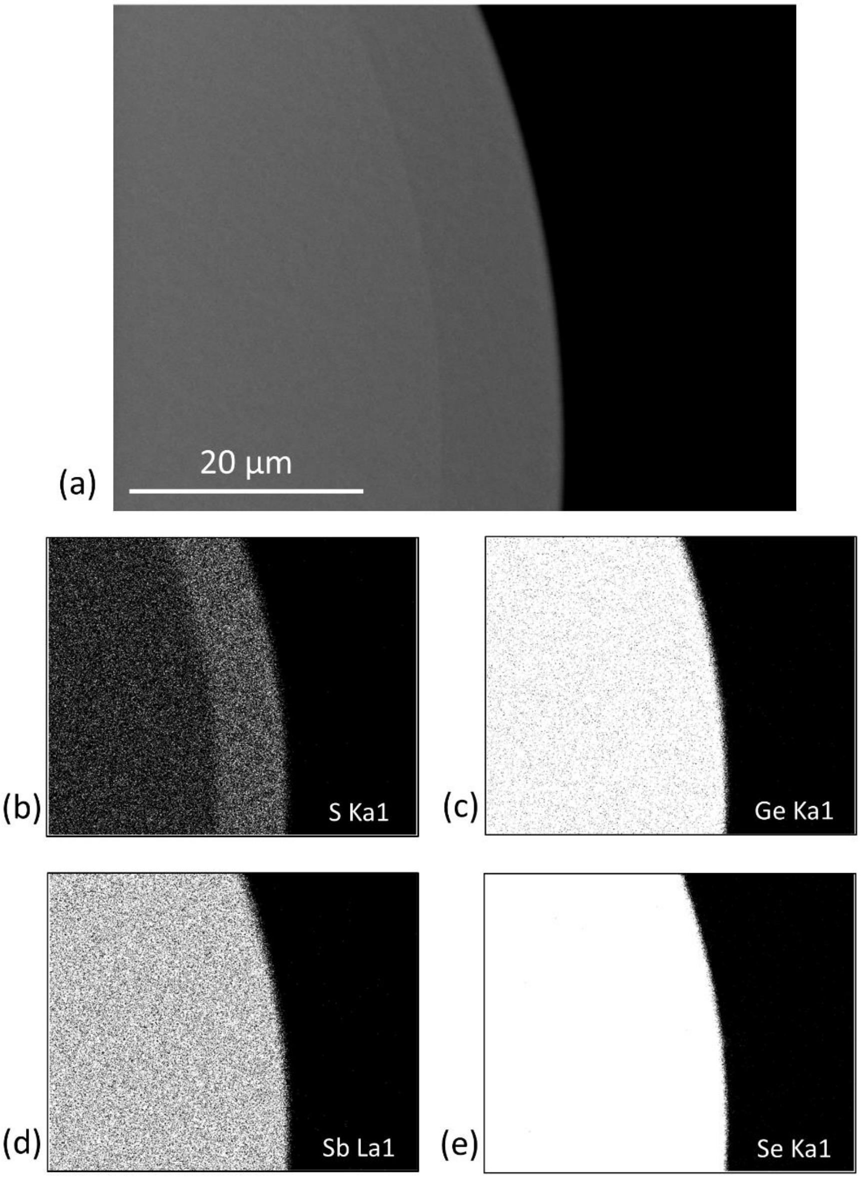

Figure 5.18: (a) Scamming electron microscopy (SEM) image of launch end cleave taken from the $Ge_{20}Sb_{10}Se_{70}$ *at. % (core, M_HAP011)* $Ge_{20}Sb_{10}Se_{67}S_3$ *at. % (cladding, M_HAP013) step index fibre (SIF) (F_HAP007). (b)- (e) show the energy dispersive X-ray spectroscopy (EDX) maps for each constituent element. Maps were collected over a ~15 min period.*

5.4 Chapter 5 summary

The main focus of this chapter, was to investigate two compositions from the Ge-Sb-Se/S glass systems, which could combine to produce low numerical aperture (NA) SIF for potential use in a MIR hyperspectral imaging probe. The most important points from chapter 5 are summarised below:

1) The prospective $Ge_{20}Sb_{10}Se_{70}$ at. % core glass was initially extruded into a 4.7 mm rod for TMA analysis.
    a. Using a parallel plate technique, viscosity-temperature curves of the $Ge_{20}Sb_{10}Se_{70}$ at. % core glass revealed that at a viscosity of $10^{7.5}$ Pa.s, the composition should be extruded at 274.7 ±0.4 °C and at a viscosity of $10^{4.5}$ Pa.s, the composition should be fibre-drawn at 357.8 ±0.7 °C.
    b. The thermal expansion coefficient (TEC) for the $Ge_{20}Sb_{10}Se_{70}$ at. % core glass was found to be 19.49 $\pm 10^{-6}$ /°C and the dilatometric softening point (M_g) was schematically measured as 217 ±2 °C.
2) For the prospective cladding glass, 3 at. % Se was substituted for 3 at. % S in the $Ge_{20}Sb_{10}Se_{70-x}S_x$ at. % system. As a novel chalcogenide composition, X-ray diffraction (XRD) initially confirmed the amorphicity of the powdered glass sample whilst, differential scanning calorimetry (DSC) revealed a glass transition temperature, T_g, at 224 ±2 °C. Although, 3 at. % substitution of Se for S had expected to increase the T_g by 3 ±1 °C, DSC results had shown a greater increase of 10 °C.
3) The prospective $Ge_{20}Sb_{10}Se_{67}S_3$ at. % cladding glass was also extruded into a 4.7 mm diameter rod for viscosity-temperature analysis. Unfortunately before the TEC could be investigated, the TMA (Perkin Elmer TMA-7) had stopped working. However, using a parallel plate technique, the viscosity-temperature curves of the $Ge_{20}Sb_{10}Se_{67}S_3$ at. % cladding glass revealed that for a viscosity of $10^{7.5}$ Pa.s, the composition should be extruded at 277.7 ±0.4 °C and for a viscosity of $10^{4.5}$ Pa.s, the composition should be fibre-drawn at 361.9 ±0.3 °C. With a core $Ge_{20}Sb_{10}Se_{70}$ at. % and cladding $Ge_{20}Sb_{10}Se_{67}S_3$ at. %temperature difference of 3 °C and 4 °C between the extrusion ($10^{7.5}$ Pa.s) and fibre-drawing ($10^{4.5}$ Pa.s) viscosities, respectively, results from the TMA viscosity-temperature investigation suggested both composition would successfully co-extrude and fibre-draw together.

4) This assumption was confirmed when the $Ge_{20}Sb_{10}Se_{70}$ at. % core and $Ge_{20}Sb_{10}Se_{67}S_3$ at. % cladding glasses were co-extruded, at 267±0.1 °C, and then fibre-drawn to a 200 ±5 µm diameter SIF. Optical fibre loss measurements, conducted on an 8 m length of 200 ±5 µm diameter SIF, found the lowest baseline loss of 0.75 dB/m at 6.06 µm wavelength whilst, also demonstrating successful MIR light-guiding in the $Ge_{20}Sb_{10}Se_{70}$ at. % core. Using SEM, backscattered electron images showed a high quality interface between the large circular $Ge_{20}Sb_{10}Se_{70}$ at. % core and the $Ge_{20}Sb_{10}Se_{67}S_3$ at. % cladding, lacking any voids, and revealed a core-cladding ratio of 95 %. Furthermore, SEM-EDX analysis confirmed the core as $Ge_{20.4}Sb_{10}Se_{69.6}$ ±0.5 at. % and the cladding as $Ge_{20.4}Sb_{9.9}Se_{66.5}S_{3.2}$ ±0.5 at. % which were both close to the nominally batched $Ge_{20}Sb_{10}Se_{70}$ at. % and $Ge_{20}Sb_{10}Se_{67}S_3$ at. %, respectively. Based on the FTIR thin film measurements, conducted by Mr Y Fang, this suggested that at a wavelength of 3.1 µm, the SIF had an NA of 0.25, where the $Ge_{20}Sb_{10}Se_{70}$ at. % core had a refractive index of 2.55 and the $Ge_{20}Sb_{10}Se_{67}S_3$ at. % cladding had a refractive index of 2.54.

Chapter 6: High purity Ge-Sb-Se glasses *via* distillation

Following the successful fabrication of a $Ge_{20}Sb_{10}Se_{70}$/ $Ge_{20}Sb_{10}Se_{67}S_3$ at. % (atomic %) core/cladding step index fibre (SIF) shown in chapter 5, the next stage of research focussed on improving the purity of the $Ge_{20}Sb_{10}Se_{70}$ at. % core which in turn would improve the mid-infrared (MIR) window. As discussed in section 2.3.2, chalcogenide glasses suffer from several impurity absorptions across the MIR spectral region, primarily from oxygen, hydrogen and carbon[8, 93]. Even with an initial bake-out purification (see section 3.3.4.1) of the 99.999 to 99.9999 % pure starting elements, large absorptions bands were still present within the final optical fibre loss spectra of Ge-Sb-Se/S glass fibres shown in sections 4.2 and 5.2.2.5.

This chapter is split into three sections. In section 6.1, the current bake-out purification temperatures, used for Se, Sb and S starting elements, are evaluated using the Antoine equation[105] to ensure that the initial precursor purification is at its optimum. Then, to reduce significantly impurity absorptions in the core $Ge_{20}Sb_{10}Se_{70}$ at. % composition, the development of a successful distillation procedure, with both oxygen and hydrogen getters, is reported in section 6.2. The final optical loss spectra for a high-purity $Ge_{20}Sb_{10}Se_{70}$ at. % un-cladded fibre is then presented and discussed in section 6.3.

6.1 Purification of batch components

As described in Table 3.6, the initial bake-out temperatures used for Se, Sb, and S were 260 °C, 570 °C and 140 °C, respectively. This preliminary purification worked on the principle that the more volatile impurity species would be removed from the surface of the starting precursors, whilst the less volatile, pure-elements would remain (see section 3.3.4.1) within the purification, silica glass ampoule. The Antoine equation (see Equation 2.5), derived from the Clausius-Clapeyron relation[105], can be used to describe the relationship between vapour pressure and temperature for pure components. Using Yaws[200] data, Antoine coefficients for A, B, and C, and their respective temperature boundaries, were taken for relevant precursors used in the Project and are presented in Table 6.1.

Table 6.1: Antoine coefficients for pure elements relevant to this Project. The minimum (MIN) and maximum (MAX) temperatures indicate the temperature boundary given in 'Yaws Handbook of Vapor Pressures: Antoine Coefficients'[200].

Pure element	**Antoine constant**			**Temperature /°C**	
	A	**B**	**C**	**MIN**	**MAX**
Se	7.05403	3441.9628	139.77	123.85	685
SeO_2	18.01392	11598.1403	451.41	115	335
Sb	5.88125	4984.6752	74.32	343.85	1587
Sb_2O_3	4.06652	1464.9462	-189.49	400	1550
S	7.8663	3464.98	250.341	115.21	1039.85
SO_2	7.33311	1013.46	237.647	-75.48	157.6

By substituting these A, B and C coefficients into the Antoine equation (equation 2.5), resulting vapour pressure-temperature curves are discussed in sections 6.1.1 to 6.1.3, to investigate whether or not the initial temperatures presented in Table 3.6, are the most appropriate for the bake-out purification of Se, Sb and S.

6.1.1 Selenium purification *via* bake-out procedure

In Figure 6.1, two temperature-vapour pressure curves are presented for pure substances of elemental Se and SeO_2. As initially advised, from the experience of senior members of the Mid-infrared Photonics Group, Se was baked in the as-prepared silica glass melting ampoule at 260 °C for 0.5 h, prior to the batching of Sb and Ge. Figure 6.1 shows that at 260 °C there was a relatively large difference in the vapour pressures between Se (0.003 kPa) and SeO_2 (6.85 kPa) suggesting that this was indeed, an appropriate temperature at which to remove SeO_2 from the surface of as-received Se (99.999 %, Materion). Furthermore, in a recent publication by Tang *et al*.[116] the use of a similar 270 °C Se bake-out temperature, which preceded the double distillation of a $Ge_{10}As_{21}Se_{69}$ at. % glass, ultimately gave a record ultra-low optical loss of 83-90 dB/km across 5.6-6.8 μm wavelength region.

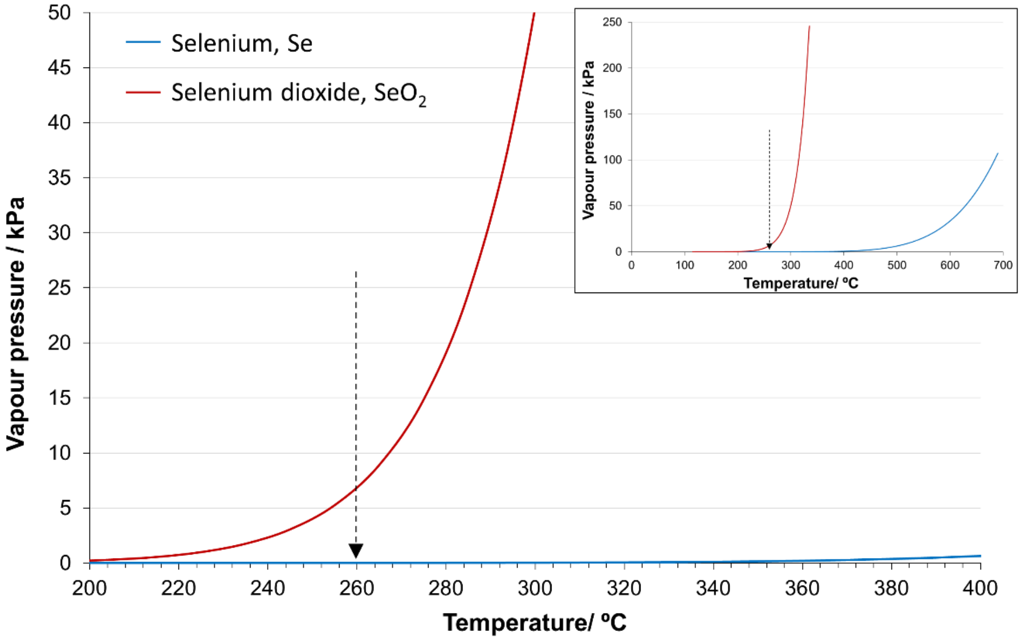

Figure 6.1: Comparison of the vapour pressures between selenium (Se) and selenium dioxide (SeO_2) between 0 °C to 400 °C. Insert shows the full temperature range between 200 °C to 700 °C. Dashed arrows indicate the temperature used for Se bake-out investigation.

6.1.2 Antimony purification *via* bake-out procedure

Whereas the as-received Se (Materion, 99.999 %) was purified by a 30 min dwell held at 260 °C during the bake-out procedure, it was shown in Table 3.6 that the as-received Sb (Cerac, 99.9999 %) had a much longer dwell for 3 hrs at 570 °C. This additional purification time proved necessary as demonstrated by the Antoine temperature-vapour pressure calculations for pure substances of Sb and Sb_2O_3, shown in Figure 6.2.

Although elemental Sb had a similar vapour pressure of 0.002 kPa (at 570 °C) to that of elemental Se (0.003 kPa at 260 °C), there was a significant difference between the calculated vapour pressures of their respective oxides. At 570 °C Sb_2O_3 had a vapour pressure of 0.220 kPa (Figure 6.2) whereas, SeO_2 had a vapour pressure of 6.85 kPa at 260 °C (Figure 6.1). Hence, a longer dwell at 570 °C was indeed appropriate for the sublimation of Sb_2O_3 from the surface of elemental Sb under a flowing vacuum. Furthermore, with two orders of magnitude difference between the vapour pressures of Sb and Sb_2O_3 (0.002 kPa and 0.220 kPa) at 570 °C, a 3 hour dwell should have provided an optimal environment for the purification of Sb *via* the sublimation of surface Sb_2O_3.

Nevertheless, a second bake-out temperature was proposed, as marked by (2) in Figure 6.2, to see whether or not an increase to 700 °C could improve the purity of the as-received Sb. Since the calculated vapour pressures of Sb and Sb_2O_3 at 700 °C were 0.037 kPa and 2.10 kPa, respectively, it was decided that the bake-out dwell would be reduced from 3 hrs (see Table 3.6 (a)) to 1 hr for an initial investigation.

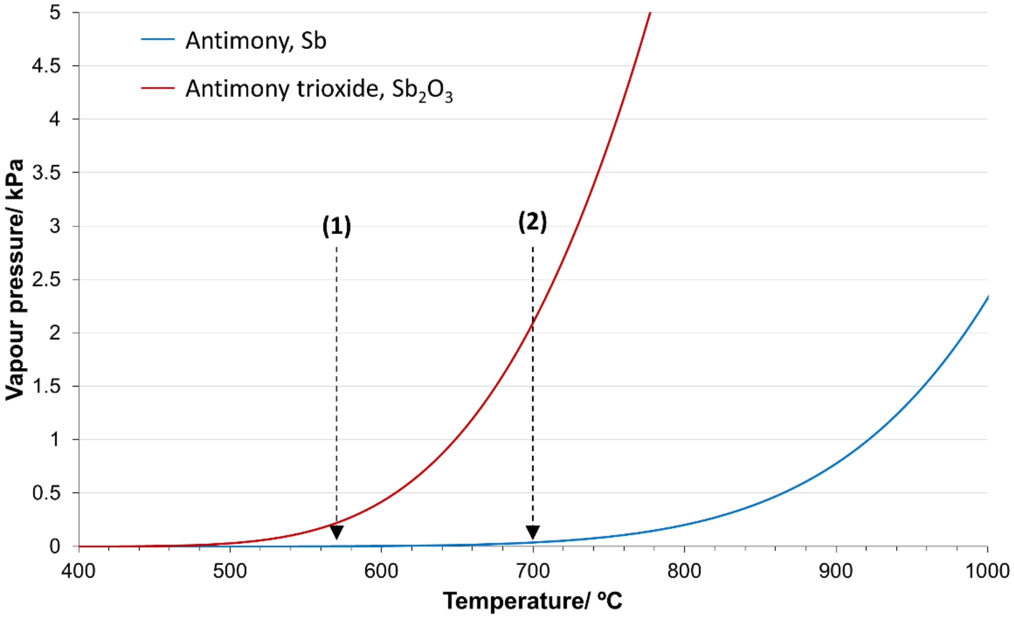

Figure 6.2: Comparison of the vapour pressures between antimony (Sb) and antimony-trioxide (Sb_2O_3) between 400 °C to 1000 °C. Dashed arrows indicate the two temperatures used for Sb bake-out investigation (1) at 570 °C.

As a visual comparison, the results of a typical ~15 g Sb (99.9999 %, Cerac) bake-out at 570 °C can be seen in Figure 6.3. Prior to purification, the as-received Sb had a dull, grey appearance, as demonstrated by the image in Figure 6.3 (a). Then, after a 3 hr dwell at 570 °C, the purified Sb had a shiny, silver appearance, as shown in Figure 6.3 (b). This colour change reflected the sublimation of impurities from the surface of elemental Sb, which were then deposited on the surface of the inner silica glass tube (7/9 mm diameter), near to where the top of the small tube furnace (in-house made, ID=28 or 38 mm) was raised to (Figure 6.3 (c)).

It was also shown in Figure 6.3 (c), that small droplets of, what looked like, elemental Sb had also condensed on a section of the inner wall of the silica glass ampoule (10/14 mm diameter), within the small tube furnace during purification. Not only did this highlight the expected, but inconsistent, temperature profile within the small tube furnace (see section 3.3.4.1), it also demonstrated the volatility of Sb, even at a relatively low bake-out purification temperature of 570 °C. Hence compounding the decision to reduce the bake-out dwell time during a second 700 °C purification investigation.

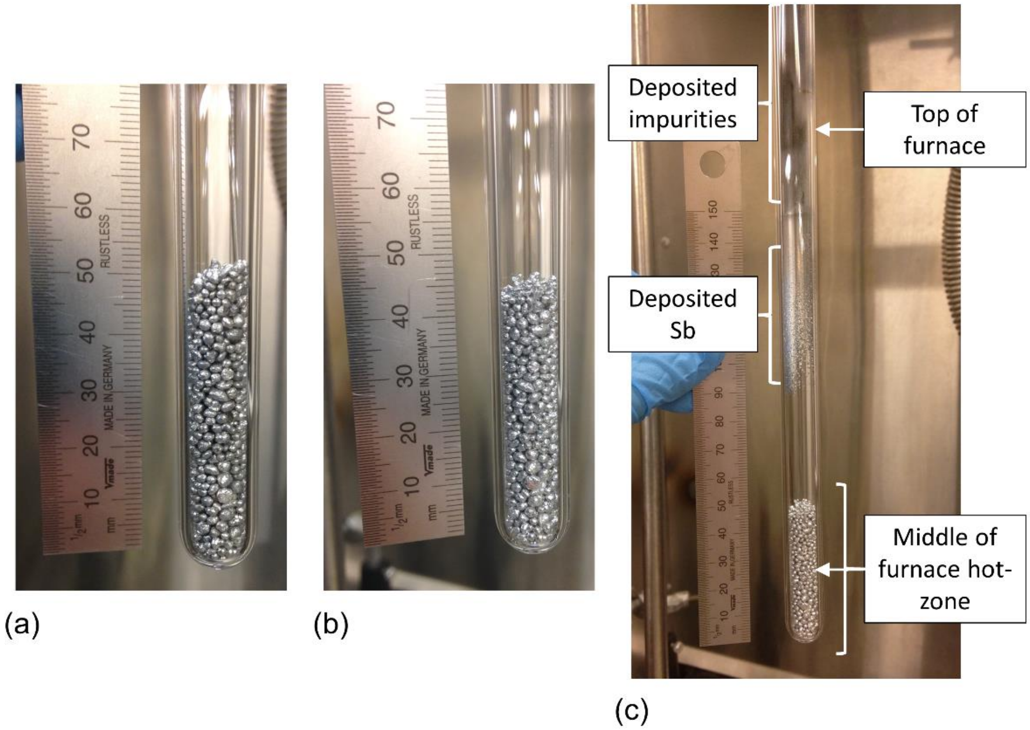

Figure 6.3: Photograph of (a) as-received Sb batched into a silica glass ampoule prior to purification and (b) purified Sb after a 0.5 h dwell at 570 °C. (c) The whole of the silica glass ampoule, post-bake-out, with annotations indicating the position of the small tube furnace (in-house made, ID=28 or 38 mm) during the bake-out procedure.

Whereas, the purified Sb shown in Figure 6.3, subsequently went on to make two ~30 g Ge-Sb-Se glasses, less Sb was required for a single investigation into the purification of Sb at 700 °C. Therefore, only ~5 g was batched into a silica glass ampoule (10/14 mm diameter).

However, as shown in Figure 6.4, following a 1 hr dwell at 700 °C, no material had been left at the bottom of the silica glass ampoule. Instead, both the impurities and the elemental Sb had vaporised and condensed at varying points along the inner surface of the silica glass ampoule (10/14 mm diameter) or inner silica glass tube (7/9 mm diameter). Similar to the 570 °C results seen in Figure 6.3 (c), the impurities baked at 700 °C were seen to condense beyond the top of the small tube furnace whilst elemental Sb condensed just below the top of the furnace (see Figure 6.4 (a)).

Enlarged regions of the resultant purification (as indicated by the dashed boxes in Figure 6.4 (a)) can be seen in Figure 6.4 (b) and (c). Although it was initially thought that all the material had left the bottom on the silica glass ampoule, trace amounts of a black deposit, which could have been carbon, were seen within the dashed circle of Figure 6.4 (c). At the very least, this suggested that Sb would be suitable for distillation.

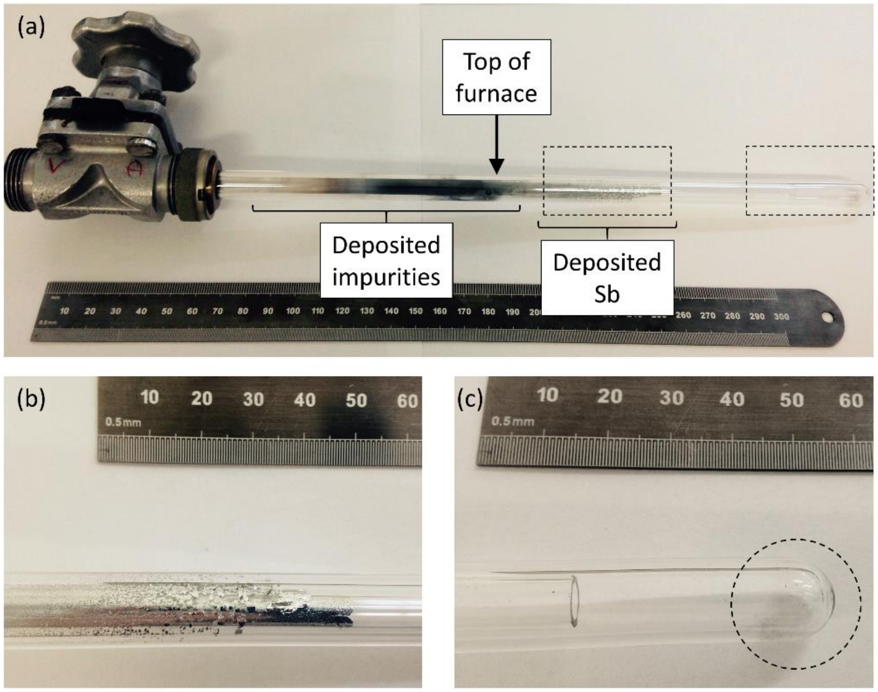

Figure 6.4: (a) Photo of Sb purification ampoule following an hour at 700 °C under vacuum. Images (b) and (c) show enlarged regions of the Sb-ampoule, as indicated by the boxes in (a).

Overall, investigations into the purification of Sb *via* a bake-out procedure, revealed that a ‘lower and slower’ approach was most successful. That is to say, that even though there was a greater difference in vapour pressures between elemental Sb and Sb_2O_3 at 700 °C (Figure 6.2), a 3 hr dwell at 570 °C was more appropriate than a 1 hr dwell at 700 °C.

6.1.3 Sulfur purification *via* bake out procedure

The calculated temperature-vapour pressures curves, shown in Figure 6.5, revealed that S and SO_2 had the greatest difference in vapour pressure, out of the three elements studied thus far. By purifying the S at 140 °C (as directed in Table 3.6 (d)), it was calculated that elemental S would have a vapour pressure of 0.013 kPa and SO_2 would have a vapour pressure of 5948.3 kPa.

However, it is known that sulfur trioxide (SO_3) and hydrogen sulfide (H_2S)[102] were also possible contaminants of the elemental sulfur. Since both impurities are gases at room temperature and pressure, they were likely to be lost in the same manner as the SO_2 contaminant, under the same temperature and pressure conditions.

Nevertheless, it has also been shown by Sanghera *et al.*[83] that it was necessary to vacuum distil sulfur five times before the impurity content was sufficiently reduced. Therefore, even though the vapour pressure of SO_2 was shown to be far greater than the vapour pressure of elemental S at 140 °C in Figure 6.5, purifying S *via* a bake-out procedure may not be the most appropriate technique (discussed in more detail in section 8.2). This assumption was supported by the large 42.0 dB/m S-H absorption band seen at 4.04 µm during the fibre loss measurements of $Ge_{20}Sb_{10}Se_{67}S_3$ at. % (F_HAP004) when only 3 at. % of S, which had been baked at 140 °C for 25 mins, substituted 3 at. % of Se (see Figure 5.15).

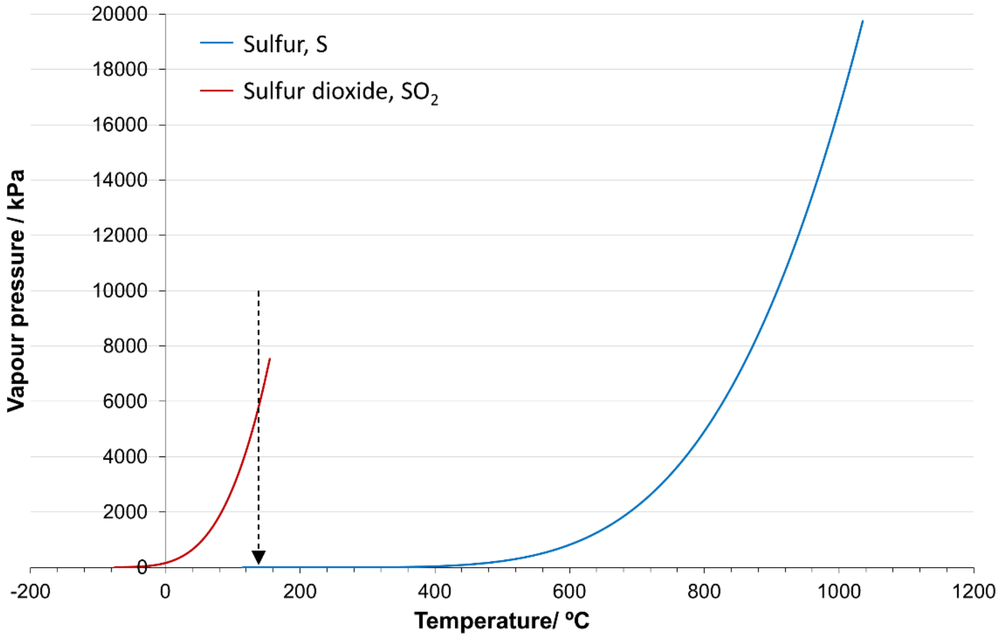

Figure 6.5: Comparison of the vapour pressures between sulfur (S) and sulfur dioxide (SO_2) between -75 °C to 1200 °C. Dashed arrow indicate the temperature used for S bake-out investigation.

6.1.4 Germanium purification *via* bake-out procedure

It was mentioned in section 3.3.4.1, that unlike Se, Sb and S, as-received Ge (99.999 %, Materion) was not purified *via* a bake-out procedure but was instead batched straight into the as-prepared silica glass melting ampoules. Whereas all the other elements, discussed in sections 6.1.1 to 6.1.3, had been shown to exhibit a distinctly lower vapour pressure than their oxide counterparts over an accessible temperature range, analogous purification of the elemental Ge precursor is technically more difficult. This is because the elemental Ge and the Ge oxides have low, and similar, vapour pressures, even up to high temperatures[190, 201]. For example, at 875 °C Ge has a vapour pressure of ~0.5 x10^{-8} kPa and at 600 °C GeO has a vapour pressure of ~0.06 kPa[190].

If elemental Ge was to be purified *via* the bake-out method, it would have to be held at 900 °C for an extended amount of time[202]. However, 900 °C is close to the normal melting point of pure elemental Ge (938.2 °C at 1 atm (1.015 x 10^5 Pa))[203] and, since impurities tend to lower the melting point, this high temperature bake-out would only exacerbate the problem of Ge and Ge-oxide vapour separation. Furthermore, too long heating of elemental Ge at 900 °C would also risk delivering hydride and hydroxide impurities from the silica glass wall of the containment, which would further contaminate the elemental Ge[102].

6.1.5 Precursor purification overview

Overall, the vapour pressure-temperature curves, calculated using the Antoine equation, have shown that the initial bake-out temperatures and dwell times (presented in Table 3.6), were suitable for the separation of SeO_2, Sb_2O_3 and SO_2 impurity vapours from their corresponding, elementally pure chemicals. Therefore, whether or not the resulting precursors went on to be distilled, this primary purification (outlined fully in section 3.3.4.1) was more or less at its optimum.

6.2 Distillation of $Ge_{20}Sb_{10}Se_{70}$ at. % core glass

Building on the Ge-Sb-Se glass distillation reports presented in section 2.4.4, the next stage of research focussed on the single distillation of the core $Ge_{20}Sb_{10}Se_{70}$ at. % glass with both [H] and [O] getters.

6.2.1 Preliminary bent tube investigation (D_HAP001)

Since there are very few reports in the literature on the distillation of Ge-Sb-Se glasses[54, 112, 113], an initial experiment was setup in which ~2.8 g of as-annealed $Ge_{20}Sb_{10}Se_{70}$ at. % glass (M_HAP005) was batched, under ambient room atmosphere, into an in-house bent 10/14 mm diameter silica glass ampoule and then sealed. With no additional getters present in the sealed silica glass ampoule, the aim of this investigation was to see whether or not $Ge_{20}Sb_{10}Se_{70}$ at. % glass would distil and, if so, what critical temperatures should be used for subsequent high-purity distillations. As this was an initial trial, the silica glassware was not pre-baked under vacuum.

In Figure 6.6 (a) and (b) the sealed silica glass bent ampoule, along with its as-annealed $Ge_{20}Sb_{10}Se_{70}$ at. % batched glass contents, can be seen before and after distillation, respectively. Whereas, the schedules of the more complex distillations discussed in sections 6.2.2 to 6.2.4 will be documented in the appendices, the relatively simple distillation programme used for D_HAP001 in a two-zone furnace (Instron, TF1798, tube ID 86mm), is shown in Table 6.2. Although current literature[113] has provided some insight into the amounts of getters that should be used during distillation (*e.g.* 700 ppm wt. Al and 1000 ppm wt. $TeCl_4$), reports show very little information regarding distillation temperatures. Therefore, once again based on the experience of the Mid-infrared Photonics Group, it was initially decided that the charged end of the bent silica glass ampoule (Figure 6.6 (a)) would be gradually increased to 850 °C, at a rate of 100 °C/hr, followed by a 4 hr dwell at 850 °C (Zone 2, step 2 and 3 in Table 6.2). At the same time, the distillate end of the bent silica glass ampoule would be increased to 450 °C, at a rate of 100 °C/hr, and dwell for 8 hr at 450 °C (Zone 1, step 2 and 3 in Table 6.2).

Using this temperature programme, results shown in Figure 6.6 (b), revealed that~2.8 g of the $Ge_{20}Sb_{10}Se_{70}$ at. % glass, did indeed successfully distil when the charge end of the bent silica glass ampoule was ramped up to 850 °C.

However, it was also shown in Figure 6.6 (b), that the distilled material began to condense just before the bend in the silica glass ampoule, rather than at the distillate end, where it was most cool (450 °C). Furthermore, the distilled material seemed to condense into several forms, as depicted by the orange and metallic-grey deposits in Figure 6.6 (b). This observation shall be discussed in more detail, later in this section.

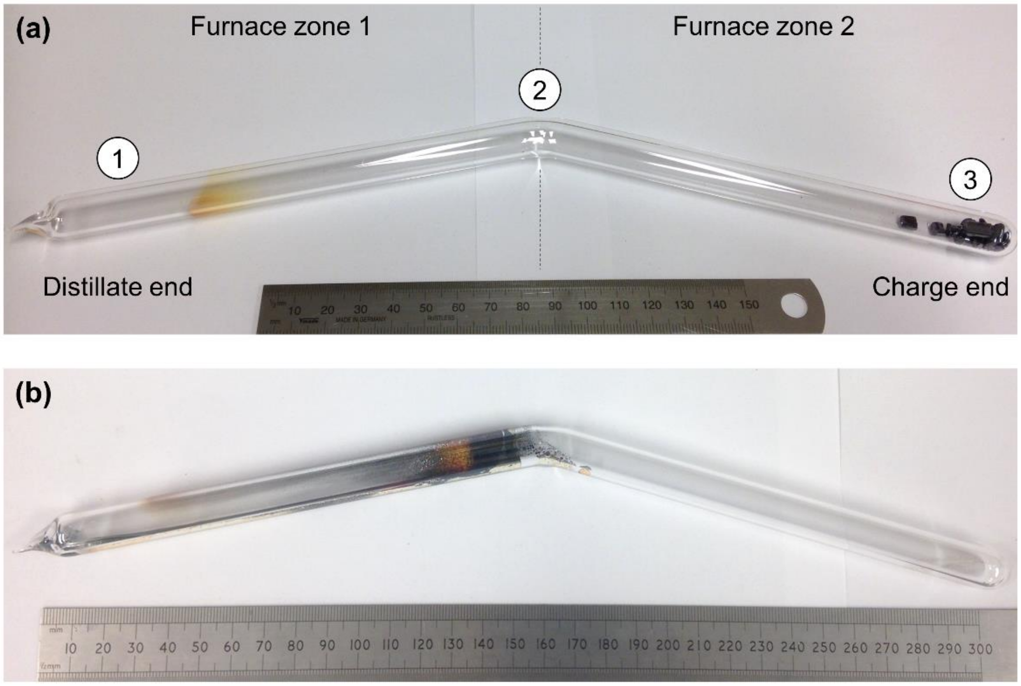

Figure 6.6: Photograph of the sealed, bent silica glass ampoule, containing the batched $Ge_{20}Sb_{10}Se_{70}$ at. % glass (M_HAP005), before (a) and after (b) distillation (D_HAP001). Circled numbers in (a) show the position of three thermocouples.

Table 6.2: Distillation schedule for the as-annealed $Ge_{20}Sb_{10}Se_{70}$ at. % glass (D_HAP001), batched in a bent silica glass ampoule, under room atmosphere.

Step	**Two-zone furnace schedule**	
	Distillate end (Zone 1)	**Charge end (Zone 2)**
1	Step to 20 °C	Step to 20 °C
2	Ramp to 450 °C @ 100 °C/hr	Ramp to 850 °C @ 100 °C/hr
3	Dwell at 450 °C for 8 hrs	Dwell at 850 °C for 4 hrs
4	End	End

Using Pico Technology logging software, the overall recorded temperatures for the distillation of as-annealed $Ge_{20}Sb_{10}Se_{70}$ at. % glass (D_HAP001), are shown in Figure 6.7. Aptly reflecting the temperature schedule outlined in Table 6.2, after ~15500 s (4.3 hrs) thermocouple 1, found at the distillate end of the bent silica glass ampoule, was the first to plateau at 445 °C. Then after ~30500 s (8.5 hrs) both thermocouple 2 (link tube) and thermocouple 3 (charge end) plateaued at 712 °C and 835 °C, respectively. Based on the temperature reading from thermocouple

2, it could therefore be assumed, that the deposited material found near the bend in the silica glass ampoule (Figure 6.6 (b)), condensed just below 712 °C.

However, an even more significant observation was seen just after ~25200 s (7 hrs), where there was an abrupt increase in temperature (629 °C) at thermocouple 2 and a slight decrease in temperature at thermocouple 3 (706 °C). This phenomenon was thought to echo a mass transfer of material from the charged end of D_HAP001, through to the distillate end. If correct, this would imply that the as-annealed $Ge_{20}Sb_{10}Se_{70}$ at. % glass, distilled at a temperature close to 706 °C.

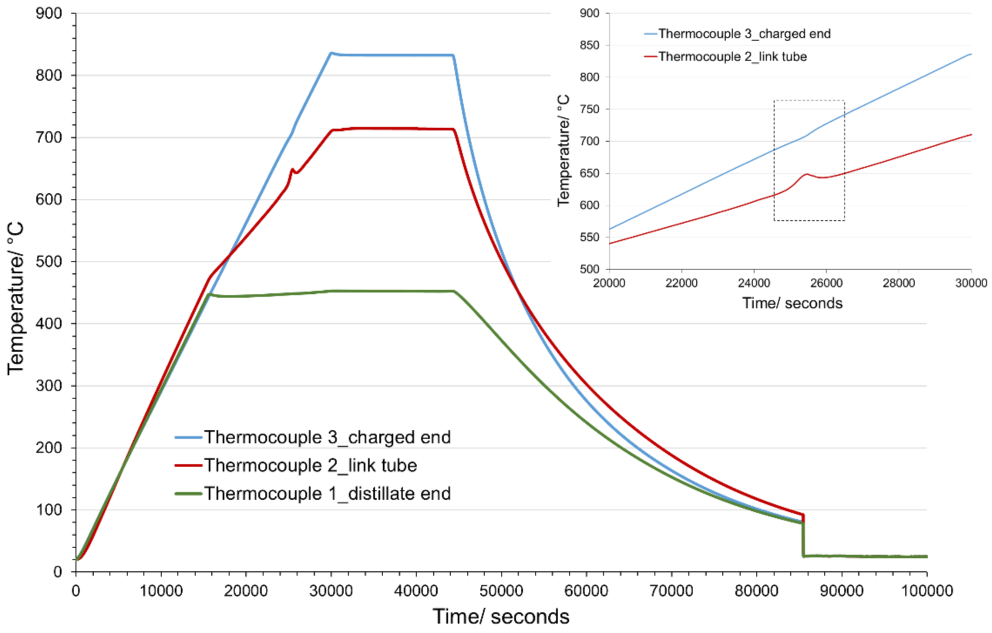

Figure 6.7: D_HAP001 temperature data logged by PLW software for the as-annealed $Ge_{20}Sb_{10}Se_{70}$ at. % glass (M_HAP005) in a bent silica glass ampoule. Inset shows an enlarged region of thermocouple 2 and 3, between 20000 and 30000 seconds.

Enlarged regions of Figure 6.6 (b), are shown in Figure 6.8. Following the successful distillation of ~2.8 g of $Ge_{20}Sb_{10}Se_{70}$ at. % glass, a black deposit was first observed around the inner silica glass surface at the charged end of D_HAP001 (Figure 6.8 (a)). Similar to the Sb-purification results at 700 °C (Figure 6.4 (c)), it was possible that this remaining deposit was carbon. However, there was no direct evidence of that.

Once the bent silica glass ampoule of D_HAP001 had been opened, it was found that there were three main deposits. The first of these was a silvery, globular-like deposit that had condensed just before the bend in D_HAP001 and is labelled as (1) in Figure 6.8 (b) and (c). The second deposit was found just after the bend and had the largest mass with a dark, metallic grey appearance. Concealed by a thin orange/black crystal-like deposit, the location of the second deposit is highlighted by the (2) in Figure 6.8 (b) and (c). The third and final deposit appeared to have had a lower viscosity and as such, had run down the distillate side of the bent silica glass ampoule, before solidifying; shown by (3) in Figure 6.8 (d).

All three deposits had a distinct appearance and seemed to resemble each of the consistent elements making up the initial as-annealed $Ge_{20}Sb_{10}Se_{70}$ at. % glass. Therefore, SEM-EDX was used to analyse the composition of each deposit.

The three deposits are described in detail in the following sub-sections: 6.2.1.1, 6.2.1.2 and 6.2.1.3, respectively.

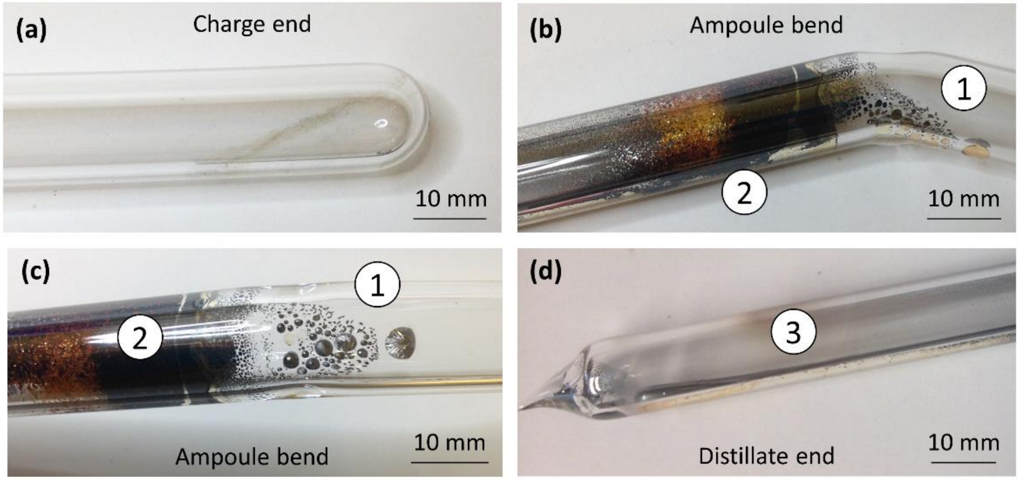

Figure 6.8: Enlarged regions of D_HAP001 post distillation, showing: (a) the charge end, (b) and (c) the linking bend and (c) the distillate end. Circled numbers highlight three main deposits of the distilled $Ge_{20}Sb_{10}Se_{70}$ at. % glass.

6.2.1.1 Deposit 1 of D_HAP001

As depicted in Figure 6.9 (a) and (b), back scattered electron SEM images of deposit 1, showed no compositional variance across the spherical sample, taken just before the bend of the silica glass distillation ampoule (Figure 6.8 (c) deposit (1)). With a similar appearance to elemental Sb, three EDX point spectra (shown in Figure 6.9 (c)) confirmed the deposit's identity as $Sb_{40.1}Se_{59.9}$ at. %. As an example, the elemental spectrum of EDX point 3 is also shown in Figure 6.9 (d); although very similar, spectra from points 1 and 2 (Figure 6.9 (c)) are not shown.

Therefore, SEM-EDX analysis had shown that a large proportion of the Sb that was initially homogenised in the $Ge_{20}Sb_{10}Se_{70}$ at. % glass, had condensed in the form of the stoichiometric phase: Sb_2Se_3, just before the bend in D_HAP001. Although there is not enough evidence to suggest what temperature the Sb_2Se_3 first condensed at, its presence at the end of the distillation programme (Table 6.2) had confirmed that it remained in this Sb_2Se_3 form throughout the ~4 hr dwell at ~712 °C.

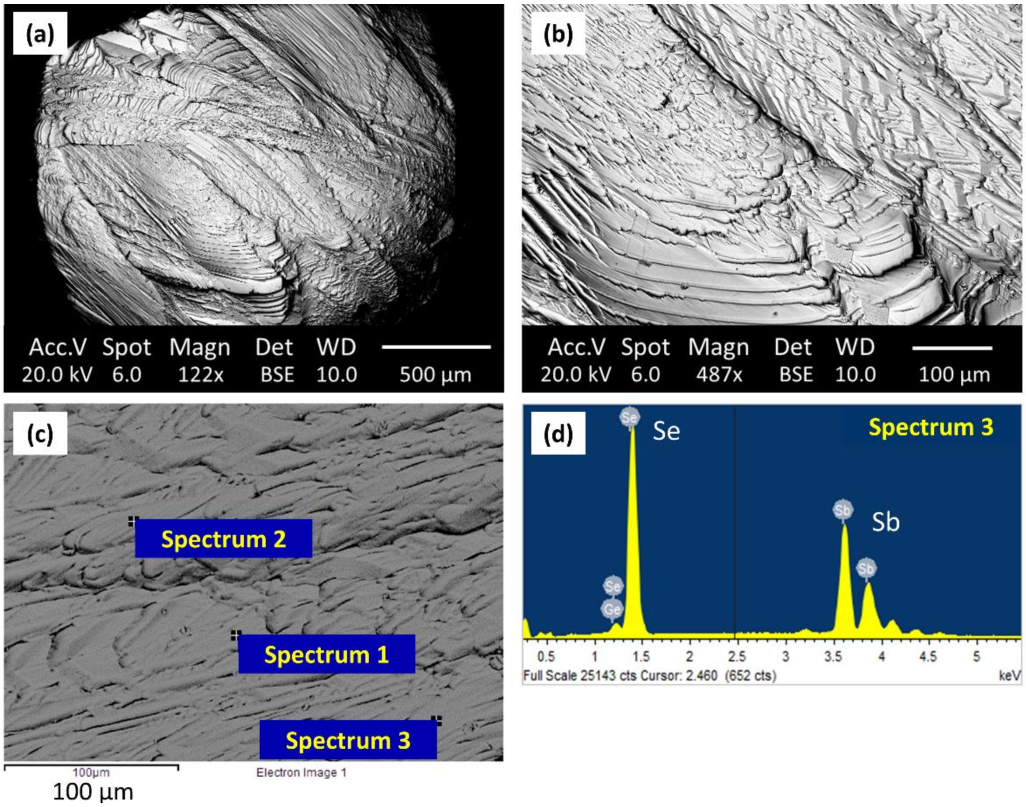

Figure 6.9: (a) Scanning electron micrograph (SEM) of deposit 1 from the bent silica glass ampoule distillation of $Ge_{20}Sb_{10}Se_{70}$ at. % glass (D_HAP001), with an enlarged region shown in (b). The three energy dispersive X-ray spectroscopy (EDX) points used to calculate the composition of the deposit are shown in (c) with spectrum 3 shown in (d) as an example.

6.2.1.2 Deposit 2 of D_HAP001

In Figure 6.10, the SEM images of deposit 2, which was found just after the bend in D_HAP001 (Figure 6.8) after the distillation of as-annealed $Ge_{20}Sb_{10}Se_{70}$ at. %

(M_HAP005), are shown. Whereas the analysis of deposit 1 (section 6.2.1.1), had found a single composition of Sb_2Se_3, the SEM-EDX analysis of deposit 2, was a little more complex as two compositional regions were identified using the BSE detector within the one deposit (Figure 6.10 (c)).

As an additional investigation, the benefit of analysing all of the deposited samples from D_HAP001 using the back scattered electron detector, is demonstrated in Figure 6.10 (a) and (b). Here, two images of the same sample are shown with firstly the secondary electron detector (Figure 6.10 (a)) and secondly the backscattered electron detector (Figure 6.10 (b)) in use. As predicted, the secondary detector was able to give a superior topological image however, the two compositional regions within deposit 2 were only seen when the backscattered electron detector was used.

Thus, at a higher magnification, EDX analysis was conducted on a backscattered electron image seen in Figure 6.10 (c), where three EDX points were investigated both within the lighter and darker regions of deposit 2.

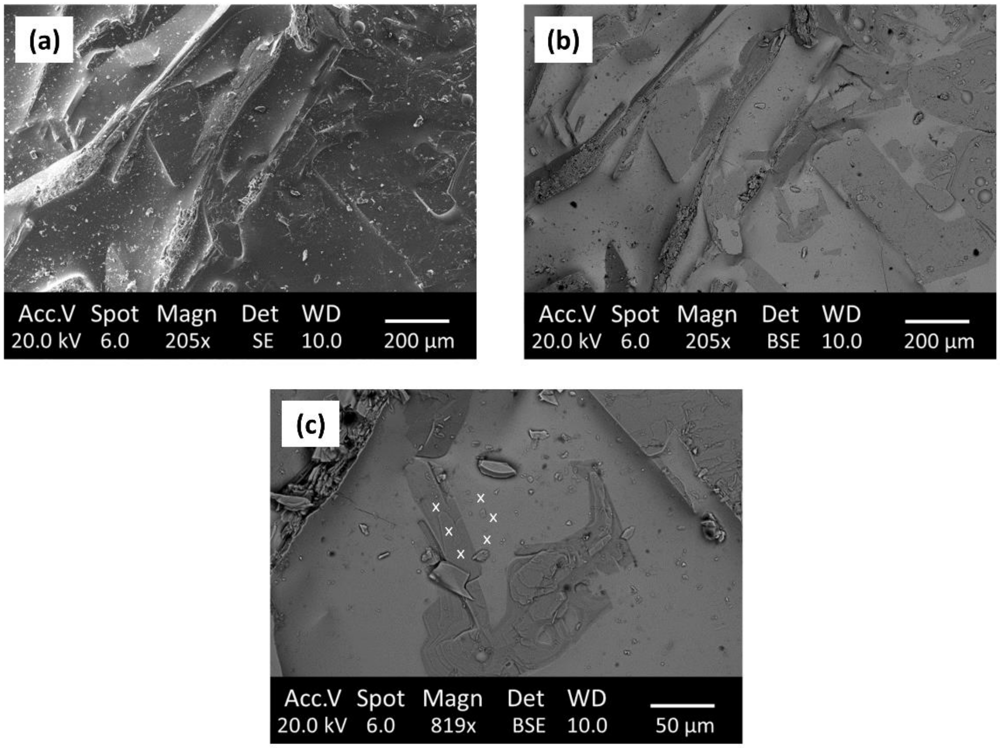

Figure 6.10: Scanning electron microscopy (SEM) image of deposit 2 within the bent silica glass distillation ampoule (D_HAP001) using (a) secondary electrons and (b) backscattered electrons. Under a higher magnification (c) several energy dispersive X-ray spectroscopy (EDX) points were analysed as shown by the white crosses.

Two elemental spectra, from the EDX analysis of Figure 6.10 (c), are presented in Figure 6.11 and show an obvious compositional difference between the lighter regions (spectrum 1) and darker regions (spectrum 2) of deposit 2. This was particularly evident amongst the lower energy peaks, as highlighted by the dashed boxes in Figure 6.11. Furthermore, quantified analysis of the lighter regions in deposit 2 found that it was close to the as-annealed batched glass ($Ge_{20}Sb_{10}Se_{70}$ at. % M_HAP005), with a mean deposited composition of $Ge_{19.4}Sb_{11.1}Se_{69.5}$ ±0.5 at. %. In contrast, the darker regions presented in Figure 6.10 (c) were found to have a mean deposited composition of $Ge_{32.9}Se_{67.1}$ ±0.5 at. %. Therefore, just like the dominant crystalline phase which grew around the surface of the stoichiometric $Ge_{25}Sb_{10}Se_{65}$ at. % glass in section 4.4.1, crystalline $GeSe_2$ once again seemed to readily grow in the deposited $Ge_{19.4}Sb_{11.1}Se_{69.5}$ ±0.5 at. % material.

Although inconclusive, it is possible that the sudden change in temperature seen at 629 °C by thermocouple 2 in Figure 6.7, did in fact reflect the sudden distillation of the as-annealed $Ge_{20}Sb_{10}Se_{70}$ at. % glass, which initially condensed as $Ge_{19.4}Sb_{11.1}Se_{69.5}$ ±0.5 at. %, but later crystallised into the dominant $GeSe_2$ phase, during the 4 hr dwell at 712 °C.

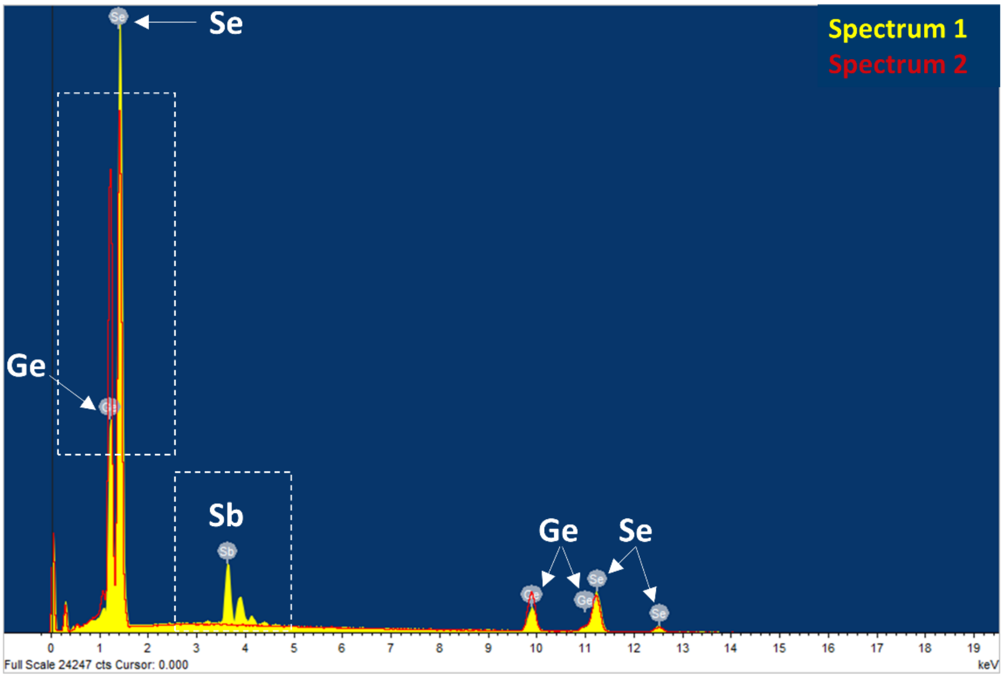

Figure 6.11: SEM-EDX spectra of two regions within deposit 2 of the bent silica glass ampoule distillation of as-annealed $Ge_{20}Sb_{10}Se_{70}$ at. % glass (D_HAP001).

6.2.1.3 Deposit 3 of D_HAP001

The final SEM-EDX spectrum, presented in Figure 6.12, showed that deposit 3 was Se-rich with a mean quantified SEM-EDX composition of $Ge_{8.8}Sb_{4.3}Se_{86.9}$ ±0.5 at. %. Although not presented here, the SEM images of deposit 3 showed no topological features and no compositional variance.

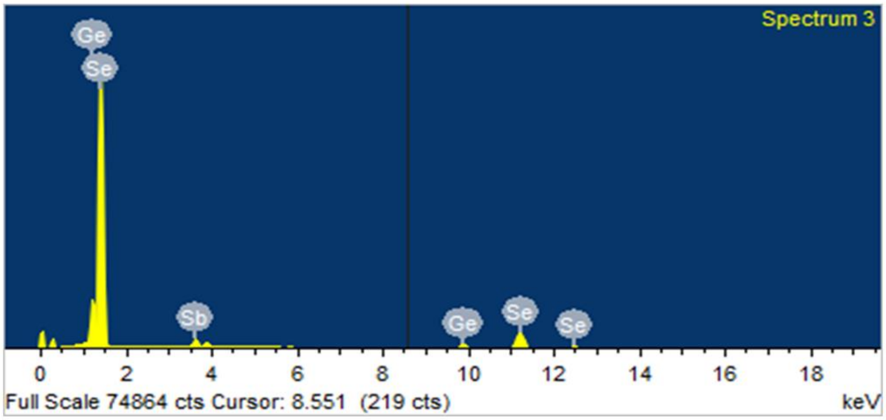

Figure 6.12: SEM-EDX spectrum of deposit 3 within the bent silica glass ampoule, following the distillation of as-annealed $Ge_{20}Sb_{10}Se_{70}$ *at. % glass (D_HAP001).*

Overall, the preliminary investigation of D_HAP001 into the distillation of $Ge_{20}Sb_{10}Se_{70}$ at. % glass, had shown that this composition would successfully distil at a temperature of 850 °C or below *i.e.* possibly even at 720 °C if the mass transfer in Figure 6.7 was correct. Even though it was not clear why the distilled material had condensed separately, the near match in composition between the original as-annealed $Ge_{20}Sb_{10}Se_{70}$ at. % glass and the bulk of deposit 2 ($Ge_{19.4}Sb_{11.1}Se_{69.5}$ ±0.5 at. %), was considered promising. So long as the distilled material condensed a little further along the distillate end, the silica glass ampoule could still be sealed and the contents re-melted, to form the final homogenised, distilled glass.

6.2.2 First $Ge_{20}Sb_{10}Se_{70}$ at. % distillation with 1000 ppm wt. $TeCl_4$ and 700 ppm wt. Al (D_HAP002)

With guidance from D_HAP001, the first distillation of $Ge_{20}Sb_{10}Se_{70}$ at. % glass with 1000 ppm wt. $TeCl_4$ and 700 ppm wt. Al getters (D_HAP002) was investigated.

In Figure 6.13, ~30 g of a premelted, as-annealed $Ge_{20}Sb_{10}Se_{70}$ at. % + 1000 ppm wt. $TeCl_4$ glass (M_HAP014) with 700 ppm wt. Al, is shown to have been batched into a silica glass distillation rig, which had been $HF_{(aq)}$ etched, air baked (twice) and vacuum baked (as detailed section 3.3.4.2). The source and purity of these chemicals can be found in Table 3.1. A silica glass distillation rig with a 10/14 mm diameter distillate end had been chosen over the 29/32 mm diameter distillate end (see Table 3.5), as it was hoped that the final distilled Ge-Sb-Se glass would produce a 10 mm diameter preform for fibre-drawing.

Since the silica glass distillation rigs (Figure 3.5 (b) and (c)) were initially designed around the geometry of the two-zone furnace (Instron, TF1798, tube ID 86mm), its alignment in Figure 6.13, shows that the charge end, and it's $Ge_{20}Sb_{10}Se_{70}$ at. % + 1000 ppm wt. $TeCl_4$ glass + 700 ppm wt. Al contents, were centred in the middle of zone 2, whilst the distillate end was centred in the middle of zone 1. Using four thermocouples (Figure 6.13), the entire procedure was once again monitored using Pico Technology logging software (**appendix 5**).

As it was briefly outlined in Table 3.7, one of the initial steps in the more complex distillation of Ge-Sb-Se glass, is the baking-out of $HCl_{(g)}$ *i.e.* the [Cl] which had combined with [H] impurities during the first melt of the $Ge_{20}Sb_{10}Se_{70}$ at. % + 1000 ppm wt. $TeCl_4$ glass. In order for this to happen, the temperature of the charge end, containing the $Ge_{20}Sb_{10}Se_{70}$ at. % + 1000 ppm wt. $TeCl_4$ glass, had to be gradually increased to its liquidus at approx. 457.5 °C (calculated by the two-thirds rule[178]). This step usually began at the end of Day 1 (as discussed in Table 3.7) so that critical silica glass sealing stages were within safe working hours. Therefore, both zones of the furnace were left overnight at 220 °C, just above the T_g of $Ge_{20}Sb_{10}Se_{70}$ at. % glass.

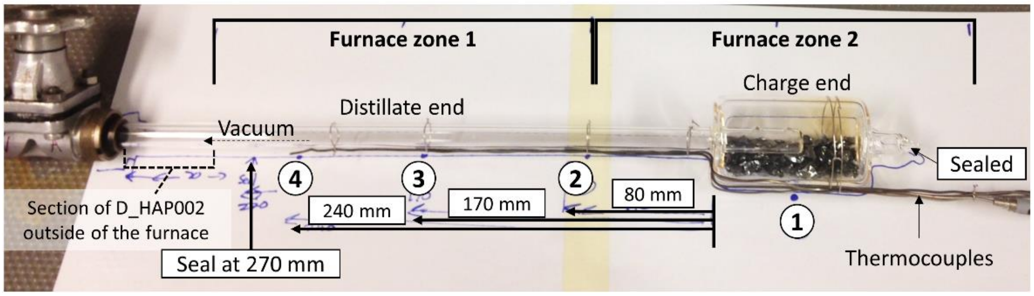

Figure 6.13: Photograph of the silica glass distillation rig, with $Ge_{20}Sb_{10}Se_{70}$ at. % + 1000 ppm wt. $TeCl_4$ glass + 700 ppm wt. Al contents sealed in the charge end of the rig, prior to distillation (D_HAP002). Circled numbers indicate the position of the four thermocouples.

As shown in Figure 6.14, the optimum point of sealing was judged, based on the colour of the protruding silica glass 10/14 mm diameter tube from the end of zone

1 (refer to Figure 6.13). Initially, following an overnight dwell at 220 °C, there was a light red deposit on the inner surface of the protruding silica glassware, as shown in the inset of Figure 6.14. When the temperature of the charged end of D_HAP002, containing $Ge_{20}Sb_{10}Se_{70}$ at. % + 1000 ppm wt. $TeCl_4$ glass + 700 ppm wt. Al, was gradually increased from 220 °C towards its liquidus, more vapour condensed in a light red/ black deposit. This implied that an appropriate amount of $HCl_{(g)}$ had been removed with the drawing vacuum. Therefore, soon after the observed colour in Figure 6.14 had been recorded, the silica glass distillation rig of D_HAP002 was sealed (see Day 2 of Table 3.7), creating a closed system in which distillation would occur. Although the liquidus of the $Ge_{20}Sb_{10}Se_{70}$ at. % glass was 457.5 °C, the temperature recorded by thermocouple (1), showed that the charge end of the silica distillation rig was at 480 °C by the point of sealing.

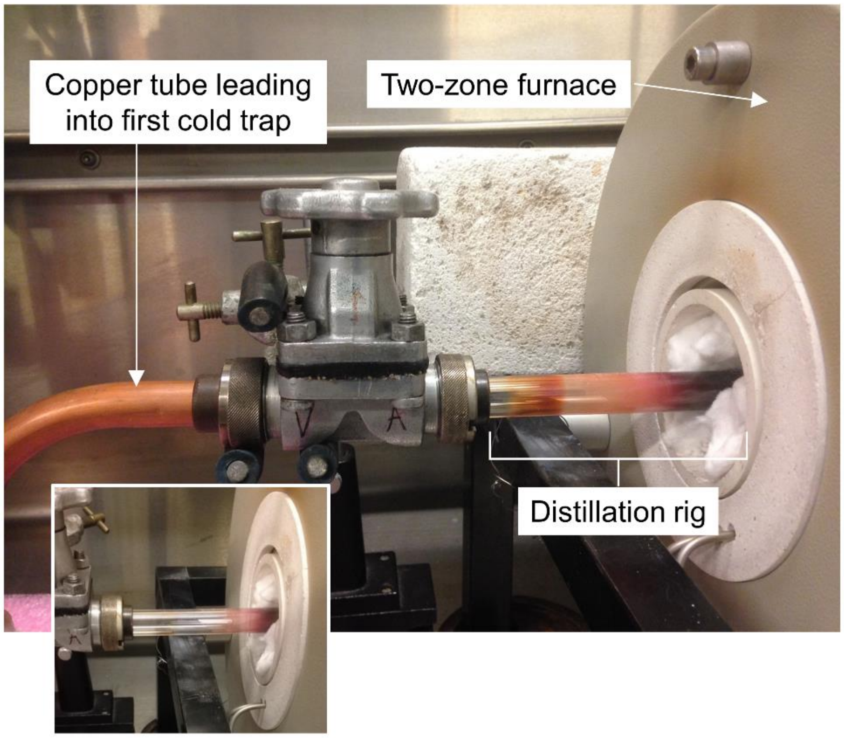

Figure 6.14: Photograph of the external section of the silica glass distillation rig (D_HAP002) just before sealing. Inset shows the same section of D_HAP002 earlier on in the schedule, just after an overnight dwell at 220 °C.

Once sealed, zone 2 of the two-zone furnace (Figure 6.13) was programmed to ramp from 450 °C to 750 °C, over a 2 hr period, whilst being manually rocked every 10 mins. Following this it would dwell at 750 °C overnight (see **appendix 5**). At the same time, zone 1 of the two-zone furnace was programmed to dwell at 200 °C overnight. These overnight steps aimed to create a suitable temperature gradient in which to start distilling the $Ge_{20}Sb_{10}Se_{70}$ at. % glass. Note that the temperature reading from thermocouple 1, showed that the charge end of D_HAP002 actually dwelled at 745 °C overnight, a little below the programmed 750 °C.

By removing a small section of the thermal blanket, which had been packed around the distillate end of D_HAP002, it was possible to estimate how much material had distilled across. However, even when zone 2 of the two zone furnace had been gradually increased to 980 °C (over an ~8 hr period), little material had distilled over. Considering the preliminary ~2.8 g of as-annealed $Ge_{20}Sb_{10}Se_{70}$ at. % glass (D_HAP001) had distilled at temperatures below 850 °C (see section 6.2.1), it was clear that something had gone wrong. As a last attempt, zone 2 of the two zone furnace was increased to 1000 °C and left for 20 hrs, before ending the distillation programme and allowing the silica glass rig, with its contents, to cool to room temperature. Note that thermocouple 1 (Figure 6.13) reached a maximum temperature of 985 °C, rather than the 1000 °C programmed.

Nevertheless, the silica glass distillation rig of D_HAP002, marked as (1) in Figure 6.15 (a), showed that the first distillation of $Ge_{20}Sb_{10}Se_{70}$ at. % with 1000 ppm wt. $TeCl_4$ glass and 700 ppm wt. Al (D_HAP002) had been unsuccessful. Two crucial observations were made.

The first addressed the small amount of chalcogenide material that had been distilled during D_HAP002. Similar to the preliminary D_HAP001 distillation (also shown in Figure 6.15 (a) marked as (2)), material in D_HAP002 had also condensed into three distinct deposits. When both distillation results we aligned with one another (see Figure 6.15 (a)), it was clear that each distilled material had condensed at the same point within the two-zone furnace (Instron, TF1798, tube ID 86mm) *e.g.* the Sb_2Se_3 deposit (see section 6.2.1.1) had condensed both times just before the gap between zone 1 and zone 2. Enlarged regions of D_HAP002, are shown in Figure 6.15 (b), (c) and (d). Due to the similarity between the condensed material of D_HAP002 and D_HAP001 (see sections 6.2.1.1 to 6.2.1.3), it was assumed that they shared a similar composition. Thus, SEM-EDX analysis was not conducted for D_HAP002.

The second crucial observation, was that although the two holes in the silica glassware (highlighted in Figure 6.15 (e)) were clear, there was still a large amount of material which had remained in the charge chamber of D_HAP002, even though temperatures had been increased to ~1000 °C. Therefore, although there was a ~635 °C temperature difference between the charge and distillate end of D_HAP002, something else was preventing the movement of $Ge_{20}Sb_{10}Se_{70}$ at. % vapour. The likely cause, was probably a build-up of $HCl_{(g)}$, which had not been fully removed prior to the sealing of D_HAP002 (see Table 3.7).

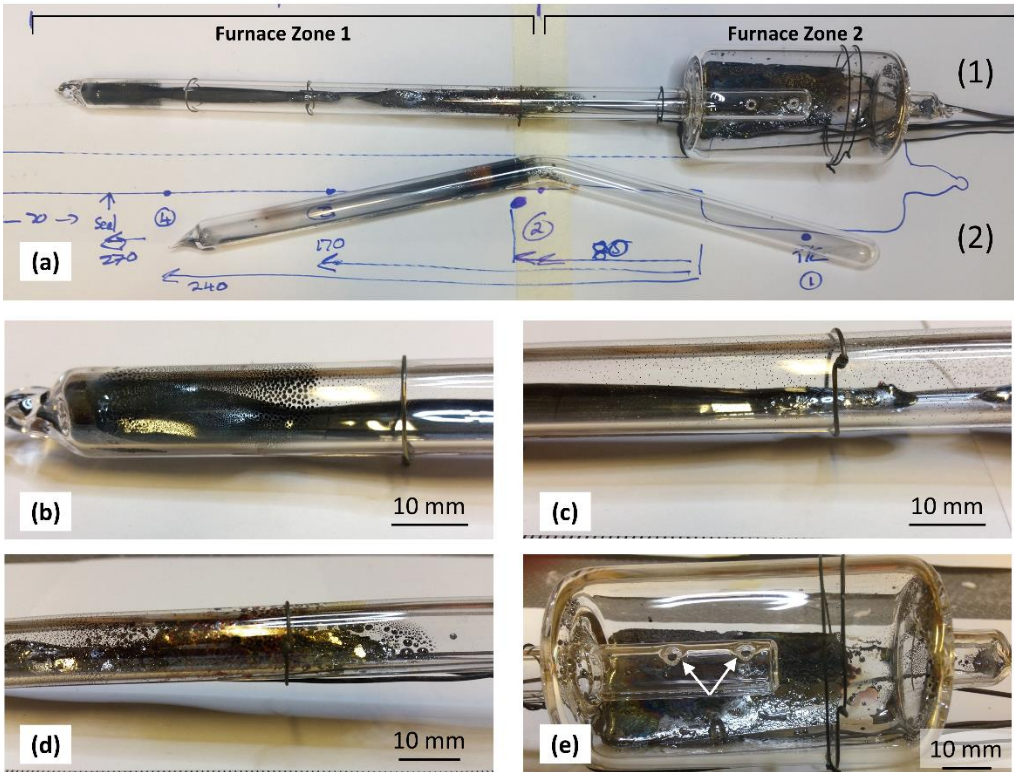

Figure 6.15: (a) Comparison between (1) D_HAP002 and (2) D_HAP001. Photographs (b)-(e) are enlarged regions of the first (D_HAP002) $Ge_{20}Sb_{10}Se_{70}$ at. % with 1000 ppm wt. $TeCl_4$ glass and 700 ppm wt. Al, after distillation.

In consideration, two fundamental changes were made for a second attempt at the distillation of $Ge_{20}Sb_{10}Se_{70}$ at. % with 1000 ppm wt. $TeCl_4$ glass and 700 ppm wt.

Al. First, it was decided that the position of the silica glass distillation rig would be moved approx. 30 mm towards the right, in respect to the two-zone furnace (Instron, TF1798, tube ID 86mm). Therefore, if any material was to condense separately in the distillate end, there would be enough room to seal the silica glass distillation rig and then homogenised the chalcogenide material during the final glass melt.

Secondly, by decreasing the initial time taken to reach the liquidus temperature (refer to Day 2 of Table 3.7), more time could be given to driving off the $HCl_{(g)}$. Therefore, it was aimed to achieve a darker vapour deposit around the protruding section of 10/14 mm diameter silica glassware (see Figure 6.14), before the system is sealed.

6.2.3 Second $Ge_{20}Sb_{10}Se_{70}$ at. % distillation with 1000 ppm wt. $TeCl_4$ and 700 ppm wt. Al (D_HAP003)

Using the preparation procedure outlined in section 3.3.4.2, ~30 g of as-annealed $Ge_{20}Sb_{10}Se_{70}$ at. % with 1000 ppm wt. $TeCl_4$ glass and 700 ppm wt. Al (M_HAP015), was batched and sealed into the charge end of a silica glass distillation rig, with a 10/14 mm diameter distillate end. Aside from the recommended ~30 mm shift within the two-zone furnace, the experimental setup of D_HAP003 was identical to that presented in Figure 6.13 and once again used four thermocouples to monitor the programme, see **appendix 6**.

Following an overnight dwell at 220 °C, both zone 1 and zone 2 of the two-zone furnace (Instron, TF1798, tube ID 86mm) were ramped up to 500 °C at a rate of 100 °C/hr, so to encourage the start of $HCl_{(g)}$ bake-out. After approx. 2 hrs the colour of the red deposit on the protruding section of D_HAP003 (refer to Figure 6.13), was already darker than that seen in Figure 6.14. Consequently, zone 1 which contained the distillate end of D_HAP003, was stepped down from 400 °C to 200 °C whilst zone 2, containing the charge end, was gradually stepped from 400 °C to 500 °C over a 2 hr time period. Soon after reaching a programmed temperature of 500 °C in zone 2, D_HAP003 was sealed.

In Figure 6.16, the colour of the protruding section of D_HAP003 can be seen just before sealing. As a result of the faster heating rate and longer time spent above the liquidus of the batched $Ge_{20}Sb_{10}Se_{70}$ at. % with 1000 ppm wt. $TeCl_4$ glass, a darker red/black deposit was able to form.

Figure 6.16: Photograph of the external section of the silica glass distillation rig (D_HAP003) just before sealing

After sealing, zone 2 of D_HAP003 was ramped from 500 °C to 750 °C, over a 2 hr period, during which the furnace was manually rocked every 10 mins. Following a 1 hr dwell at 750 °C, zone 2 was then ramped to 900 °C, over another 2 hr period, before dwelling at 900 °C overnight. Note that thermocouple 1 showed that the actual temperature of the D_HAP003 charge chamber, dwelled at ~874 °C overnight.

However, even with the additional time given for the removal of $HCl_{(g)}$ and a 30 mm shift within the two-zone furnace, the distillation (D_HAP003) of $Ge_{20}Sb_{10}Se_{70}$ at. % with 1000 ppm wt. $TeCl_4$ glass and 700 ppm wt. Al was still unsuccessful.

Furthermore, as demonstrated in Figure 6.17 (a), the result of D_HAP003 distillation was slightly different to that seen in D_HAP002. Although the condensed material in the distillate end of D_HAP003 had once again separated into two sections, there was no noticeable difference in its appearance *i.e.* both deposits were a dark, metallic colour. This was seen more clearly in Figure 6.17 (b) and (c).

The most significant difference, was instead found within the charge chamber of silica glass distillation rig, as shown in Figure 6.17 (d). The light, silver-coloured deposits had seemingly condensed in three main parts. The first had a needle-like structure at the bottom of the charge chamber on the left hand side (deposit 1 in Figure 6.17 (d)); the second had a smoother surface at the bottom of the charge chamber on the right hand side (deposit 2 in Figure 6.17 (d)); and the third had condensed in spherical, globular deposits on the right hand side wall of the charge chamber (deposit 3 in Figure 6.17 (d)). From the position of the condensed material within the charge chamber of D_HAP003, it was likely that the right hand side of the silica glass chamber had been too close to the end of the furnace (Figure 6.17 (a)). This would have allowed, what looked like a Sb-rich material, to condense on its cooler silica glass surface, rather than travelling through to the distillate end of the rig.

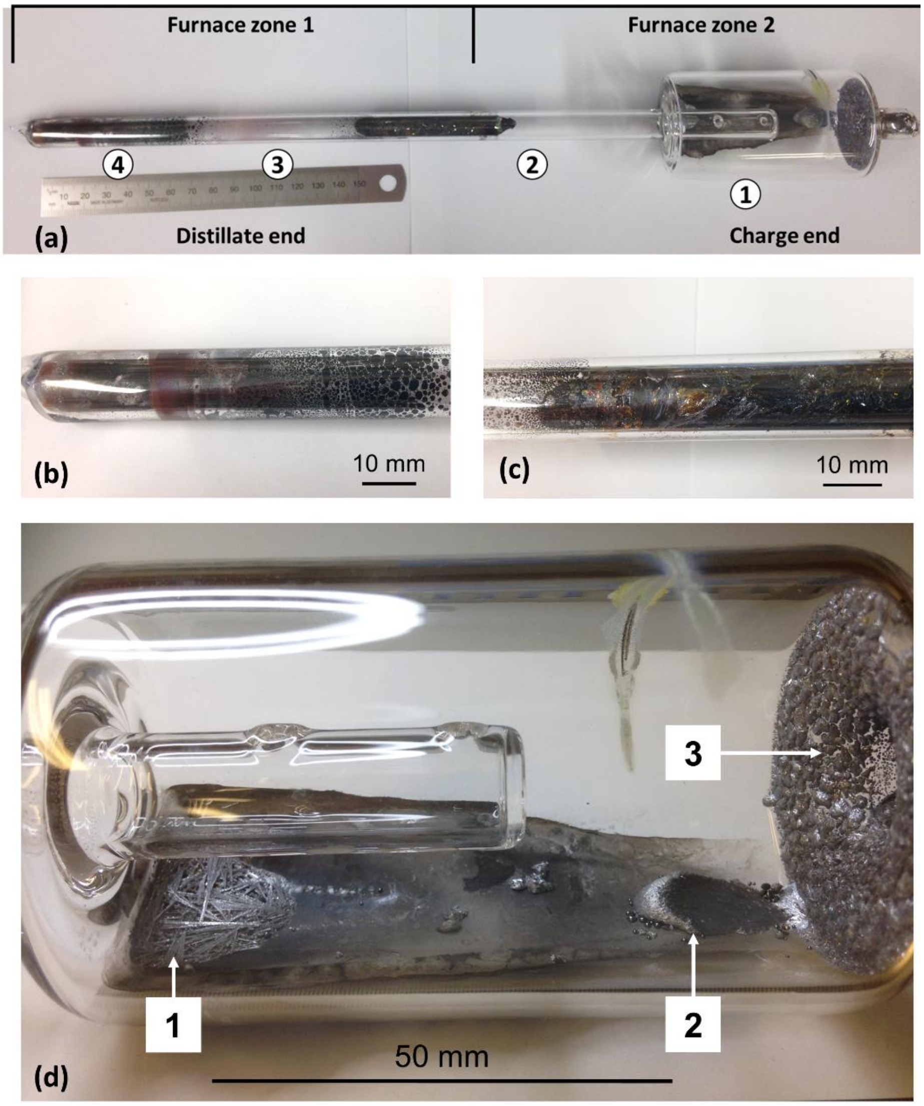

Figure 6.17: (a) Overview of D_HAP003 with enlarged photographs of the distillate end in (b) and (c), and an enlarged region of the charge end in (d). Circled numbers in (a) indicate position of thermocouple whilst square numbers in (d) indicate the three main deposits.

Similar to the condensed material investigated during D_HAP001 (section 6.2.1), SEM-EDX was once again used to analyse each of the three deposits identified in Figure 6.17 (d). Furthermore, during the sample preparation, it was also noticed that some of the deposits had a different morphology, depending on whether the material was observed from the top or from the ampoule side *i.e.* the side which had been in contact with the silica glass. As such, all deposits were analysed from both angles.

6.2.3.1 Deposit 1 of D_HAP003

In Figure 6.18 (a), the top side of deposit 1 is shown, using the backscattered electron detector during SEM. Under a higher magnification, shown in Figure 6.18 (b), it was clear that the top side of deposit 1 had two compositionally distinct regions that were either lighter or darker in colour. EDX point spectra, taken from each region, was directly compared and shown in Figure 6.18 (c). Whereas, the lighter material (spectrum 1) was confirmed as ~Sb_2Se_3 (specifically $Ge_{0.4}Sb_{38.8}Se_{60.8}$ ±0.5 at. %), the darker regions (spectrum 2) were found to have a higher proportion of Si. Since deposit 1 had remained in the charge chamber of D_HAP003 throughout the whole of the distillation procedure, it is possible that it may have reacted with the silica glass container. This type of reaction has previously been discussed by Churbanov *et al.*[95]. Furthermore, the increased peak height of both Si and O in spectrum 2 of Figure 6.18 (c), suggested that the darker regions within the top side of deposit 1, most likely had a composition close to SiO_2.

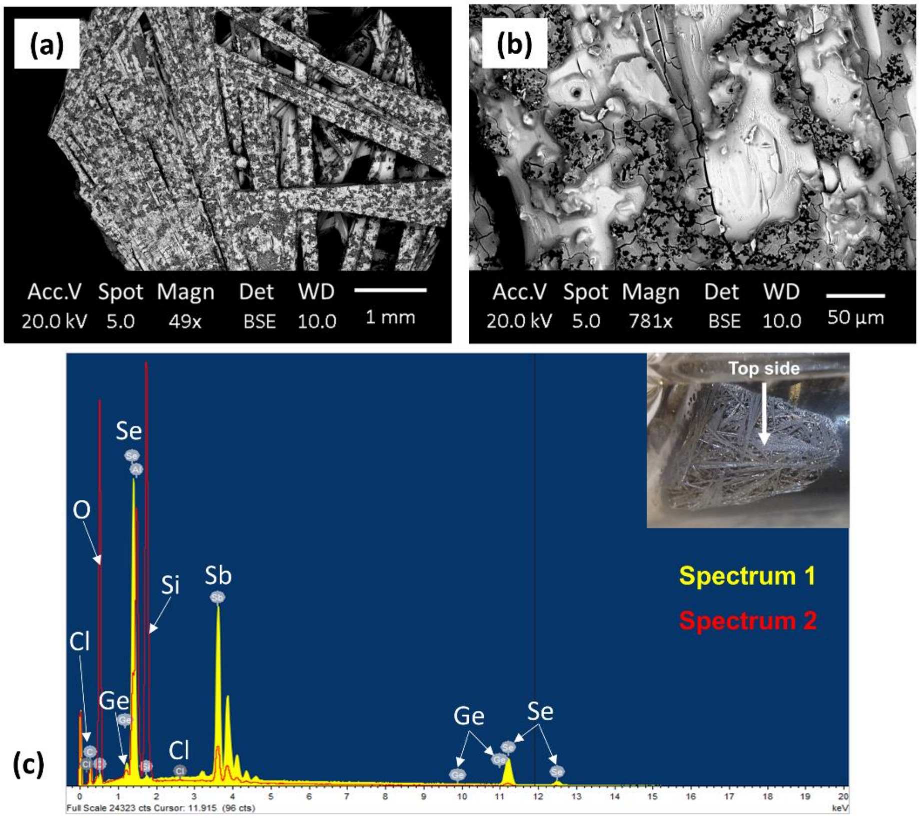

Figure 6.18: Scanning electron micrographs of the top side of deposit 1 (D_HAP003) at a lower (a) and higher (b) magnification. (c) Comparison of the SEM-EDX spectra from both the lighter (spectrum 1) and darker (spectrum 2) regions of (b).

In contrast, when the ampoule side of deposit 1 was analysed, as shown in Figure 6.19 (a), the darker Si-rich regions were no longer present. Furthermore, the needle-like morphology, initially seen on the top side of deposit 1, had also disappeared and instead had a relatively smooth, yet cracked, appearance. Although there was still a high content of Sb and Se present in the quantified data, EDX analysis of several points revealed a more varied $Ge_{8.7}Sb_{25.4}Se_{59.3}Si_{6.6}$ composition on the ampoule side of deposit 1. Note that EDX analysis only focussed on the four elements (Ge, Sb, Se and Si) and so this may not be the exact composition.

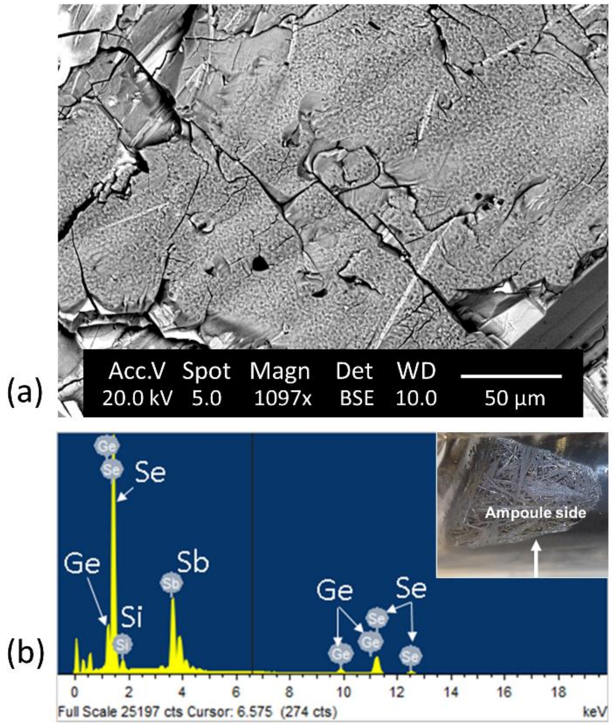

Figure 6.19: (a) Scanning electron micrographs of the ampoule side of deposit 1 (D_HAP003) and corresponding (b) SEM-EDX spectrum.

It is possible, that the difference in structure between the top and ampoule side of deposit 1 (D_HAP003), may have been caused by Si-rich impurities acting as sites for heterogeneous nucleation. If the darker regions of Figure 6.18 (b) were indeed SiO_2, this lower density impurity (2650 kg/m^3) [204] may have floated to the top of deposit 1, when the higher density chalcogenide material was still liquid. Then, when the charged end of D_HAP003 was cooled, the SiO_2 heterogeneous inclusions may have initiated the growth of Sb_2Se_3 crystals, seen on the top side of deposit 1.

Whatever the reason for the difference in structure, SEM-EDX results from Figure 6.18 and Figure 6.19, had demonstrated that the main bulk of deposit 1 was Sb-rich.

6.2.3.2 Deposit 2 of D_HAP003

In Figure 6.20, the SEM-EDX results of deposit 2 (D_HAP003) are presented and show, that unlike deposit 1, both the top and ampoule surfaces were very similar to one another. The backscattered electron SEM images, shown in Figure 6.20 (a) and (c), revealed that the deposit had a granular-like structure, which was relatively homogeneous. Aside from the few impurities, highlighted by the dashed circles in Figure 6.20 (a) and (c), quantified EDX analysis of both the top and ampoule side of deposit 2 (Figure 6.20 (b) and (d) respectively), revealed a composition of $Ge_{0.7}Sb_{39.6}Se_{59.7}$ ±0.5 at. %. Therefore, deposit 2 was also Sb-rich, with a composition close to Sb_2Se_3.

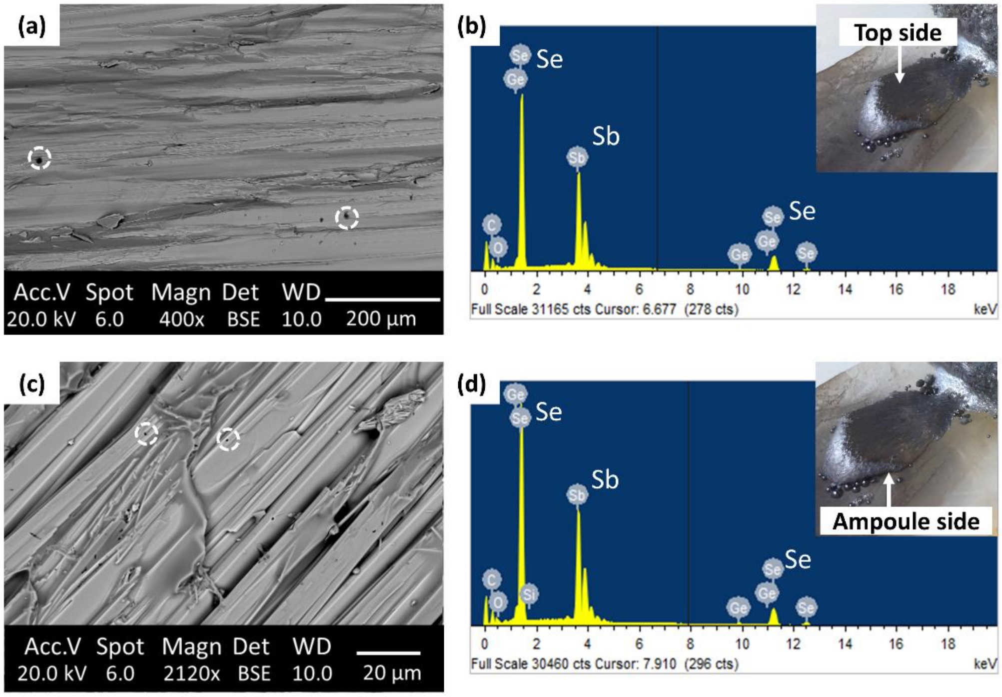

Figure 6.20: (a) Scanning electron micrograph of the top side of deposit 2 (D_HAP003) and corresponding (b) SEM-EDX spectrum. (c) Scanning electron micrograph of the ampoule side of deposit 2 (D_HAP003) and corresponding (d) SEM-EDX spectrum. Dashed circles in (a) and (c) highlight impurities.

6.2.3.3 Deposit 3 of D_HAP003

The final deposit investigated from the charge chamber of D_HAP003, is shown in Figure 6.21 and, like deposit 1, reveals a slight discrepancy between its different surfaces. Whereas, the backscattered electron SEM image shown in Figure 6.21 (a) revealed a relatively rough topography on the top side of deposit 3, the surface shown in Figure 6.21 (c), revealed a smooth, needle-like topography on its ampoule side. Although the surface of deposit 3 was largely influenced by whether or not it was in contact with the silica glass chamber, elemental analysis using EDX (Figure 6.21 (b) and (d)), once again found a relatively large difference between compositions.

Whereas the top side of deposit 3 (Figure 6.21 (b)), had a quantified EDX composition of $Ge_{0.6}Sb_{40.3}Se_{59.1}$ ±0.5 at. %, the ampoule side of deposit 3 (Figure 6.21 (d)) had an EDX composition of $Ge_{15.5}Sb_{24.5}Se_{60.0}$ ±0.5 at. %. Furthermore, there were more Si-rich impurities seen on the ampoule side of deposit 3, which may have influenced the final composition.

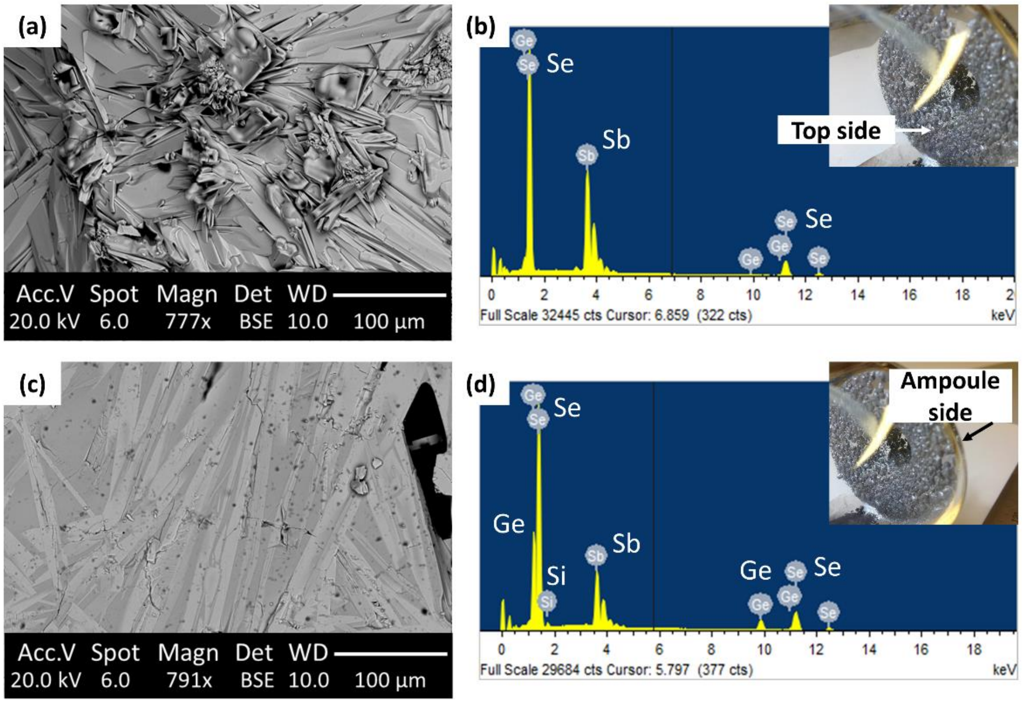

Figure 6.21: (a) Scanning electron micrograph of the top side of deposit 3 (D_HAP003) and corresponding (b) SEM-EDX spectrum. (c) Scanning electron micrograph of the ampoule side of deposit 3 (D_HAP003) and corresponding (d) SEM-EDX spectrum.

6.2.3.4 D_HAP003 overview

Overall, the second attempt at distilling $Ge_{20}Sb_{10}Se_{70}$ at. % with 1000 ppm wt. $TeCl_4$ glass and 700 ppm wt. Al was unsuccessful, primarily due to the separation of material within the charge end of D_HAP003. The in-depth EDX analysis of each deposit left in the charge chamber of D_HAP003, revealed that although there was some variance within each sample, all deposits were Sb-rich. As discussed in section 2.4.2, it took Hilton *et al.*[104] approx. eight days to distil 178 g of Sb at a temperature of 1000 °C. Therefore, the separation of as-annealed $Ge_{20}Sb_{10}Se_{70}$ at. % glass seen in the charge chamber of D_HAP003, was significantly detrimental to its overall success.

Although the extra time allowed for the removal of $HCl_{(g)}$ had helped to increased the amount of material distilled (Figure 6.17), the ~3 cm shift in the position of the silica glass distillation rig in respect to the two-zone furnace, no doubt exacerbated the separation problem. As such, the experimental setup within the two-zone furnace (Instron, TF1798, tube ID 86mm), was deemed unsuitable for the distillation of Ge-Sb-Se glass with [O] and [H] getters.

Furthermore, the separation of the batched $Ge_{20}Sb_{10}Se_{70}$ at. % glass prior to distillation, was thought to be worsened by a relatively slow heating rate, which was used to bring the charge end of D_HAP003 up to ~874 °C (see **appendix 6**).

6.2.4 Third $Ge_{20}Sb_{10}Se_{70}$ at. % distillation with 1000 ppm wt. $TeCl_4$ and 700 ppm wt. Al (D_HAP004)

Considering the problems that had been encountered during D_HAP002 and D_HAP003 (sections 6.2.2 and 6.2.3, respectively), two major changes were made to the third distillation attempt of $Ge_{20}Sb_{10}Se_{70}$ at. % with 1000 ppm wt. $TeCl_4$ glass and 700 ppm wt. Al. The first of these was the type of furnace used. Whereas D_HAP002 and D_HAP003 had been conducted using the two-zone (Instron, TF1798, tube ID 86mm) furnace, it was decided that a smaller, clamshell furnace (Cabrolite, VST 12/200) would be used for the distillation of D_HAP004. Along with several wire-heated regions, this offered far greater control over the temperatures of each region within the silica glass distillation rig. A schematic representation of this setup can be seen in Figure 6.22 (a).

The second major change involved the environment within which distillation occurred. Whereas, D_HAP002 and D_HAP003 had been conducted using a closed system (*i.e.* both ends of the silica glass rig had been sealed prior to distillation), the distillation of $Ge_{20}Sb_{10}Se_{70}$ at. % glass within D_HAP004 (although unintentionally) was conducted within an open system, *i.e.* the silica glass distillation rig was still attached to the vacuum system, see **appendix 7**.

Accompanying the two major distillation changes during D_HAP004, were several smaller alterations such as the use of a silica glass distillation rig, with a combined 10/14 mm diameter and 29/32 mm diameter distillate end (Figure 6.22 (a)). It was thought that the presence of a larger 29/32 mm diameter chamber would help collect any material that may distil across and perhaps, minimise the separation within the distillate end. Along with the improved temperature control, as a result of the wire-heated regions (Figure 6.22 (a)), there was also an increase in the number of thermocouples used. Whereas, D_HAP002 and D_HAP003 had worked around four thermocouple readings, D_HAP004 was monitored by eight.

However, these extra precautions, almost proved detrimental to the third, and final, distillation attempt of $Ge_{20}Sb_{10}Se_{70}$ at. % with 1000 ppm wt. $TeCl_4$ glass (M_HAP016) and 700 ppm wt. Al.

In Figure 6.22, an overview is presented of a critical fracture that had occurred within the silica glass distillation rig of D_HAP004, moments it was attached to the vacuum system. As previously discussed, the initial experimental setup shown in Figure 6.22 (a) highlighted five wire regions (A-E) that had been assembled round incremental silica dots, which had been attached in-house to the silica glass distillation rig. In order to heat these separate regions, each end of the wire had to be connected to a power supply. In Figure 6.22 (b), the entire assembly is shown *in-situ*, including the alumina beads used to insulate the wire leading to a power supply. Nevertheless, soon after Figure 6.22 (b) was recorded, a section of the silica glass distillation rig cracked, allowing ambient atmosphere to enter the prepared silica glassware (see section 3.3.2). This is highlighted by the inset of Figure 6.22 (b).

However, since D_HAP004 contained glovebox (MBraun) atmosphere, rather than a vacuum, there was a small possibility that the ambient atmosphere had not quite reached the carefully prepared $Ge_{20}Sb_{10}Se_{70}$ at. % with 1000 ppm wt. $TeCl_4$ batched glass in the charge end. Consequently, the broken silica glass distillation rig was immediately moved into the glovebox (MBraun) and subsequently fixed, using a smaller 7/9 mm diameter silica glass tube, as demonstrated by the schematic diagram in Figure 6.22 (c). Whereas the final melt of D_HAP004 had intended to use the 10/14 mm diameter tube to the left of the 29/32 mm diameter chamber (silica glass region under wire E in Figure 6.22 (a)), the fracture meant that any material that may have distilled during D_HAP004 would instead have to use the 10/14 mm diameter tube to the right of the 29/32 mm diameter chamber (silica glass region under wire A and B in Figure 6.22 (a)).

The final experimental setup, presented in Figure 6.22 (c), showed that wire region E had been removed from the 10/14 mm diameter distillate end, in an attempt to reduce the weight around the weakened area. Once all the wires had been reattached to the power supply and the charge chamber had been loosely packed with thermal blanket, the clamshell furnace (Cabrolite, VST 12/200) was closed and the system was placed under vacuum. Even with the repair, a vacuum of 1.2 $\times10^{-5}$ mbar (1.2 $\times10^{-3}$ Pa) was achieved.

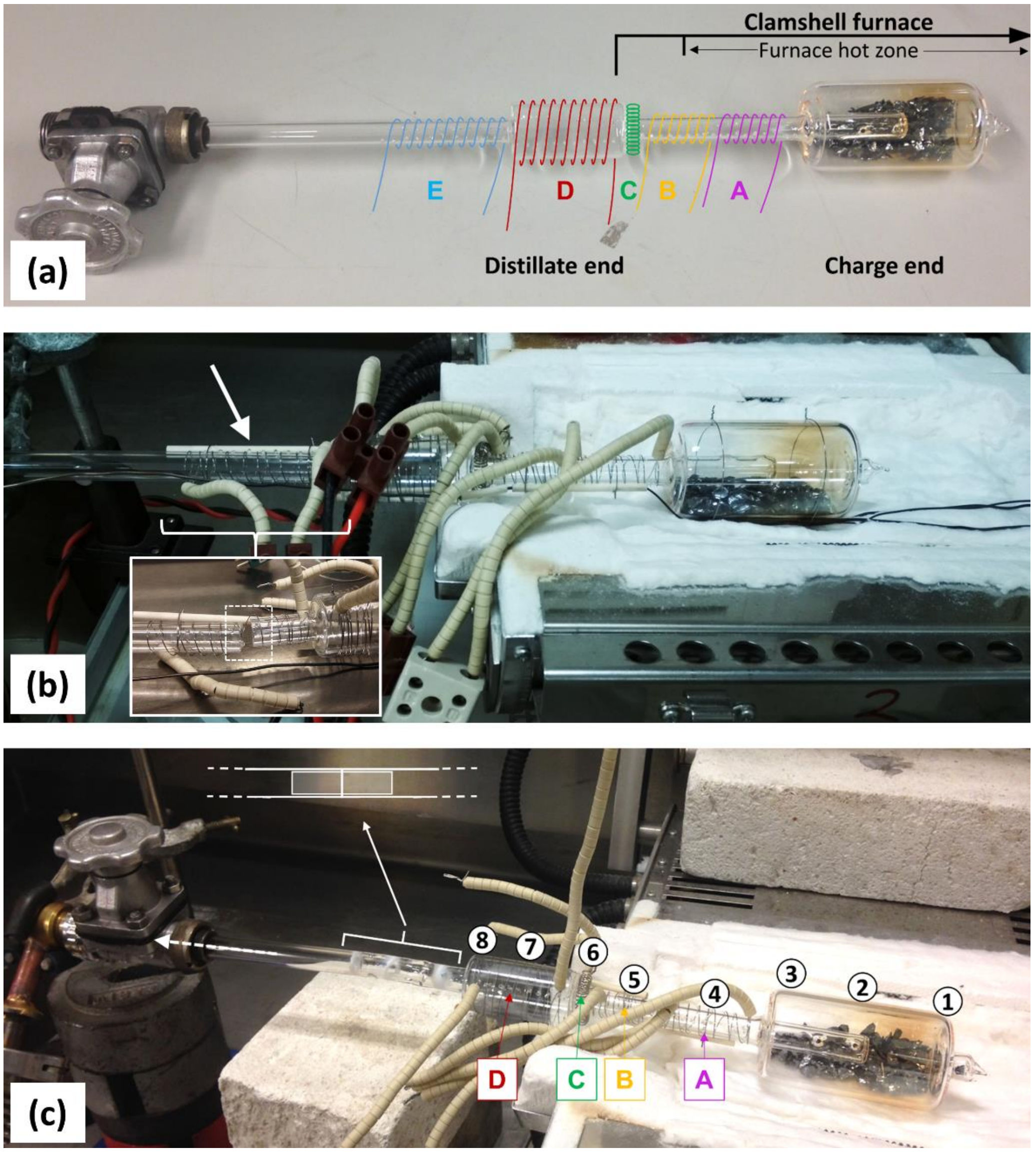

Figure 6.22: (a) D_HAP004 silica glass distillation rig, with $Ge_{20}Sb_{10}Se_{70}$ *at. % glass with 1000 ppm wt.* $TeCl_4$ *and 700 ppm wt. Al batched into charge chamber. Initial wire regions A-E are schematically shown. (b) Initial D_HAP004 experimental setup, shown in-situ, prior to cracking. Inset in (b) shows the fractured 10/14 mm diameter silica glassware, with arrow pinpointing the exact failure location. (c) Repaired D_HAP004 silica glass distillation rig, with wire heated regions shown A-D. Final thermocouple positions are also highlighted in (c) by circle numbers.*

Prior to the overnight dwell, the entire silica glass distillation rig and its contents, were briefly heated to try and remove some of the oxygen and hydrogen that had been introduced from exposure to the atmosphere. Whilst the clamshell furnace was heated to ~350 °C, wires A, B, C and D were heated to approx. 600 °C for 30 mins. Following this bake, the charge end of D_HAP004 was kept at ~300 °C overnight, whilst the distillate end was kept ~250 °C.

After a 12 hr overnight dwell, the temperature was then increased to bring the $Ge_{20}Sb_{10}Se_{70}$ at. % glass to its liquidus (~457 °C) and start the $HCl_{(g)}$ bake-out. Unlike the limited two-zone (Instron, TF1798, tube ID 86mm) temperature control used during D_HAP002 and D_HAP003, the heated wire regions present during D_HAP004 meant that the linking 10/14 mm diameter silica glass tube (encased by wire regions A, B and C in Figure 6.22 (a)) could be maintained at temperatures higher than the charge chamber. As such, material would be less likely to condense before reaching the distillate end.

Within 2 hrs, the charge end of D_HAP004 had been ramped from 300 °C to 460 °C and the wire regions A, B and C were 525 °C, 462 °C and 435 °C, respectively. Although wire D had been wrapped round the 29/32 mm diameter distillate chamber (Figure 6.22 (c)), heat generated from wires A, B and C begun to influence its temperature and so once thermocouple 7 (Figure 6.22 (c)) had reached ~316 °C, the power supply to wire D was switched off completely.

Even though the vapour, deposited near the repair of D_HAP004, had developed a dark red colour (greater than that seen in D_HAP002 and D_HAP003), it was decided that the temperatures would continue to increase, beyond the liquidus of $Ge_{20}Sb_{10}Se_{70}$ at. % glass, before sealing the silica glass rig (refer to Table 3.7). Therefore, the colour and thickness of the dark red deposit, was carefully monitored so that it did not get too thick.

Within another 2 hrs the charge chamber had been increased from 460 °C to ~665 °C, whilst thermocouples 4 and 5 (see Figure 6.22 (c)) were at 710 °C and 677 °C, respectively. Satisfied that the dark red deposit was not too thick, the temperature was increased again so to avoid the charge end material from separating. After 0.3 h the charge chamber had reached ~693 °C and thermocouples 4 and 5 were reading 728 °C and 695 °C, respectively.

As shown in Figure 6.23 (a), by the time the charge end had reached ~693 °C, there was a significant increase of dark red deposit within the protruding 10/14 mm silica glass tube. Concerned that the thickness of the deposit was reaching its limit for successful sealing of the silica glass D_HAP004 rig, the programmed was paused with the charge end thermocouples reading ~709 °C.

However, when the thermal blanket covering the 29/32 mm diameter distillate chamber was briefly removed (Figure 6.23 (b)), it was clear that a large amount of material had already been distilled. At this point thermocouples 7 and 8 (Figure 6.22 (c)) were reading 356 °C and 197 °C, respectively. After seeing that almost all the material had left the charge chamber, D_HAP004 was sealed near to the 29/32 mm diameter distillate chamber as shown in Figure 6.23 (b). Due to the delicate nature of the repaired silica glass distillation rig, sealing took approx. 15 mins.

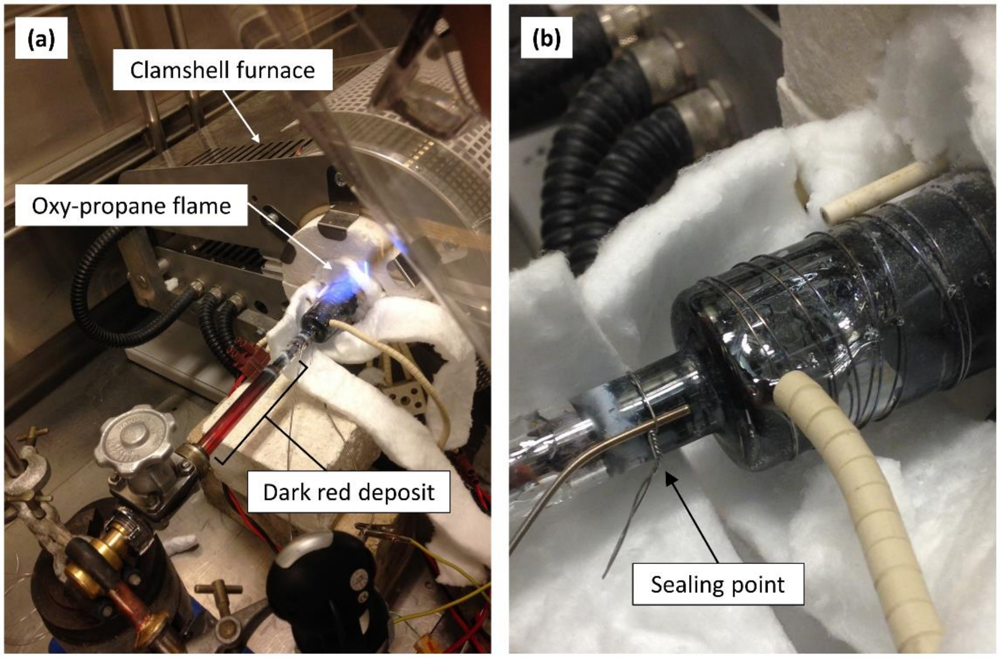

Figure 6.23: (a) Photograph of the dark red deposit on the 10/14 mm diameter silica tube in D_HAP004, prior to sealing. (b) Enlarged region of the 29/32 mm diameter distillate chamber, showing significant amount of distilled material.

Overall, the amended distillation procedure using both the clamshell furnace (Cabrolite, VST 12/200) and wire-heating had unintentionally, but successfully, distilled the $Ge_{20}Sb_{10}Se_{70}$ at. % glass in an open system under flowing vacuum (1.2 x10^{-3} Pa). Whereas the unsuccessful attempts of D_HAP002 and D_HAP003 had had to increase temperatures up to 985 °C and 874 °C, respectively, the

$Ge_{20}Sb_{10}Se_{70}$ at. % glass in D_HAP004 had distilled at temperatures below ~693 °C.

Once the whole of the silica glass distillation rig had cooled to room temperature, D_HAP004 was sealed again just to the left of the charge chamber (Figure 6.22 (c)) and the chalcogenide contents melted (see Table 3.8). The only change made to the melting, quenching and annealing procedures outlined section 3.3.5, was that the high temperature dwell (step 5 in Table 3.8) at 900 °C, was reduced from 12 hr to 10 hr for the distilled D_HAP004 glass.

6.3 Low-loss $Ge_{20}Sb_{10}Se_{70}$ at. % core glass

Even though, the $Ge_{20}Sb_{10}Se_{70}$ at. % core glass had successfully distilled during D_HAP004 (section 6.2.4), it was presumed that due to the critical fracture which occurred early on in the procedure (Figure 6.22 (b)), large impurity bands would still be present within the optical fibre loss spectrum.

However, as demonstrated in Figure 6.24, an 18 m length of distilled fibre-drawn $Ge_{20}Sb_{10}Se_{70}$ at. % core glass (F_HAP008) had remarkably low optical fibre loss between 2 µm and 10 µm wavelength. So much so that, to the best of the Author's knowledge, the optical fibre loss presented in Figure 6.24 (F_HAP008) is currently the best in the world for Ge-Sb-Se optical fibres.

To highlight the improved chalcogenide purity, the optical fibre-loss from an extruded, undistilled $Ge_{20}Sb_{10}Se_{70}$ at. % (F_HAP003) glass was also included in Figure 6.24 as a comparison. Whereas, F_HAP003 presented large impurity absorptions, particularly at 4.5 µm (Se-H, 16.1 dB/m) and 7.9 µm (Ge-O, 18.3 dB/m), results from F_HAP008 had shown that the distillation of $Ge_{20}Sb_{10}Se_{70}$ at. % glass with 1000 ppm wt. $TeCl_4$ ([H] getter) and 700 ppm wt. Al ([O] getter) had significantly reduced, if not completely removed, the impurity.

As discussed in section 2.3.2, Harrington[13] explained that it is extremely difficult to remove all the hydrogen impurities from a chalcogenide glass and that even the most purified glasses will present a hydrogen peak *e.g.* at 4.6 µm wavelength. Therefore, just like the high-purity chalcogenide optical fibres presented by Tang *et al.*[116], Zhang *et al.*[205] and Snopatin *et al.*[93], small Se-H impurity absorptions were still present in the distilled $Ge_{20}Sb_{10}Se_{70}$ at. % glass (Figure 6.24) at 3.5 µm (0.88 dB/m), 4.1 µm (0.74 dB/m) and 4.5 µm (2.53 dB/m). The only other impurity observed in the optical loss spectrum of F_HAP008, was a broad Si-O peak at ~9.2 µm (4.22 dB/m)[35, 89]. Initially thought to be part of the multiphonon absorption edge (see section 2.3.1), the long ~15 min seal used to close the D_HAP004 silica glass distillation rig (described in section 6.2.4), was thought to have contributed to this longer ~9.2 µm wavelength absorption.

Furthermore, with a background loss of 0.44 dB/m found at 6.4 µm, not only was the optical loss spectrum shown in Figure 6.24, the best within this Project, it was also the lowest background loss found within the literature for Ge-Sb-Se optical fibres[54, 96, 206].

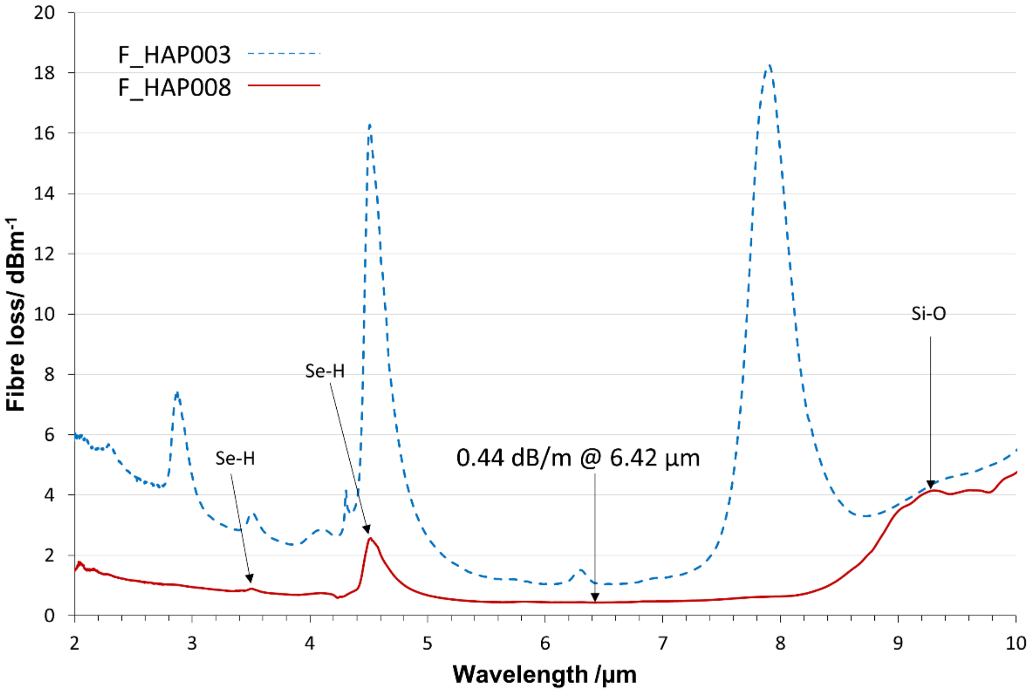

Figure 6.24: Optical fibre loss spectra for the uncladded, distilled $Ge_{20}Sb_{10}Se_{70}$ at. % glass (F_HAP008 from D_HAP004) measured over an 18 m length of ~200 µm diameter fibre. Undistilled F_HAP003 $Ge_{20}Sb_{10}Se_{70}$ at. % optical fibre has been included for comparison,

However, as demonstrated in Figure 6.25 (a)-(c), it was believed that the optical fibre loss presented in Figure 6.24 could have been even lower, since some of the cleaves used to measure the F_HAP008 fibre, presented irregular shapes.

Although the launch end, seen in Figure 6.25 (a), was almost perfectly circular with a horizontal and vertical diameter of 200 µm, cleaves made during Group 1 were non-spherical as shown by Figure 6.25 (b) and (c). Concerned that this may have arisen from an inhomogeneity within the original $Ge_{20}Sb_{10}Se_{70}$ at. % distilled glass, SEM-EDX analysis was conducted on several cleaves used to measure the fibre loss of F_HAP008. However, the composition was found to be relatively stable from the launch end ($Ge_{21.1}Sb_{11.2}Se_{67.7}$ ±0.5 at. %), through Group 1 ($Ge_{21.1}Sb_{10.6}Se_{68.3}$ ±0.5 at. %) and then to Group 2 ($Ge_{20.7}Sb_{10.5}Se_{68.8}$ ±0.5 at. %). Furthermore, the SEM-EDX analysis of F_HAP008 had confirmed that the final distilled composition (D_HAP004) was close to the nominally batched, $Ge_{20}Sb_{10}Se_{70}$ at. % glass (M_HAP016).

Since the cleaved fibres in Group 2 (see section 3.6), were of a similar spherical nature to the launch end (see Figure 6.25 (a)), it was not clear why the irregular structure of Group 1 cleaves had occurred. However, one possible explanation could lie with the silica glass melting vessel used to make the final distilled glass. As discussed in section 6.2.4, the final section of the silica glass distillation rig (D_HAP004) used to melt and homogenised the $Ge_{20}Sb_{10}Se_{70}$ at. % glass, had to be changed due to the critical break seen in Figure 6.22 (b). Whereas, it had been initially indented to use the 10/14 mm diameter silica tube encased by wire region E (Figure 6.22 (a)), the distilled $Ge_{20}Sb_{10}Se_{70}$ at. % glass instead had to be melted, quenched and annealed into the 10/14 mm diameter silica tube encased by wire regions A and B *i.e.* the section of glassware which had been modified with the silica glass dots. Although inconclusive, it is possible that this 10/14 mm silica tube could have been misshaped during the thermal welding of silica dots (Figure 6.25 (d)).

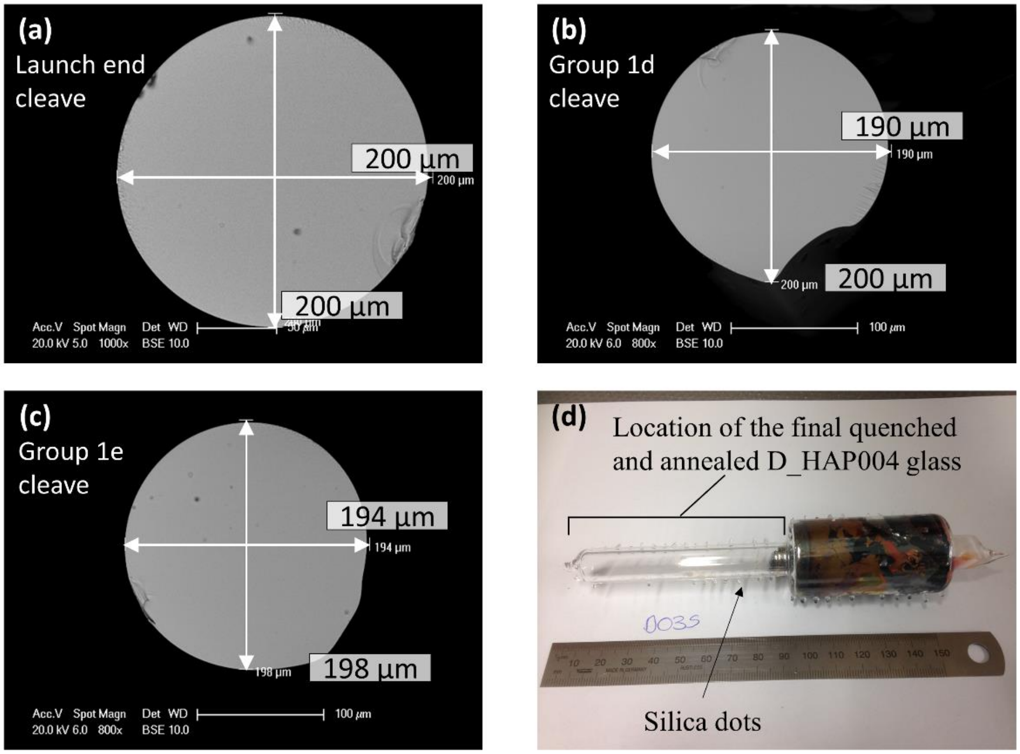

Figure 6.25: Scanning electron micrographs (SEM) of F_HAP008 cleaves from (a) the launch end, (b) Group 1d and (c) Group 1e. (d) Photograph of the distilled D_HAP004 $Ge_{20}Sb_{10}Se_{70}$ at. % glass, within the final silica glass melting vessel, prior to melting.

Nevertheless, as demonstrated by the 22 mm wide loop presented in Figure 6.26, the nominally distilled $Ge_{20}Sb_{10}Se_{70}$ at. % optical glass fibre (F_HAP008), had good strength and ductility.

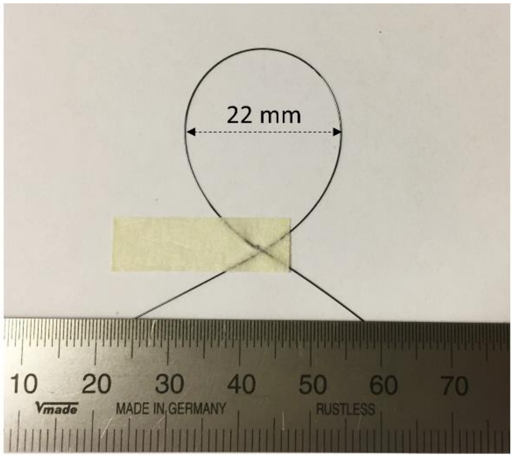

Figure 6.26: Photograph of nominally distilled $Ge_{20}Sb_{10}Se_{70}$ at. % optical fibre (F_HAP008), bent into a 22 mm wide loop without breaking.

6.4 Chapter 6 summary

The overall aim of this chapter was to produce low loss $Ge_{20}Sb_{10}Se_{70}$ at. % optical fibres. An investigation into both the precursor purification and glass distillation with getters were reported, as well as bulk and fibre characterisation. The most important points from chapter 6 are summarised below:

1) Using the Antoine equation, vapour pressure-temperature curves were calculated for each of the relevant precursors (Se, Sb and S) and their corresponding oxides (SeO_2, Sb_2O_3 and SO_2, respectively). At 260 °C it was found that there was a relatively large difference in the calculated vapour pressures between Se (0.003 kPa) and SeO_2 (6.85 kPa) likewise, at 160 °C for S (0.013 kPa) and SO_2 (5948.3 kPa). This confirmed that the initial temperatures used for Se and S bake-out purification were adequate. Furthermore, a 'lower and slower' approach was also found to be most appropriate for the bake-out purification of Sb since, all the material had vapourised after a short 1 hr dwell at 700 °C. Therefore, the longer 3 hr dwell at 570°C confirmed that the calculated vapour pressures of Sb (0.002 kPa) and Sb (0.220 kPa) were suitable.

2) Developing a suitable distillation procedure for $Ge_{20}Sb_{10}Se_{70}$ at. % glass with 1000 ppm wt. $TeCl_4$ [H getter] and 700 ppm wt. Al [O getter], proved challenging. It was found that an inefficient removal of $HCl_{(g)}$ as well as, chalcogenide material

separation, either in the charge or distillate end, were the main two factors preventing the $Ge_{20}Sb_{10}Se_{70}$ at. % glass from successfully distilling.

3) To overcome this, the silica glass distillation container was modified with silica glass dots, so that wire could be wrapped around specific regions. Connecting these wire sections to a power supply, along with a smaller clamshell furnace over the charge chamber, allowed the distillation temperatures to be controlled more precisely. Using eight thermocouples, the $Ge_{20}Sb_{10}Se_{70}$ at. % glass was shown to successfully distil at temperatures close to 693 °C in an open, vacuum system.

4) The as-annealed 10 mm diameter, distilled $Ge_{20}Sb_{10}Se_{70}$ at. % glass rod was drawn into optical fibres with a ~200 µm diameter. Using an 18 m long section, the optical fibre loss of the distilled $Ge_{20}Sb_{10}Se_{70}$ at. % glass was measured and showed remarkably low loss between 2 µm and 10 µm. Furthermore, SEM-EDX analysis showed that the final distilled glass composition ($Ge_{21.1}Sb_{10.6}Se_{68.3}$ ±0.5 at. %) was close to the nominally batched $Ge_{20}Sb_{10}Se_{70}$ at. % glass.

Chapter 7: Cytotoxicity investigations of Ge-Sb-Se optical fibres

Although much research has focussed on the development of novel chalcogenides for a variety of biophotonic applications, no comprehensive study has been made towards the biocompatibility of their glasses. Therefore, this final section aims to provide an initial insight into *in-vitro* cytotoxicity of chalcogenide optical fibres.

7.1 Chapter overview

In accordance with ISO 10993-5[182] two *in-vitro* tests are used to study the cytotoxicity of several chalcogenide compositions: 1) a direct contact protocol and 2) an elution protocol. The end point assays used to measure these tests were: 1) an alamarBlue® assay and 2) a Neutral Red (NR) assay, respectively. Under close supervision by this Author, the experimental work was conducted by two 4th year undergraduate Mechanical Engineering students Mr T. Kubiena (2015/16) and Mr W. Gan (2016/17). Figure 7.1 provides an overview of the work to be reported in this chapter as well as indicating which trial was conducted by which student. It should also be noted that as well as investigating cell viability *via* a direct-contact alamarBlue® assay, Trial 1 also takes a brief look at contact angle measurements on bulk $Ge_{20}Sb_{10}Se_{70}$ at. % glass (M_HAP006).

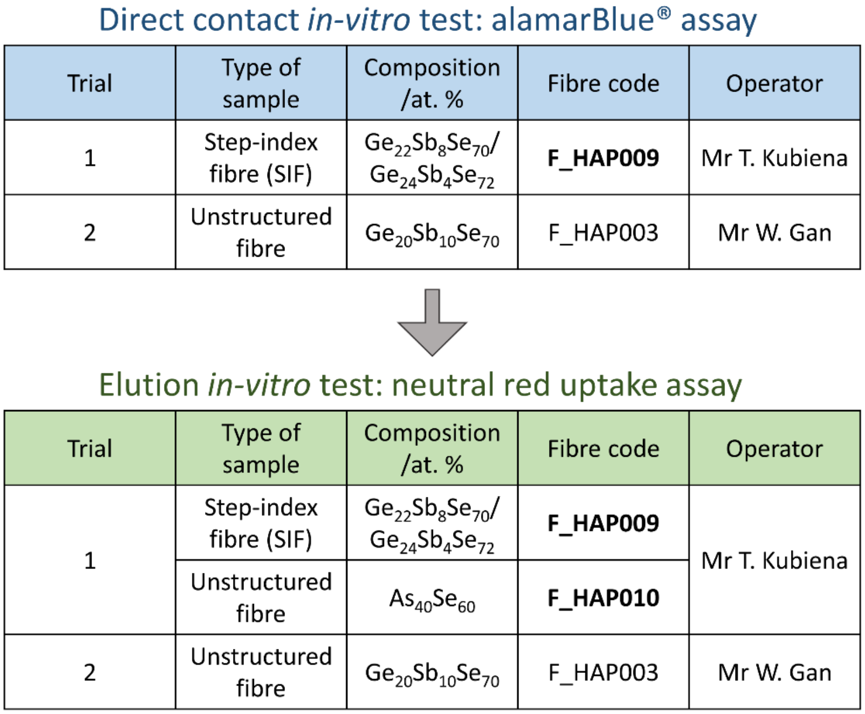

Direct contact *in-vitro* test: alamarBlue® assay

Trial	Type of sample	Composition /at. %	Fibre code	Operator
1	Step-index fibre (SIF)	$Ge_{22}Sb_8Se_{70}$/ $Ge_{24}Sb_4Se_{72}$	**F_HAP009**	Mr T. Kubiena
2	Unstructured fibre	$Ge_{20}Sb_{10}Se_{70}$	F_HAP003	Mr W. Gan

Elution *in-vitro* test: neutral red uptake assay

Trial	Type of sample	Composition /at. %	Fibre code	Operator
1	Step-index fibre (SIF)	$Ge_{22}Sb_8Se_{70}$/ $Ge_{24}Sb_4Se_{72}$	**F_HAP009**	Mr T. Kubiena
	Unstructured fibre	$As_{40}Se_{60}$	**F_HAP010**	
2	Unstructured fibre	$Ge_{20}Sb_{10}Se_{70}$	F_HAP003	Mr W. Gan

Figure 7.1: Overview of the experimental work presented in chapter 7 and conducted by final year Mechanical Engineering undergraduate students. Bold fibre codes indicate the use of glass fibres made by another member of the Mid-infrared Phtonics Group.

Ideally, the same Ge-Sb-Se composition would have been used throughout the investigation however, due to a lack of availability, Mr T. Kubiena had to test a similar Ge-Sb-Se step-index fibre (SIF) (F_HAP009), previously drawn by another member of the Mid-infrared Photonics Group. The impact of this inconsistency, will be discussed in a later section.

7.2 Direct contact protocol with alamarBlue® assay

AlamarBlue® (resazurin) is a nontoxic assay, ideal for *in-vitro* cytotoxicity investigations, as it is simple, rapid and sensitive to cell viability[181]. Fundamentally, it works through the reduction of non-fluorescent (blue) resazurin into the fluorescent (pink) resorufin form (see Figure 7.2) by cell activity, which is associated with the consumption of oxygen during metabolism[181].

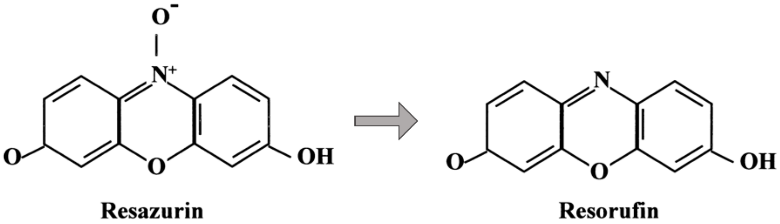

Figure 7.2: Structures of resazurin (alamarBlue®) and resarufin (reduced alamarBlue®) structures. Adapted from[181].

A direct correlation between the reduction of alamarBlue® in growth media and the proliferation of mammalian cells has been shown *in-vitro*[181]. Therefore, this test was chosen for cytotoxicity evaluation of Ge-Sb-Se chalcogenide fibres based on the response of 3T3 fibroblast cells.

Each direct contact test, presented in Trial 1 (section 7.2.1) and Trial 2 (section 7.2.2), was based on three types of material: etched Ge-Sb-Se fibres, non-etched Ge-Sb-Se fibres and a negative control polycarbonate membrane. As shown in Figure 3.21, each type of material was repeated four times and from each sample well, three aliquots were taken for analysis. Therefore, each alamarBlue® reading was based on 12 fluorescence readings *i.e.* n= 12.

7.2.1 Trial 1

7.2.1.1 Direct contact test- alamarBlue® assay

In Figure 7.3, the direct contact cytotoxicity results of $Ge_{22}Sb_{8}Se_{70}/Ge_{24}Sb_{4}Se_{72}$ at. % SIFs (F_HAP009) are presented using the alamarBlue® end point assay. Compared to the polycarbonate membrane, *i.e.* an empty Corning Transwell Insert (see Figure 3.20) which acted as a negative control, there was an obvious difference in 3T3 fibroblast response towards the etched and non-etched fibres (F_HAP009). After 1 day of exposure, there was very little fluorescence from any of the test samples however, after 3 days Figure 7.3 shows that there was an average 151 relative fluorescence (RFU) from the polycarbonate membrane negative control, 1 RFU from the non-etched Ge-Sb-Se fibre (F_HAP009) and 124 RFU from the etched Ge-Sb-Se fibre (F_HAP009). This response was further enhanced after 7 days of exposure where the polycarbonate control exhibited 257

RFU and the etched Ge-Sb-Se (F_HAP009) fibre showed 233 RFU. The non-etched Ge-Sb-Se fibre (F_HAP009) showed little improvement. On day 14, there was a decrease in fluorescence from both the polycarbonate control and etched Ge-Sb-Se samples, which showed an average of 181 RFU and 145 RFU, respectively. Once again, the fluorescence from non-etched fibres (F_HAP009) remained low at 18 RFU.

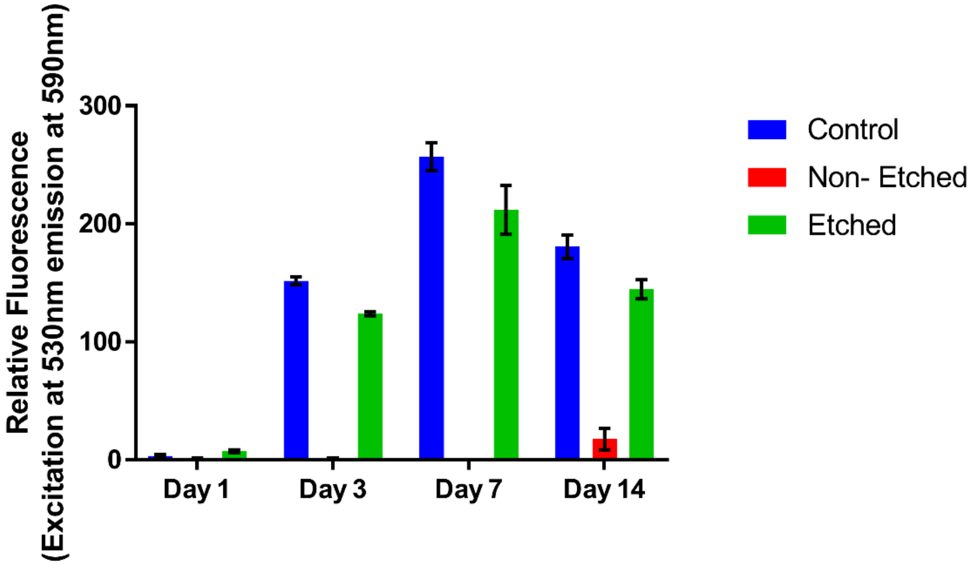

Figure 7.3: Relative fluorescence of 3T3 cell's exposure to $Ge_{22}Sb_8Se_{70}/Ge_{24}Sb_4Se_{72}$ at. % SIFs (F_HAP009) with a polycarbonate membrane as a negative control for the durations of: 1, 3, 7 and 14 days. Results measured through the reduction of resazurin into fluorescent resarufin, normalised against blank reading. Error bars show the standard error of the mean (SEM).

As expected, results from 2way analysis of variance (ANOVA) concluded that after 3 days of exposure, there were significant differences between the control *vs.* non-etched samples (P <0.0001) and the non-etched *vs.* etched samples (P <0.0001). However, there was not a significant difference between the control *vs.* etched samples (P= 0.0510). By day 7, there was significant difference between all three samples. Whilst the control *vs.* non-etched samples and the non-etched *vs.* etched samples both remained at P <0.0001, the control *vs.* etched samples also had a significant difference (P= 0.0006). After 14 days exposure, all three samples were still showing a significant difference in response with the control *vs.* non-etched samples and the non-etched *vs.* etched samples, once again remaining at P= <0.0001 and the control *vs.* etched samples at P=0.0077.

From quantitative alamarBlue® results alone, it would seem that propylamine-etched Ge-Sb-Se fibres (F_HAP009) did not elicit a cytotoxic response when exposed to 3T3 fibroblast cells whereas, non-etched Ge-Sb-Se fibres (F_HAP009) did.

Based on the work by Wilhelm *et al.*[174], this discrepancy was likely due to an oxide layer present on the surface of non-etched Ge-Sb-Se fibres. Within their report, Wilhelm *et al.*[174] demonstrate that once their chalcogenide samples had been etched in water, the resulting surface was then compliant with cell proliferation. Therefore, it would seem from Figure 7.3, that as long as the Ge-Sb-Se fibres were in their fresh state *i.e.* no presence of an oxide layer, they are non-toxic to 3T3 fibroblast cells.

7.2.1.2 Direct contact test- scanning electron microscopy (SEM) images

However, conclusions should not be drawn from the quantitative result alone, particularly as there are a number of pitfalls associated with the alamarBlue® assay *e.g.* the further reduction of fluorescent (pink) resorufin into non-fluorescent (colourless) hydroresorufin. O'Brien *et al.*[181] explains that for investigations which have not checked the reduction rate of cells in culture prior to testing, a weak signal produced from the additional reduction of resorufin by healthy cells, could be misinterpreted as a low level of metabolic activity.

Therefore, to compliment the quantitative assay shown so far, SEM imaging was used at each time point to qualitatively evaluate each sample. Here results from both techniques will be directly compared, beginning with the empty polycarbonate membrane (negative control) seen in Figure 7.4.

After a single day of exposure, Figure 7.4(a) revealed that very few 3T3 fibroblasts were present on the surface of the polycarbonate membrane which correlated with the low fluorescence result presented in Figure 7.3. Of those 3T3 fibroblasts that were present however, the inset in Figure 7.4 (a) suggests that they were in a healthy state as demonstrated by the presence of numerous filopodia (fibrous projections[207]).

To provide a brief context, when a cell comes into contact with a material, there are a sequence of events that may occur which ultimately dictate whether or not a cell will attach[208]. For materials with a hydrophilic surface, this process begins with the adherence of water molecules, followed by a layer of proteins. Relevant cells will then explore the surface of the material, using the filopodia extensions, until a specific protein-binding site is found. Once attached to the substratum, lamellipodia extend towards the protein-binding site which, in turn, encourages cytoplasm from the cell to flow into the projection[207]. Eventually the cells will assume a flat morphology, as schematically demonstrated in Figure 2.18.

This behaviour was made even more apparent in Figure 7.4 (b) which shows an increased number of cells on the surface of the polycarbonate membrane, after 3 days of exposure. Long filopodia projections were once again visible from numerous 3T3 fibroblast cells and thus supported the increase in fluorescence seen in by the alamarBlue® results in Figure 7.3.

By day 7, the polycarbonate membrane was almost entirely covered by a confluent layer of 3T3 fibroblast cells as shown in Figure 7.4 (c). This reflected the maximum level of fluorescence recorded through the alamarBlue® assay in Figure 7.3 and could provide some explanation as to why the fluorescence subsequently dropped. As depicted in Figure 7.4 (d), after 14 days of exposure 3T3 fibroblast cells had proliferated so much that the surface seemed to have an over confluent layer. If correct, this may have created an environment where cells were several layers deep and thus began to die *i.e.* reflecting the reduction in fluorescence observed in Figure 7.3.

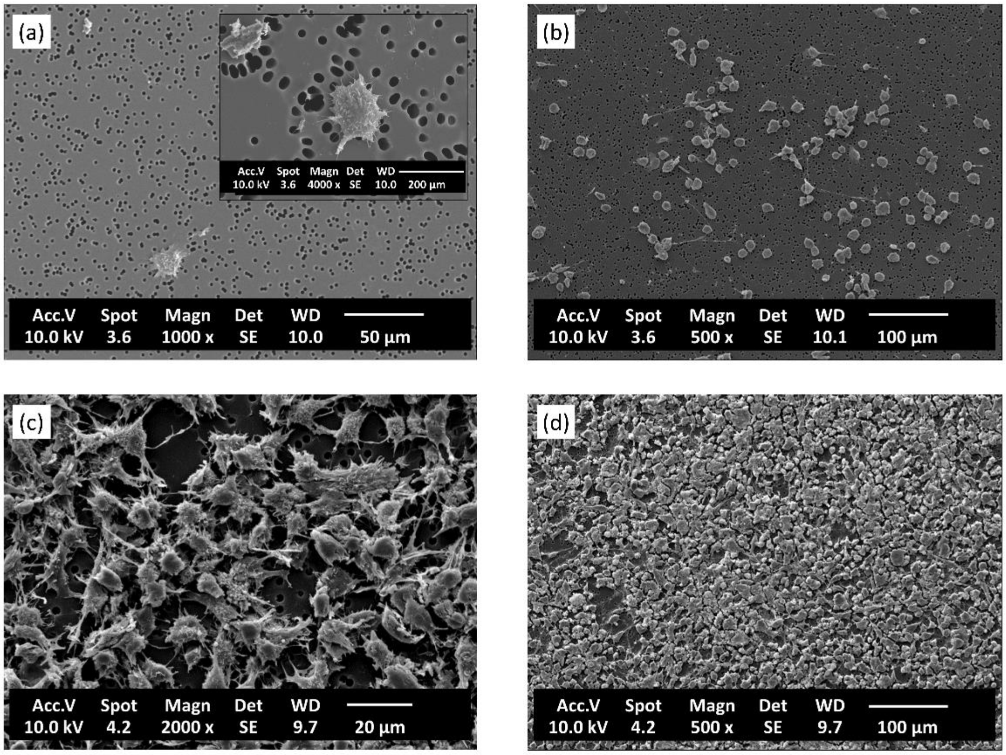

Figure 7.4: Scanning electron microscopy (SEM) images of 3T3 fibroblast cell growth on polycarbonate membrane incubated at 37 °C and 5 % CO$_2$ for 1 day (a), 3 days (b), 7 days (c) and 14 days (d).

In Figure 7.5, the SEM images of non-etched Ge-Sb-Se fibres (F_HAP009) are presented and show, that unlike the negative control polycarbonate membrane (Figure 7.4), very few cells were observed on both the surfaces of the non-etched Ge-Sb-Se fibres (F_HAP009) and the sample polycarbonate membrane. These results supported the low levels of fluorescence seen during the alamarBlue® assay (Figure 7.3) and suggest that the non-etched Ge-Sb-Se fibres were toxic to 3T3 fibroblast cells. Similar to the work conducted by Wilhelm *et al.*[174](see section 2.7), it is possible that the non-etched Ge-Sb-Se fibres (F_HAP009) also presented an oxide layer on their surface which solubilised during the direct contact protocol (see section 3.7.2) thus, creating an environment in which the 3T3 fibroblast cell could not survive.

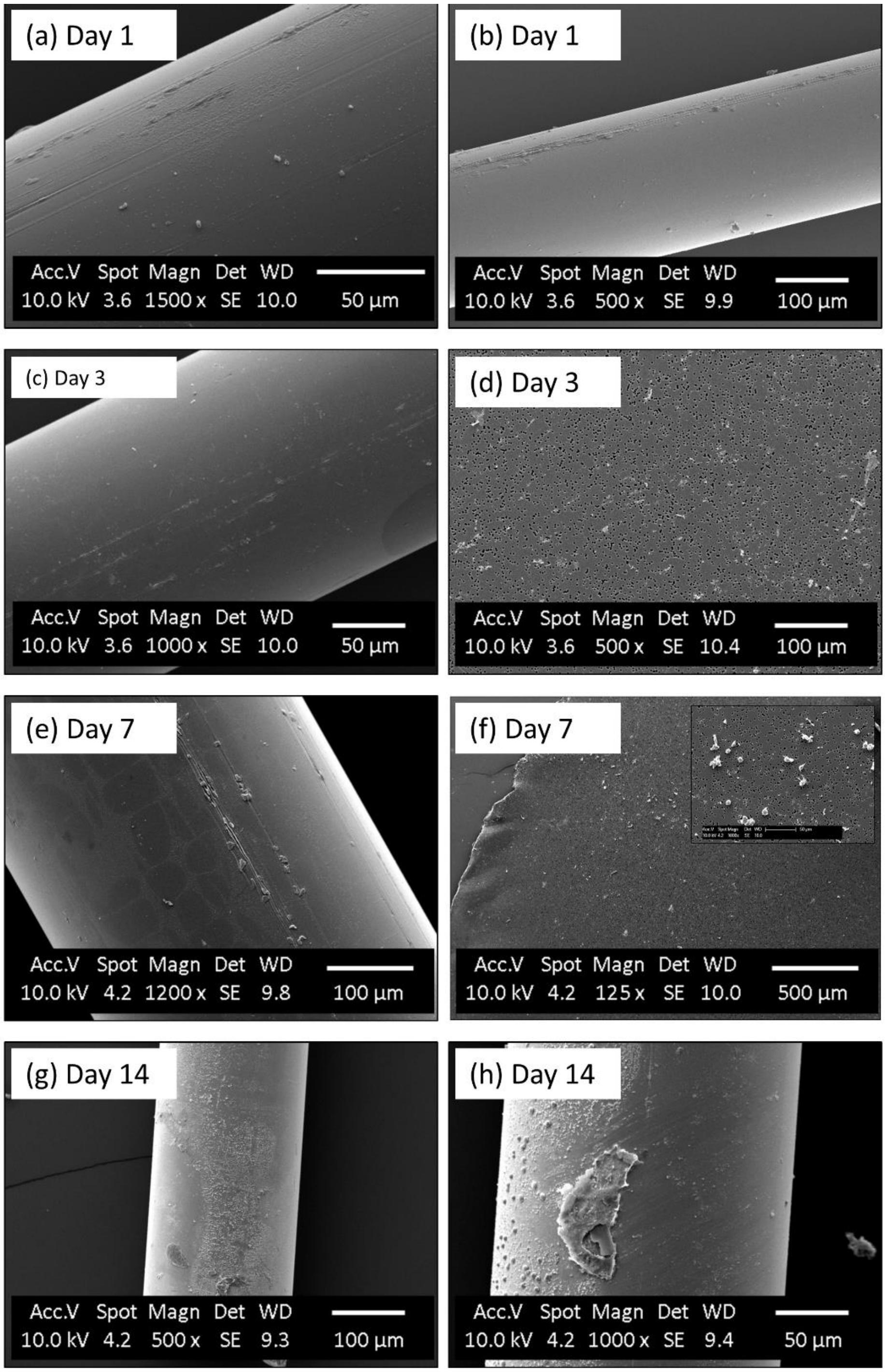

Figure 7.5: Scanning electron microscopy (SEM) images of 3T3 fibroblast cell growth on non-etched $Ge_{22}Sb_8Se_{70}/Ge_{24}Sb_4Se_{72}$ at. % SIFs incubated at 37 °C and 5 % CO_2 for 1 day (a) and (b), 3 days (c) and (d), 7 days (e) and (f), and 14 days (g) and (h). Images (d) and (f) show the polycarbonate membrane below non-etched fibres. Note that the surface features present in (e), (g) and (h) were likely caused by inadequate PBS washing prior to sample fixing or possibly from faulty SEM platinum sputtering.

Considering the successful match between alamarBlue® and the SEM images for both the negative control and the non-etched Ge-Sb-Se fibres, qualitative examination of the propylamine-etched Ge-Sb-Se was expected to follow suit.

However, as the SEM images in Figure 7.6 demonstrate, there was no significant growth of 3T3 fibroblasts on the surface of the etched Ge-Sb-Se fibres (F_HAP009). Instead, as Figure 7.6 (d), (f) and (h) show, most of the growth was found on the sample polycarbonate membrane below. Therefore, although the alamarBlue® results for etched Ge-Sb-Se fibres (F_HAP009) in Figure 7.3 had shown relatively high levels of fluorescence for days 3, 7 and 14, the reduction of resazurin to resorufin had most likely come from the 3T3 fibroblasts attached to the sample polycarbonate membrane. Consequently, it would have been wrong to assume that the surface of etched Ge-Sb-Se fibres (F_HAP009) had fully supported 3T3 fibroblast proliferation. Nevertheless, the fact that healthy cells were present within the well (Figure 7.6) suggested that, unlike the non-etched Ge-Sb-Se fibres (F_HAP009), there were no leachable toxins in the etched Ge-Sb-Se fibre (F_HAP009) media and, even though SEM images seemed to suggest that the 3T3 fibroblasts preferred to attached to the sample polycarbonate membrane, evidence that there were 3T3 fibroblasts proliferating on the surface of the etched Ge-Sb-Se fibre (F_HAP009) (Figure 7.6 (b), (c) and (e)) implies that there was no cytotoxic response.

Similar to the negative control polycarbonate membrane in Figure 7.4 (d), by day 14 an over-confluent layer of 3T3 fibroblasts had developed on the sample polycarbonate membrane of the etched Ge-Sb-Se fibre (F_HAP009) well, shown in Figure 7.6 (h). Once again this correlated with the drop in alamarBlue® fluorescence as demonstrated in Figure 7.3.

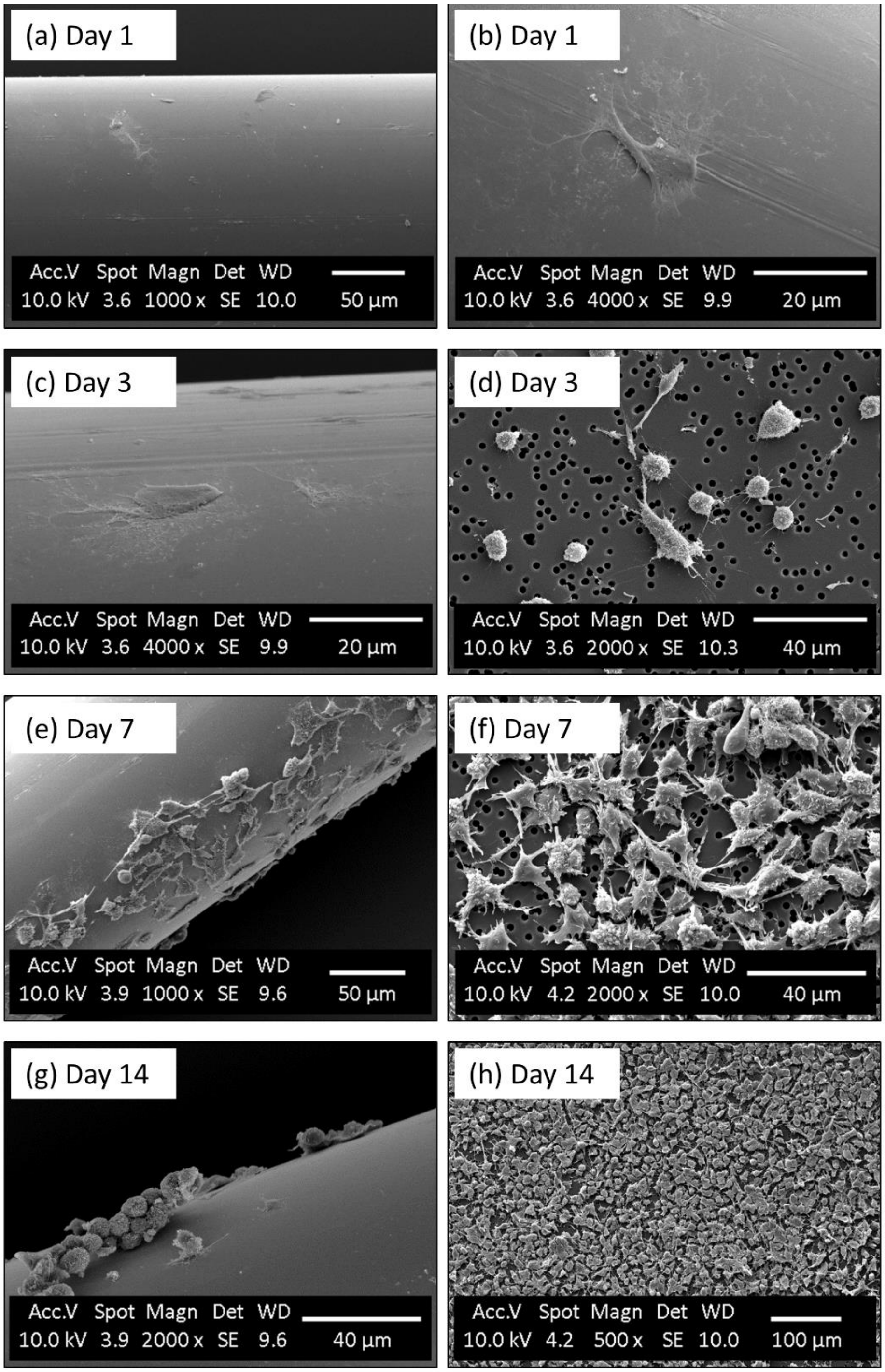

Figure 7.6: Scanning electron microscopy (SEM) images of 3T3 fibroblast cell growth on propylamine etched $Ge_{22}Sb_8Se_{70}$/$Ge_{24}Sb_4Se_{72}$ at. % SIFs incubated at 37 °C and 5 % CO_2 for 1 day (a) and (b), 3 days (c) and (d), 7 days (e) and (f), and 14 days (g) and (h). Images (d), (f) and (h) show polycarbonate membrane below etched fibres.

7.2.1.3 Contact angle measurements

As previously discussed in section 7.2.1.2, the attachment of cells onto a material is only possible through a cascade of events. The disposition for 3T3 fibroblasts to attach primarily to the surface of the sample polycarbonate membrane rather than etched Ge-Sb-Se fibre (F_HAP009), could be explained by an initial lack of water molecule/protein adhesion from the cell culture media. The nature of the interface between the material and cells is largely dictated by surface topography, energy and chemistry. Of these, the surface energy is considered the most important, as this controls its wettability and thus, affiliation with proteins and cells[208]. Since SEM results seen in Figure 7.6 (a) and (c) are typical of a hydrophobic surface, contact angle measurements using a goniometer (KRÜSS, DSA 10-MK 2) were investigated on a polished (Figure 7.7) and an oxidised (Figure 7.8), as-annealed Ge-Sb-Se bulk glass. These sample conditions aimed to imitate the worse-case scenario for etched and non-etched Ge-Sb-Se fibres, respectively.

Unfortunately, for this investigation, there were no bulk glasses available for either of the $Ge_{22}Sb_{8}Se_{70}$/$Ge_{24}Sb_{4}Se_{72}$ at. % glasses at the time of Trial 1 (section 7.2.1.1). Therefore, a similar bulk glass (made by the Author) with a composition of $Ge_{20}Sb_{10}Se_{70}$ at. % (M_HAP006) was used for analysis.

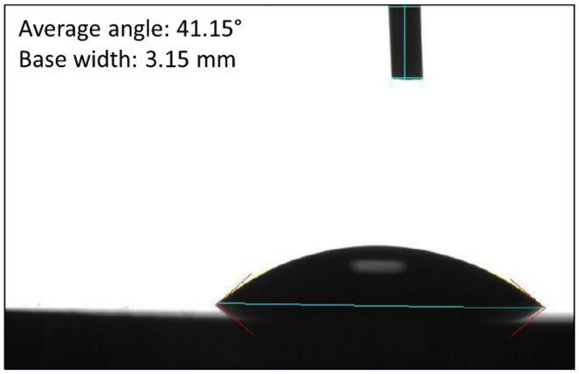

Figure 7.7: Contact angle measurements of a 5 µl drop of deionised water on a polished as-annealed $Ge_{20}Sb_{10}Se_{70}$ at. % bulk sample (M_HAP006).

The hydrophobicity of chalcogenide glass has previously been studied by Lucas *et al.*[209] who studied bulk chalcogenide samples prepared by the same procedure to that outlined in section 3.7.1. They found that Te-As-Se glasses exhibited a hydrophobic character, most likely due to a non-polar surface arising from a strong covalent network of similar electronegative atoms. Lucas *et al.*[209] also explained that a 5 µl water droplet, with a dielectric constant of 80.1, had a dense/round morphology on the surface of the Te-As-Se glass whilst 5 µl of THF (tetrahydrofuran), with a dielectric constant of 7.5, spread over the entire 10 mm diameter. Each had a contact angle measurement of 73 ±3 ° and <5 °, respectively. It should be mentioned that the threshold of hydrophobicity is relatively inconsistent within the literature, as McKenzie *et al.*[208] state that contact angle measurements must be greater than 90° to be considered hydrophobic.

So although previous studies[209] have shown chalcogenide glasses to be hydrophobic in character, Figure 7.7 showed that a 5 µl drop of deionised water on the surface of the polished $Ge_{20}Sb_{10}Se_{70}$ at. % sample (M_HAP006), produced a contact angle of ~41.2 ±0.7 °. If this $Ge_{20}Sb_{10}Se_{70}$ at. % bulk glass (M_HAP006) was indeed a good representation of the etched Ge-Sb-Se fibre seen in Figure 7.6, then contact angle measurements suggest its hydrophilic surface should have promoted the adherence of water molecules.

Nevertheless, material properties do not simply dictate whether or not water molecules and proteins will adhere. Instead, its surface topography, energy and chemistry will specifically regulate what type of proteins can adsorb, how many can adsorb and what their final conformation shall be[208]. Therefore, the lack of 3T3 fibroblast cells present on the surface of the etched Ge-Sb-Se fibres (F_HAP009) in Figure 7.6, cannot necessarily be attributed to a total lack of protein adherence. Instead, it is possible the surface chemistry of the fibre may have promoted the wrong type of protein attachment or may have even obscured correct cell binding sites.

Regardless of the cause, the apparent hydrophilic character of $Ge_{20}Sb_{10}Se_{70}$ at. % bulk glass (M_HAP006) shown in Figure 7.7 (a), cannot entirely be used to explain the results from the $Ge_{22}Sb_{8}Se_{70}$/ $Ge_{24}Sb_{4}Se_{72}$ at. % fibre in Figure 7.6. Although Ge-Sb-Se glass samples were homogeneously fabricated as outlined in sections 3.3 and 3.4, there is always the possibility that atomic ordering and bonding can vary even within the same material, let alone from one glass composition to another. Thus, the surface properties of each Ge-Sb-Se sample may well be different in character.

However, for an additional insight into the potential toxicity of non-etched $Ge_{20}Sb_{10}Se_{70}$ at. % bulk glasses, a second sample was prepared (as described in section 3.7.1) and oxidised using hydrogen peroxide. As shown in Figure 7.8, the liquid-surface angle was further reduced to ~5.1 ±2.8 ° suggesting that the oxide-layer was extremely hydrophilic. Since, material surfaces this hydrophilic have been shown to prevent the adsorption of proteins, or cause them to weakly bond in rigid and denatured forms[210], contact angle measurements from the oxidised, as-annealed $Ge_{20}Sb_{10}Se_{70}$ at. % bulk glass could explain why very few 3T3 fibroblasts were attached to the non-etched Ge-Sb-Se fibres (F_HAP009). However, this highly hydrophilic surface also supported the assumption that substances, most likely an oxide layer, had become soluble during the alamarBlue® investigation of non-etched Ge-Sb-Se fibres (F_HAP009), which created a toxic environment within the entirety of the test well. Hence, explaining why no 3T3 fibroblast cells were observed on the sample polycarbonate membrane.

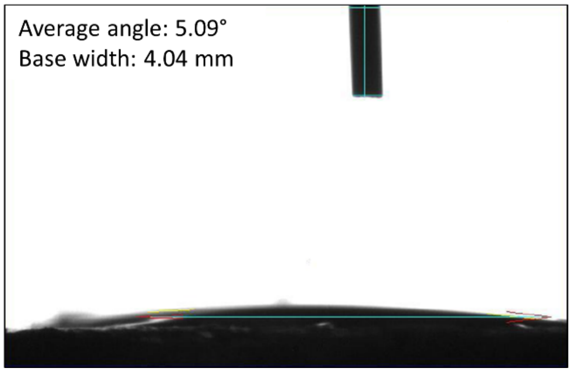

Figure 7.8: Contact angle measurements of a 5 µl drop of deionised water on an oxidised as-annealed $Ge_{20}Sb_{10}Se_{70}$ at. % bulk sample (M_HAP006).

7.2.2 Trial 2

To confirm the results presented in Trial 1, the entire direct-contact alamarBlue® investigation was repeated once more using $Ge_{20}Sb_{10}Se_{70}$ at. % fibres (F_HAP003), which were now readily available to the operator.

7.2.2.1 Direct contact test- alamarBlue®

Cytotoxicity tests in Trial 2 were conducted on an unstructured $Ge_{20}Sb_{10}Se_{70}$ at. % fibre (F_HAP003) which had been exposed to atmosphere for approx. 9 months (similar timescale to Trial 1, section 7.2.1). Since there was such a dramatic difference between the cytotoxicity of etched and non-etched Ge-Sb-Se fibres from Trial 1, results from the alamarBlue® assay, presented in Figure 7.9, were unexpected as both types of Ge-Sb-Se fibres (F_HAP003) now showed relatively high levels of florescence.

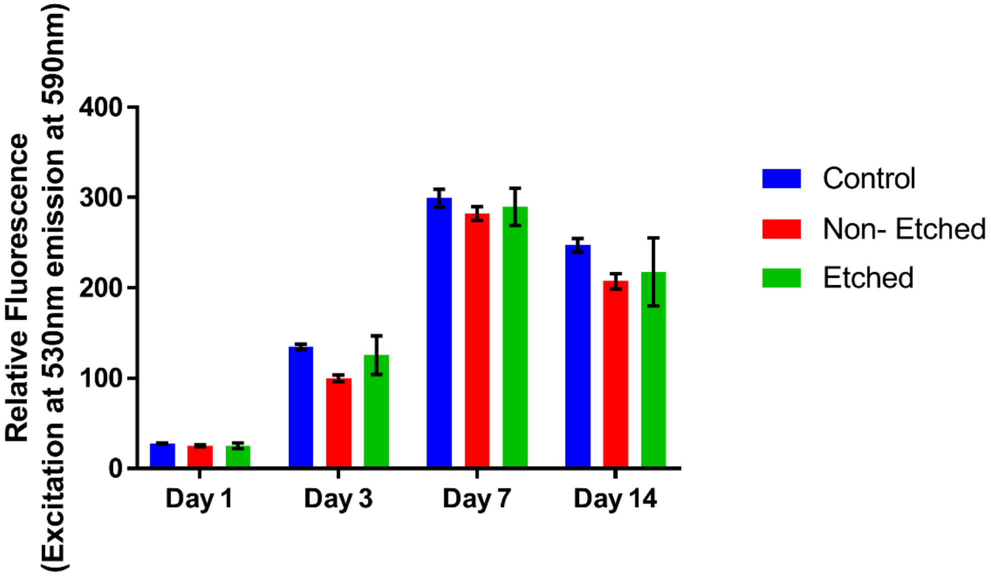

Figure 7.9: Relative fluorescence of 3T3 cell's exposure to unstructured $Ge_{20}Sb_{10}Se_{70}$ at. % fibres (F_HAP003) with a polycarbonate membrane as a negative control for the durations of: 1, 3, 7 and 14 days. Results measured through the reduction of resazurin into fluorescent resarufin, normalised against blank readings. Error bars show the standard error of the mean (SEM).

Furthermore, 2way ANOVA found that very few data points were significant. Those that did, included the control *vs.* non-etched Ge-Sb-Se fibres (F_HAP003) on day 3 (P= 0.0006); the non-etched *vs.* etched Ge-Sb-Se fibres (F_HAP003) on day 3 (P= 0.0158); the control *vs.* non-etched Ge-Sb-Se fibre (F_HAP003) on day 14 (P <0.0001) and finally the control *vs.* etched Ge-Sb-Se fibre (F_HAP003) on day 14 (P= 0.0048). Overall, the level of fluorescence from each sample in Figure 7.9 was also higher than Trial 1 *e.g.* on day 7 the negative control polycarbonate membrane showed 257 RFU from Trial 1 and 299 RFU from Trial 2.

However, both alamarBlue® investigations did share a similar trend in results, expressing the highest level of fluorescence on day 7, followed by a gradual decrease to day 14.

7.2.2.2 Direct contact test- scanning electron microscopy (SEM) images

Once again, quantitative alamarBlue® results were compared to relevant SEM images, beginning with the negative control polycarbonate membrane shown in Figure 7.10.

Similar to Trial 1, 3T3 fibroblasts were shown to readily attach to the surface of the polycarbonate membrane and adopt a flattened morphology with filopodia projections. As with Figure 7.4, the progression of a 3T3 fibroblast confluent layer was well mapped from Figure 7.10 (a) to (d), whilst demonstrating a greater number of cells at each stage when compared to the SEM images from Trial 1. Not only did each time point match its corresponding alamarBlue® measurement (Figure 7.9), it also reflected the slight increase in fluorescence from Trial 1 to 2.

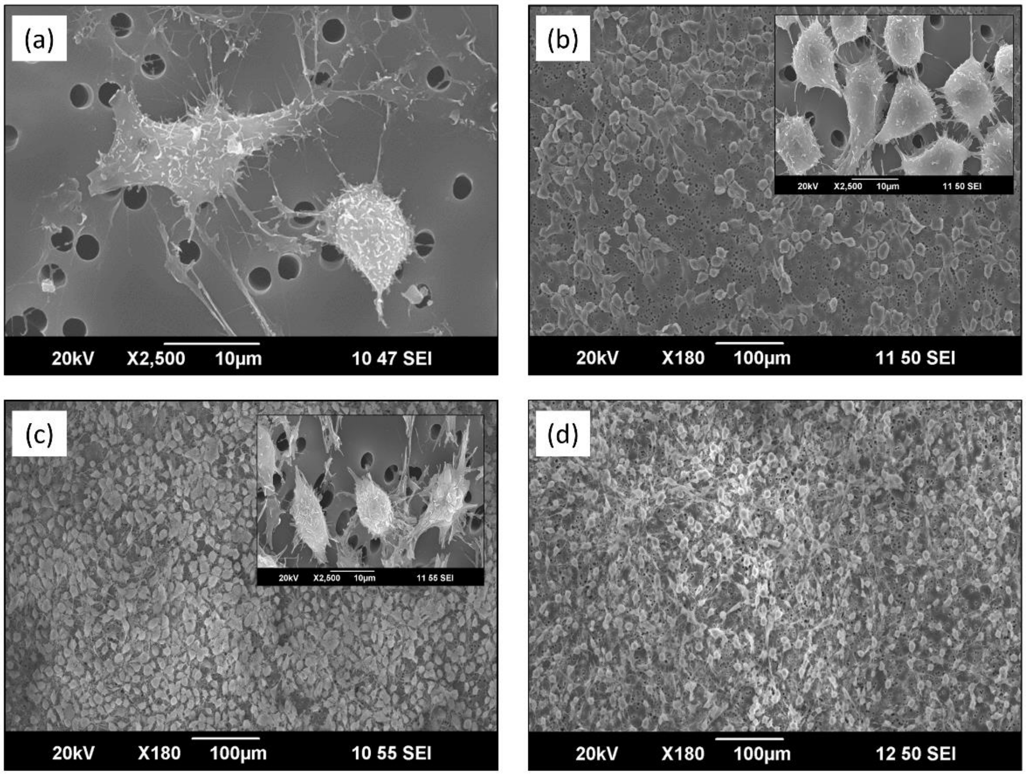

Figure 7.10: Scanning electron microscopy (SEM) images of 3T3 fibroblast cell growth on the negative control polycarbonate membrane incubated at 37 °C and 5 % CO_2 for 1 day (a), 3 days (b), 7 days (c) and 14 days (d).

In Figure 7.11, the SEM images of the non-etched Ge-Sb-Se fibres (F_HAP003) are presented. Whereas very little cell viability was seen on the non-etched Ge-Sb-Se fibres (F_HAP009) from Trial 1, Figure 7.11 reveals a significant increase in cell adhesion during Trial 2.

Adhered 3T3 fibroblasts were clearly seen on the surface of the non-etched Ge-Sb-Se fibres (F_HAP003) by day 3 (Figure 7.11 (c)), day 7 (Figure 7.11 (e) and (f)) and to some extent on day 14 (Figure 7.11 (h)). Not only did this show that the non-etched Ge-Sb-Se fibres (F_HAP003) could support initial attachment of 3T3 fibroblasts onto their surface but, it also showed that the samples could sustain cell viability for approx. 14 days. This completely contradicted the results found in Trial 1 for both the alamarBlue® assay and SEM imaging, Figure 7.3 and Figure 7.5, respectively.

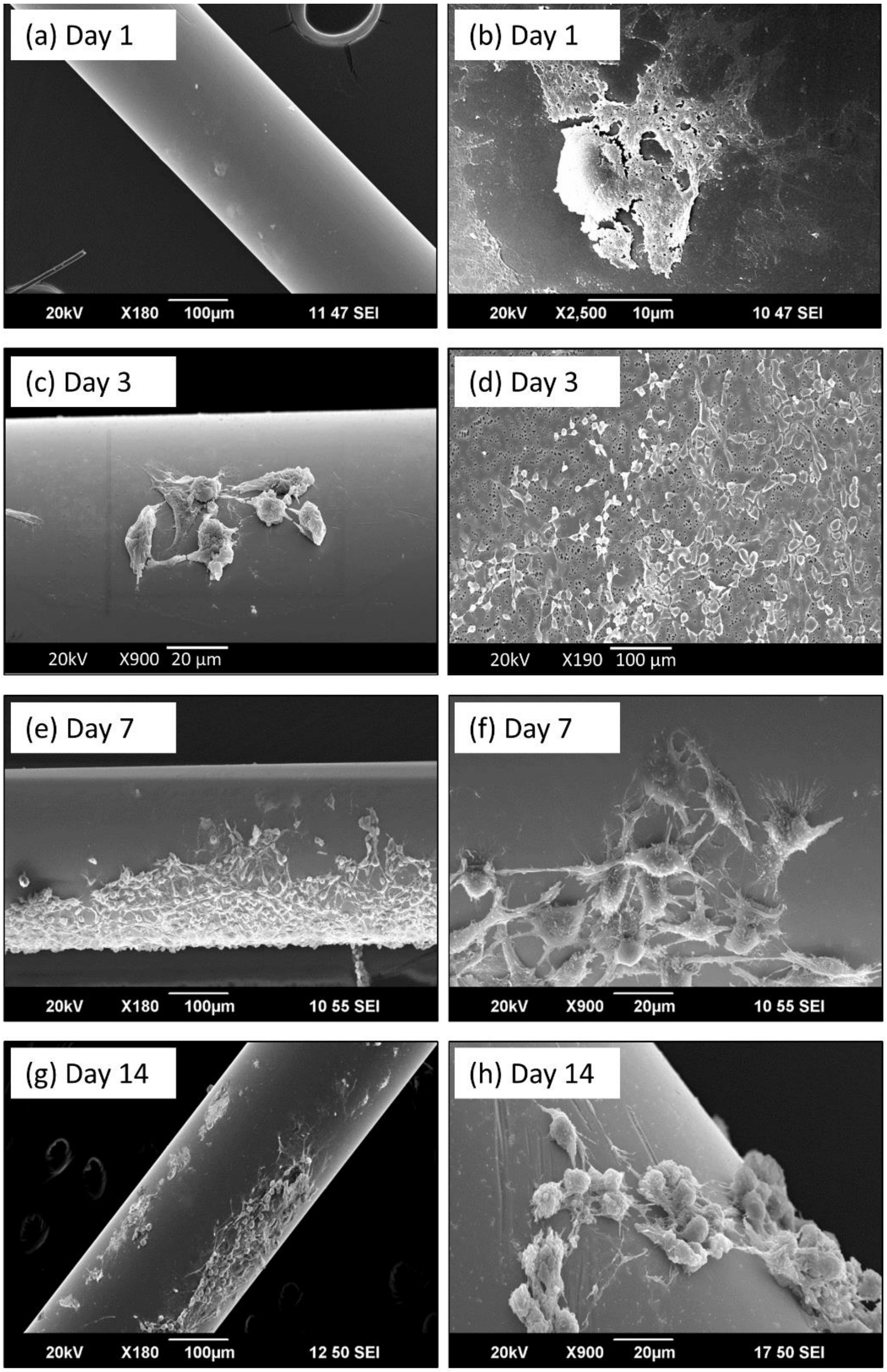

Figure 7.11: Scanning electron microscopy (SEM) images of 3T3 fibroblast cell growth on non-etched $Ge_{20}Sb_{10}Se_{70}$ *at. % fibres (F_HAP003) incubated at 37 °C and 5 %* CO_2 *for 1 day (a) and (b), 3 days (c) and (d), 7 days (e) and (f), and 14 days (g) and (h). Image (d) shows the polycarbonate membrane below the non-etched fibre.*

Finally, in Figure 7.12, SEM images for the etched Ge-Sb-Se fibres (F_HAP003) from Trial 2 can be seen. Whereas most of the 3T3 fibroblasts from Trial 1 (Figure 7.6) were found on the polycarbonate membrane below the etched Ge-Sb-Se fibres (F_HAP009), results from Trial 2 (Figure 7.12) show that a greater number of cells had adhered to the surface of the etched Ge-Sb-Se fibres (F_HAP003). So much so, that by day 14 (Figure 7.12 (g)) there was almost a confluent layer of healthy 3T3 fibroblasts present. Since, both Trials used an identical protocol (see section 3.7.2) it is possible that the difference in cell attachment was due to a subtle change in Ge-Sb-Se composition *i.e.* Trial 1 had used $Ge_{22}Sb_8Se_{70}$/ $Ge_{24}Sb_4Se_{72}$ at. % SIFs (F_HAP009) and Trial 2 had used unstructured $Ge_{20}Sb_{10}Se_{70}$ at. % fibres (F_HAP003). As previously discussed in section 7.2.1.3, this compositional variance could have altered the surface chemistry of the Ge-Sb-Se fibre and in doing so, impacted the type of protein which could adhere. Of course, there is also a possibility that the change in operator (see Figure 7.1) could have introduced additional errors.

However, as demonstrated most clearly in Figure 7.12 (b) and (f), the surface of the etched Ge-Sb-Se fibres (F_HAP003) from Trial 2, were also covered in micron-sized grooves. Initially, there were concerns that this may have arisen from the operator's handling during experiments however, special precautions were taken to ensure that the fibres were handle as little as possible whilst also minimising contact throughout the procedure *e.g.* all samples were stored and etched in individual vials. Furthermore, Wilhelm *et al.*[174] and Lucas *et al.*[180] have both reported the appearance of sub-micron pits following 24 hours of water etching on Te-As-Se samples. They found that the formation of an oxide layer was relatively non-uniform at the microscopic level and so once etched, it caused the chalcogenide surface to become pitted. Therefore, it is possible that this micro-pitting occurred following propylamine etching of the $Ge_{20}Sb_{10}Se_{70}$ at. % samples (F_HAP003), particularly as there was no evidence of pitting on the surfaces of the non-etched Ge-Sb-Se fibres (F_HAP003) in Figure 7.11.

As previously discussed by McKenzie *et al.*[208], surface topography plays an important role in protein adsorption. Therefore, the presence of nano/micro-sized pits on the surface of propylamine-etched Ge-Sb-Se fibres (F_HAP003) could have provided greater opportunities for protein adsorption and thus, subsequent cellular attachment. However, the extent to which this influenced a change in adherence of 3T3 fibroblast cells to the surface of non-etched Ge-Sb-Se fibres, from Trial 1 to Trial 2, remains unclear.

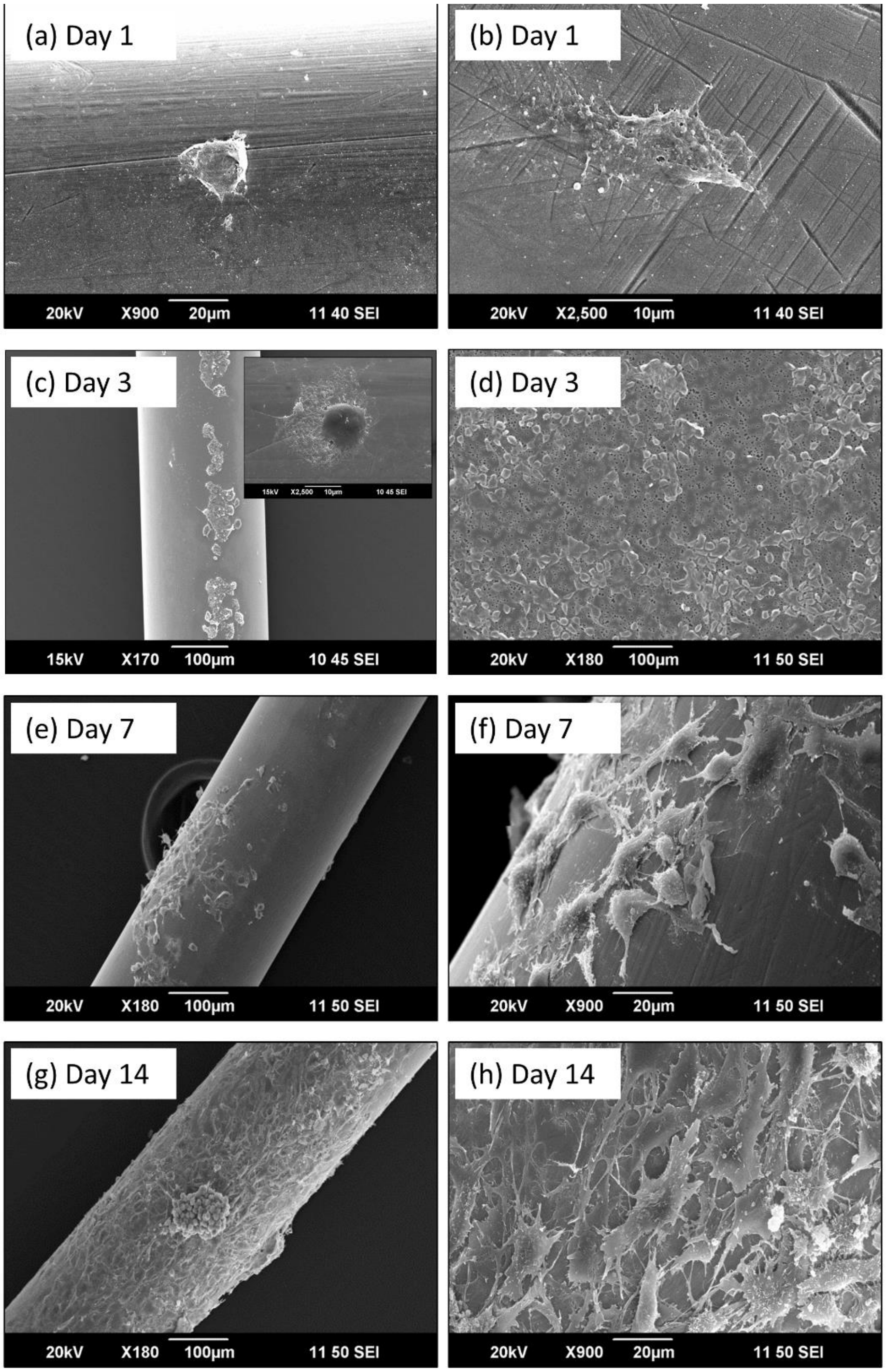

Figure 7.12: Scanning electron microscopy (SEM) images of 3T3 fibroblast cell growth on propylamine etched $Ge_{20}Sb_{10}Se_{70}$ at. % (F_HAP003) incubated at 37 °C and 5 % CO_2 for 1 day (a) and (b), 3 days (c) and (d), 7 days (e) and (f), and 14 days (g) and (h). Image (d) shows the polycarbonate membrane below etched the fibre.

7.3 Elution test with neutral red assay

To further investigate the cytotoxicity of Ge-Sb-Se glasses, an elution test was also conducted, using an endpoint neutral red (NR) assay (see section 3.7.3). Whereas, several discrepancies had been observed from the alamarBlue® assays and SEM imaging (section 7.2), a non-direct elution protocol aimed to remove the effect of protein adhesion, and thus cell adhesion, from the cytotoxic response of Ge-Sb-Se samples.

Unlike the alamarBlue® assay which relied on the reduction of resazurin to resorufin by healthy cells, the NR assay relied on the ability of living cells to incorporate and bind the weak, cationic NR dye, in lysosomes[211]. Once within the cell, the charged NR dye would then create a proton gradient, resulting in a more acidic pH environment[212]. If xenobiotics -which are defined as any foreign material or chemical found within the body[213]- were toxic, cell surfaces or lysosomal membranes would become altered, leading to a decrease in NR uptake. Measurements from NR cytotoxicity assessments were expressed as a concentration-dependent reduction of NR uptake following exposure to test samples. Results are normalised against a 100 % DMEM-FBS negative control. As discussed in section 3.7.3, four replicates of each sample (*i.e.* n= 4) were used to measure the NR uptake.

7.3.1 Trial 1

The first elution test was conducted by a supervised MEng student, Mr T. Kubiena, who used a variety of surface treatments on $Ge_{22}Sb_{8}Se_{70}$/$Ge_{24}Sb_{4}Se_{72}$ at. % (F_HAP009) and $As_{40}Se_{60}$ at. % (F_HAP010) fibres (see section 3.7.1). As an early investigation into the cytotoxicity of Sb- *vs.* As-containing glasses, fibre samples were initially prepared with either an etched or non-etched surface *i.e.* similar to the direct contact investigation (section 7.2). The results of these two surface treatments can be seen in Figure 7.13 (a). For clarity during the discussion, percentages that refer to the fibre-solution concentration will appear in **bold** whilst, NR percentage measurements will appear as normal text to 1 decimal place.

In Figure 7.13 (a), NR results from Ge-Sb-Se (F_HAP009) samples showed that with an increasing Ge-Sb-Se solution concentration, there was a decrease in NR uptake by 17.5 ±2 % of the DMEM-FBS control for etched Ge-Sb-Se fibres (F_HAP009) and approx. 26.5 ±4 % of the DMEM-FBS control for non-etched Ge-Sb-Se fibres (F_HAP009). Although not as obvious as the alamarBlue® results seen during section 7.2.1, 2way ANOVA once again found that there was a significant (P= 0.0022) cytotoxicity difference between the NR results for etched and non-etched Ge-Sb-Se fibres (F_HAP009). However, it was not clear why lower Ge-Sb-Se fibre-solution concentrations *i.e.* **25 %** and **50 %**, both expressed greater cell viability than the DMEM-FBS control.

Nevertheless, in a similar trend, non-etched As-Se fibres (F_HAP010) (Figure 7.13 (a)) also presented a decrease in cell viability with increasing fibre-solution concentration. However, this time the reduction of cell viability was a lot greater than the equivalent Ge-Sb-Se fibre (F_HAP009). For example, the non-etched As-Se fibre (F_HAP010) containing **100 %** fibre-solution concentration had a decreased NR uptake of 59.8 ±2 % when compared to the DMEM-FBS control whereas, the equivalent **100 %** non-etched Ge-Sb-Se fibre- solution concentration (F_HAP009) had a NR uptake decrease of only 26.5 % when compared to the DMEM-FBS. This suggested that less 3T3 fibroblasts had survived in solutions containing non-etched As-Se extracts.

The NR results of the non-etched Ge-Sb-Se (F_HAP009) *vs.* As-Se (F_HAP010) fibres were also compared using 2way ANOVA and found that all concentrations showed a significant difference between the cell viability of 3T3 fibroblasts, *e.g.* at **100 %** fibre-solution concentration, P <0.0001. To the best of our knowledge, this is the first time that As-containing glasses have been shown to be more cytotoxic than similar Sb-containing glasses.

Unlike the moderately-sigmoidal trends observed from non-etched As-Se (F_HAP010) in Figure 7.13 (a), etched As-Se fibres (F_HAP010) seemed to have a dramatic decrease in cell viability from **25-50 %** fibre-solution concentration before plateauing at a reduced NR uptake of 19.2 ±1 % cell viability for the remaining concentrations. A similar plateauing trend has been seen by Lucas *et al.*[180] who investigated the dissolution kinetics for a series of As-containing fibres immersed in water. They found that dissolution was complete after a couple of hours, following which the As-content became constant due to the insolubility of the chalcogenide glass itself. As such, apart from the **100 %** fibre-solution concentration in Figure 7.13 (a), 2way ANOVA found no significant difference between the etched and non-etched As-Se fibres (F_HAP010).

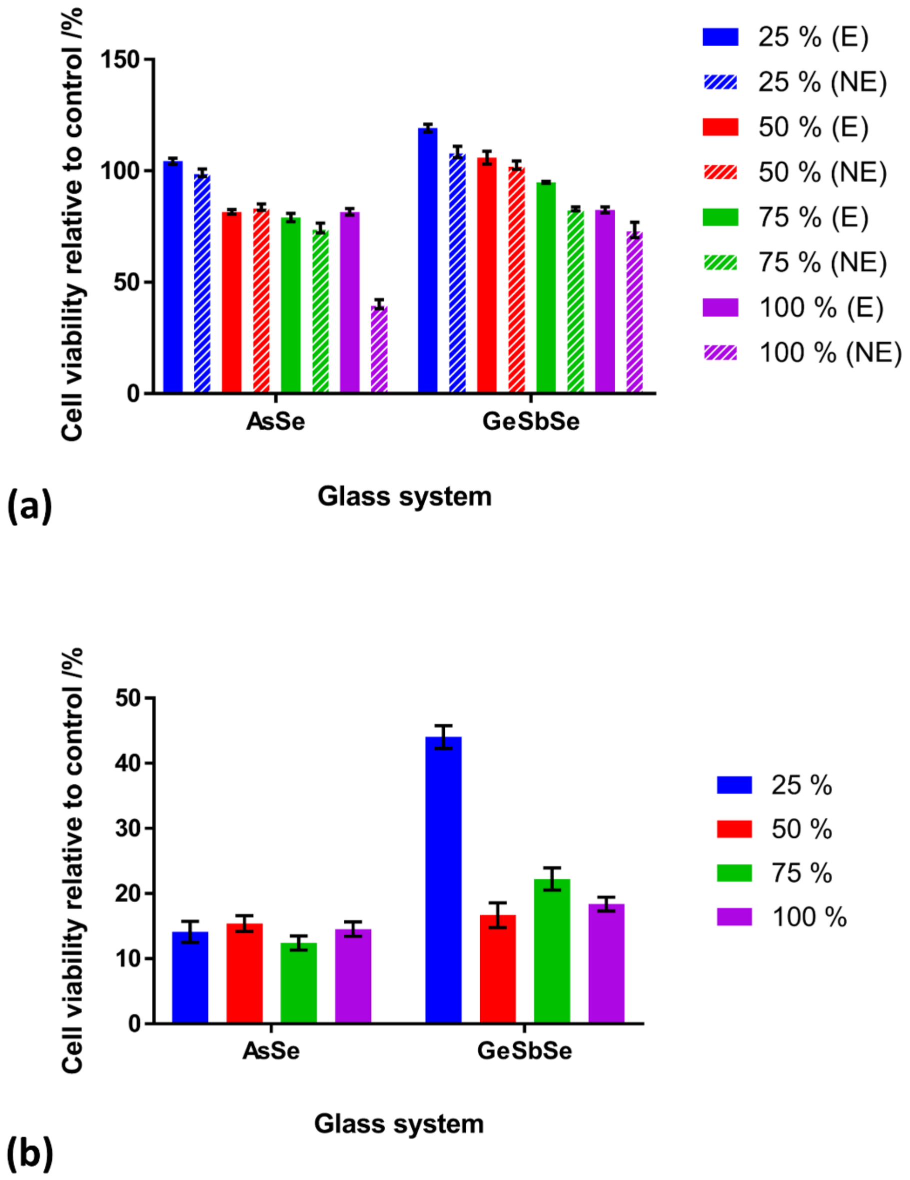

Figure 7.13: Viability of 3T3 fibroblast cells exposed for 24 hours to (a) etched and non-etched $Ge_{22}Sb_8Se_{70}/Ge_{24}Sb_4Se_{72}$ at. % (F_HAP009) and $As_{40}Se_{60}$ at. % (F_HAP010) extractables and (b) oxidised $Ge_{22}Sb_8Se_{70}/Ge_{24}Sb_4Se_{72}$ at. % (F_HAP009) and $As_{40}Se_{60}$ at. % (F_HAP010) extractables in DMEM-FBS elutant at varying concentrations: 100 %, 75 %, 50 % and 25 %. Results are normalised to 100 % DMEM-FBS control.

So far, results from Trial 1 of alamarBlue® and Trial 1 of NR assays have both agreed, that there is a significant difference between the cytotoxicity of etched and non-etched $Ge_{22}Sb_8Se_{70}/Ge_{24}Sb_4Se_{72}$ at. % SIFs (F_HAP009) and non-etched $As_{40}Se_{60}$ at. % fibres (F_HAP010). These results suggest that chalcogenide fibres, which have been left in atmosphere for a certain length of time, do indeed develop a peripheral layer which is relatively cytotoxic to 3T3 fibroblasts. Since Wilhelm *et al.*[174] reported that the identity of this surface layer was some form of oxide, $Ge_{22}Sb_8Se_{70}$/$Ge_{24}Sb_4Se_{72}$ at. % (F_HAP009) and $As_{40}Se_{60}$ at. % (F_HAP010) fibres were then treated with hydrogen peroxide to create an enhanced oxide surface. This treatment produced a thick oxide layer that was visible to the naked eye. As expected, Figure 7.13 (b) showed that the NR uptake of 3T3 fibroblasts exposed to oxidised-samples decreased dramatically for both chalcogenide compositions thus, confirming that the presence of an oxide layer is cytotoxic.

Results found that regardless of the fibre-solution concentration, all samples from the oxidised As-Se fibres (F_HAP010) had a similar decrease in 3T3 fibroblast NR uptake of 85.9 ±2 % when compared to the DMEM-FBS control *i.e.* severe cytotoxicity. Similarly, oxidised Ge-Sb-Se samples with **50 %**, **75 %**, and **100 %** fibre-solution concentrations, also had relatively similar reduction in the NR uptake (80.9 ±3 %). However, the Ge-Sb-Se **25 %** fibre-solution concentration had notably less reduction than all the other oxidised samples, at 56.0 ±4 %; the reason for this was not clear.

On the whole, cytotoxicity results from both Trial 1 investigations, *i.e.* direct contact (section 7.2.1) and elution (section 7.3.1), correlated well with one another and suggested that non-etched $Ge_{22}Sb_8Se_{70}$/$Ge_{24}Sb_4Se_{72}$ at. % fibres (F_HAP009) were indeed more cytotoxic than etched $Ge_{22}Sb_8Se_{70}$/$Ge_{24}Sb_4Se_{72}$ at. % fibres (F_HAP009).

Therefore, this raised a question over the validity of the direct contact results from Trial 2 (section 7.2.2) which had shown no significant difference between the cytotoxicity of etched *vs.* non-etched $Ge_{20}Sb_{10}Se_{70}$ at. % fibres (F_HAP003). Consequently, an elution test was also conducted on $Ge_{20}Sb_{10}Se_{70}$ at. % fibres (F_HAP003) with a NR end point assay. Unfortunately due to time constraints, no other chalcogenide glass compositions or surface finishes could be investigated.

7.3.2 Trial 2

In Figure 7.14, the NR results for both etched and non-etched $Ge_{20}Sb_{10}Se_{70}$ at. % fibres (F_HAP003) are presented and once again, using 2-way ANOVA, no significant difference was found between the two surface treatments. Furthermore, even at **100 %** fibre-solution concentration, both etched and non-etched $Ge_{20}Sb_{10}Se_{70}$ at. % samples (F_HAP003) still had relatively high levels of 3T3 fibroblast viability with only an averaged 12.6 % and 11.2 % decrease in the NR uptake, respectively. Therefore, results from Trials 1 and 2 repeatedly disagreed with one another over the cytotoxicity difference of etched and non-etched Ge-Sb-Se samples.

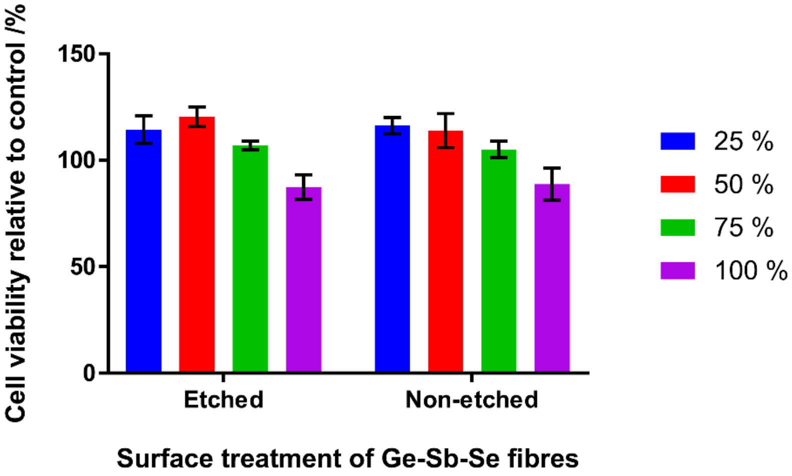

Figure 7.14: Viability of 3T3 fibroblast cells exposed for 24 hours to etched and non-etched $Ge_{20}Sb_{10}Se_{70}$ at. % fibre (F_HAP003) extractables in DMEM-FBS elutant at varying concentrations: 100 %, 75 %, 50 % and 25 %. Results are normalised to 100 % DMEM-FBS control.

When considering the reasons for this discrepancy, there were two variables that changed from Trial 1 to Trial 2.

As previously discussed in section 7.2.2.2, the first of these changes was the operator conducting *in-vitro* cytotoxicity measurements. Prior to the final results presented here in section 7.3.2, there were concerns that the similarity in alamarBlue® results between etched and non-etched Ge-Sb-Se fibres (F_HAP003) from section 7.2.2, could have arisen from human error. However, following the

NR assay shown in Figure 7.14, the similarity in results within Trial 2, made this explanation less plausible.

The second variable that could have caused the inconsistency, was the Ge-Sb-Se fibres used during investigations. Ideally, both MEng students would have conducted *in-vitro* measurements on the $Ge_{20}Sb_{10}Se_{70}$ at. % composition, which has been central to this Project, forming both the core of the SIF (F_HAP007) in Chapter 5 and the low-loss optical fibre (F_HAP008) result from single distillation in Chapter 6. However, due to material availability, a $Ge_{22}Sb_{8}Se_{70}/Ge_{24}Sb_{4}Se_{72}$ at. % SIF (not fabricated by the Author of this Thesis) had to be substituted in for Trial 1. Therefore, the change in Ge-Sb-Se fibre was most likely accompanied by a change in glass chemistry, stability and/or surface energy (not exhausted) which could have all influenced the response of 3T3 fibroblasts during each *in-vitro* cytotoxicity investigation.

7.4 Chapter summary

The overall aim of this chapter was to provide an initial insight into the *in-vitro* cytotoxicity of chalcogenide optical fibres. Said to be less toxic than similar As-containing glasses, investigations focussed on the Ge-Sb-Se glass system and the most important points from chapter 7 are summarised below:

1) In agreement with ISO 10993-5, the cytotoxicity of Ge-Sb-Se optical fibres was explored using a direct contact protocol, with an alamarBlue® endpoint assay, and a non-direct elution test, with a neutral red endpoint assay. Two Trials were completed for each test which had two significant variables: 1) the operator and 2) the Ge-Sb-Se glass composition. Unfortunately due to a lack of material availability, $Ge_{22}Sb_{8}Se_{70}/Ge_{24}Sb_{4}Se_{72}$ at. % SIFs had to be used during Trial 1 (of both protocols) instead of the desired $Ge_{20}Sb_{10}Se_{70}$ at. % composition, which was used during Trial 2.

2) Trial 1 overview:

- Overall, the direct contact and elution tests from Trial 1 showed that non-etched Ge-Sb-Se fibres were more cytotoxic than etched Ge-Sb-Se fibres.

On days 3, 7 and 14 of the direct contact procedure, alamarBlue® results revealed that there was a P <0.0001 significant difference in the relative fluorescence values, for etched *vs.* non-etched Ge-Sb-Se fibres. This was supported by SEM imaging which showed that there were very few 3T3 fibroblasts present on any of the non-etched Ge-Sb-Se samples. Although quantitative analysis of the etched Ge-Sb-Se fibres had shown a high level of relative fluorescence from the alamarBlue® assay, SEM imaging revealed that the majority of the 3T3 fibroblasts were found on the sample's polycarbonate membrane, rather than on the surface of the etched Ge-Sb-Se fibre.

- Since cell attachment is initially dictated by water molecule and protein adhesion, an as-annealed $Ge_{20}Sb_{10}Se_{70}$ at. % bulk glass, prepared with either a 1 µm polished surface or an oxidised surface (*i.e.* to replicate and enhance the etched and non-etched Ge-Sb-Se fibre surfaces, respectively), was used to measure its hydrophobicity. It was found that a 5 µl drop of deionised water had a hydrophilic 41.2 ° contact angle on the surface of the polished bulk Ge-Sb-Se glass and an extremely hydrophilic 5.1 ° contact angle on the surface of the oxidised bulk Ge-Sb-Se glass. Contradicting the apparent hydrophobic nature of the etched Ge-Sb-Se fibres (from direct contact results), a second *in-vitro* cytotoxicity test was investigated which aimed to remove the influence of cell adhesion.
- Using an elution technique with a neutral red end point assay, results once again revealed a significant difference in 3T3 fibroblast viability between etched and non-etched Ge-Sb-Se fibres.
- As an initial insight into the cytotoxicity of As- *vs.* Sb-containing chalcogenide glasses, elution test results also showed that there was a P <0.0001 significant difference in the reduction of NR uptake between As-Se and Ge-Sb-Se fibre samples, with As-Se fibres being more cytotoxic. Furthermore As-Se and Ge-Sb-Se fibres treated with hydrogen peroxide also confirmed that the presence of an oxide layer dramatically reduced the

3T3 fibroblast viability by 85.9 ±1.7 % and 80.9 ±3.1 %, for the As-Se and Ge-Sb-Se samples, respectively.

3) Trial 2 overview:

- Unlike Trial 1, the direct contact and elution tests from Trial 2 showed that there was no significant difference between the cytotoxicity results of etched and non-etched Ge-Sb-Se fibres.
- Following the alamarBlue® assay in Trial 2, SEM images revealed that 3T3 fibroblasts had flattened morphologies with filopodia projections, on the surfaces of both the etched and non-etched Ge-Sb-Se fibres *i.e.* both samples supported the attachment and proliferation of 3T3 fibroblast cells.
- Furthermore, the non-direct elution test in Trial 2, also revealed that there was no significant difference between the neutral red results of etched and non-etched Ge-Sb-Se fibres. For 100 % concentration of the etched and non-etched Ge-Sb-Se extractables, there was a reduction in the NR uptake of 12.6 % and 11.2 %, respectively. Overall, the 3T3 fibroblast viability was also greater than the decreased NR uptake values seen during Trial 1.

4) Overall, cytotoxicity results from Trial 1and Trial 2 were inconsistent with their comparison of etched *vs.* non-etched Ge-Sb-Se optical fibres. Whereas the direct contact procedure during Trial 1 had shown a cytotoxic response from non-etched Ge-Sb-Se fibres, Trial 2 had shown adequate 3T3 fibroblast viability. Although both Trials had shown that 3T3 fibroblasts were able to survive in the etched Ge-Sb-Se environment (*i.e.* promising for biomedical applications), SEM images had shown that very few cells had attached to the surface of the etched Ge-Sb-Se in Trial 1 whereas, there was almost a confluent layer in Trial 2. As such, it was concluded that the number of variables should be minimised and that a third Trial should be conducted (see Chapter 8) using $Ge_{20}Sb_{10}Se_{70}$ at. % fibres.

Chapter 8: Conclusions and future work

The main conclusions drawn from the work undertaken in this Project are presented in section 8.1. Future work considered relevant by the Author for further development of the underlying research themes, are presented in in section 8.2.

8.1 Conclusions

8.1.1 Chapter 4: Crystallisation behaviour of Ge-Sb-Se glasses relevant to optical fibres

-Chapter 4 focussed on two compositions from the $Ge_xSb_{10}Se_{90-x}$ at. % glass series: stoichiometric $Ge_{25}Sb_{10}Se_{65}$ at. % and non-stoichiometric $Ge_{20}Sb_{10}Se_{70}$ at. %.

-Bulk characterisations showed that both compositions could form X-ray amorphous glasses and that the non-stoichiometric $Ge_{20}Sb_{10}Se_{70}$ at. % and stoichiometric $Ge_{25}Sb_{10}Se_{65}$ at. % glasses, had an onset-glass transition temperature (T_g) of 214 °C and 314 °C, respectively.

-The fibre-drawing capability of the non-stoichiometric $Ge_{20}Sb_{10}Se_{70}$ at. % was first explored. It was found that regardless of preform fabrication, the non-stoichiometric $Ge_{20}Sb_{10}Se_{70}$ at. % composition was able to produce optical fibres with low baseline losses. For an uncladded non-stoichiometric $Ge_{20}Sb_{10}Se_{70}$ at. % optical fibre, drawn from an as-annealed 10 mm diameter preform, the lowest loss was measured as 0.6 dB/m at 6.04 µm wavelength. For an uncladded non-stoichiometric $Ge_{20}Sb_{10}Se_{70}$ at. % optical fibre, drawn from an extruded ~4.7 mm diameter preform, the lowest loss was measured as 1.03 dB/m at 6.06 µm wavelength.

-Using an identical procedure, the fibre-drawing capability of the stoichiometric $Ge_{25}Sb_{10}Se_{65}$ at. % composition was then investigated. However, during fibre-drawing, a skin-like layer appeared around the neck-down region of both the as-annealed and extruded stoichiometric $Ge_{25}Sb_{10}Se_{65}$ at. % preforms, which proved detrimental to fibre-drawing. Using XRD, the skin-like feature was identified as monoclinic $GeSe_2$ (ICDD-PDF-01-071-0117), for both the as-annealed and extruded $Ge_{25}Sb_{10}Se_{65}$ at. % preforms. The identity of this single phase was also supported *via* TEM-EDX, which confirmed the composition as $Ge_{34.3}Se_{65.7}$ ± 0.5 at. % and, using the TEM-SAED patterns, matched the crystalline region to the monoclinic $GeSe_2$ (ICDD-PDF-01-071-0117) phase.

-Differential thermal analysis (DTA) was used to explore the thermal properties of both the non-stoichiometric $Ge_{20}Sb_{10}Se_{70}$ at. % and the stoichiometric $Ge_{25}Sb_{10}Se_{65}$ at. % glasses with a 10 °C/min heating rate. Whereas, the thermogram of the non-stoichiometric $Ge_{20}Sb_{10}Se_{70}$ at. % glass smoothly progressed from its T_g into a true melt-liquid, the thermogram of the stoichiometric $Ge_{25}Sb_{10}Se_{65}$ at. % glass presented a crystallisation transition at 530 °C and a solidus transition at 608 °C.

-From an enlarged region of the stoichiometric $Ge_{25}Sb_{10}Se_{65}$ at. % thermogram, it was observed that there were two smaller peaks, which had overlapped, forming the crystallisation (T_c) and melting (T_m) transitions. Based on literature, T_{c1} (the first, lower temperature crystallisation peak) was identified as Sb_2Se_3 and T_{c2} (the second, higher temperature crystallisation peak) was identified as $GeSe_2$.

-Whereas DTA had shown that under a controlled environment stoichiometric $Ge_{25}Sb_{10}Se_{65}$ at. % glass could crystallise into two phases, as suggest by literature, the fast heating rate (>100 °C/min) used during fibre-drawing, was thought to have caused the single phase crystallisation of $GeSe_2$.

-Overall, it was concluded that due to the discrepancy in fibre-drawing results observed between the non-stoichiometric $Ge_{20}Sb_{10}Se_{70}$ at. % and the stoichiometric $Ge_{25}Sb_{10}Se_{65}$ at. % compositions, there was a significant difference in their thermal stability at each respective fibre-drawing temperatures. Even though both Ge-Sb-Se glasses fell within the same topological, overconstrained region, results had shown that unlike other chalcogenide glass systems, Ge-Sb-Se glasses are best described by their chemical composition (i.e. using the CONM) rather than by their MCN.

8.1.2 Chapter 5: Towards Ge-Sb-Se/S step-index fibres for hyperspectral imaging

- For the investigated SIF, it was decided that $Ge_{20}Sb_{10}Se_{70}$ at. % and $Ge_{20}Sb_{10}Se_{67}S_3$ at. % would act as the core and cladding glasses, respectively.

-Using TMA, viscosity-temperature curves revealed that the $Ge_{20}Sb_{10}Se_{70}$ at. % core glass should be held at 274.7 ±0.4 °C during extrusion (to achieve a viscosity of $10^{7.5}$ Pa s) and 357.8 ±0.7 °C during fibre-drawing (to achieve a viscosity of $10^{4.5}$ Pa s).

-Also investigated *via* TMA, the $Ge_{20}Sb_{10}Se_{70}$ at. % core glass was found to have a thermal expansion coefficient (TEC) of 19.49 x10^{-6} °C *i.e.* measured from the gradient of the TEC curve between 40 °C and 100 °C. Using a geometrical technique, the dilatometric softening point (M_g), found at a viscosity of $10^{11.5}$ Pa s, was found to be 217 ±2 °C.

-Using XRD and DSC, the $Ge_{20}Sb_{10}Se_{67}S_3$ at % cladding glass was shown to be X-ray amorphous and exhibited an onset-T_g at 224 ±2 °C.

-From viscosity-temperature curves it was found that the $Ge_{20}Sb_{10}Se_{67}S_3$ at % cladding glass should be held at 277.7 ±0.4 °C during extrusion (to achieve a viscosity of $10^{7.5}$ Pa s) and 361.9 ±0.7 °C during fibre-drawing (to achieve a viscosity of $10^{4.5}$ Pa s). This meant that both the $Ge_{20}Sb_{10}Se_{70}$ at. % core and $Ge_{20}Sb_{10}Se_{67}S_3$ at % cladding glasses deviated in extrusion and fibre-drawing temperatures by 3 °C and 4 °C, respectively.

-A 4.7 mm diameter extruded $Ge_{20}Sb_{10}Se_{67}S_3$ at % rod was used to investigate the fibre-drawing capability of the proposed cladding glass. Although the 200 ±10 µm diameter $Ge_{20}Sb_{10}Se_{67}S_3$ at % optical fibre had a low baseline loss of 0.53 dB/m at 5.99 µm wavelength, the addition of 3 at. % S to the $Ge_{20}Sb_{10}Se_{70-x}S_x$ at. % system also introduced a large S-H impurity absorption at 4.03 µm wavelength (42.4 dB/m).

-Refractive index measurements found that at 3.1 µm wavelength, the $Ge_{20}Sb_{10}Se_{70}$ at. % core thin film had a refractive index of 2.553 and the

$Ge_{20}Sb_{10}Se_{67}S_3$ at. % cladding thin film had a refractive index of 2.540. Therefore, it was calculated that a SIF composed of a $Ge_{20}Sb_{10}Se_{70}$ at. % core and a $Ge_{20}Sb_{10}Se_{67}S_3$ at. % cladding glass would have an NA of 0.25 at 3.1 µm wavelength.

-Co-extruded at 267±0.1 °C, a 29 mm diameter $Ge_{20}Sb_{10}Se_{70}$ at. % core and $Ge_{20}Sb_{10}Se_{67}S_3$ at. % cladding glass, polished to a 1 µm finish on the mating surfaces, produced a 9.56 ±0.03 mm diameter rod with a length of 240 ±5 mm.

-From a section of this preform taken 100 mm from the start of co-extrusion, SIFs were drawn with a diameter of 200 ±5 µm, 300 ±10 µm and 400 ±10 µm. Optical loss measurements were conducted on an 8 m length of 200 ±5 µm diameter fibre with its lowest loss measured as 0.72 dB/m at 6.06 µm wavelength. Using impurity absorptions present in both the individual $Ge_{20}Sb_{10}Se_{70}$ at. % core and $Ge_{20}Sb_{10}Se_{67}S_3$ at. % cladding optical fibres and the SIF, fibre loss spectra revealed that MIR light had been guided through the $Ge_{20}Sb_{10}Se_{70}$ at. % core of the SIF *i.e.* there was no evidence of the prominent 42. 0 dB/m impurity band at 4.04 µm, which had been seen in the individual $Ge_{20}Sb_{10}Se_{67}S_3$ at. % cladding fibre.

-Furthermore, SEM conducted on cleaves made during fibre loss measurements, revealed the presence of a large circular core with a core to cladding ratio of 95 %. Using SEM-EDX analysis, the nominally batched $Ge_{20}Sb_{10}Se_{70}$ at. % core and $Ge_{20}Sb_{10}Se_{67}S_3$ at. % cladding regions, were found to have a composition of $Ge_{20.4}Sb_{10.0}Se_{69.6}$ ±0.5 at. % and $Ge_{20.4}Sb_{9.9}Se_{66.5}S_{3.2}$ ±0.5 at. %, respectively.

8.1.3 Chapter 6: High purity Ge-Sb-Se glasses *via* distillation

-Using the Antoine equation, vapour-pressure temperature curves were investigated for each of the relevant precursors (Se, Sb and S) and their associated oxides (SeO_2, Sb_2O_3 and SO_2, respectively). Based on the current bake-out temperatures: at 260 °C, Se and SeO_2 had vapour pressures of 0.003 kPa and 6.85 kPa, respectively; at 140 °C, S and SO_2 had vapour pressures of 0.013 kPa and

5948.3 kPa, respectively and at 570 °C, Sb and Sb_2O_3 had vapour pressures of 0.002 kPa and 0.220 kPa, respectively.

-Under the current conditions, it was concluded that Se and SeO_2 had a large enough difference in vapour pressure for impurities to be adequately removed during a 0.5 hr dwell at 260 °C. It was also concluded that with a calculate vapour pressure difference of 5948.287 kPa, between S and SO_2, the current bake-out procedure of a 25 min dwell at 140 °C was also at its optimum. Particularly as literature had suggested that it was necessary to vacuum distil sulfur five times before the impurity content was sufficiently reduced. Although the purification of Sb was investigated at a higher bake-out temperature of 700 °C, so that a greater vapour pressure difference was achieved between Sb and Sb_2O_3, it was found that the best results were achieved after a 3 hr dwell at 570 °C.

-Within section 6.2, there were four distillation investigations of $Ge_{20}Sb_{10}Se_{70}$ at. % core glass (D_HAP001 to D_HAP004).

-D_HAP001 was a simple bent tube distillation without any [O] or [H] getters. Results showed that 2.7 g of $Ge_{20}Sb_{10}Se_{70}$ at. % glass was able to distil as the charge end of the chamber was increased to 850 °C. However, observation of an abrupt change in temperature during the ramp up to 850 °C, implied that the $Ge_{20}Sb_{10}Se_{70}$ at. % glass may have distilled closer to 706 °C.

-Material that distilled during D_HAP001 condensed into three distinct deposits. Using SEM-EDX these were confirm as: 1) a single-phase deposit of $Sb_{40.1}Se_{59.9}$ ±0.5 at. %; 2) a two-phase deposit primarily consisting of $Ge_{19.4}Sb_{11.1}Se_{69.5}$ ±0.5 at. % with $Ge_{32.9}Se_{67.1}$ ±0.5 at. % regions and 3) a single-phase deposit of $Ge_{8.8}Sb_{4.3}Se_{86.9}$ ±0.5 at. %.

-D_HAP002 was the first distillation attempt of 30 g of $Ge_{20}Sb_{10}Se_{70}$ at. % glass with 1000 ppm wt. $TeCl_4$ and 700 ppm wt. Al.

-Using a two-zone furnace (Instron, TF1798, tube ID 86mm), it was found that even after 20 hrs spent at 1000 °C (thermocouple reading was 985 °C), very little $Ge_{20}Sb_{10}Se_{70}$ at. % was able to distil over. Since there was no material blocking the passage of $Ge_{20}Sb_{10}Se_{70}$ at. % vapour inside the silica glass distillation rig, it was concluded that a barrier of $HCl_{(g)}$ had prevented the $Ge_{20}Sb_{10}Se_{70}$ at. % glass from distilling, due to its insufficient removal during an initial bake.

-Of the small amount of material that had distilled during D_HAP002, not only were the deposits similar in appearance to those analysed in D_HAP001, they had also condensed at a similar position, in respect to the two-zone furnace (Instron, TF1798, tube ID 86mm).

- D_HAP003 was the second distillation attempt of 30 g of $Ge_{20}Sb_{10}Se_{70}$ at. % glass with 1000 ppm wt. $TeCl_4$ and 700 ppm wt. Al.

-Even with an increased $HCl_{(g)}$ bake-out time and a 30 mm shift in the silica distillation rig, with respect to the two-zone furnace, distillation of $Ge_{20}Sb_{10}Se_{70}$ at. % glass was once again unsuccessful.

-Although more material had distilled during D_HAP003, the appearance of the deposit was unlike D_HAP001 and D_HAP002. Furthermore, it was found that the remaining material within the charge chamber of D_HAP003 had also separated into three deposits. Using SEM-EDX the charge chamber deposits were primarily identified as: 1) $Ge_{0.4}Sb_{38.8}Se_{60.8}$ ±0.5 at. %, 2) $Ge_{0.7}Sb_{39.6}Se_{59.7}$ ±0.5 % and 3) $Ge_{0.6}Sb_{40.3}Se_{60.0}$ ±0.5 at. % *i.e.* all close to Sb_2Se_3.

- D_HAP004 was the third and final distillation attempt of 30 g of $Ge_{20}Sb_{10}Se_{70}$ at. % glass with 1000 ppm wt. $TeCl_4$ and 700 ppm wt. Al.

-Unlike previous attempts, D_HAP004 used a combination of wires and a clamshell furnace (Cabrolite, VST 12/200) for finer temperature control. Within an open system, *i.e.* under flowing vacuum, it was found that the $Ge_{20}Sb_{10}Se_{70}$ at. % glass had successfully distilled at temperatures close to 693 °C.

-Following a re-melt, the 10 mm diameter as-annealed $Ge_{20}Sb_{10}Se_{70}$ at. % distilled glass was fibre-drawn. Optical fibre loss was conducted on an 18 m length sample and revealed that the distillation of $Ge_{20}Sb_{10}Se_{70}$ at. % with 1000 ppm wt. $TeCl_4$ and 700 ppm wt. Al getters, had removed the Ge-O absorption peak at 7.9 µm and significantly reduced, if not removed, all of the Se-H peaks as well. Furthermore, the lowest background loss was 0.44 dB/m found at 6.4 µm. To the best of the Author's knowledge, the optical fibre loss presented for the distilled $Ge_{20}Sb_{10}Se_{70}$ at. % glass, is currently the best in the world.

-Although some of distilled $Ge_{20}Sb_{10}Se_{70}$ at. % fibre cleaves had been shown to have an irregular cross-section *via* SEM, EDX analysis confirmed that the 18 m length of optical fibre, used during fibre loss measurements, was homogeneous with a composition of $Ge_{21.1}Sb_{10.6}Se_{68.3}$ ±0.5 at. % *i.e.* close to the nominally batched.

8.1.4 Chapter 7: Cytotoxicity investigations of Ge-Sb-Se optical fibres

-*In-vitro* cytotoxicity assessments of Ge-Sb-Se optical fibres were conducted using two techniques *viz.:* 1) direct contact protocol with an alamarBlue® end point assay and 2) elution protocol with a neutral red end point assay. Both techniques were run twice. Trial 1 was based on the results by MEng student Mr T. Kubiena and Trial 2 was based on the results by MEng student Mr W. Gan.

Direct contact *in-vitro* cytotoxicity assessment:

TRIAL 1

-Trial 1 of the direct contact protocol was based on etched and non-etched $Ge_{22}Sb_{8}Se_{70}/Ge_{24}Sb_{4}Se_{72}$ at. % SIFs. Using a polycarbonate membrane (*i.e.* an empty sample well) as a negative control, the alamarBlue® results showed that etched $Ge_{22}Sb_{8}Se_{70}/Ge_{24}Sb_{4}Se_{72}$ at. % SIFs did not elicit a cytotoxic response to 3T3 fibroblast cells yet, the non-etched $Ge_{22}Sb_{8}Se_{70}/Ge_{24}Sb_{4}Se_{72}$ at. % SIFs did.

-Using SEM, direct contact samples from Trial 1 were analysed and overall supported the quantitative results seen by alamarBlue®. Although the etched $Ge_{22}Sb_{8}Se_{70}/Ge_{24}Sb_{4}Se_{72}$ at. % SIFs had shown a high level of fluorescence (233 RFU) during the alamarBlue® investigation, the majority of the 3T3 fibroblast cells observed under SEM, had attached to the polycarbonate membrane, below the Ge-Sb-Se sample.

-Contact angle measurements on as-annealed $Ge_{20}Sb_{10}Se_{70}$ at. % bulk samples were used as an initial investigation into the hydrophobicity of Ge-Sb-Se glasses. A 5 µl drop of deionised water was found to have a contact angle of 41.2 ±0.7 ° on the surface of a 1 µm polished $Ge_{20}Sb_{10}Se_{70}$ at. % bulk sample and 5.1 ±2.8 ° on the surface of an oxidised $Ge_{20}Sb_{10}Se_{70}$ at. % bulk sample.

TRIAL 2

- Trial 2 of the direct contact protocol was based on etched and non-etched $Ge_{20}Sb_{10}Se_{70}$ at. % fibres. Using a polycarbonate membrane as a negative control, the alamarBlue® results showed that neither the etched nor the non-etched $Ge_{20}Sb_{10}Se_{70}$ at. % fibres caused a cytotoxic response from the 3T3 fibroblast cells.

-Quantitative alamarBlue® results from Trial 2 were also supported using SEM. All samples were shown to support the attachment and proliferation of 3T3 fibroblasts.

Elution *in-vitro* cytotoxicity assessment:

TRIAL 1

- Trial 1 of the elution protocol was based on etched and non-etched $Ge_{22}Sb_8Se_{70}/Ge_{24}Sb_4Se_{72}$ at. % SIFs. Results from the neutral red assay revealed that there was significant difference in 3T3 fibroblast viability between the etched and non-etched $Ge_{22}Sb_8Se_{70}/Ge_{24}Sb_4Se_{72}$ at. % SIFs.

-Furthermore, neutral red results revealed that there was a significant decrease in the viability 3T3 fibroblast when exposed to solutions containing etched and non-etched As-Se extractables.

-Oxidised samples of As-Se and Ge-Sb-Se significantly reduced the viability of 3T3 fibroblasts, resulting in decreased neutral red uptake of 85.9 ±1.7 % and 80.9 ±3.1 %, respectively.

TRIAL 2

- Trial 2 of the elution protocol was based on etched and non-etched $Ge_{20}Sb_{10}Se_{70}$ at. % fibres. Results from the neutral red assay showed that there was no significant difference between the cytotoxicity of etched and non-etched $Ge_{20}Sb_{10}Se_{70}$ at. % fibres.

8.2 Future work

Conclusions drawn in section 8.1 have shown that significant progress has been made towards the fabrication of high purity Ge-Sb-Se/S SIFs for use in a MIR imaging probe for early cancer diagnosis. However, several steps still need to be taken before this goal is reached.

High purity $Ge_{20}Sb_{10}Se_{70}$ at. % core and $Ge_{20}Sb_{10}Se_{67}S_3$ at. % cladding SIFs:

-The next stage of research should focus on the distillation of a $Ge_{20}Sb_{10}Se_{70}$ at. % core glass into a 29 mm diameter boule, for co-extrusion with a $Ge_{20}Sb_{10}Se_{67}S_3$ at. % cladding, to create a high purity SIF. Although results presented in this Project have shown that the majority of MIR travelled through the $Ge_{20}Sb_{10}Se_{70}$ at. % core of a Ge-Sb-Se/S SIF, future work could consider distilling the $Ge_{20}Sb_{10}Se_{67}S_3$ at. % as well. At the very least, it would be worth investigating the distillation of as-received S so that the large S-H absorption band (42.4 dB/m at 4.03 µm wavelength) could be significantly reduced in the cladding glass.

-For an ultra-low loss $Ge_{20}Sb_{10}Se_{70}$ at. % core glass, double distillation could also be considered.

Investigation into the optimal $Ge_{20}Sb_{10}Se_{70-x}S_x$ at. % composition

-Further compositional work could investigate whether or not the $Ge_{20}Sb_{10}Se_{67}S_3$ at. % was the optimum glass for this SIF. Results have shown that with a 3 at. % substitution of Se for S in the $Ge_{20}Sb_{10}Se_{70-x}S_x$ at. % series increases the T_g by 10 °C and the decreases the refractive index by 0.01. This produced a SIF with a relatively low NA of 0.25 at 3.1 µm wavelength. Since the temperature required for extrusion and fibre-drawing only differed by 3 °C and 4 °C, respectively, between the $Ge_{20}Sb_{10}Se_{70}$ at. % core and $Ge_{20}Sb_{10}Se_{67}S_3$ at. % cladding, it is possible that a larger substitution of Se for S (*e.g.* 6 at. %) could still produce a stable SIF and offer a higher NA *e.g.* 0.4.

-As systematic study into the thermal and optical effects accompanying a substitution of Se for S in the $Ge_{20}Sb_{10}Se_{70-x}S_x$ at. % series would not only be novel but results would also be invaluable to this work.

-To quantitatively assess the quality of various $Ge_{20}Sb_{10}Se_{70-x}S_x$ at. % SIF combinations, tensile testing could be used to investigate the mechanical strength of each sample.

Fabrication of a coherent Ge-Sb-Se/S optical fibre bundle

-Work towards the fabrication of a Ge-Sb-Se/S coherent bundle. Using the 300 µm or 400 µm diameter SIFs fabricated in this Project, manually produce a small coherent fibre bundle *e.g.* 5 x 5 fibre array. Consider the packing factor, potential buffer layer *i.e.* to stop fibre cross-talk and the detector's array *i.e.* active area.

-Investigate several coherent fibre bundle fabrication techniques such as: 1) the stack and draw and 2) the ribbon method.

Spectroscopy of biological sample using high purity Ge-Sb-Se/S SIF

-Continuing working towards a remote/portable spectroscopy technique. Until significant progress has made with the coherent Ge-Sb-Se/S SIF bundle, use a single high purity SIF to deliver and collected MIR light to and from a biological sample (*e.g.* phantom skin) for analysis. Gain a greater understanding of the optical-setup requirements and final MIR fingerprints.

Further investigations into the biocompatibility of Ge-Sb-Se glasses

-Conduct a third trial into the *in-vitro* cytotoxicity assessment of Ge-Sb-Se fibres by direct contact and elution protocols. This third repeat should use the same $Ge_{20}Sb_{10}Se_{70}$ at. % composition as Trial 2. Alternatively, *in-vitro* cytotoxicity investigations could be repeated two more times (Trial 3 and Trial 4), so that both the $Ge_{20}Sb_{10}Se_{70}$ at. % composition and operator remained the same.

-The $Ge_{20}Sb_{10}Se_{67}S_3$ at. % cladding glass should also be evaluated.

-Since *in-vitro* cytotoxicity assessments are only a small part of the required biocompatibility testing, consider future *in-vivo* studies.

References

1. Ahmad AS, Ormiston-Smith N, and Sasieni PD, Trends in the lifetime risk of developing cancer in Great Britain: comparison of risk for those born from 1930 to 1960. *British Journal of Cancer*. 2015;**112:**943-947.
2. *Cancer Research UK*. Accessed: [02, 2018]]; Available from: http://www.cancerresearchuk.org/about-cancer/what-is-cancer.
3. Bigio IJ, Mourant JR, Optical Biopsy,in *Encyclopedia of Optical Engineering* Driggers RG, Marcel Dekker: New York. 2003. p. 1577-1593.
4. Seddon AB. *Mid-infrared photonics for early cancer diagnosis*. in *Transparent Optical Networks (ICTON), 2014 16th International Conference on*. 2014.
5. Seddon AB, A Prospective for New Mid-Infrared Medical Endoscopy Using Chalcogenide Glasses. *International Journal of Applied Glass Science*. 2011;**2:**177-191.
6. Pilling M and Gardner P, Fundamental developments in infrared spectroscopic imaging for biomedical applications. *Chem. Soc. Rev.* 2016;**45:**1935-1957.
7. Sanghera J and Gibson D, Optical properties of chalcogenide glasses and fibers,in *Chalcogenide Glasses: Preparation, Properties and Applications*, Adam J-L and Zhang X, Woodhead Publishing Limited. 2014.
8. Shiryaev VS and Churbanov MF, Recent advances in preparation of high-purity chalcogenide glasses for mid-IR photonics. *J. Non-Cryst. Solids*. 2017;**475:**1-9.
9. Calvez L, Chalcogenide glasses and glass-ceramics: Transparent materials in the infrared for dual applications. *Comptes Rendus Physique*. 2017;**18:**314-322.
10. Mackanos MA and Contag CH, Fiber-optic probes enable cancer detection with FTIR spectroscopy. *Trends Biotechnol.* 2010;**28:**317-323.
11. Baker MJ, Trevisan J, Bassan P, Bhargava R, Butler HJ, Dorling KM, Fielden PR, Fogarty SW, Fullwood NJ, and Heys KA, Using Fourier

transform IR spectroscopy to analyze biological materials. *Nature protocols*. 2014;**9:**1771-1791.

12. Nallala J, Piot O, Diebold M-D, Gobinet C, Bouché O, Manfait M, and Sockalingum GD, Infrared imaging as a cancer diagnostic tool: Introducing a new concept of spectral barcodes for identifying molecular changes in colon tumors. *Cytometry Part A*. 2013;**83A:**294-300.
13. Harrington JA, *Infrared fibers and their applications*. 2004, United States of America: SPIE Press.
14. Parnell H, Furniss D, Tang Z, Neate NC, Benson TM, and Seddon AB, Compositional dependence of crystallization in Ge–Sb–Se glasses relevant to optical fiber making. *J. Am. Ceram. Soc.* 2018;**101:**208-219.
15. Charles R. Kurkjian WRP, Perspectives on the history of glass composition. *J. Am. Ceram. Soc.* 1998;**81:**795-813.
16. Shelby JE, Introduction,in *Introduction to glass science and technology*, The Royal Society of Chemistry: Cambridge, UK. 2005. p. 1-6.
17. Zarzycki J, Historical overview,in *Glasses and the vitreous state* Cambridge University Press: Cambridge. 1991. p. xxv-xxviii.
18. Carter BC and Norton MG, Glass and glass-ceramics,in *Ceramic materials: science and engineering*, Springer New York: New York, NY. 2007. p. 379-399.
19. Stanworth JE, The chemical composition of glasses,in *Physical properties of glass*, Jackson W FH, Mott N.F, Clarendon Press: Oxford. 1950.
20. Rawson H, *Inorganic glass-forming systems*, ed. J. P. Roberts PP. 1967, London: Academic Press.
21. *ASTM Standards on Glass and Glass Products*. April 1955, prepared by ASTM Committee C14, American Society for Testing Materials.
22. Rawson H, *Properties and applications of glass*. 1980, Amsterdam: Elsevier Scientific Publishing Company.
23. Debenedetti PG and Stillinger FH, Supercooled liquids and the glass transition. *Nature*. 2001;**410:**259-267.

24. Badrinarayanan P, Zheng W, Li Q, and Simon SL, The glass transition temperature versus the fictive temperature. *J. Non-Cryst. Solids*. 2007;**353:**2603-2612.
25. Moynihan CT, Assignment of the glass transition, ASTM,in, Seyler R.J: Philadelphia. 1994.
26. Moynihan CT, Easteal AJ, De Bolt MA, and Tucker J, Dependence of the fictive temperature of glass on cooling rate. *J. Am. Ceram. Soc.* 1976;**59:**12-16.
27. Zachariasen WH, The atomic arrangement in glass. *J. Am. Chem. Soc.* 1932;**54:**3841-3851.
28. Vogel W, *Glass chemistry / Werner Vogel*. 2nd ed. ed. 1994, Berlin: Berlin : Springer-Verlag.
29. Holand W and Beall GH, *Glass ceramic technology*. Second ed. 2012, USA: Wiley.
30. Volmer M, Kinetik der Phasenbildung. *Steinkopff: Dresden/Leipzig*. 1939;
31. Becker R and Döring W, Kinetische Behandlung der Keimbildung in übersättigten Dämpfen. *Annalen der Physik*. 1935;**416:**719-752.
32. Frenekel J, Kinetic theory of liquids,in, Oxford University Press: New York. 1946. p. 366.
33. Zeldovich YB, *J. Exp. Theor. Phys (Russ.)* 1942;**12:**525.
34. Meyer K, *Physikalisch-chemische Kristallographie*. 1968, Leipzig: Deutscher Verlag für Grundstoffindustrie.
35. Lezal D, Chalcogenide glasses- survey and progress. *Optoelectronics and Advanced Materials*. 2003;**5:**23-34.
36. D. Lezal JP, J. Zavadil, Chalcogenide glasses for optical and photonics applications. *Optoelectronics and Advanced Materials*. 2004;**6:**133-137.
37. Seddon AB, Chalcogenide glasses: a review of their preparation, properties and applications. *J. Non-Cryst. Solids*. 1995;**184:**44-50.
38. Rao KJ, Chapter 13 - Chalcogenide glasses,in *Structural Chemistry of Glasses*, Rao KJ, Elsevier Science Ltd: Oxford. 2002. p. 513-534.

39. Bureau B, Boussard-Pledel C, Lucas P, Zhang X, and Lucas J, Forming glasses from Se and Te. *Molecules*. 2009;**14:**4337.

40. Lucas J, Infrared glasses. *Curr. Opin. Solid State Mater. Sci.* 1999;**4:**181-187.

41. Sanghera JS, Brandon Shaw L, and Aggarwal ID, Chalcogenide glass-fiber-based mid-IR sources and applications. *Selected Topics in Quantum Electronics, IEEE* 2009;**15:**114-119.

42. Aggarwal ID and Sanghera JS, Development and applications of chalcogenide glass optical fibers at nrl. *Optolectronics and Advanced Materials*. 2002;**4:**665-678.

43. Masayuki Yamane YA, *Glasses for photonics*. 2000, Cambridge: Cambridge University Press.

44. Frerichs R, New optical glasses with good transparency in the infrared. *J. Opt. Soc. Am.* 1953;**43:**1153-1157.

45. Fraser WA, A new triaxial system of infrared glasses. *J. Opt. Soc. Am.* 1953;**43:**823.

46. Tsuchihashi S, Yano A, Komatsu T, and Adachi K, *Yogyo-Kyokai-Shi*. 1966;**74:**353.

47. Wei W-H, Fang L, Shen X, and Wang R-P, Transition threshold in $Ge_xSb_{10}Se_{90-x}$ glasses. *J. Appl. Phys.* 2014;**115:-**.

48. Wang T, Wei WH, Shen X, Wang RP, Davies BL, and Jackson I, Elastic transition thresholds in Ge–As(Sb)–Se glasses. *J. Phys. D: Appl. Phys.* 2013;**46:**165302.

49. Wei W-H, Wang R-P, Shen X, Fang L, and Luther-Davies B, Correlation between structural and physical properties in Ge–Sb–Se glasses. *The Journal of Physical Chemistry C*. 2013;**117:**16571-16576.

50. Zhang W, Dai S, Shen X, Chen Y, Zhao S, Lin C, Zhang L, and Bai J, Rib and strip chalcogenide waveguides based on Ge–Sb–Se radio-frequency sputtered films. *Mater. Lett.* 2013;**98:**42-46.

51. Němec P, Olivier M, Baudet E, Kalendová A, Benda P, and Nazabal V, Optical properties of $(GeSe_2)_{100-x}(Sb_2Se_3)_x$ glasses in near- and middle-infrared spectral regions. *Mater. Res. Bull.* 2014;**51:**176-179.

52. Tanwar N and Saraswat VK, A study of kinetics of phase transformation of $Ge_{10}Se_{75}Sb_{15}$ chalcogenide glass. *J. Non-Cryst. Solids*. 2014;**394-395:**1-5.

53. Chen L, Chen F, Dai S, Tao G, Yan L, Shen X, Ma H, Zhang X, and Xu Y, Third-order nonlinearity in Ge–Sb–Se glasses at mid-infrared wavelengths. *Mater. Res. Bull.* 2015;**70:**204-208.

54. Zhang B, Yu Y, Zhai C, Qi S, Wang Y, Yang A, Gai X, Wang R, Yang Z, and Luther-Davies B, High brightness 2.2–12 μm mid-infrared supercontinuum generation in a nontoxic chalcogenide step-index fiber. *J. Am. Ceram. Soc.* 2016;**99:**2565-2568.

55. Baudet E, Cardinaud C, Girard A, Rinnert E, Michel K, Bureau B, and Nazabal V, Structural analysis of RF sputtered Ge-Sb-Se thin films by Raman and X-ray photoelectron spectroscopies. *J. Non-Cryst. Solids*. 2016;**444:**64-72.

56. Lee JH, Lee WH, Park JK, Yi JH, Shin SY, Park BJ, So B, Heo J, Choi JH, Kim HJ, and Choi YG, Thermal properties of ternary Ge–Sb–Se chalcogenide glass for use in molded lens applications. *J. Non-Cryst. Solids*. 2016;**431:**41-46.

57. Lee JH, Yi JH, Lee WH, and Choi YG, Broken chemical order in Ge-Sb-Se glasses for use as infrared-transmitting lenses. *J. Non-Cryst. Solids*. 2017;**456:**27-32.

58. Ghayebloo M, Tavoosi M, and Rezvani M, Compositional modification of Se-Ge-Sb chalcogenide glasses by addition of arsenic element. *Infrared Phys Techn*. 2017;**83:**62-67.

59. Luo B, Wang Y, Sun Yn, Dai S, Yang P, Zhang P, Wang X, Chen F, and Wang R, Fabrication and characterization of bare Ge-Sb-Se chalcogenide glass fiber taper. *Infrared Phys Techn*. 2017;**80:**105-111.

60. Han X, You C, Dai S, Zhang P, Wang Y, Guo F, Xu D, Luo B, Xu P, and Wang X, Mid-infrared supercontinuum generation in a three-hole

Ge20Sb15Se65 chalcogenide suspended-core fiber. *Optical Fiber Technology*. 2017;**34:**74-79.

61. Lin L, Wang G, Shen X, Dai S, Xu T, and Nie Q, Photo-induced structural changes in Ge-Sb-Se films. *Infrared Phys Techn*. 2017;**81:**59-63.
62. Savage JA, Webber PJ, and Pitt AM, An assessment of Ge-Sb-Se glasses as 8 to 12μm infra-red optical materials. *Journal of Materials Science*. 1978;**13:**859-864.
63. Hilton AR and Hayes DJ, The interdependence of physical parameters for infrared transmitting glasses. *J. Non-Cryst. Solids*. 1975;**17:**339-348.
64. Frumar M, Tichá H, Klikorka J, and Tomíška P, Optical absorption in vitreous $GeSb_2Se_4$. *J. Non-Cryst. Solids*. 1973;**13:**173-178.
65. Rechtin MD, Hilton AR, and Hayes DJ, Infrared transmission in Ge-Sb-Se glasses. *J. Electron. Mater.* 1975;**4:**347-362.
66. Lucovsky G NRaGF. in *W. Spear (Ed.), Proceedings of Seventh International Conference on Amorphous Liquid Semiconductors*. (1977). Center for Industrial Consultancy and Liaison, Univ. of Edinburgh, Edinburgh, p. 130.
67. Bicerano J and Ovshinsky SR, Chemical bond approach to the structures of chalcogenide glasses with reversible switching properties. *J. Non-Cryst. Solids*. 1985;**74:**75-84.
68. Mahadevan S, Giridhar A, and Singh AK, Elastic properties of Ge-Sb-Se glasses. *J. Non-Cryst. Solids*. 1983;**57:**423-430.
69. Phillips JC and Thorpe MF, Constraint theory, vector percolation and glass formation. *Solid State Commun.* 1985;**53:**699-702.
70. Tanaka K, Structural phase transitions in chalcogenide glasses. *Physical Review B*. 1989;**39:**1270-1279.
71. Vinod EM, Ramesh K, and Sangunni KS, Structural transition and enhanced phase transition properties of Se doped Ge2Sb2Te5 alloys. *Scientific Reports*. 2015;**5:**8050.
72. Opletal G, Drumm DW, Petersen TC, Wang RP, and Russo SP, Ab initio comparison of bonding environments and threshold behavior in

$Ge_xAs_{10}Se_{90-x}$ and $Ge_xSb_{10}Se_{90-x}$ glass models. *The Journal of Physical Chemistry A*. 2015;**119:**6421-6427.

73. Popescu MA, *Non-Crystalline Chalcogenicides*. 2006: Springer Netherlands.
74. Vateva E and Savova E, New medium-range order features in Ge・Sb・S glasses. *J. Non-Cryst. Solids*. 1995;**192-193:**145-148.
75. Du Q, Huang Y, Li J, Kita D, Michon J, Lin H, Li L, Novak S, Richardson K, Zhang W, and Hu J, Low-loss photonic device in Ge–Sb–S chalcogenide glass. *Opt. Lett.* 2016;**41:**3090-3093.
76. Li Z, Lin C, Qu G, Nie Q, Xu T, and Dai S, Phase separation in nonstoichiometry Ge–Sb–S chalcogenide glasses. *J. Am. Ceram. Soc.* 2014;**97:**793-797.
77. Petit L, Carlie N, Adamietz F, Couzi M, Rodriguez V, and Richardson KC, Correlation between physical, optical and structural properties of sulfide glasses in the system Ge–Sb–S. *Mater. Chem. Phys.* 2006;**97:**64-70.
78. Kavetskyy TS, Kovalskiy AP, Pamukchieva VD, and Shpotyuk OI, IR impurity absorption in $Sb_2S3–GeS_2(Ge_2S_3)$ chalcogenide glasses. *Infrared Phys Techn*. 2000;**41:**41-45.
79. Pamukchieva V, Szekeres A, Sharlandjiev P, Alexia Z, and Gartner M. *Effect of composition on refractive index dispersion in Ge-Sb-S thin films*. in *Semiconductor Conference, 1998. CAS '98 Proceedings. 1998 International*. 1998.
80. Wang R, Xu Q, Liu H, Sheng Y, and Yang X, Structure and physical properties of $Ge_{15}Sb_{20}Se_{65-x}S_x$ glasses. *J. Am. Ceram. Soc.* 2017;**101:**201-207.
81. Guery G, Musgraves JD, Labrugere C, Fargin E, Cardinal T, and Richardson K, Evolution of glass properties during a substitution of S by Se in $Ge_{28}Sb_{12}S_{60-x}Se_x$ glass network. *J. Non-Cryst. Solids*. 2012;**358:**1740-1745.
82. Sanghera JaA, I. D., Development of chalcogenide glass fibre optics at NRL. *J. Non-Cryst. Solids*. 1997;**213 & 214:**63-67.

83. Sanghera JS, Nguyen VQ, Pureza PC, Miklos RE, Kung FH, and Aggarwal ID, Fabrication of long lengths of low-loss IR transmitting $As_{40}S_{60-x}Se_x$ glass fibers. *Journal of Lightwave Technology*. 1996;**14:**743-748.

84. Weaire D and Thorpe MF, Electronic properties of an amorphous solid. I. A simple tight-binding theory. *Physical Review B*. 1971;**4:**2508-2520.

85. Urbach F, The long-wavelength edge of photographic sensitivity and of the electronic absorption of solids. *Physical Review*. 1953;**92:**1324-1324.

86. Wood DL and Tauc J, Weak absorption tails in amorphous semiconductors. *Physical Review B*. 1972;**5:**3144-3151.

87. Kanamori T, Terunuma Y, Takahashi S, and Miyashita T, Transmission loss characteristics of $As_{40}S_{60}$ and $As_{38}Ge_5Se_{57}$ glass unclad fibers. *J. Non-Cryst. Solids*. 1985;**69:**231-242.

88. Suriñach S, Illeková E, Baró MD, Jha A, and Jordery S, Evaluation of crystal nucleation and growth from crystallization kinetics data of new halide glasses. *J. Non-Cryst. Solids*. 1996;**205–207, Part 2:**546-549.

89. Borisevich. VG, Voitsekhovsky VV, Scripachev IV, and PV, and MF C, Investigation of the influence of extrinsic hydrogen on the optical properties of chalcogenide glasses in the system As-Se. *Vysokochist. Vesch*. 1991;**1:**65.

90. Moynihan CT, Macedo PB, Maklad MS, Mohr RK, and Howard RE, Intrinsic and impurity infrared absorption in As2Se3 glass. *J. Non-Cryst. Solids*. 1975;**17:**369-385.

91. Shibata S, Terunuma Y, and Manabe T, Sulfide glass fibers for infrared transmission. *Mater. Res. Bull.* 1981;**16:**703-714.

92. Kanamori T, Terunuma Y, Takahashi S, and Miyashita T, Chalcogenide glass fibers for mid-infrared transmission. *Journal of Lightwave Technology*. 1984;**2:**607-613.

93. Snopatin G, Churbanov M, Pushkin A, Gerasimenko V, Dianov E, and Plotnichenko V, High purity arsenic-sulfide glasses and fibers with minimum attenuation of 12 dB/km. *Optoelectronics and advanced materials-rapid communications*. 2009;**3:**669-671.

94. Shiryaev VS, Boussard-Plédel C, Houizot P, Jouan T, Adam JL, and Lucas J, Single-mode infrared fibers based on Te-As-Se glass system. *Materials Science and Engineering: B*. 2006;**127:**138-143.
95. Churbanov MF, Snopatin GE, Shiryaev VS, Plotnichenko VG, and Dianov EM, Recent advances in preparation of high-purity glasses based on arsenic chalcogenides for fiber optics. *J. Non-Cryst. Solids*. 2011;**357:**2352-2357.
96. Klocek P, Roth M, and Rock RD, Chalcogenide glass optical fibers and image bundles: properties and applications. *Opt Eng*. 1987;**26:**88-95.
97. Devyatykh G, Churbanov M, Scripachev I, Dianov E, and Plotnichenko V, Middle infrared As-S, As-Se, Ge-As-Se chalcogenide glass fibres. *International Journal of Optoelectronics*. 1992;**7:**237-254.
98. Zhang X, Ma H, and Lucas J, Applications of chalcogenide glass bulks and fibres. *Optoelectronics and Advanced Materials*. 2003;**5:**1327-1333.
99. Vlček M, Tichý L, Klikorka J, Tříska A, Influence of oxygen traces on physical properties of glassy GeSe2. *Journal of Materials Science*. 1987;**22:**2119-2123.
100. Shiryaev VS, Adam JL, Zhang XH, Boussard-Plédel C, Lucas J, and Churbanov MF, Infrared fibers based on Te–As–Se glass system with low optical losses. *J. Non-Cryst. Solids*. 2004;**336:**113-119.
101. Nishii J, Yamashita T, and Yamagishi T, Oxide impurity absorptions in Ge-Se-Te glass fibres. *Journal of Materials Science*. 1989;**24:**4293-4297.
102. Shiryaev VS and Churbanov MF, 1 - Preparation of high-purity chalcogenide glasses,in *Chalcogenide Glasses*, Woodhead Publishing. 2014. p. 3-35.
103. Danto S, Thompson D, Wachtel P, Musgraves JD, Richardson K, and Giroire B, A comparative study of purification routes for As2Se3 chalcogenide glass. *International Journal of Applied Glass Science*. 2013;**4:**31-41.
104. Hilton AR, Hayes DJ, and Rechtin MD, Infrared absorption of some high-purity chalcogenide glasses. *J. Non-Cryst. Solids*. 1975;**17:**319-338.

105. Thomson GW, The Antoine equation for vapor-pressure data. *Chem. Rev.* 1946;**38:**1-39.

106. Waitkins GR and Clark CW, Selenium Dioxide: Preparation, Properties, and Use as Oxidizing Agent. *Chem. Rev.* 1945;**36:**235-289.

107. Dean JA, *Lange's handbook of chemistry*. 15th ed. / John A. Dean. ed. Handbook of chemistry. 1999, London: London : McGraw-Hill.

108. *PubChem Compound Database*. National Center for Biotechnology Information [Accessed: Feb. 25, 2018]; Available from: https://pubchem.ncbi.nlm.nih.gov/compound/1119.

109. Compton BW, *Sulfur Dioxide: Properties, Applications and Hazards*. 2011, Hauppauge, United States: Nova Science Publishers, Inc.

110. Keith LS, Faroon OM, Maples-Reynolds N, and Fowler BA, Chapter 37 - Germanium,in *Handbook on the Toxicology of Metals (Fourth Edition)*, Academic Press: San Diego. 2015. p. 799-816.

111. Hultgren R, Desai PD, Hawkins DT, Gleiser M, and Kelley KK, *Selected values of the thermodynamic properties of the elements*. 1973, National standard reference data system.

112. Zhang X, Ma H, Adam J-L, Lucas J, Chen G, and Zhao D, Thermal and optical properties of the Ga–Ge–Sb–Se glasses. *Mater. Res. Bull.* 2005;**40:**1816-1821.

113. Karaksina EV, Shiryaev VS, Kotereva TV, and Churbanov MF, Preparation of high-purity Pr(3+) doped Ge–Ga–Sb–Se glasses with intensive middle infrared luminescence. *J. Lumin.* 2016;**170, Part 1:**37-41.

114. Troles J, Shiryaev V, Churbanov M, Houizot P, Brilland L, Desevedavy F, Charpentier F, Pain T, Snopatin G, and Adam JL, $GeSe_4$ glass fibres with low optical losses in the mid-IR. *Opt. Mater.* 2009;**32:**212-215.

115. Snopatin GE, Shiryaev VS, Plotnichenko VG, Dianov EM, and Churbanov MF, High-purity chalcogenide glasses for fiber optics. *Inorg. Mater.* 2009;**45:**1439.

116. Tang Z, Shiryaev VS, Furniss D, Sojka L, Sujecki S, Benson TM, Seddon AB, and Churbanov MF, Low loss Ge-As-Se chalcogenide glass fiber,

fabricated using extruded preform, for mid-infrared photonics. *Opt. Mater. Express*. 2015;**5:**1722-1737.

117. Churbanov MF, Shiryaev VS, Suchkov AI, Pushkin AA, Gerasimenko VV, Shaposhnikov RM, Dianov EM, Plotnichenko VG, Koltashev VV, Pyrkov YN, Lucas J, and Adam J-L, High-purity As-S-Se and As-Se-Te glasses and optical fibers. *Inorg. Mater.* 2007;**43:**441-447.
118. Shiryaev VS, Churbanov MF, Snopatin GE, and Chenard F, Preparation of low-loss core–clad As–Se glass fibers. *Opt. Mater.* 2015;**48:**222-225.
119. Shiryaev VS, Churbanov MF, Snopatin GE, Plotnichenko VG, Karaksina EV, Kotereva TV, Koltashev VV, and Plekhovich AD, Preparation of core-clad arsenic rich AsSe glass fiber. *J. Non-Cryst. Solids*. 2016;**448:**11-15.
120. Shiryaev V, Churbanov M, Dianov E, Plotnichenko V, Adam J and Lucas J, Recent progress in preparation of chalcogenide As-Se-Te glasses with low impurity content. *J Optoelectron Adv M*. 2005;**7:**1773-1779.
121. Désévédavy F, Renversez G, Brilland L, Houizot P, Troles J, Coulombier Q, Smektala F, Traynor N, and Adam J-L, Small-core chalcogenide microstructured fibers for the infrared. *Appl. Opt.* 2008;**47:**6014-6021.
122. Karaksina EV, Shiryaev VS, Kotereva TV, Velmuzhov AP, Ketkova LA, and Snopatin GE, Preparation of high-purity Pr^{3+} doped Ge–As–Se–In–I glasses for active mid-infrared optics. *J. Lumin.* 2016;**177:**275-279.
123. Karaksina EV, Shiryaev VS, Churbanov MF, Anashkina EA, Kotereva TV, and Snopatin GE, Core-clad Pr(3+)-doped Ga(In)-Ge-As-Se-(I) glass fibers: Preparation, investigation, simulation of laser characteristics. *Opt. Mater*. 2017;**72:**654-660.
124. Churbanov MF, Mishinov SV, Shiryaev VS, and Ketkova LA, Contamination of glassy arsenic sulfide by SiO_2 particles during melt solidification in silica glassware. *J. Non-Cryst. Solids*. 2017;
125. Churbanov M, Purification of chalcogenide glasses.,in *In Properties, Processing and Applications of Glass and Rare Earth Doped Glasses for Optical Fibers*, Hewak D: London. 1998. p. 340-343.

126. Devyatykh G, Dianov E, Plotnichenko V, Skripachev I and Churbanov M, Fiber waveguides based on high-purity chalcogenide glasses. *High-Purity Substances* 1991;**5:**1-27.

127. Crisp J and Elliott B, *Introduction to fiber optics* 3ed. 2005, Amsterdam: Elsevier Science.

128. Graham-Smith F, *Optics and photonics : and introduction / F. Graham Smith and Terry A. King*, ed. King TA. 2000, Chichester: Chichester : Wiley.

129. Paschotta R. *Field guide to optical fiber technology*. 2010. SPIE.

130. Tang J, Liu S, Zhu Q, Sun Y, Li G, Yang Z, Zhang X, Wang X, Zhang P, Dai S, and Xu Y, $As_{40}S_{59}Se_1/As_2S_3$ step index fiber for 1–5μm supercontinuum generation. *J. Non-Cryst. Solids*. 2016;**450:**61-65.

131. Cheng T, Nagasaka K, Tuan TH, Xue X, Matsumoto M, Tezuka H, Suzuki T, and Ohishi Y, Mid-infrared supercontinuum generation spanning 2.0 to 15.1 μm in a chalcogenide step-index fiber. *Opt. Lett.* 2016;**41:**2117-2120.

132. Savage SD, Miller CA, Furniss D, and Seddon AB, Extrusion of chalcogenide glass preforms and drawing to multimode optical fibers. *J. Non-Cryst. Solids*. 2008;**354:**3418-3427.

133. Jiang C, Wang X, Zhu M, Xu H, Nie Q, Dai S, Tao G, Shen X, Cheng C, Zhu Q, Liao F, Zhang P, Zhang P, Liu Z, and Zhang X-H, Preparation of chalcogenide glass fiber using an improved extrusion method. *Opt Eng*. 2016;**55:**

134. Tao G, Shabahang S, Dai S, and Abouraddy AF, Multimaterial disc-to-fiber approach to efficiently produce robust infrared fibers. *Opt. Mater. Express*. 2014;**4:**2143-2149.

135. Conseil C, Coulombier Q, Boussard-Plédel C, Troles J, Brilland L, Renversez G, Mechin D, Bureau B, Adam JL, and Lucas J, Chalcogenide step index and microstructured single mode fibers. *J. Non-Cryst. Solids*. 2011;**357:**2480-2483.

136. Sanghera JS, Aggarwal ID, Busse LE, Pureza PC, Nguyen VQ, Miklos RE, Kung FH, and Mossadegh R. *Development of low-loss IR transmitting chalcogenide glass fibers*. in *Photonics West '95*. 1995. SPIE.

137. Sanghera J and Aggarwal ID, *Infrared Fiber Optics*. 1998, Florida: CRC Press, LLC.

138. Nishii J, Morimoto S, Inagawa I, Iizuka R, Yamashita T, and Yamagishi T, Recent advances and trends in chalcogenide glass fiber technology: a review. *J. Non-Cryst. Solids*. 1992;**140:**199-208.

139. Busse L, Moon J, Sanghera J and Aggarwal I, Chalcogenide fibers deliver high IR power. *Laser Focus World*. 1996;**32:**143-166.

140. Busse L, Moon J, Sanghera J, Aggarwal I, Harrington J and Lum K. in *Proceedings of the 1995 IRIS, Speciality Group on Materials*. 1995. EIRM, Ann Arbor, MI, p. 973.

141. Aggarwal I, Busse L, SHaw L, Cole and Sanghera J. *Proceedings of the Diode Laser Technology*. 1998. Albuquerque, NM.

142. Sanghera J, and Aggarwal I. *Proceedings of the 18th International Congress on Glass*. 1998. San Francisco, CA.

143. Shibata S, Manabe T, and Horiguchi M, Preparation of Ge-S Glass Fibers with Reduced OH, SH Content. *Japanese Journal of Applied Physics*. 1981;**20:**L13.

144. Heo J, Rodrigues M, Saggese SJ, and Sigel GH, Remote fiber-optic chemical sensing using evanescent-wave interactions in chalcogenide glass fibers. *Appl. Opt.* 1991;**30:**3944-3951.

145. Sanghera JS, Kung FH, Busse LE, Pureza PC, and Aggarwal ID, Infrared evanescent absorption spectroscopy of toxic chemicals using chalcogenide glass fibers. *J. Am. Ceram. Soc.* 1995;**78:**2198-2202.

146. Nau G, Bucholtz F, Ewing K, Vohra S, Sanghera J and Aggarwal I. *Proceeding of the SPIE*. 1996, 2883: 682.

147. Sanghera JS, Pureza PC, Aggarwal ID, and Nau G, *Selective multi-chemical fiber optic sensor*. 1996, US Patent No. 5,525,800.

148. Rigas B and Wong PTT, Human colon adenocarcinoma cell lines display infrared spectroscopic features of malignant colon tissues. *Cancer Research*. 1992;**52:**84.

149. Ueda T, Yamada K, and Sugita T, Measurement of grinding temperature of ceramics using infrared radiation pyrometer with optical fiber. *Journal of Engineering for Industry*. 1992;**114:**317-322.

150. Suto H, Chalcogenide fiber bundle for 3D spectroscopy. *Infrared Phys Techn*. 1997;**38:**93-99.

151. Saito M, Takizawa M, Sakuragi S, and Tanei F, Infrared image guide with bundled As–S glass fibers. *Appl. Opt.* 1985;**24:**2304-2308.

152. Nishii J, Yamashita T, Yamagishi T, Tanaka C, and Sone H, Coherent infrared fiber image bundle. *Appl. Phys. Lett.* 1991;**59:**2639-2641.

153. Sanghera JS, Shaw LB, Busse LE, Talley DB, and Aggarwal ID. *Infrared-transmitting fiber optics for biomedical applications*. in *BiOS '99 International Biomedical Optics Symposium*. 1999. San Diego, CA: SPIE.

154. Schaafsma DT, Moon JA, Sanghera JS, and Aggarwal ID, Fused taper infrared optical fiber couplers in chalcogenide glass. *Journal of Lightwave Technology*. 1997;**15:**2242-2245.

155. Woess C, Drach M, Villunger A, Tappert R, Stalder R, and Pallua JD, Application of mid-infrared (MIR) microscopy imaging for discrimination between follicular hyperplasia and follicular lymphoma in transgenic mice. *The Analyst*. 2015;**140:**6363-6372.

156. Fabian H, Lasch P, Boese M, and Haensch W, Mid-IR microspectroscopic imaging of breast tumor tissue sections. *Biopolymers*. 2002;**67:**354-357.

157. Wood BR, Chiriboga L, Yee H, Quinn MA, McNaughton D, and Diem M, Fourier transform infrared (FTIR) spectral mapping of the cervical transformation zone, and dysplastic squamous epithelium. *Gynecologic Oncology*. 2004;**93:**59-68.

158. Hughes C and Baker MJ, Can mid-infrared biomedical spectroscopy of cells, fluids and tissue aid improvements in cancer survival? A patient paradigm. *The Analyst.* 2016;**141:**467-475.

159. Kendall C, Isabelle M, Bazant-Hegemark F, Hutchings J, Orr L, Babrah J, Baker R, and Stone N, Vibrational spectroscopy: a clinical tool for cancer diagnostics. *The Analyst*. 2009;**134:**1029-45.

160. Zhang B, Zhai CC, Qi SS, Guo W, Yang ZY, Yang AP, Gai X, Yu Y, Wang RP, Tang DY, Tao GM, and Luther-Davies B, High-resolution chalcogenide fiber bundles for infrared imaging. *Opt. Lett.* 2015;**40:**4384-4387.

161. Yang K, Wu P, Wei G, and Yu B, IR imageguide with As-S glass fibers. *J. Non-Cryst. Solids*. 1995;**184:**40-43.

162. Hilton AR, Infrared imaging bundle development at Amorphous Materials. *P Soc Photo-Opt Ins*. 1999;**3849:**60-66.

163. Zhan H, Yan X, Guo H, Xu Y, He J, Li F, Yang J, Si J, Zhou Z, and Lin A, Line–plane-switching infrared bundle for push-broom sensing fiber imaging. *Opt. Mater.* 2015;**42:**491-494.

164. Shaw B, Gibson D, Nguyen V, Gattass R, Sanghera J, and Aggarwal I. *IR imaging bundles for HWIL testing*. 2011.

165. Qi S, Zhang B, Zhai C, Li Y, Yang A, Yu Y, Tang D, Yang Z, and Luther-Davies B, High-resolution chalcogenide fiber bundles for longwave infrared imaging. *Opt. Express*. 2017;**25:**26160-26165.

166. Williams D.F., Definitions in Biomaterials,in *Progress in Biomedical Engineering*, Elsevier: Amsterdam. 1987. p. 72.

167. Ratner BD, Biological testing of biomaterials,in *Biomaterials science : an introduction to materials in medicine*, Ratner BD, Hoffman AS, Schoen FJ, Lemons JE, and Yaszemski M, Elsevier Science: San Diego, United States. 2012.

168. Peters K, Unger R E and Kirkpatrick C J, Biocompatibility Testing in *Biomedical Materials*, Narayan R, Springer: USA. 2009.

169. Tao S-H and Bolger PM, Hazard assessment of germanium supplements. *Regul. Toxicol. Pharm.* 1997;**25:**211-219.

170. Mauro MO, Sartori D, Oliveira RJ, Ishii PL, Mantovani MS, and Ribeiro LR, Activity of selenium on cell proliferation, cytotoxicity, and apoptosis

and on the expression of CASP9, BCL-XL and APC in intestinal adenocarcinoma cells. *Mutation Research/Fundamental and Molecular Mechanisms of Mutagenesis*. 2011;**715:**7-12.

171. Ramos JF and Webster TJ, Cytotoxicity of selenium nanoparticles in rat dermal fibroblasts. *International Journal of Nanomedicine*. 2012;**7:**3907-3914.

172. Tylenda CA, Sullivan Jr DW, and Fowler BA, Chapter 27 - Antimony,in *Handbook on the Toxicology of Metals (Fourth Edition),* Academic Press: San Diego. 2015. p. 565-579.

173. Keirsse J, Boussard-Plédel C, Loréal O, Sire O, Bureau B, Leroyer P, Turlin B, and Lucas J, IR optical fiber sensor for biomedical applications. *Vib. Spectrosc*. 2003;**32:**23-32.

174. Wilhelm AA, Lucas P, DeRosa DL, and Riley MR, Biocompatibility of Te–As–Se glass fibers for cell-based bio-optic infrared sensors. *J. Mater. Res.* 2007;**22:**1098-1104.

175. Gotshal Y, Simhi R, Sela B-A, and Katzir A, Blood diagnostics using fiberoptic evanescent wave spectroscopy and neural networks analysis. *Sensors and Actuators B: Chemical*. 1997;**42:**157-161.

176. Bureau B, Zhang XH, Smektala F, Adam J-L, Troles J, Ma H-l, Boussard-Plèdel C, Lucas J, Lucas P, Le Coq D, Riley MR, and Simmons JH, Recent advances in chalcogenide glasses. *J. Non-Cryst. Solids*. 2004;**345-346:**276-283.

177. Zou Y, Moreel L, Lin H, Zhou J, Li L, Danto S, Musgraves JD, Koontz E, Richardson K, Dobson KD, Birkmire R, and Hu J, Solution Processing and Resist-Free Nanoimprint Fabrication of Thin Film Chalcogenide Glass Devices: Inorganic–Organic Hybrid Photonic Integration. *Advanced Optical Materials*. 2014;**2:**759-764.

178. Furniss D and Seddon AB, Thermal Analysis of Inorganic Compound Glasses and Glass-Ceramics,in *Principles and Applications of Thermal Analysis*, Blackwell Publishing Ltd. 2008. p. 410-449.

179. *Personal communication with Dr N. Neate, Senior Research Technician, Wolfson Centre for Materials Research Department of Mechanical, Materials and Manufacturing Engineering, Faculty of Engineering, University of Nottingham, UK*. 2014-2017.

180. Lucas P, Wilhelm AA, Videa M, Boussard-Plédel C, and Bureau B, Chemical stability of chalcogenide infrared glass fibers. *Corros. Sci.* 2008;**50:**2047-2052.

181. O'Brien J, Wilson I, Orton T, and Pognan F, Investigation of the Alamar Blue (resazurin) fluorescent dye for the assessment of mammalian cell cytotoxicity. *Eur. J. Biochem.* 2000;**267:**5421-6.

182. *Part 5: Tests for in vitro cytotoxicity*, in *ISO 10993-5: 2009 Biological evaluation of medical devices* 2009.

183. Phillips JC, Topology of covalent non-crystalline solids I: Short-range order in chalcogenide alloys. *J. Non-Cryst. Solids*. 1979;**34:**153-181.

184. Moynihan CT, Easteal AJ, Wilder J, and Tucker J, Dependence of the glass transition temperature on heating and cooling rate. *The Journal of Physical Chemistry*. 1974;**78:**2673-2677.

185. Sharda S, Sharma N, Sharma P, and Sharma V, Glass transition and crystallization kinetics analysis of Sb–Se–Ge chalcogenide glasses. *J. Therm. Anal. Calorim.* 2014;**115:**361-366.

186. Singh K and Saxena NS, Kinetics of $Ge_{20}Se_{80-x}As_x$ (x = 0, 5, 10, 15 and 20) in glass transition region. *Bull. Mater. Sci.* 2003;**26:**543-546.

187. Sharda S, Sharma N, Sharma P, and V aS, Basic physical analysis of new Sb-Se-Ge-In chalcogenide glassy alloys by predicting structural units: a theoretical approach. *Chalcogenide Letters*. 2012;**9:**389-395.

188. Barták J, Koštál P, Podzemná V, Shánělová J, and Málek J, Crystal growth kinetics and viscous behavior in Ge2Sb2Se5 undercooled melt. *The Journal of Physical Chemistry B*. 2016;**120:**7998-8006.

189. Wakkad MM, Shokr EK, and Mohamed SH, Crystallization kinetics and some physical properties of as-prepared and annealed Ge–Sb–Se chalcogenide glasses. *Physica Status Solidi (a)*. 2001;**183:**399-411.

190. Pizzini S, Physical Chemistry of Semiconductor Materials Processing,in *Physical Chemistry of Semiconductor Materials and Processes*, John Wiley & Sons, Ltd. 2015. p. 363-398.
191. Bletskan DI, Chepur DV, Mitrovtskii IM, Polazhinets NV, and Potorii MV, Electrical and photoelectric properties of layered crystals of $GeSe_2$ obtained by various methods. *Inorg. Mater. (Engl. Transl.); (United States)*. 1985;**21:**214-220.
192. Petkov V, Qadir D, and Shastri SD, Rapid structure determination of disordered materials: study of $GeSe_2$ glass. *Solid State Commun.* 2004;**129:**239-243.
193. Aleksandrovich EV, Minaev VS, and Timoshenkov SP, Structural relaxation of glassy $GeSe_2$ during isothermal annealing below and above T g. *Technical Physics*. 2015;**60:**510-514.
194. Ligero RA, Va´zquez J, Villares P, and Jime´nez-Garay R, Resolving overlapping peaks in differential scanning calorimetry. *J. Non-Cryst. Solids*. 1990;**124:**63-70.
195. Seddon AB, *Personal communication*. Jan 2018.
196. Fang Y, Jayasuriya D, Furniss D, Tang ZQ, Sojka Ł, Markos C, Sujecki S, Seddon AB, and Benson TM, Determining the refractive index dispersion and thickness of hot-pressed chalcogenide thin films from an improved Swanepoel method. *Optical and Quantum Electronics*. 2017;**49:**
197. El-Sayed SM, Far-infrared studies of the amorphous $Sb_{x}Ge_{28-x}Se_{72}$ glassy semiconductor. *Semicond. Sci. Technol.* 2003;**18:**337.
198. Boolchand P, Chen P, and Vempati U, Intermediate Phases, structural variance and network demixing in chalcogenides: The unusual case of group V sulfides. *J. Non-Cryst. Solids*. 2009;**355:**1773-1785.
199. Wang R, Yan K, Yang Z, and Luther-Davies B, Structural and physical properties of $Ge_{11.5}As_{24}S_{64.5\cdot}xSe_{64.5\cdot}(1-x)$ glasses. *J. Non-Cryst. Solids*. 2015;**427:**16-19.
200. Yaws CL, *The Yaws Handbook of Vapor Pressure: Antoine Coefficients*. Second ed. 2015, Texas, USA: Gulf Professional Publishing

201. Jolly WL and Latimer WM, The Equilibrium $Ge_{(s)} + GeO_{2(s)} = 2GeO_{(g)}$. The Heat of Formation of Germanic Oxide. *J. Am. Chem. Soc.* 1952;**74:**5757-5758.

202. Nishii J, Yamashita T, and Yamagishi T, Chalcogenide glass fiber with a core–cladding structure. *Appl. Opt.* 1989;**28:**5122-5127.

203. Rumble JR, Lide DR, and Bruno TJ, *CRC handbook of chemistry and physics : a ready-reference book of chemical and physical data*. 98th ed. / editor-in-chief John Rumble ; associate editors David R. Lide, Thomas J. Bruno. ed. Handbook of chemistry and physics. 2017, Boca Raton ; London: Boca Raton ; London : CRC Press.

204. Yaws CL, Chapter 2 - Physical Properties – Inorganic Compounds,in *The Yaws Handbook of Physical Properties for Hydrocarbons and Chemicals (Second Edition)*, Gulf Professional Publishing: Boston. 2015. p. 684-810.

205. Zhang B, Guo W, Yu Y, Zhai C, Qi S, Yang A, Li L, Yang Z, Wang R, Tang D, Tao G, and Luther-Davies B, Low loss, high NA chalcogenide glass fibers for broadband mid-infrared supercontinuum generation. *J. Am. Ceram. Soc.* 2015;**98:**1389-1392.

206. Jiang C, Cheng C, Zhu Q, Wang X, Nie Q, Dai S, Tao G, Zhu M, Liao F, Zhang P, Shen X, Xu T, Zhang P, Liu Z, and Zhang X, Fabrication and characterization of Ge–Sb–Se–I glasses and fibers. *Appl. Phys. A*. 2015;**120:**127-135.

207. Albrecht-Buehler G, Filopodia of spreading 3T3 cells. Do they have a substrate-exploring function? *The Journal of Cell Biology*. 1976;**69:**275-286.

208. McKenzie JL and Webster TJ, Protein Interactions at Material Surfaces,in *Biomedical Materials*, Narayan R, Springer US: Boston, MA. 2009. p. 215-237.

209. Lucas P, Solis MA, Coq DL, Juncker C, Riley MR, Collier J, Boesewetter DE, Boussard-Plédel C, and Bureau B, Infrared biosensors using hydrophobic chalcogenide fibers sensitized with live cells. *Sensors and Actuators B: Chemical*. 2006;**119:**355-362.

210. Bacakova L, Filova E, Parizek M, Ruml T, and Svorcik V, Modulation of cell adhesion, proliferation and differentiation on materials designed for body implants. *Biotechnol. Adv.* 2011;**29:**739-767.

211. Borenfreund E and Puerner JA, A simple quantitative procedure using monolayer cultures for cytotoxicity assays (HTD/NR-90). *Journal of tissue culture methods*. 1985;**9:**7-9.

212. Repetto G, del Peso A, and Zurita JL, Neutral red uptake assay for the estimation of cell viability/cytotoxicity. *Nature protocols*. 2008;**3:**1125-31.

213. Wolf MF, Coleman KP, and Lewerenz GM, In Vitro Assessment of Cell and Tissue Compatibility,in *Biomaterials Science: An Introduction to Materials in Medicine*, Ratner BD, Hoffman AS, Schoen FJ, and Lemons JE, Elsevier. 2013. p. 593-608.

Appendices

Appendix 1 Personal codes

a) Glass melting codes

Personal melt code	Corresponding Mid-Infrared Photonics Group melt code	Composition /at. %	Melting ampoule (ID/OD mm)	HF etched?	Details
M_HAP001	M106HAP	$Ge_{25}Sb_{10}Se_{65}$	8/12 Baumbach	N	Bulk characterisations
M_HAP002	M110HAP	$Ge_{25}Sb_{10}Se_{65}$	10/14 Baumbach	N	First fibre drawing investigation
M_HAP003	M118HAP	$Ge_{25}Sb_{10}Se_{65}$	10/14 Baumbach	N	Second fibre drawing investigation (new fibre-drawing tower BOC gas)
M_HAP004	M133HAP	$Ge_{25}Sb_{10}Se_{65}$	10/14 Baumbach	N	The ampoule failed during melting
M_HAP005	M135HAP	$Ge_{20}Sb_{10}Se_{70}$	15/18 Baumbach	Y	Enough for two small-scale extrusions: 1) for TMA analysis and 2) for fibre-drawing
M_HAP006	M146HAP	$Ge_{20}Sb_{10}Se_{70}$	10/14 Baumbach	Y	Cytotoxicity (Teo) and characterisation bulk samples
M_HAP007	M156HAP	$Ge_{20}Sb_{10}Se_{67}S_3$	10/14 Baumbach	Y	Bulk characterisations

Glass melting codes (continued)

Personal melt code	Corresponding Mid-Infrared Photonics Group melt code	Composition /at. %	Melting ampoule (ID/OD mm)	HF etched?	Details
M_HAP008	M157HAP	$Ge_{20}Sb_{10}Se_{67}S_3$	15/18 Baumbach	Y	Enough for two small-scale extrusions: 1) for TMA analysis and 2) for fibre-drawing
M_HAP009	M164HAP	$Ge_{25}Sb_{10}Se_{65}$	15/18 Baumbach	Y	Enough for two small-scale extrusions: 1) for TMA analysis and 2) for fibre-drawing
M_HAP010	M167HAP	$Ge_{20}Sb_{10}Se_{70}$	10/14 Multilab	Y	Aim to fibre-draw from an as-annealed preform
M_HAP011	M182HAP	$Ge_{20}Sb_{10}Se_{70}$	29/32 Multilab	Y	Core glass for co-extrusion
M_HAP012	M183HAP	$Ge_{25}Sb_{10}Se_{65}$	8/12 Multilab	Y	Potential TMA measurements
M_HAP013	M191HAP	$Ge_{20}Sb_{10}Se_{67}S_3$	29/32 Multilab	Y	Cladding glass for co-extrusion
M_HAP014	M198HAP	$Ge_{20}Sb_{10}Se_{70}$ + 1000 ppm wt. $TeCl_4$	29/32 Multilab	Y	First distillation attempt of core glass

Glass melting codes (continued)

Personal melt code	Corresponding Mid-Infrared Photonics Group melt code	Composition /at. %	Melting ampoule (ID/OD mm)	HF etched?	Details
M_HAP015	M203HAP	$Ge_{20}Sb_{10}Se_{70}$ + 1000 ppm wt. $TeCl_4$	29/32 Multilab	Y	Second distillation attempt of core glass
M_HAP016	M210HAP	$Ge_{20}Sb_{10}Se_{70}$ + 1000 ppm wt. $TeCl_4$	29/32 Multilab	Y	Third distillation attempt of core glass

(b) Extrusion codes

Personal extrusion code	Corresponding Mid-infrared Photonics Group code	Composition /at. %	From which melt?	Details
E_HAP001	E057HAP	$Ge_{20}Sb_{10}Se_{70}$	M_HAP005	~4.7 mm diameter samples for TMA investigations
E_HAP002	E059HAP	$Ge_{20}Sb_{10}Se_{70}$	M_HAP005	~4.7 mm diameter fibre-drawing preform
E_HAP003	E062HAP	$Ge_{20}Sb_{10}Se_{67}S_3$	M_HAP008	~4.7 mm diameter samples for TMA investigations
E_HAP004	E064HAP	$Ge_{20}Sb_{10}Se_{67}S_3$	M_HAP008	~4.7 mm diameter fibre-drawing preform
E_HAP005	E065HAP	$Ge_{25}Sb_{10}Se_{65}$	M_HAP009	~4.7 mm diameter fibre-drawing preform
E_HAP006	E077HAP	$Ge_{20}Sb_{10}Se_{70}$/ $Ge_{20}Sb_{10}Se_{67}S_3$	M_HAP011/ M_HAP013	~10 mm diameter co-extrusion of core/ cladding glasses

c) Fibre-drawing codes

Personal fibre-drawing code	Corresponding Mid-infrared Photonics Group code	Composition /at. %	From which melt (or extrusion) code?	Details
F_HAP001	F036HAP	$Ge_{25}Sb_{10}Se_{65}$	M_HAP002	Unsuccessful fibre-drawing
F_HAP002	F042HAP	$Ge_{25}Sb_{10}Se_{65}$	M_HAP003	Unsuccessful fibre-drawing
F_HAP003	F051HAP	$Ge_{20}Sb_{10}Se_{70}$	M_HAP005 (E_HAP002)	Fibre-drawing unstructured core glass
F_HAP004	F057HAP	$Ge_{20}Sb_{10}Se_{67}S_3$	M_HAP008 (E_HAP004)	Fibre-drawing unstructured cladding glass
F_HAP005	F060HAP	$Ge_{25}Sb_{10}Se_{65}$	M_HAP009 (E_HAP005)	Unsuccessful fibre-drawing
F_HAP006	F063HAP	$Ge_{20}Sb_{10}Se_{70}$	M_HAP010	Fibre-drawing unstructured core glass
F_HAP007	F074HAP	$Ge_{20}Sb_{10}Se_{70}$/ $Ge_{20}Sb_{10}Se_{67}S_3$	M_HAP011/M_HAP013 (E_HAP006)	Co-extruded SIF
F_HAP008	F080HAP	$Ge_{20}Sb_{10}Se_{70}$	M_HAP016 (D_HAP004*)	Fibre-drawing distilled core glass
F_HAP009	F022JHB	$Ge_{22}Sb_8Se_{70}$/ $Ge_{24}Sb_4Se_{72}$	-	Fibre for cytotoxicity measurements
F_HAP010	ZQT024	$As_{40}Se_{60}$	-	Fibre for cytotoxicity measurements

d) Distillation codes

Personal distillation code	Corresponding Mid-infrared Photonics Group code	Composition /at. %	From which melt code?	Details
D_HAP001	D028HAP	$Ge_{20}Sb_{10}Se_{70}$	M_HAP005 (E_HAP001)	Bent tube distillation
D_HAP002	D033HAP	$Ge_{20}Sb_{10}Se_{70}$ + 1000 ppm wt. $TeCl_4$	M_HAP014	Unsuccessful distillation attempt 1
D_HAP003	D034HAP	$Ge_{20}Sb_{10}Se_{70}$ + 1000 ppm wt. $TeCl_4$	M_HAP015	Unsuccessful distillation attempt 2
D_HAP004	D035HAP	$Ge_{20}Sb_{10}Se_{70}$ + 1000 ppm wt. $TeCl_4$	M_HAP016	Successful core glass distillation

Appendix 2

MELT CODE: M167HAP

AIM AND HISTORY

Composition investigated: Ge$_{20}$Sb$_{10}$Se$_{70}$ at. %
Melted in 10/14 mm ID/OD Multilab ampoule (HF etched)
Predicted Tg: 214°C annealed at this temperature so was a direct comparison to previous Ge$_{25}$Sb$_{10}$Se$_{65}$ glass.
The main aim of this glass was compare fibre drawing from an as-annealed preform to that from M110HAP and M18HAP.

PRIOR PURIFICATION

Se weight: 19.5885 g   Ampoule ID/OD= 10/14

Same ampoule for batching later?	Y
Step	**Schedule**
1	Pr1 200 PL1 200 Pd1 0h
2	Pr2 100 PL2 260 Pd2 0.5h
3	Pr3 300 PL3 30
4	

Sb weight: 15.1779 g   Ampoule ID/OD= 10/14

Step	**Schedule**
1	Pr1 250 PL1 500 Pd1 0.1
2	Pr2 100 PL2 570 Pd3 3
3	Pr3 300 PL3 30
4	
5	

HOST GLASS (H1) BATCH INFORMATION

Date: 28/09/16   Weight: ~30 g   Batched by: HAP

Component	Mol. (%)	Weight (%)	Source	Product ID	Purity (%)	Theory (g)	Added (g)
Ge	20	-	Materion	-	5N	5.1466	5.1468
Sb	10	-	Cerac	-	6N	4.3152	4.3153
Se	70	-	Materion	-	5N	19.5885	19.5885

Ampoule Notes and MELTING, QUENCHING AND ANNEALING SCHEDULES

Ampoule prepared by	HAP
Ampoule quality	Good
Ampoule ID/OD (mm)	10/14
Ampoule length (mm)	400
Ampoule HF? / conc.	Y (by DF 40%, for 5 mins)
Ampoule annealed?	Y
Air baking time/temperature	6h @ 1000
Vacuum baking time/temperature	6h @ 1000
Other note	
Ampoule sealed by	HAP
Sealing vacuum (mbar)	<2 x 10^{-5}
Sealing time	~10 mins

Which furnace?	New	
Rock type	Timed	
Rock angle	Horizontal	
Rock interval	0.5 min	
Step	**Melting Schedule**	**Rock?**
1	RT to 450°C @ 40°C/h	No rocking
2	Dwell @450 °C for 2 h	No rocking
3	450°C to 900°C @ 40°C/h	Rocking
4	Dwell @ 900°C for 12 h	Rocking
5	900°C to 700°C @ 50°C/h	No rocking (v)
6	Dwell for ~1 hr	No rocking
7		

Melted by	HAP
Start date	30/09/16

Quenching & annealing by	**HAP**	
Dwell time before quenching	**1 hour vertical at 700 C**	
Date	**03/10/16**	
Which annealing furnace?	**New**	
Quenching type	**T(°C)**	**Time**
Air quenching	Room temp	45 s
Quenching furnace	214	45 s

Step	**Annealing Schedule**
1	Step to 214 C
2	Dwell 0.5 h
3	End
4	
5	Note: I annealed at Tg for direct comparison

GLASS QUALITY NOTES AND OBSERVATIONS:

	Comments
Glass fracture?	N
Ampoule fracture?	N
Other notes	Glass quenched well

Appendix 2

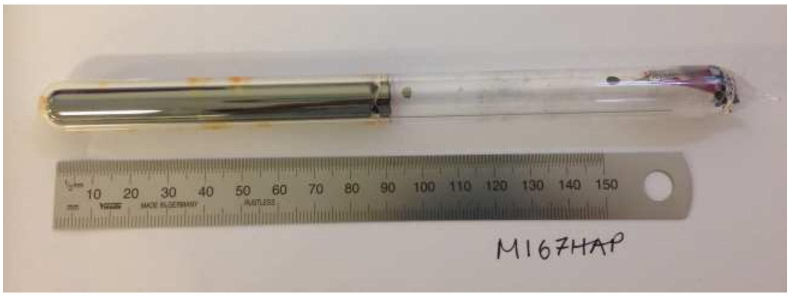

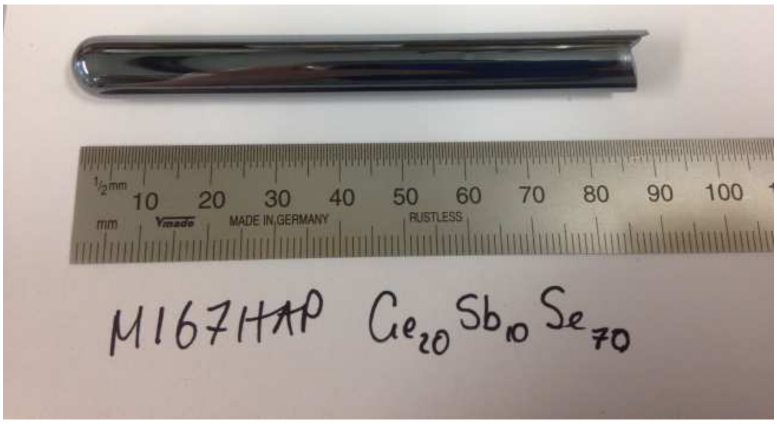

Appendix 3

Core Extrusion E057HAP

Date: 17/03/2016 **By: David Furniss** **Assistant:** Harriet Parnell

EXTRUSION BOULE DESCRIPTION

Description	
Core	$Ge_{20}Sb_{10}Se_{70}$
Glass codes used (inner working out)	M135HAP
Length(s) (mm)	13.66 mm
Diameter(s) (mm)	15.0 mm

Boule glass purification	Sb,Se,: purified

Description	
Boule polished?	**no**
Other description	n/a

EXTRUSION PLAN

Core glass
Melt M135HAP
Ge20 Sb10 Se70
13.66mm h, 15.0mm OD
Tg=214°C

15mm BARREL, bronze bobbin
Die 4.7mm ID graphite
Punch with Viton O-ring
Vacuum
Furnace at start 270°C
Contact at 176.5mm so end at 190.1mm

EXTRUSION RECORD

Glass T_g (ºC)	Die ID (mm)	Barrel ID (mm)
214	**4.7**	**15**

Gas?	Gas speed
Vac	

Time(s)	Die temperature (ºC)	Furnace temperature(ºC)	Load (kg)	Position(mm)
0	22	270	0	159.8
4320	273.4	265	100	176.5
5350	275.26	263	100	177.8
6150	276.5	261	100	178.36
6470	276.5	260	100	178.58
8940	277.59	259	100	180.27
20767	276.16	260	100	188.5

EXTRUDED ROD RESULT

Rod diameter (mm)	4.7
Rod length (mm)	**125**
Rod bended?	**No, good**
Rod surface?	**good**

Appendix 3

OTHER EXTRUSION RESULT NOTES AND OBSERVATIONS

We went straight to 270 C because JHB had run the same composition before (E042) and so we knew roughly what temperature we should aim for.

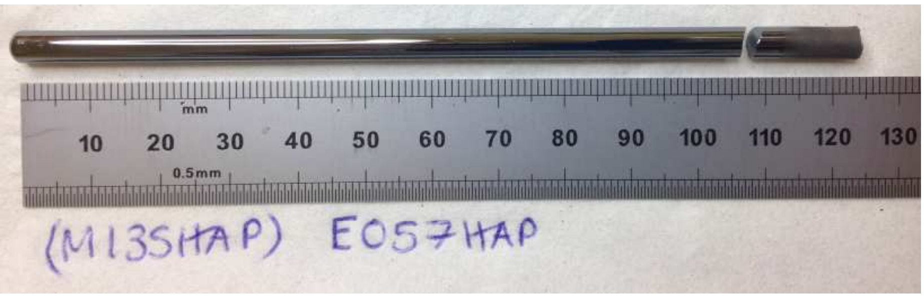

Figure 1. Over view of extrusion

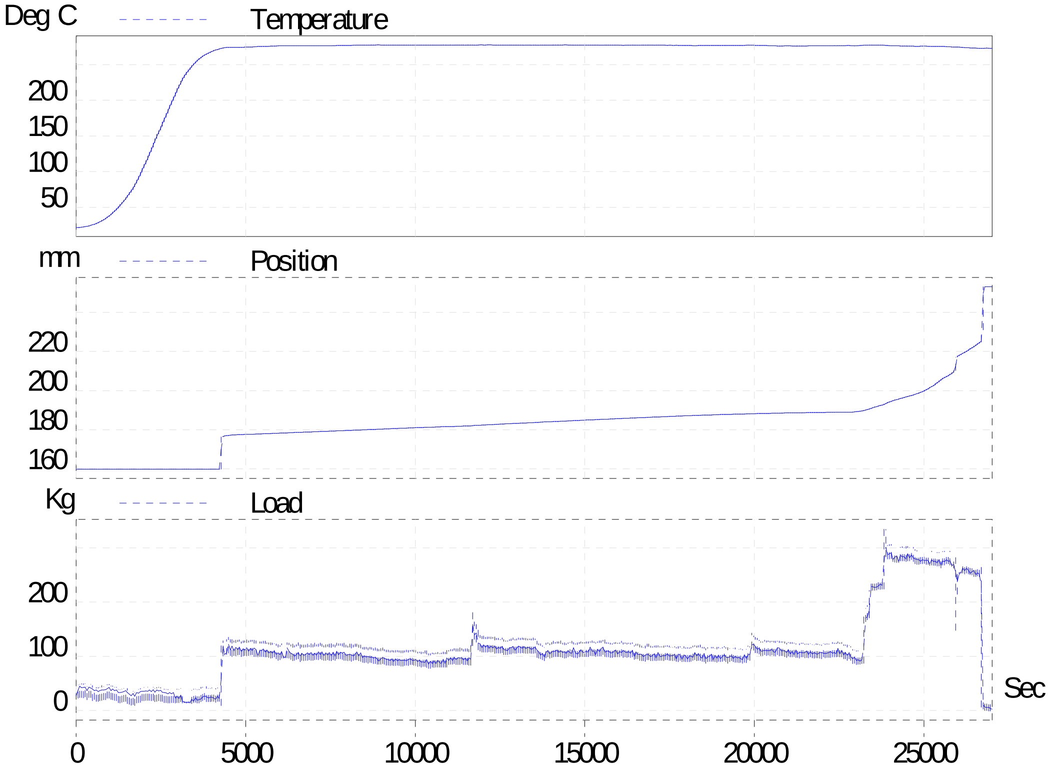

Appendix 3

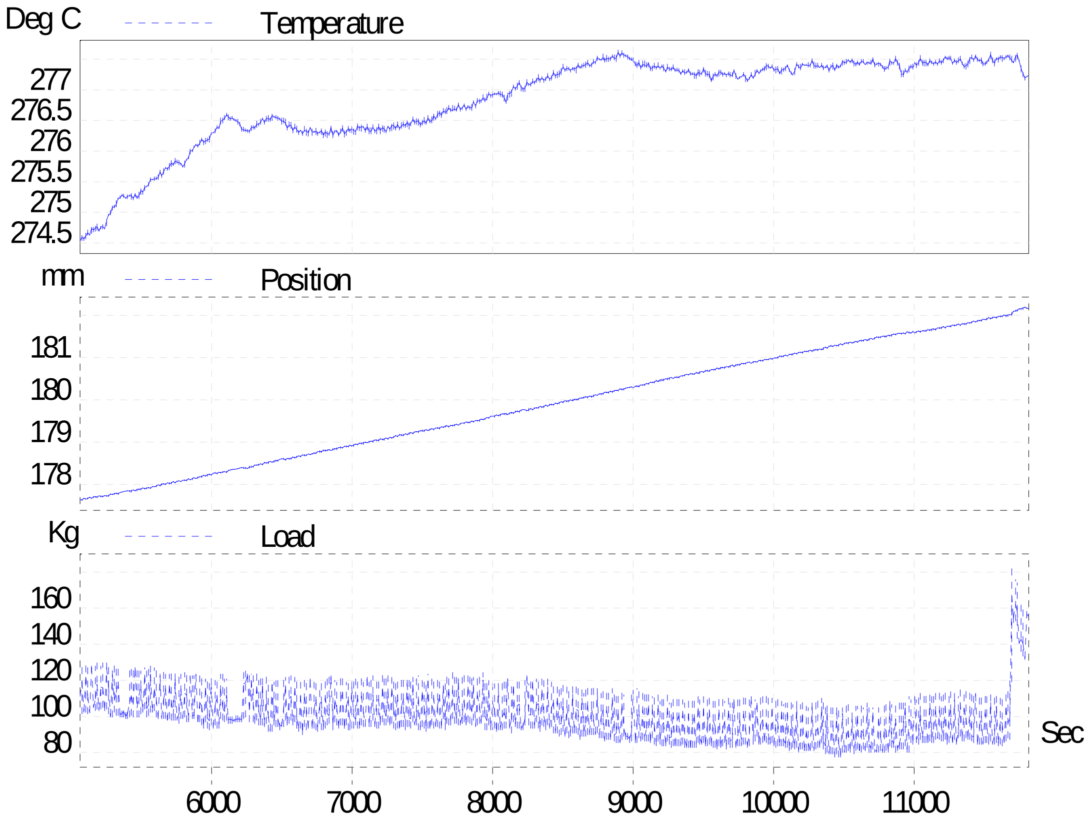
Deg C
Temperature
277
276.5
276
275.5
275
274.5
mm
Position
181
180
179
178
Kg
Load
160
140
120
100
80
Sec
6000
7000
8000
9000
10000
11000

Appendix 4

Fibre Drawing Document: F051

Date: 19/04/16 **By:** DF **Assistant:** HAP

PREFORM DESCRIPTION

Description	
Core/cladding?	Core $Ge_{20}Sb_{10}Se_{70}$ at. %
Glass codes used (inner working out)	**M135HAP (E059)**
Length (mm)	115 mm
Diameter (mm)	4.7 mm
Made from extrusion/ melt-quenching?	Extrusion (E059)
Preform purification key points	Sb and Se purified prior to batching

Surface quality?	**Good**
Etched?	N
Etching liquid	n/a
Etching time/ /temperature /pressure	n/a
Other preform history description	n/a

Description

FIBRE DRAWING PLAN

First attempt at drawing non-stoichiometric $Ge_{20}Sb_{10}Se_{70}$ at. % core glass composition, from extruded ~4.7 mm diameter preform.

Fibre use for?	**Fibre diameter (µm)**	**Fibre length (m)**
Fibre loss	200	~10
Refractive index	200	~2
Cytotoxicity	200	~5

FIBRE DRAWING RECORD

Preform diameter (mm)	4.7		
Fibre diameter (µm)	**200**		
Preform feed speed (mm/min)	5		
Draw speed (m/min)	2.75		
Total Fibre Length	~69 m		

Receptor	**ID/ OD (mm)**
Graphite	*

Coating?	**No**
Coating material	n/a

Fibre diameter	
Stage	**Power**
1	6 %
2	8 %
3	10 %
4	12 %

Fibre diameter	
Stage	**Power**
10	26 %
11	28 % (first section dropped)
12	30 %
13	32 % (stable 200 ±10 µm fibre)

FIBRE DRAWING RESULTS NOTES AND OBSERVATIONS

	Notes and Observations
Successful?	Yes
Fibre quality	Good
Other	Slight fibre diameter fluctuation over the first 5 meters.

PLW data logging for D_HAP002

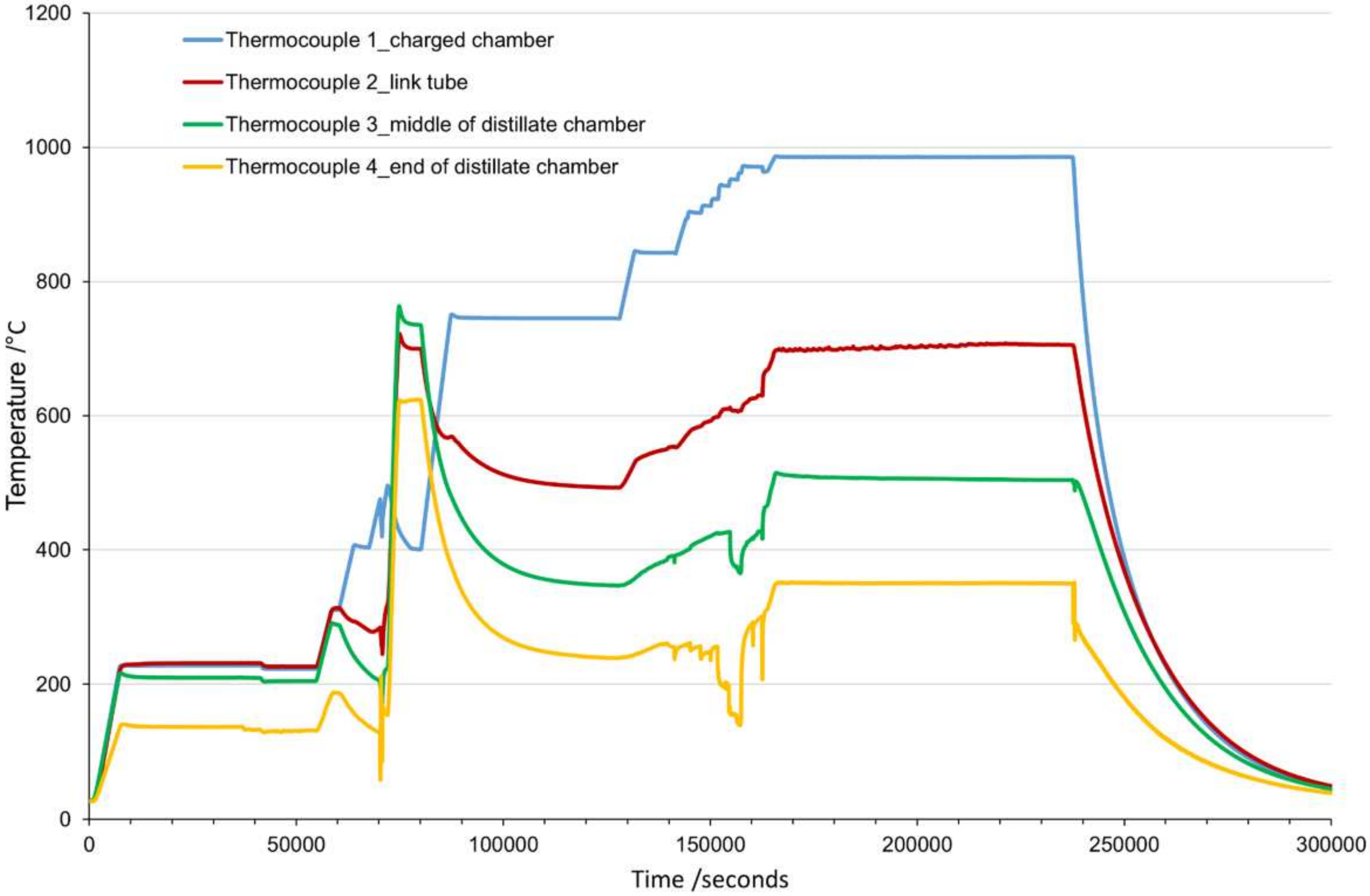

Appendix 5

PLW data logging for D_HAP003

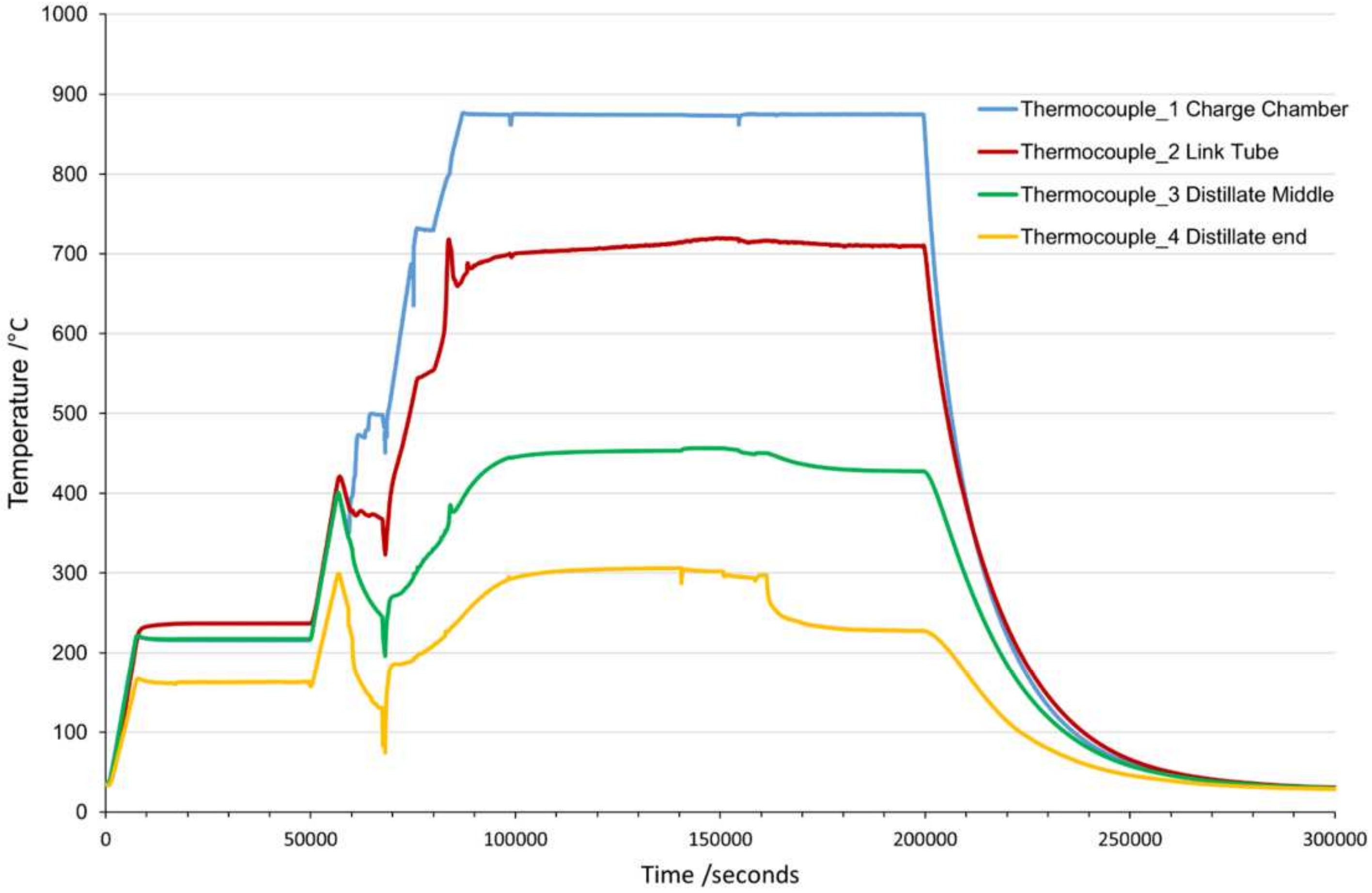

Appendix 6

PLW data logging for D_HAP004

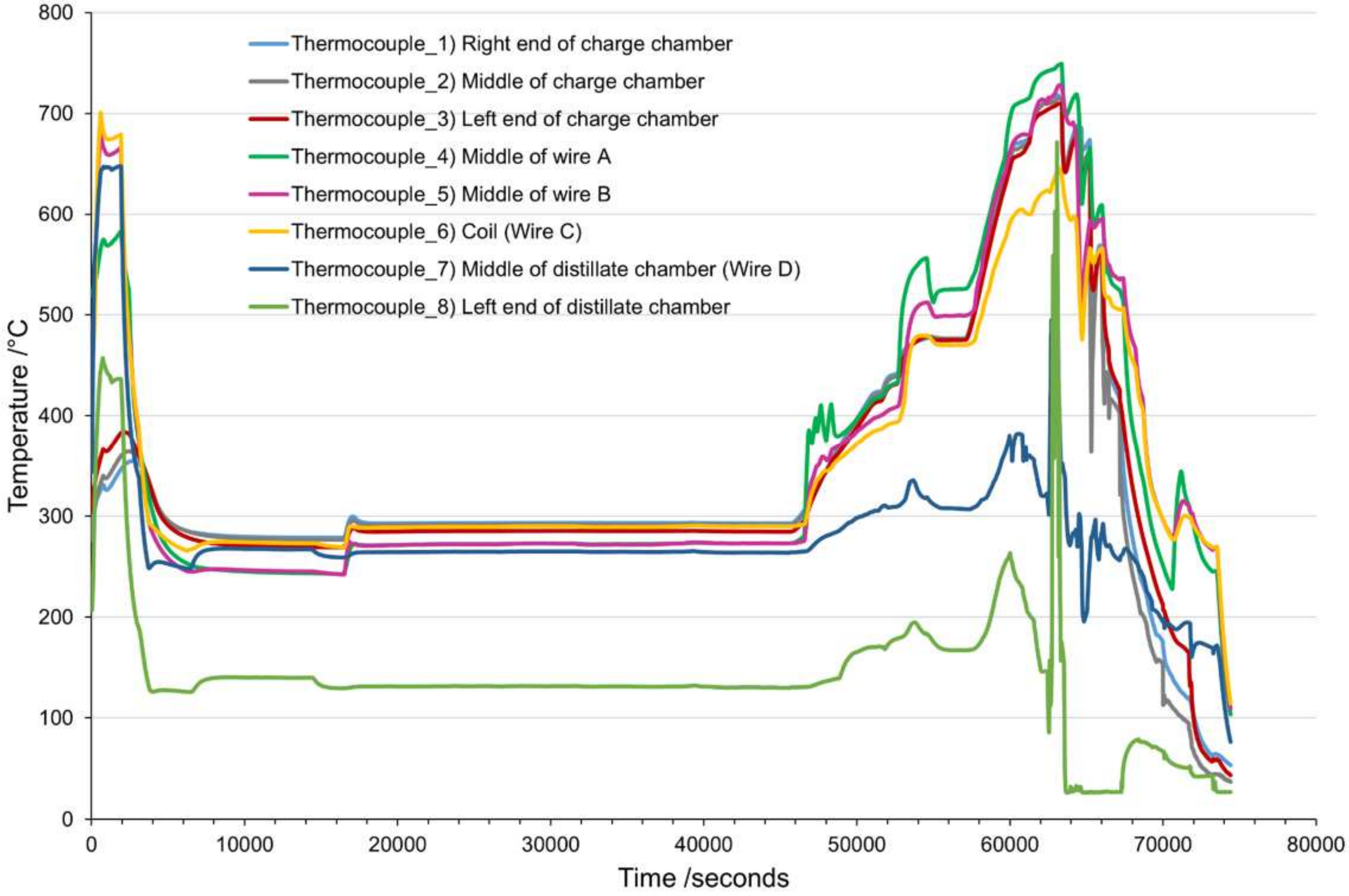

Appendix 7